

Electronic Thesis and Dissertation Repository

---

8-11-2017 12:00 AM

## Pulmonary Image Segmentation and Registration Algorithms: Towards Regional Evaluation of Obstructive Lung Disease

Fumin Guo, *The University of Western Ontario*

Supervisor: Dr. Grace Parraga, *The University of Western Ontario*

Co-Supervisor: Dr. Aaron Fenster, *The University of Western Ontario*

A thesis submitted in partial fulfillment of the requirements for the Doctor of Philosophy degree  
in Biomedical Engineering

© Fumin Guo 2017

Follow this and additional works at: <https://ir.lib.uwo.ca/etd>



Part of the [Biomedical Commons](#)

---

### Recommended Citation

Guo, Fumin, "Pulmonary Image Segmentation and Registration Algorithms: Towards Regional Evaluation of Obstructive Lung Disease" (2017). *Electronic Thesis and Dissertation Repository*. 4746.  
<https://ir.lib.uwo.ca/etd/4746>

This Dissertation/Thesis is brought to you for free and open access by Scholarship@Western. It has been accepted for inclusion in Electronic Thesis and Dissertation Repository by an authorized administrator of Scholarship@Western. For more information, please contact [wlsadmin@uwo.ca](mailto:wlsadmin@uwo.ca).

## Abstract

Pulmonary imaging, including pulmonary magnetic resonance imaging (MRI) and computed tomography (CT), provides a way to sensitively and regionally measure spatially heterogeneous lung structural-functional abnormalities. These unique imaging biomarkers offer the potential for better understanding pulmonary disease mechanisms, monitoring disease progression and response to therapy, and developing novel treatments for improved patient care. To generate these regional lung structure-function measurements and enable broad clinical applications of quantitative pulmonary MRI and CT biomarkers, as a first step, accurate, reproducible and rapid lung segmentation and registration methods are required. In this regard, a  $^1\text{H}$  MRI lung segmentation algorithm that employs complementary hyperpolarized  $^3\text{He}$  MRI functional information was developed for improved lung segmentation. The  $^1\text{H}$ - $^3\text{He}$  MRI joint segmentation algorithm was formulated as a *coupled continuous min-cut model* and solved through convex relaxation, for which a dual *coupled continuous max-flow model* was proposed and a *max-flow*-based efficient numerical solver was developed. Experimental results on a clinical dataset of 25 chronic obstructive pulmonary disease (COPD) patients ranging in disease severity demonstrated that the algorithm provided rapid lung segmentation with high accuracy, reproducibility and diminished user interaction. Then a general  $^1\text{H}$  MRI left-right lung segmentation approach was developed by exploring the left-to-right lung volume proportion *prior*. The challenging volume proportion-constrained multi-region segmentation problem was approximated through convex relaxation and equivalently represented by a max-flow model with bounded flow conservation conditions. This gave rise to a multiplier-based high performance numerical implementation based on convex optimization theories. In 20 patients with mild-to-moderate and severe asthma, the approach demonstrated high agreement with manual segmentation, excellent reproducibility and computational efficiency. Finally, a CT- $^3\text{He}$  MRI deformable registration approach that coupled the complementary CT- $^1\text{H}$  MRI registration was developed. The joint registration problem was solved by exploring optical-flow techniques, primal-dual analyses and convex optimization theories. In a diverse group of patients with asthma and COPD, the

registration approach demonstrated lower target registration error than single registration and provided fast regional lung structure-function measurements that were strongly correlated with a reference method. Collectively, these lung segmentation and registration algorithms demonstrated accuracy, reproducibility and workflow efficiency that all may be clinically-acceptable. All of this is consistent with the need for broad and large-scale clinical applications of pulmonary MRI and CT.

**Keywords:** Anatomical CT, structural-functional MRI, COPD, asthma, regional pulmonary structure-function, segmentation, registration, convex optimization

## Co-Authorship Statement

The following thesis contains three manuscripts published in scientific journals. As the first author of these peer-reviewed manuscripts, I made significant contributions to all aspects of the studies as well as manuscript preparation, submission and revisions. Specifically, I was responsible for literature review, algorithm design, code development, experimental setup, image processing and analysis, statistical analysis and interpretation, drafting and submitting the manuscripts. As the Principal Investigators and Supervisors, Dr. Grace Parraga and Dr. Aaron Fenster provided ongoing guidance and contributed to study design, algorithm development, experimental setup, validation, data analysis and interpretation, drafting and final revisions of all work. Patient visits and pulmonary function measurements were managed by Sandra Blamires.  $^3\text{He}$  gas polarization was performed by Andrew Wheatley. MRI acquisition was performed by Trevor Szekeres and David Reese. Specific contributions for other co-authors for the manuscripts contained in this thesis are summarized as follows.

Chapter 2 is an original research article titled “Globally Optimal Co-Segmentation of Three-Dimensional Pulmonary  $^1\text{H}$  and Hyperpolarized  $^3\text{He}$  MRI with Spatial Consistency Prior” and was published in *Medical Image Analysis* in 2015. This manuscript was co-authored by Fumin Guo, Jing Yuan, Martin Rajchl, Sarah Svenningsen, Dante PI Capaldi, Khadija Sheikh, Aaron Fenster and Grace Parraga. I performed literature review, designed the experiments, optimized and implemented the algorithm, conducted algorithm evaluation, analysed and interpreted the results, drafted and revised the manuscript. Jing Yuan derived the algorithm, developed the code and aided in writing the method section. Martin Rajchl assisted with experimental setup. Sarah Svenningsen provided manual segmentation as the reference standard. Dante PI Capaldi and Khadija Sheikh initialized the algorithm. All the authors assisted with revising the manuscript. Permission to reproduce this article was granted by Elsevier and is provided in Appendix G.

Chapter 3 is an original research article titled “Anatomical Pulmonary Magnetic Resonance

Imaging Segmentation for Regional Structure-Function Measurements of Asthma” and was published in Medical Physics in 2016. This manuscript was co-authored by Fumin Guo, Sarah Svenningsen, Rachel L Eddy, Dante PI Capaldi, Khadija Sheikh, Aaron Fenster and Grace Parraga. As the first author of this manuscript, I performed literature review, algorithm design, optimization and implementation, experiment setup, algorithm validation, results analysis and interpretation, and manuscript preparation. Sarah Svenningsen provided manual segmentation of the images as the reference standard and seeded the images for algorithm initialization. Rachel L Eddy seeded the images for algorithm initialization and revised the manuscript. Dante PI Capaldi and Khadija Sheikh assisted with manuscript revisions. Permission to reproduce this article was granted by John Wiley and Sons and is provided in Appendix G.

Chapter 4 is an original research article titled “Thoracic CT-MRI Co-Registration for Regional Pulmonary Structure-Function Measurements of Obstructive Lung Disease” and was published in Medical Physics in 2017. This manuscript was co-authored by Fumin Guo, Sarah Svenningsen, Miranda Kirby, Dante PI Capaldi, Khadija Sheikh, Aaron Fenster and Grace Parraga. I performed literature review, algorithm design, optimization and implementation, software development, fiducial marker identification, lung segments generation, algorithm performance evaluation, results analysis and interpretation, and manuscript preparation and revisions. Sarah Svenningsen, Miranda Kirby, Dante PI Capaldi and Khadija Sheikh assisted with revising the manuscript. Permission to reproduce this article was granted by John Wiley and Sons and is provided in Appendix G.

# Acknowledgements

First, I would like to thank my supervisors Drs. Grace Parraga and Aaron Fenster for providing me the opportunity and ongoing support as well as guidance throughout this journey. I am appreciative for the unique research environment you created and your endless support along this road. Thank you for giving me the opportunity to collaborate with the brightest minds and excel my research abilities. Your wisdom, knowledge and experience have shaped me so much in all aspects of my graduate career that I cannot thank you enough. The invaluable experiences that I have gained in the past four years at Robarts will accompany me throughout my future professional endeavors, and for this I am grateful.

I would also like to take the opportunity to thank my advisory committee, Drs. Terry Peters and Aaron Ward. Thank you for mentoring, guiding my research and pointing me the directions. Your challenges, criticisms and comments are insightful and your encouragement as well as guidance have been imperative to develop and improve my professional skills. Furthermore, I would like to thank Dr. David G McCormack for helping me identify the clinical problems and this has motivated my research.

To the Parraga lab members, I am grateful for your kindness, patience, mentorship and assistance. To John Drozd - thank you for leading me into the field of medical image processing and sitting together going through my abstracts. To Alexi Ouriadov - thank you for teaching me MRI physics and answering my questions. To Andrew Wheatley - thank you for guiding me through the segmentation software, helping me with computer issues, and training me on noble gas polarization. To David Reese and Trevor Szekeres - thank you for acquiring high quality images and solving my Ubuntu problems. To David Tessier - thank you for installing a GPU for me as well as providing me access to other computational resources. To Lyndsey Reid-Jones - thank you for taking wonderful pictures for us and being a great listener.

To my labmates and friends, thank you for being my side for the past years and making my time at Robarts memorable. To Sarah Svenningsen - thank you for taking time to provide me

the manual segmentation and motivating me to improve and refine my image processing algorithms. Your assistance with my manuscript preparation and course assignments is invaluable. To Dante Capaldi - you are one of the funniest people I have ever met and became friends with. Your help with medical imaging physics and my presentation is greatly appreciated. Thank you for telling me the many stories about western world, watching the Transformer with me and buying dollar jokes in the US. To Khadija Sheikh - thank you for helping me with MRI physics and discussing the big picture and clinical impact. Thank you for inviting me to your Christmas party and buying me the tea and mug. To Anurag Bhalla - thank you for helping me with pulmonary medicine and clinical problems. To Meng Tang and Dr. Yuri Boykov - our discussions of computational image processing methods and optimization models provide invaluable insights into my research. To Christine Ellwood - thank you for organizing the club runs and providing me numerous documents. Additional thanks go to Damien Pike, Eric Lessard, Rachel L Eddy, Heather Young, Amir Owrangi, Miranda Kirby, Nikhil Kanhere, Weijing Ma, Tamas Lindenmaier, Gregory Paulin, Nanxi Zha, Emma Bluemke, Megan Fennema, Michal Stankiewicz, Christiane Sarah, Tomi Nano, Terenz Escartin, Jing Yuan and Martin Rajchl.

Finally and most importantly, I would like to thank my family and friends. To my parents – thank you for supporting me to pursue my dreams and encouraging me to make through the challenges with unconditional love.

# Contents

<b>Abstract</b>	<b>i</b>
<b>Co-Authorship Statement</b>	<b>iii</b>
<b>Acknowledgements</b>	<b>v</b>
<b>List of Figures</b>	<b>xii</b>
<b>List of Tables</b>	<b>xxi</b>
<b>List of Appendices</b>	<b>xxiii</b>
<b>List of Abbreviations</b>	<b>xxiv</b>
<b>1 Introduction</b>	<b>1</b>
1.1 Burden of Obstructive Lung Disease . . . . .	1
1.2 The Respiratory System . . . . .	4
1.2.1 The Airways . . . . .	4
1.2.2 The Alveoli . . . . .	6
1.2.3 Ventilation and Diffusion . . . . .	7
1.3 COPD and Asthma Pathophysiology . . . . .	8
1.3.1 Normal Aging Lung . . . . .	8
1.3.2 COPD and Asthma . . . . .	10
1.4 Clinical Managements of COPD and Asthma . . . . .	13
1.4.1 Lung Function Measurements . . . . .	13



1.4.2	Lung Functional Decline . . . . .	17
1.5	Pulmonary Imaging and Imaging Biomarkers . . . . .	20
1.5.1	Chest x-ray . . . . .	20
1.5.2	X-ray Computed Tomography . . . . .	22
1.5.3	Nuclear Medicine . . . . .	27
1.5.4	Pulmonary Magnetic Resonance Imaging . . . . .	30
1.6	Medical Image Segmentation, Registration and Evaluation Methods . . . . .	39
1.6.1	Image Segmentation . . . . .	39
1.6.2	Medical Image Segmentation Algorithms . . . . .	39
1.6.3	Segmentation Performance Evaluation . . . . .	51
1.6.4	Image Registration . . . . .	54
1.6.5	Medical Image Registration Algorithms . . . . .	55
1.6.6	Registration Performance Evaluation . . . . .	59
1.7	Thesis Objectives . . . . .	61
<b>2</b>	<b>Pulmonary <math>^1\text{H}</math>-<math>^3\text{He}</math> MRI Co-Segmentation</b>	<b>103</b>
2.1	Introduction . . . . .	103
2.1.1	Previous Studies . . . . .	104
2.1.2	Contributions . . . . .	106
2.2	Methods . . . . .	108
2.2.1	Spatially Continuous Co-Segmentation Model . . . . .	108
2.2.2	Convex Relaxed Co-Segmentation Model . . . . .	111
2.3	Coupled Continuous Max-Flow Approach . . . . .	111
2.3.1	Coupled Continuous Max-Flow Model . . . . .	111
2.3.2	Duality and Exactness of Convex Relaxation . . . . .	114
2.3.3	Coupled Continuous Max-Flow Algorithm . . . . .	115
2.4	Experiments . . . . .	118
2.4.1	Study Subjects . . . . .	118

2.4.2	MRI . . . . .	119
2.4.3	Segmentation Pipeline . . . . .	120
2.4.4	Evaluation Methods . . . . .	123
2.4.5	Comparison to Single Modality Segmentation . . . . .	125
2.4.6	Sensitivity to $^1\text{H}$ - $^3\text{He}$ MRI Registration Error . . . . .	125
2.4.7	Operator Variability . . . . .	126
2.5	Results . . . . .	126
2.5.1	3D Co-Segmentation: Representative Results . . . . .	126
2.5.2	Comparison to Manual Segmentation . . . . .	127
2.5.3	Comparison to Single Modality Segmentation . . . . .	131
2.5.4	Influence of $^1\text{H}$ - $^3\text{He}$ MRI Registration on Co-Segmentation . . . . .	131
2.5.5	Operator Variability . . . . .	132
2.5.6	Computation Time . . . . .	132
2.6	Discussion . . . . .	133
2.6.1	Accuracy . . . . .	133
2.6.2	Co-Segmentation vs Single Segmentation . . . . .	135
2.6.3	Influence of Pre-Registration for Co-Segmentation . . . . .	136
2.6.4	Reproducibility . . . . .	137
2.6.5	Runtime . . . . .	137
2.6.6	Comparison to Previous Studies . . . . .	138
2.7	Conclusion . . . . .	139
<b>3</b>	<b><math>^1\text{H}</math> MRI Volume Proportion Preserved Segmentation</b>	<b>146</b>
3.1	Introduction . . . . .	146
3.2	Materials and Methods . . . . .	148
3.2.1	Study Subjects and Data Acquisition . . . . .	148
3.2.2	Pulmonary $^1\text{H}$ MRI Multi-Region Segmentation with Volume Proportion Prior . . . . .	149

3.2.3	Algorithm Implementation . . . . .	155
3.2.4	Evaluation Methods . . . . .	157
3.3	Results . . . . .	159
3.3.1	Subject Demographics . . . . .	159
3.3.2	Algorithm and Manual Segmentation Measurement Reproducibility . . . . .	160
3.3.3	Multi-region Segmentation and Parameter Sensitivity . . . . .	161
3.3.4	Relationship and Agreement of Manual and Algorithm Lung Volumes . . . . .	163
3.3.5	Computation Time . . . . .	165
3.4	Discussion . . . . .	167
3.5	Conclusion . . . . .	174
<b>4</b>	<b>CT-<sup>1</sup>H/<sup>3</sup>He MRI Joint Registration</b>	<b>183</b>
4.1	Introduction . . . . .	183
4.2	Materials and Methods . . . . .	185
4.2.1	Study Subjects and Image Acquisition . . . . .	185
4.2.2	Overview . . . . .	187
4.2.3	Algorithm Implementation . . . . .	194
4.2.4	Validation Methods . . . . .	196
4.3	Results . . . . .	199
4.3.1	Subject Demographics . . . . .	199
4.3.2	Joint CT- <sup>1</sup> H/ <sup>3</sup> He MRI Registration Accuracy . . . . .	200
4.3.3	Effect of Coupled <sup>1</sup> H MRI on Registration Accuracy . . . . .	201
4.3.4	Effect of CT- <sup>1</sup> H MRI Rigid Registration Matrix and Choice of $\beta$ on Registration Accuracy . . . . .	202
4.3.5	Runtime . . . . .	202
4.4	Discussion . . . . .	203
4.5	Conclusion . . . . .	210

<b>5</b>	<b>Conclusions and Future Directions</b>	<b>219</b>
5.1	Overview of Rationale and Research Objectives . . . . .	219
5.2	Summary and Conclusions . . . . .	221
5.3	Limitations . . . . .	223
5.3.1	General Limitations . . . . .	223
5.3.2	Specific Limitations . . . . .	225
5.4	Future Directions . . . . .	228
5.4.1	2D Free-Breathing <sup>1</sup> H MRI Ventilation Measurements Pipeline . . . . .	228
5.4.2	Fast and High Resolution MRI Acquisition and Reconstruction . . . . .	233
5.4.3	UTE MRI Lung Structure-Function Measurements . . . . .	235
5.4.4	Pulmonary Imaging Platform: A GUI-Oriented Pulmonary MRI and CT Image Processing Platform . . . . .	239
5.5	Significance and Impact . . . . .	242
<b>Appendix A</b>	<b>Discrete and Continuous Min-Cut/Max-Flow</b>	<b>252</b>
<b>Appendix B</b>	<b>A Dual Volume Proportion-Preserved Max-Flow Model</b>	<b>257</b>
<b>Appendix C</b>	<b>A Volume Proportion-Preserved Continuous Max-Flow Algorithm</b>	<b>260</b>
<b>Appendix D</b>	<b>Proof of Proposition 2</b>	<b>263</b>
<b>Appendix E</b>	<b>An Efficient Numerical Solver</b>	<b>266</b>
<b>Appendix F</b>	<b>Supplementary Materials</b>	<b>269</b>
<b>Appendix G</b>	<b>Permission for Reproduction of Scientific Articles</b>	<b>272</b>
<b>Appendix H</b>	<b>Health Science Research Ethics Board Approval Notices</b>	<b>276</b>
<b>Appendix I</b>	<b>Curriculum Vitae</b>	<b>282</b>

# List of Figures

1.1	Global leading causes of death. Adapted from the World Health Organization’s Global Health Observatory (GHO) data (2015) [4]. . . . .	2
1.2	Repeat hospitalizations by conditions at first admission. Adapted from Canadian Institute of Health Information (2008) [12]. . . . .	3
1.3	Schematic representation of human airways with generations and dimensions. Reproduced from <i>Pulmonary Physiology</i> , 8 <sup>th</sup> edition [22]. . . . .	5
1.4	Lobar and segmental bronchi (indicated by dark circles) that correspond to lung lobes and segments. Adapted from Folch <i>et al.</i> . Seminars in respiratory and critical care medicine [26]. . . . .	7
1.5	Small airway and lung parenchyma pathologies. Top panel: normal, COPD and asthma airways are shown from left to right. COPD airways: infiltration with inflammatory cells, reduced airway caliber, thickened smooth muscle, connective tissue deposition, and disrupted alveolar attachments; Asthma airways: inflammatory cells exudation, thickened smooth muscle and basement membrane with increased airway wall thickness. Bottom panel: normal and COPD lung parenchyma. Adapted from Hogg <i>et al.</i> , <i>Lancet</i> (2004) [51] and Woods <i>et al.</i> , <i>Magnetic Resonance in Medicine</i> (2006) [52]. . . . .	13
1.6	Handheld spirometer and volume-time airflow curve depicting FEV <sub>1</sub> and FVC.	14
1.7	Body plethysmograph and measurements of lung volumes using a volume-time curve. Adapted from Wanger <i>et al.</i> , <i>European Respiratory Journal</i> (2005) [54]. .	16

1.8	Normal lung function decline during aging in never smokers and accelerated lung function decline in regular smokers. However, following smoking cessation, lung function decline rates return to normal. Adapted from Fletcher <i>et al.</i> British Medical Journal (1977) [57]. . . . .	18
1.9	X-ray radiograph of a healthy, COPD and asthma subject. Healthy case courtesy of Dr. Ian Bickle, Radiopaedia.org, rID: 50318. COPD (predominantly emphysema) case from The Townsville Hospital, Radiopaedia.org, rID: 19446. The lung is hyper-inflated as evidenced by more than 10 posterior ribs, flattened diaphragm, narrowed mediastinum and regions of hyper-lucency that are indicative of emphysema. Asthma case courtesy of Dr. Ian Bickle, Radiopaedia.org, rID: 33470. Lung hyper-inflation is indicated by flattened diaphragm and more than 6 anterior or 10 posterior ribs at the lung diaphragm level. . . . .	22
1.10	Representative CT images of a healthy, COPD and asthma subject. . . . .	26
1.11	Representative conventional FGRE and UTE MR coronal images of a healthy, COPD and asthma subject. In conventional FGRE MRI, lung structural abnormalities inherent to obstructive lung disease cannot be visually distinguished due to low tissue and <sup>1</sup> H density. In contrast, UTE MRI provides enhanced visualization of the lung with higher signal intensities and regions of low signal intensities are visible in obstructive lung disease compared to the healthy volunteer. . . . .	35
1.12	Representative co-registered hyperpolarized <sup>3</sup> He (cyan) and <sup>1</sup> H (gray) MR coronal images of a healthy, COPD and asthma subject. Homogeneous <sup>3</sup> He MRI signal intensities are observed in the healthy while heterogeneous signal intensities are seen in obstructive lung disease. . . . .	38

2.1	Complementary edge information in $^1\text{H}$ and $^3\text{He}$ MRI. A <sub>i</sub> ) $^1\text{H}$ MRI coronal slice with inset box A <sub>1</sub> shown expanded in A <sub>ii</sub> ) and A <sub>2</sub> shown expanded in A <sub>iii</sub> ). B <sub>i</sub> ) $^3\text{He}$ MRI coronal slice with inset box B <sub>1</sub> shown expanded in B <sub>ii</sub> ) and B <sub>2</sub> shown expanded in B <sub>iii</sub> ). . . . .	105
2.2	Coupled flow-maximization settings. For two image domains $\Omega_i, i \in \{1, 2\}$ , two source terminals $s_i$ and two sink terminals $t_i$ were linked to each pixel $x \in \Omega_i$ . The source flow $p_s^i(x)$ was directed from $s_i$ and the sink flow $p_t^i(x)$ was directed to $t_i$ along with a spatial flow $q_i(x)$ around each $x$ . An extra flow $r(x)$ was also directed from $x \in \Omega_1$ to the same position in $\Omega_2$ . . . . .	112
2.3	Block diagram of the proposed co-segmentation pipeline. . . . .	121
2.4	User seeds on co-registered $^3\text{He}$ and $^1\text{H}$ MRI. A) Combined view of $^3\text{He}$ (cyan) and $^1\text{H}$ MRI (grayscale). B) User-defined seeds on $^1\text{H}$ MRI. C) User-defined seeds on $^3\text{He}$ MRI. . . . .	122
2.5	Representative algorithm co-segmentation for a single COPD subject. A) Three-dimensional co-segmentation results are shown for two-dimensional anterior to posterior slices. B) Co-segmented whole lung volume rendered result. (Yellow: manual segmentation, purple: co-segmentation. $DSC = 94.3\%$ , $RMS E = 3.4$ mm, $\delta V_E = 0.15$ L, $\delta V_P = 2.3\%$ ) . . . . .	127
2.6	Relationship and agreement of algorithm- ( $V_A$ ) and manually- ( $V_M$ ) generated lung volumes. A) Linear correlation of algorithm- and manually-generated lung volumes. B) Bland-Altman plots of algorithm- and manually-generated lung volumes, <i>solid line</i> indicates the mean difference and <i>dotted lines</i> represent the 95% limits of agreement. . . . .	130
3.1	Pulmonary $^1\text{H}$ MRI segmentation challenges. Centre coronal $^1\text{H}$ MRI slices for three asthma participants with yellow arrows showing representative weak edges and protruding structures. . . . .	148

3.2	The volume-proportion preserved approach and pipeline for pulmonary $^1\text{H}$ MRI multi-region segmentation. A) Max-flow configuration for the volume-proportion preserved Potts model. B) Pipeline for volume-proportion preserved multi-region $^1\text{H}$ MRI segmentation. . . . .	153
3.3	Representative user seeds and the generated probability density function for algorithm segmentation for three asthmatic subjects. Top panel: Green, blue and purple lines represent user seeds on the left and right lung and image background. Bottom panel: Corresponding MRI signal intensity distributions shown in colour as demonstrated in the middle panel images. . . . .	156
3.4	Representative $^1\text{H}$ MRI left (green) and right (blue) lung segmentation results. Solid and dashed lines represent algorithm and manual segmentation, respectively. A) 2D and 3D coronal view of the lung contours and the rendered left and right lung volumes. B) 2D and 3D sagittal view of the lung boundaries and the rendered lung volumes. C) 2D and 3D axial view of the lung contours and the rendered individual lung volumes. . . . .	162
3.5	Comparison of two and three-region segmentation approach. A) Whole lung Dice-similarity-coefficient and <i>RMSE</i> , and, B) absolute volume error and absolute percent volume error for the three-region (white) and two-region (gray) segmentation approaches. Values are means for all subjects and error bars are <i>SD</i> . * $p < 0.0001$ . . . . .	164
3.6	Algorithm segmentation parameter sensitivity tests. The optimized parameters ( $\alpha$ : red, $\lambda_1$ : green, $\lambda_2$ : blue, $\lambda_3$ : black ) were changed by -15% ~ 15% and the algorithm segmentation accuracy results are shown in terms of A) <i>DSC</i> , B) <i>RMSE</i> , C) absolute volume error, and D) absolute percent volume error for the left lung. . . . .	165



3.7 Relationships and Agreement for algorithm- and manually-generated Lung volumes. Black dots show linear regression for algorithm- and manually-generated A) left ( $VA_L$  and  $VM_L$ ), C) right ( $VA_R$  and  $VM_R$ ), and, E) whole ( $VA_W$  and  $VM_W$ ) lung volumes. Bland-Altman analysis of agreement is shown for B) left ( $VA_L$  and  $VM_L$ ), D) right ( $VA_R$  and  $VM_R$ ), and, F) whole ( $VA_W$  and  $VM_W$ ) lung. Dotted lines indicate the upper and lower limits and solid lines represent the biases. Coloured circles identify three algorithm to manual lung volume outliers corresponding to S2 (red), S14 (blue) and S16 (green) in Table 2. Gray dots in E) and F) represent the linear correlation ( $r = 0.75$ ,  $p = 0.0002$ ,  $y = 0.7x+1.33$ ) and Bland-Altman plots for algorithm and plethysmography measured (FRC+1L) lung volume. . . . . 166

4.1 Representative CT,  $^1\text{H}/^3\text{He}$  MR images, and the proposed CT- $^3\text{He}$  MRI structure-function measurements workflow. A) CT,  $^1\text{H}$  and  $^3\text{He}$  MR images of an asthma and a COPD patient. B) CT- $^3\text{He}$  MRI structure-function measurements workflow in three steps (S1, S2 and S3). S1-A) CT to  $^1\text{H}$  MRI rigid registration. S1-B)  $^3\text{He}$  to  $^1\text{H}$  MRI rigid and deformable registration. S2-A) Joint CT- $^1\text{H}$  and CT- $^3\text{He}$  MRI deformable registration. S2-B) CT lung segments generation using segmented airways. S2-C)  $^3\text{He}$  MRI ventilation and defects segmentation. S3-A) Segmental  $^3\text{He}$  MRI VDP calculation. . . . . 189

4.2 Representative CT and  $^3\text{He}$  MRI fiducials and the spatial distribution throughout the lung. A) Top panel: a CT fiducial within inset boxes expanded and identified by crosshairs in coronal, sagittal and axial plane. Bottom panel: a  $^3\text{He}$  MRI fiducial within inset boxes expanded and identified by crosshairs in coronal, sagittal and axial plane. B) Spatial distribution of the 109 pairs of CT (“+”) and  $^3\text{He}$  (“x”) MRI fiducials projected in coronal, sagittal and axial plane. Each fiducial position is normalized to the respective image and shown in anterior/posterior, right/left and superior/inferior directions with “0” representing the right-most, anterior-most and inferior-most, “1” for the left-most, posterior-most and the superior-most of the respective images. . . . . 197

4.3 CT- $^3\text{He}$  MRI registration accuracy and  $^3\text{He}$  MRI WL VDP measurements. A) *TRE* distribution for joint deformable CT- $^1\text{H}/^3\text{He}$  MRI registration (black), direct CT- $^1\text{H}$  MRI free-form deformation registration (gray), and direct CT- $^1\text{H}$  MRI rigid registration (light gray). Representative improvements of using the joint CT- $^1\text{H}/^3\text{He}$  MRI registration method are indicated by yellow arrows. B) Linear correlation of two sets of WL VDP generated by the proposed approach and a semi-automated method. C) Bland-Altman analysis of the two sets of WL VDP. Dotted lines indicate the upper and lower limits and solid lines represent the bias (0.97%). . . . . 201

4.4 Illustration of joint CT-<sup>1</sup>H/<sup>3</sup>He MRI registration using consistent deformation *prior*.  
 The 1<sup>st</sup> row shows representative registered <sup>3</sup>He (cyan) and <sup>1</sup>H (gray) MRI as inputs.  
 The 2<sup>nd</sup>, 3<sup>rd</sup> and 4<sup>th</sup> rows show CT-<sup>3</sup>He MRI registration by registering CT to <sup>1</sup>H  
 MRI (no <sup>3</sup>He information), <sup>3</sup>He MRI (no <sup>1</sup>H information), and both <sup>1</sup>H and <sup>3</sup>He MRI,  
 respectively, where the respective displacement fields (purple vectors) within the in-  
 set boxes are shown expanded in yellow boxes. The 1<sup>st</sup> column shows representative  
 improvements of joint CT-<sup>1</sup>H/<sup>3</sup>He MRI registration on image edges compared with  
 individual CT-<sup>1</sup>H MRI and CT-<sup>3</sup>He MRI registration, where the joint registration dis-  
 placement field is consistent with both individual registration but dominated by CT-<sup>1</sup>H  
 MRI registration (no <sup>3</sup>He information). The 2<sup>nd</sup> column shows similar results on im-  
 age landmarks, where the joint registration displacement field is consistent with both  
 individual registration but dominated by CT-<sup>3</sup>He MRI registration (no <sup>1</sup>H informa-  
 tion). Note that CT-<sup>1</sup>H MRI, CT-<sup>3</sup>He MRI and joint CT-<sup>1</sup>H/<sup>3</sup>He MRI registration were  
 independently optimized. . . . . 207

5.1 FD (left) and hyperpolarized <sup>3</sup>He MRI (right) ventilation maps for a COPD  
 patient. . . . . 232

5.2 Algorithm lung segmentation accuracy and FD-VDP measurements for the 10  
 subjects. A) Comparison of algorithm lung segmentation and manual lung de-  
 lineation using DSC. B) Pearson correlation of algorithm FD-VDP and <sup>3</sup>He  
 MRI VDP. C) Bland-Altman analysis of agreement for FD-VDP and <sup>3</sup>He-VDP,  
 where solid lines indicate the mean difference and dotted lines represent the up-  
 per and lower limits. . . . . 232

5.3	Representative UTE MRI lung and voxel labelling probability maps using the adaptive kernel K-mean approach. A) UTE MRI lung signal intensity inhomogeneity and example user seeds (red). B) K-nearest neighbour (cyan) of the user seeds (red) using signal intensity only. C) K-nearest neighbour (cyan) of the user seeds (red) by combining signal intensity and voxel spatial location information. The density of cyan dots relates to the probability of assigning a “lung” label to the voxels. Yellow contours represent manual segmentation and the arrows indicate improvements by incorporating voxel spatial location information (same user seeds used for B) and C)). . . . .	238
5.4	Automated UTE MRI lung segmentation workflow and example results for three asthma patients. An atlas image is registered to each individual volume and the pre-segmented lung mask is deformed to initialize the segmentation algorithm. Dash contours represent deformed atlas lung masks and solid contours indicate automated algorithm segmentation results. . . . .	239
5.5	Preliminary automated UTE MRI lung segmentation results. Anterior-to-posterior slices and 3D-rendered lung volumes are shown from upper left to lower right. .	240
5.6	Graphical user interface of Pulmonary Imaging Platform. . . . .	241
A.1	Max-flow/min-cut graph in A) discrete and B) continuous domain. . . . .	253

F.1 Illustration of joint CT- $^1\text{H}/^3\text{He}$  MRI registration using consistent deformation prior. The 1<sup>st</sup> row shows representative registered  $^3\text{He}$  (cyan) and  $^1\text{H}$  (gray) MRI as inputs. The 2<sup>nd</sup>, 3<sup>rd</sup>, and 4<sup>th</sup> rows show CT- $^3\text{He}$  MRI registration by registering CT to  $^1\text{H}$  MRI only,  $^3\text{He}$  MRI only, and  $^1\text{H}$  and  $^3\text{He}$  MRI both, respectively, where the respective displacement fields (purple vectors) within the inset boxes are shown expanded in yellow boxes. The 1<sup>st</sup> and 4<sup>th</sup> columns show representative improvements of joint CT- $^1\text{H}/^3\text{He}$  MRI registration on image edges and landmarks compared with individual CT- $^1\text{H}$  MRI and CT- $^3\text{He}$  MRI registration, where the joint registration displacement field is consistent with both individual registration but dominated by CT- $^1\text{H}$  MRI registration (no  $^3\text{He}$  information). The 2<sup>nd</sup> and 5<sup>th</sup> columns show similar results on image edges and landmarks, where the joint registration displacement field is consistent with both individual registration but dominated by CT- $^3\text{He}$  MRI registration (no  $^1\text{H}$  information). The 3<sup>rd</sup> and 6<sup>th</sup> columns show CT- $^1\text{H}/^3\text{He}$  MRI registration displacement fields consistent with both individual registrations on image edges and landmarks. . . 270

# List of Tables

1.1	Grading of COPD airflow limitation severity based on post-bronchodilator FEV <sub>1</sub>	19
2.1	Subject demographic and pulmonary function measurements . . . . .	119
2.2	Parameters for <sup>1</sup> H- <sup>3</sup> He co-segmentation and <sup>1</sup> H MRI single segmentation . . .	123
2.3	Group-by-group comparison of <sup>1</sup> H segmentation and <sup>1</sup> H- <sup>3</sup> He co-segmentation. * <i>p</i> < 0.05 . . . . .	128
2.4	Evaluation of <sup>3</sup> He- <sup>1</sup> H registration accuracy on algorithm performance . . . . .	128
2.5	Co-segmentation and single <sup>1</sup> H MRI segmentation performance. * <i>p</i> < 0.0001 .	129
2.6	Relationship of algorithm and manually-generated lung volumes by subject subgroup . . . . .	129
2.7	Impact of manual segmentation: co-segmentation results based on three rounds of manual segmentation . . . . .	130
2.8	Intra and inter-observer variability . . . . .	132
2.9	Time required for manual segmentation and partial runtime (s) for co-segmentation algorithm . . . . .	132
3.1	Subject demographics and pulmonary function measurements . . . . .	160
3.2	Algorithm and manual segmentation reproducibility . . . . .	161
3.3	Dice-similarity-coefficient and <i>RMSE</i> reproducibility . . . . .	163
3.4	Dice-similarity-coefficient and root-mean-squared-error for algorithm segmen- tation within and between observers . . . . .	163
3.5	Expert manual segmentation variability for five rounds (R1-R5): mean(SD). (n = 20) . . . . .	167

4.1 Subject demographics and pulmonary function measurements . . . . . 199

4.2 CT-<sup>3</sup>He MRI registration accuracy using the comparative registration methods  
for the entire and each patient group. (n=35) . . . . . 200

4.3 Influence of CT-<sup>1</sup>H MRI initial rigid alignment on joint CT-<sup>1</sup>H/<sup>3</sup>He deformable  
registration accuracy. Rotation<sub>x,y,z</sub> represent ±10% error (random sign) added  
to the rotation components of base CT-<sup>1</sup>H MRI rigid transformation matrixes.  
Translation<sub>x,y,z</sub> represent ±10% error (random sign) added to the translation  
components of base CT-<sup>1</sup>H MRI rigid transformation matrixes. (n=35) . . . . . 202

4.4 Computation time [mean(*SD*)] of the regional CT-<sup>3</sup>He MRI structure-function  
measurements workflow shown in Fig 4.1B. (n=35) . . . . . 203

5.1 Subject demographics and pulmonary function measurements. (n=10) . . . . . 237

F.1 <sup>3</sup>He MRI segmental ventilation defect percent (VDP) for the entire database.  
(n=35) . . . . . 271

# List of Appendices

Appendix A Discrete and Continuous Min-Cut/Max-Flow . . . . .	252
Appendix B A Dual Volume Proportion-Preserved Max-Flow Model . . . . .	257
Appendix C A Volume Proportion-Preserved Continuous Max-Flow Algorithm . . . . .	260
Appendix D Proof of Proposition 2 . . . . .	263
Appendix E An Efficient Numerical Solver . . . . .	266
Appendix F Supplementary Materials . . . . .	269
Appendix G Permission for Reproduction of Scientific Articles . . . . .	272
Appendix H Health Science Research Ethics Board Approval Notices . . . . .	276
Appendix I Curriculum Vitae . . . . .	282



## List of Abbreviations

<b>COPD</b>	Chronic Obstructive Pulmonary Disease
<b>ES</b>	Ex-smokers
<b>GOLD</b>	Global Initiative for chronic Obstructive Lung Disease
<b>ATS</b>	American Thoracic Society
<b>BMI</b>	Body Mass Index
<b>FEV<sub>1</sub></b>	Forced Expiratory Volume in 1 second
<b>FVC</b>	Forced Vital Capacity
<b>IC</b>	Ex-smokers
<b>FRC</b>	Functional Residual Capacity
<b>TLC</b>	Total Lung Capacity
<b>RV</b>	Residual Volume
<b>DL<sub>co</sub></b>	Diffusing Capacity of the Lung for Carbon Monoxide
<b>PET</b>	Positron Emission Tomography
<b>SPECT</b>	Single Positron Emission Computed Tomography
<b>CT</b>	Computed Tomography
<b>MRI</b>	Magnetic Resonance Imaging
<b><sup>1</sup>H</b>	Proton
<b><sup>3</sup>He</b>	Helium-3
<b><sup>129</sup>Xe</b>	Xenon-129
<b>N<sub>2</sub></b>	Nitrogen
<b>O<sub>2</sub></b>	Oxygen
<b>FD</b>	Fourier Decomposition
<b>CS</b>	Compressive Sensing
<b>RF</b>	Radiofrequency
<b>FGRE</b>	Fast Gradient-Recalled Echo
<b>UTE</b>	Ultra-Short Echo-Time
<b>TR</b>	Repetition Time
<b>TE</b>	Echo Time
<b>FOV</b>	Field-of-View
<b>VDP</b>	Ventilation Defect Percent
<b>VDV</b>	Ventilation Defect Volume
<b>CoV</b>	Coefficient of Variation
<b>ICC</b>	Intra-class Correlation Coefficient
<b>CI</b>	Confidence Interval
<b>ANOVA</b>	Analysis of Variance
<b>SPSS</b>	Statistical Package for the Social Sciences
<b>SD</b>	Standard Division
<b>SDD</b>	Smallest Detectable Difference
<b>SNR</b>	Signal-to-Noise Ratio
<b>RB</b>	Right Bronchi
<b>LB</b>	Left Bronchi
<b>DSC</b>	Dice-Similarity-Coefficient
<b>RMSE</b>	Root-Mean-Squared-Error

<b>MAXD</b>	Maximum Absolute Distance
<b>MAD</b>	Mean Absolute Distance
$\delta V_E$	Volume Error
$\delta V_P$	Percent Volume Error
$ \delta V_E $	Absolute Volume Error
$ \delta V_P $	Absolute Percent Volume Error
<b>TRE</b>	Target Registration Error
<b>FLE</b>	Fiducial Localization Error
<b>FRE</b>	Fiducial Registration Error
<b>PDF</b>	Probability Density Function
<b>CPU</b>	Central Processing Unit
<b>GPU</b>	Graphics Processing Unit
<b>GPGPU</b>	General-Purpose Programming on Graphics Processing Units
<b>GUI</b>	Graphical User Interface
<b>ANTs</b>	Advanced Normalization Tools
<b>2D</b>	Two-dimensions
<b>3D</b>	Three-dimensions

# Chapter 1

## Introduction

*Chronic Obstructive Pulmonary Disease (COPD) and asthma are the most chronic and obstructive lung disease characterized by airflow limitation resulting from inflammation. In this Chapter, I will provide an overview of the burden of COPD and asthma, the underlying disease mechanisms, the current tools for disease management and their limitations. I will also introduce a number of lung imaging methods that bring new hopes for improved lung disease care and the image processing challenges associated with generating these imaging biomarkers, specifically, pulmonary magnetic resonance imaging and computed tomography. Finally, I will provide an overview of the commonly used medical image segmentation and registration algorithms and the valuation methods.*

### 1.1 Burden of Obstructive Lung Disease

According to World Health Organization's estimates, 600 million people are affected by chronic obstructive pulmonary disease (COPD) [1] with 65 million suffering from moderate to severe COPD [2] worldwide. In 2015, over three million people died of COPD as shown in Fig. 1.1 and this accounted for ~5% of global deaths [3]. COPD was the fourth leading cause of death globally [4] and recent estimates showed that it will rise to third by 2030 [2]. Asthma is another debilitating obstructive lung disease that affects approximately 334 million people worldwide, causing ~345,000 deaths annually and is most common among children [5].

In Canada, it is reported that ~4% of the population aged 35 to 79 has been diagnosed with COPD although ~13% of Canadians have clinical measurements indicative of COPD [6].

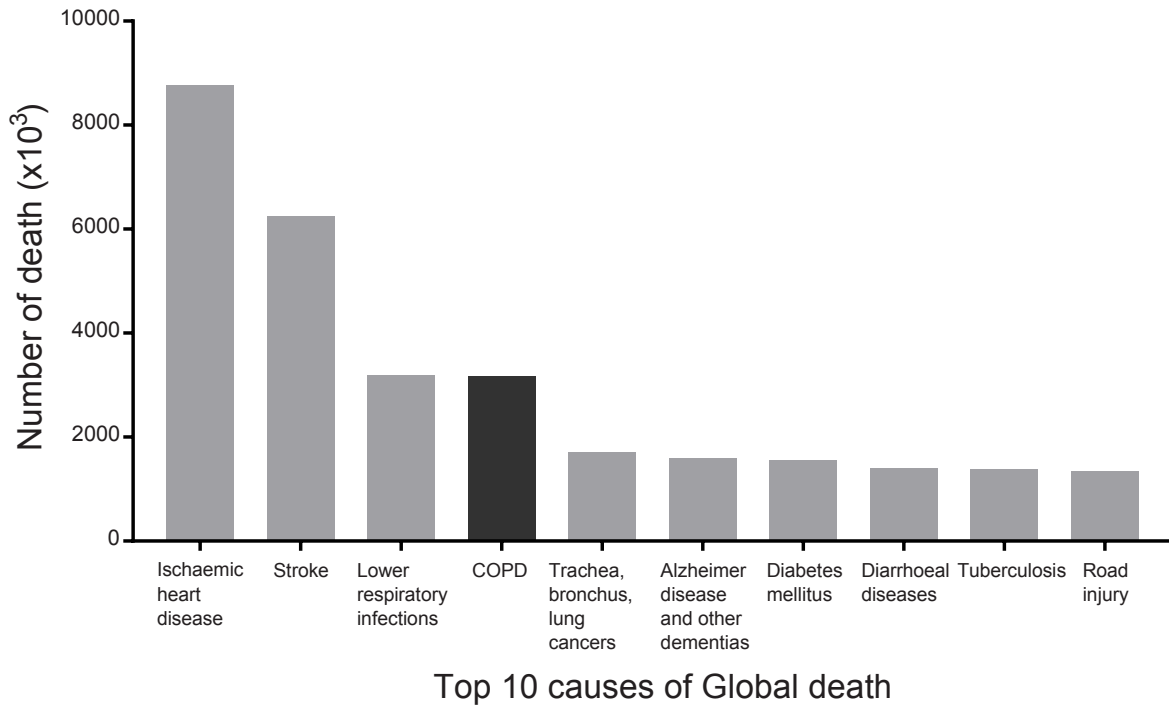


Figure 1.1: Global leading causes of death. Adapted from the World Health Organization's Global Health Observatory (GHO) data (2015) [4].

Importantly, COPD caused  $\sim 4.4\%$  of all deaths in Canada in 2011 [7] and accounted for the highest rate of hospitalization, followed by angina and asthma in the country [8], as shown in Fig. 1.2. According to a recent study performed by Statistics Canada, asthma affects 2.4 million or  $\sim 8\%$  of Canadians with a higher rate observed in Canadian children and youths [9]. In Ontario, it was estimated over 780,000 ( $\sim 5.9\%$ ) Ontarians were living with COPD in 2011 and the number will increase to  $\sim 1.2$  million ( $6.9\%$ ) by 2041 with the number of deaths increasing from 36,000 to 57,133 [10]. The same study [10] estimated that asthma affected another  $\sim 1.7$  million (or  $13.0\%$ ) Ontarians and the number will increase to  $\sim 2.5$  million ( $\sim 14.7\%$ ) by 2041. The total economic burden, including direct costs in health care and indirect costs due to loss of workplace productivity, were  $\sim \$3.9$  and  $\sim \$1.8$  billion for COPD and asthma, respectively. Together, COPD and asthma represent an economic burden of  $\sim \$5.7$  billion out of the  $\sim \$124$  billion total expenses for the government of Ontario [11].

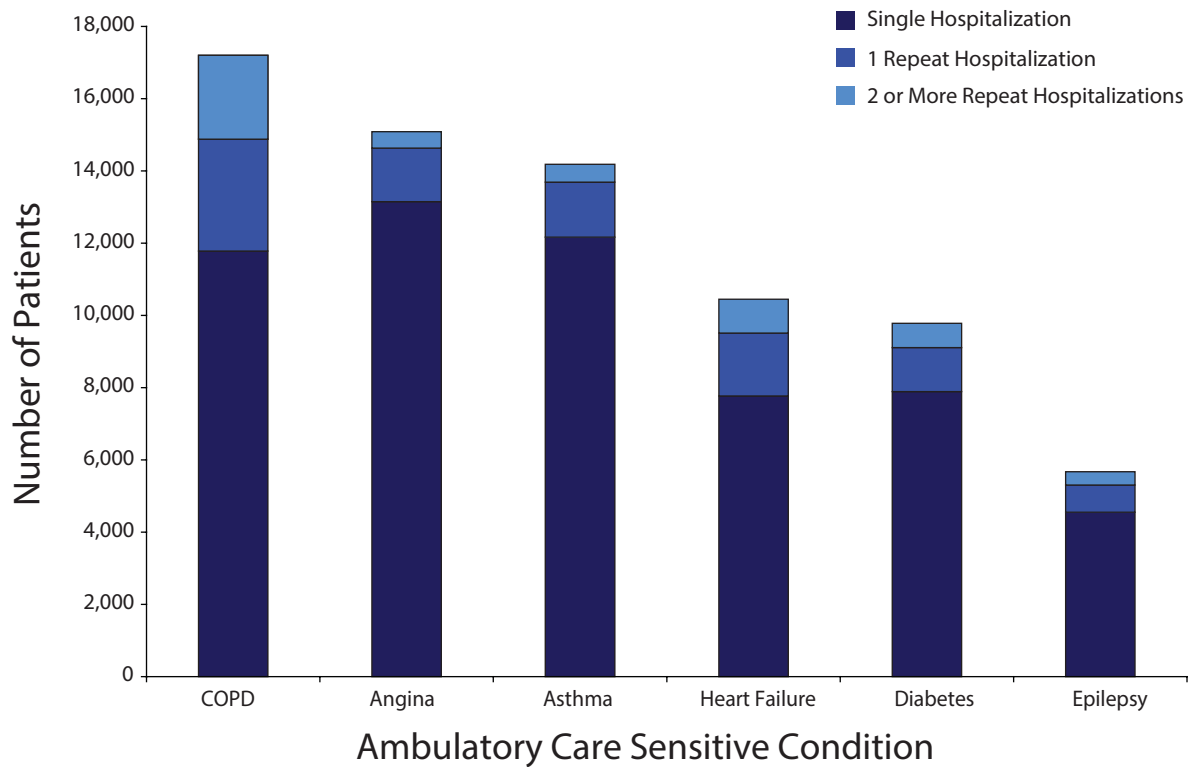


Figure 1.2: Repeat hospitalizations by conditions at first admission. Adapted from Canadian Institute of Health Information (2008) [12].

COPD and asthma have varying degrees of impacts on the physical, psychological and social aspects of daily life for patients living with these conditions [13, 14, 15]. COPD is not a single disease but a group of progressive lung disorders that cause airflow limitation and difficulty in breathing [16]. The most common subtypes of COPD include chronic bronchitis and emphysema and many COPD patients have both conditions [17]. Typically, individuals with COPD present a variety of symptoms, including shortness of breath, wheezing, chronic cough, chest tightness and excessive mucus production, and the symptoms worsen with disease progression [18, 19]. While COPD encompasses both airway and lung parenchyma components, asthma affects predominantly the airways [20, 21]. Although asthma patients present symptoms similar to COPD, there are striking differences between the two types of lung disease, which will be discussed in more detail.

In this Chapter, I will provide a summary of the relevant background knowledge necessary to understanding the motivation behind the research presented in Chapters 2 to 4. I will first briefly introduce the respiratory system (Sec. 1.2) before discussing the pathophysiology and underlying disease mechanisms of COPD and asthma (Sec. 1.3), then introduce the standard clinical tools for obstructive lung disease management (Sec. 1.4). Following this, I will provide a summary of the currently available imaging methods and biomarkers developed to provide a better understanding of chronic lung disease (Sec. 1.5). The introduction of imaging components for lung disease management fundamentally requires reliable image processing techniques and accordingly I will provide a brief review of the currently available and commonly used image analysis methods (Sec. 1.6). Finally, I will summarize the overall and specific objectives of this thesis (Sec. 1.7).

## **1.2 The Respiratory System**

The respiratory system provides oxygen into the body for cellular metabolism and removes carbon dioxide to the external environment to sustain the body's other physiological systems. The respiratory system includes the oral and nasal cavities, the lung, the airways, nervous systems that control the respiratory muscles, and the chest wall [22]. In this section, I will discuss the pathways of airflow from the external environment to the sites of gas exchange within the lung.

### **1.2.1 The Airways**

During inspiration, air enters the nasal cavity and is filtered, heated to body temperature and humidified. Air flows through the oral cavity, the pharynx, and the larynx followed by the trachea. The trachea is a cartilaginous tube that bifurcates into the left and right main bronchi, feeding the left and right lung, respectively. As shown in Fig. 1.3, the left and right bronchi then divide into lobar bronchi that are related to the five lobes (two lobes for the left lung and

	Branch name	Generation	Diameter (cm)
Conducting Zone	Trachea	0	1.80
	Bronchi	1	1.22
	Lobar Bronchi	2	0.83
	Segmental Bronchi	3	0.56
	Bronchioles	4	0.45
	Terminal Bronchioles	16	0.06
Respiratory Zone	Respiratory Bronchioles	17	0.05
	Alveolar Ducts	20	↓
	Alveolar Sacs	23	0.04
			↓

Figure 1.3: Schematic representation of human airways with generations and dimensions. Reproduced from *Pulmonary Physiology*, 8<sup>th</sup> edition [22].

three lobes for the right lung). The lobar bronchi then divide into segmental bronchi that supply the 18-19 lung segments that are anatomically and functionally independent. As shown in Fig. 1.4, there are 10 segmental bronchi in the right lung with 3 in the upper lobe, 2 in the middle lobe and 5 in the lower lobe. There are 8-10 segmental bronchi in the left lung with 4-5 in the upper lobe and 4-5 in the lower lobe. The segmental bronchi continue to divide dichotomously until they reach all regions of the lung. The small bronchi are bronchioles that have smooth muscle but no cartilage and are subject to collapse when compressed. The airways branch into more than 20 generations and become progressively narrower, shorter and more numerous. Starting from the trachea, the first 16 airway generations comprise the conducting zone, which ends with the terminal bronchioles [23]. It is important to note that the conducting zone is

responsible for directing inhaled air to the respiratory zone and does not participate directly in gas exchange. Therefore, following inspiration, some of the inhaled air remains in this space without participating in gas exchange. This is also known as anatomic dead space and typically has a volume of  $\sim 150$  ml for healthy adults [24].

Following the terminal bronchioles, the respiratory bronchioles compose the respiratory zone that consists of the last seven generations of the airways. The respiratory bronchioles have few alveoli lining the airway walls and as they divide, the number of alveoli increases dramatically and forms the alveolar ducts followed by alveolar sacs that are comprised completely of alveoli, where gas exchange occurs. The respiratory bronchioles and the following alveolar ducts and alveolar sacs are referred to as an acinus, the anatomical unit of the lung. Due to the large number of branching bronchioles in the respiratory zone, although the diameters are small, the total cross sectional area of these airways rapidly expands [25], reducing the overall airflow resistance. The respiratory zone constitutes a majority of the lung volume with a size of 2.5-3.0 L during rest [24].

## 1.2.2 The Alveoli

The respiratory bronchioles are terminated by the alveoli and are the primary site of gas exchange in the lung. There are  $\sim 480$  million alveoli on average in the human lung and the mean size of a single alveolus is  $\sim 4.2 \times 10^6 \mu\text{m}^3$  or  $\sim 200 \mu\text{m}$  in diameter [25]. Each alveolus is enveloped by a dense pulmonary capillary network that facilitates efficient gas exchange through diffusion of oxygen and carbon dioxide across the blood-air barrier. The blood-air barrier consists of the alveolar epithelium, the capillary endothelium, and a thin basement membrane between them with a thickness of 0.2–0.5  $\mu\text{m}$  [22]. The alveolar wall is a layer of epithelium that contains two main types of cells with a thickness of  $\sim 0.2 \mu\text{m}$  [22]. Type I or squamous epithelial cells form the majority of the alveolar surface. Type II cells secrete surfactant to lower the alveolar surface tension, allowing the membrane to separate and prevent the alveoli from collapsing during exhalation. The numerous alveoli and pulmonary capillaries result in a



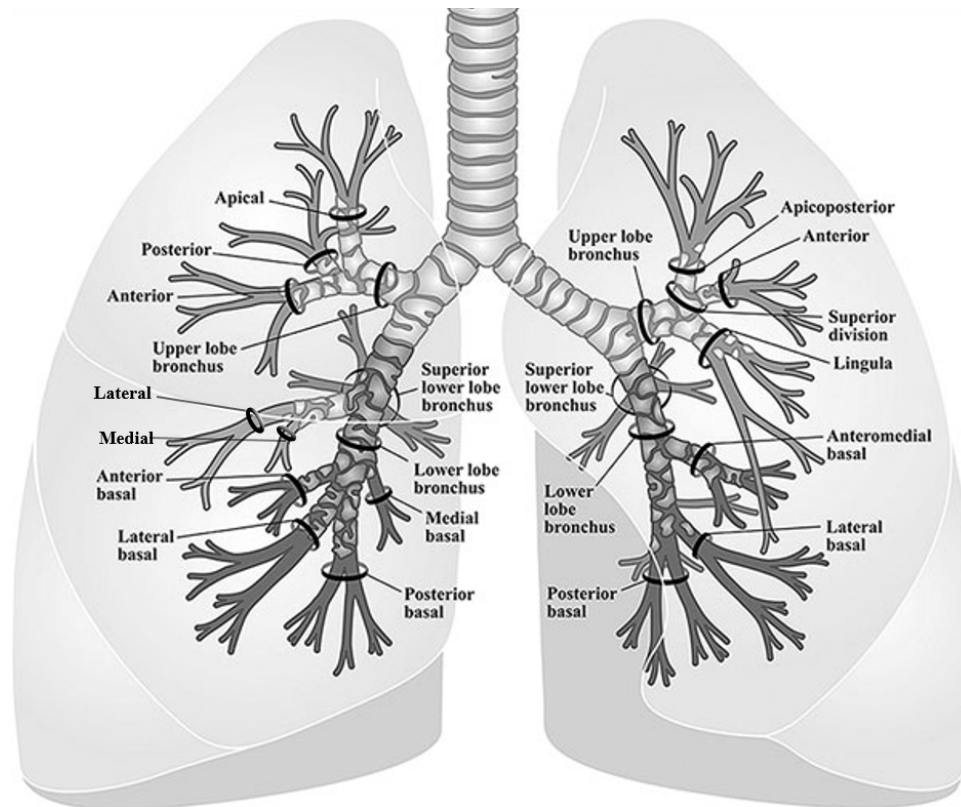


Figure 1.4: Lobar and segmental bronchi (indicated by dark circles) that correspond to lung lobes and segments. Adapted from Folch *et al.*. Seminars in respiratory and critical care medicine [26].

Left lung: Apicoposterior–LB1-2, Anterior–LB3, Lingula–LB4-5, Superior lower lobe bronchus–LB6, Anteromedial basal–LB8, Lateral basal–LB9, Posterior basal–LB7,10; Right lung: Apical–RB1, Posterior–RB2, Anterior–RB3, Lateral–RB4, Medial–RB5, Superior lower lobe bronchus–RB6, Medial basal–RB7, Anterior basal–RB8, Lateral basal–RB9, Posterior basal–RB10.

vast surface area of 50-100 m<sup>2</sup> for gas exchange [22].

### 1.2.3 Ventilation and Diffusion

During inspiration, the contraction of the diaphragm and intercostal muscles causes the diaphragm to descend and ribs to rise, increasing the volume of the thoracic cavity and decreasing the alveolar pressure. Inhaled air passes through the conducting airways and reaches the respiratory bronchioles and finally the alveoli, where the diffusion of gas becomes the dominant mechanism of ventilation [24]. Expiration occurs when the respiratory muscles passively relax and alveolar pressure increases. During a normal breath, approximately 500 ml of air is taken

from the external environment and resides in the conducting zone and the respiratory zone, and this is referred to as the tidal volume [24]. Total ventilation is calculated as the total volume of air that leaves the lung per minute. For normal breathing at a rate of  $\sim 15$  breaths/min, the total ventilation is  $\sim 7.5$  L/min [24]. However, the inhaled air that resides in the conducting zone ( $\sim 150$  ml) does not participate in gas exchange. Therefore, the volume of air that enters the respiratory zone and participates in gas exchange is  $\sim 5.25$  L/min, which is termed as alveolar ventilation [24].

When air reaches alveoli, it transfers across the blood-air barrier through diffusion according to Fick's law. That is, the rate of gas transfer through a tissue is proportional to the area of the tissue, the difference in gas partial pressure between the two sides of the tissue, and inversely proportional to the tissue thickness [27]. The partial pressure of  $O_2$  in a red blood cell entering the pulmonary capillaries is  $\sim 40$  mm Hg compared with that of  $\sim 100$  mm Hg in the alveoli [24].  $O_2$  in the alveoli diffuses across the blood-air barrier along the pressure gradient and finally the pressure of  $O_2$  in the red blood cell reaches that in the alveoli. The large area of blood-air barrier, the thin blood-air surface and the large differences in partial pressure of  $O_2$  ensure rapid gas exchange between the body and the external environment.

## **1.3 COPD and Asthma Pathophysiology**

### **1.3.1 Normal Aging Lung**

Aging is a biological factor that affects lung function. In order to better appreciate obstructive lung disease, it is necessary to separate the physiological changes of the lung due to pulmonary complications from normal aging. Here I briefly describe the effects of aging on pulmonary function.

The predominant physiological changes [28, 29] in respiratory function related to aging are due to decreases in: 1) lung elastic recoil, 2) chest wall compliance, and, 3) respiratory muscle strength. The lung contains elastic fibers, collagen, smooth muscle, pulmonary blood,

bronchial mucus, and surface-active materials and has elastic recoil properties similar to an elastic band that tends to recoil when stretched. The elastic recoil of the lung decreases and the compliance increases with aging [30] and this is most evident at high lung volumes, i.e., greater than 40-50% of TLC. Compliance is the change in volumes relative to the change in pressure [31]. The decline of lung elastic recoil is associated with lung connective tissue, i.e., elastin, collagen and proteoglycans. However, the exact mechanism is not well understood and conflicting hypotheses have been proposed. Currently, it is hypothesized that changes in the spatial arrangement or the cross-linking of the elastic fibers or the presence of a pseudoelastin contribute to lung elastic recoil decline [29]. The chest wall progressively stiffens due to decalcification of the ribs, calcification of the costal cartilage, rib-vertebral articulations and narrowing of the intervertebral disk space [29]. The shape of the chest may also change due to osteoporosis that results in vertebral fractures, leading to increased dorsal kyphosis and anterior-posterior diameter [29]. These changes not only decrease chest compliance (increasing the work for breathing) [29] but also affect the force-generating abilities of the diaphragm during breathing [28]. Respiratory muscle strength has been shown to be lower in elderly subjects than in younger controls [32], as well as the generated pressure involved in breathing [33]. The loss of respiratory muscle strength with age is thought to be due to a decrease in muscle mass, number of muscle fibers, motor units, and alternations of neuro-muscular junctions. Other functional deficits, i.e., oxygen content, heart failure and Parkinson's disease, may also affect respiratory muscle strength [28]. Minor changes were observed in airways during aging, including calcification of bronchial cartilage in large airways (increased anatomic deadspace) [34] and decrease in the diameter of bronchioles (loss of elastic recoil) [35]. In addition, alveolar ducts are dilated typically after the age of 40 due to elastic fiber degeneration, resulting in enlarged airspaces [36]. The alveoli appear more flattened and the alveolar surface area reduces from  $\sim 70 \text{ m}^2$  at the age of 20 to  $\sim 60 \text{ m}^2$  at the age of 70 [29, 28], leading to decreased lung surface-to-volume ratio [37]. The reduction of support tissue around small airways leads to premature closure of small airways during tidal breathing [28].

### 1.3.2 COPD and Asthma

COPD and asthma are obstructive lung disease characterized by airflow limitation resulting from chronic inflammation. In this section, I briefly review the pathology and pathophysiology related to COPD and asthma while the cellular mechanisms of the disease are out of the scope of this thesis.

#### 1.3.2.1 COPD

According to the Global Initiative for Chronic Obstructive Lung Disease (GOLD) guidelines [17], COPD is defined as “*a preventable and treatable disease with some significant extra-pulmonary effects that may contribute to the severity in individual patients. Its pulmonary component is characterized by airflow limitation that is not fully reversible. The airflow limitation is usually progressive and associated with an abnormal inflammatory response of the lung to noxious particles or gases*”. The risk factors that contribute to the development of COPD include cigarette smoking in particular, as well as exposure to occupational dusts and chemicals, air pollution, respiratory infections in childhood, genetic conditions like  $\alpha_1$ -antitrypsin deficiency, and socioeconomic status [17, 38]. Tobacco smoking is a major risk factor that leads to the development of COPD [38] and ~50% of elderly smokers developed COPD [39]. Non-smoking factors account for more than 50% of COPD cases but the relative contribution of each risk factor varies [38]. COPD encompasses three clinical phenotypes including emphysema, chronic bronchitis and small airway disease. Emphysema is defined as “*a condition of the lung characterized by abnormal, permanent enlargement of airspaces distal to the terminal bronchioles, accompanied by the destruction of their walls, and without obvious fibrosis*” [40]. Based on the morphology and anatomic distribution, emphysema can be divided into three main subtypes: centrilobular, panlobular and paraseptal emphysema [41]. Centrilobular emphysema mainly affects the respiratory bronchioles in the central portion of the acini while the alveolar ducts and sacs are preserved. The disease is usually distributed to the upper zones of

the lung with a patchy fashion. Panlobular emphysema, in contrast, uniformly affects the entire acini from respiratory bronchioles to the alveoli and exhibits even distribution. This disease is frequently associated with  $\alpha_1$ -antitrypsin deficiency but may also be associated with other factors. Paraseptal emphysema predominately affects the distal acini with areas of destruction often mitigated by inter-lobular septa. Chronic bronchitis is defined as “*the presence of cough and sputum production for at least 3 months in each of two consecutive years*”. It is thought that chronic cough and sputum production are associated with inflammation in the central and large airways (>4 mm in diameter) and mucous glands. Small airway disease is associated with the obstruction of small airways or bronchioles (<2 mm in diameter), which are considered as the major sites of airflow limitation in COPD [42]. As the airways branch dichotomously, the number of airways increases rapidly and their radii decrease with increased resistance per single airway segment. However, the overall airway resistance of the small airways is small when considering the total cross sectional area of the airways arranged in parallel. Previous studies have shown the airway resistance is mainly attributed to large airways and the small airways contributed very little [42]. This suggests that small airway disease may accumulate over long timeframes without being detected.

COPD pathologies include changes in large airways, small airways, and alveolar space [43]. Inhaled particles cause abnormal or enhanced inflammatory response throughout the lung that is characteristic of COPD. The inflammatory process recruits and activates a number of inflammatory cells that release a series of factors. The complex process results in destruction of alveolar wall and pulmonary capillaries, mucus hyper-production, degradation of elastin fibers, loss of lung elastic recoil and alveolar attachments [43, 44, 45] typified by emphysema.  $\alpha_1$ -antitrypsin is a type of proteinase inhibitor that protects lung tissues from being damaged by neutrophil elastase. In subjects with  $\alpha_1$ -antitrypsin deficiency, the decreased production and activity of proteinase inhibitor result in destruction of the elastin fibers in alveolar walls and development of emphysema [43]. Airway epithelial cells can be activated by cigarette smoke and generate mediators that induce airway fibrosis (chronic bronchitis) [44]. Inflam-

mation in the large airways (>2 mm in diameter) also causes epithelial squamous metaplasia, goblet cell hyperplasia and enlarged mucus gland that lead to ciliary dysfunction (difficulty in expectorating), mucus over-production (or chronic bronchitis) but generally no airflow limitation. Inflammation in the small airways, the major sites of airflow limitation, causes goblet cell hyperplasia, increased number of mucus-secreting cells, smooth muscle hypertrophy and inflammatory cell infiltration. These pathological changes results in peribronchial fibrosis and airway narrowing (due to excess mucus, edema and cellular infiltration), as shown in Fig. 1.5. Airway narrowing is further worsened due to the destruction of the alveolar attachments on the outer walls that provide radial traction on the bronchioles. Destruction of small airways may directly contribute to an increase in flow resistance through destruction of parallel conducting pathways.

### 1.3.2.2 Asthma

According to the 2017 updates of Global Initiative for Asthma Report [46], asthma is “*a heterogeneous disease, usually characterized by chronic airway inflammation. It is defined by the history of respiratory symptoms such as wheeze, shortness of breath, chest tightness and cough that vary over time and in intensity, together with variable expiratory airflow limitation*”. Asthma is a respiratory disorder resulting from complex gene-environment interactions and characterized by airway inflammation, airflow obstruction, and bronchial hyperresponsiveness [47]. Environmental stimuli (i.e., allergens, respiratory viruses and other environmental irritants) lead to airway inflammation in genetically susceptible individuals. Upon antigen sensitization, asthma inflammatory cells are recruited and activated [48]. The activated inflammatory cells generate a series of cytokines [49, 50] that cause epithelial damage (a source of airway hyperresponsiveness), vascular leakage and edema (a source of airway obstruction), airway smooth muscle proliferation (airway remodeling) and contraction, mucous secretions and acute exacerbation of asthma symptoms. Taken together, the asthma inflammatory processes cause airway wall thickening, airway lumen narrowing, edema, mucous hypersecretion

and bronchoconstriction, as shown in Fig. 1.5. These pathologies contribute to airway obstruction with increased airflow resistance typically found in asthmatics. These effects also lead to increased difficulty in lung emptying and may result in hyperinflation.

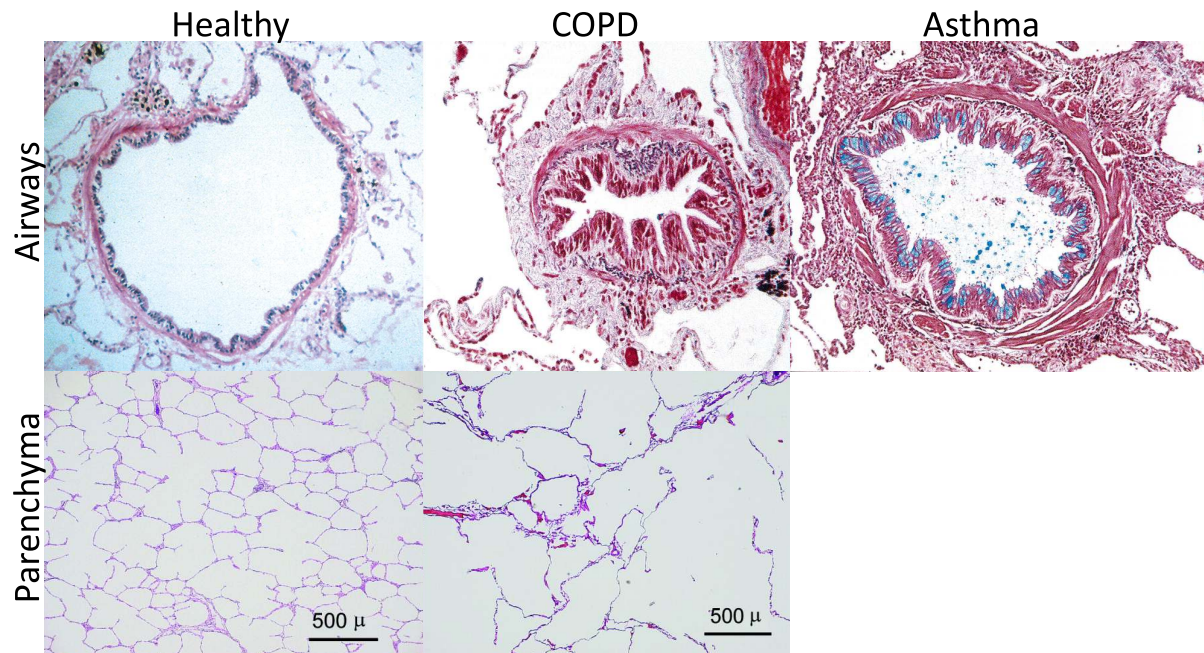


Figure 1.5: Small airway and lung parenchyma pathologies. Top panel: normal, COPD and asthma airways are shown from left to right. COPD airways: infiltration with inflammatory cells, reduced airway caliber, thickened smooth muscle, connective tissue deposition, and disrupted alveolar attachments; Asthma airways: inflammatory cells exudation, thickened smooth muscle and basement membrane with increased airway wall thickness. Bottom panel: normal and COPD lung parenchyma. Adapted from Hogg *et al.*, *Lancet* (2004) [51] and Woods *et al.*, *Magnetic Resonance in Medicine* (2006) [52].

## 1.4 Clinical Managements of COPD and Asthma

### 1.4.1 Lung Function Measurements

Pulmonary function tests (PFTs) provide the most common clinical measurements of lung function for the diagnosis and management of obstructive lung disease. PFTs provide three sets of overall lung function measurements including dynamic air flow, lung volumes and gas

exchange. These measurements play an important role in pulmonary disease diagnosis, monitoring, and treatment effectiveness evaluation.

### 1.4.1.1 Spirometry

Spirometry provides a physiological evaluation of lung function by measuring the volume of air that an individual inhales or exhales as a function of time [53]. Spirometry is usually performed using a hand-held spirometer and provides two main measurements - the forced expiratory volume in 1 second ( $FEV_1$ ) and the forced vital capacity (FVC). This procedure is performed with the subject in a seated position and breathing through a mouthpiece attached to the spirometer. The subject starts with normal breathing and then inhales maximally followed by a maximally forced exhalation as fast and as long as possible. Figure 1.6 shows a spirometer and the plot on the right depicts the volume of air inhaled and exhaled as a function of time during this procedure. Following the maximal inhalation, the volume of air that is exhaled in the first second is referred to as  $FEV_1$  and the total volume of air that can be maximally exhaled is FVC, from which an additional index,  $FEV_1/FVC$ , is derived. To mitigate the dependence of  $FEV_1$  and FVC measurements on age, height, gender and ethnicity, these values are usually reported in “percentage predicted” or  $\%_{pred}$ .

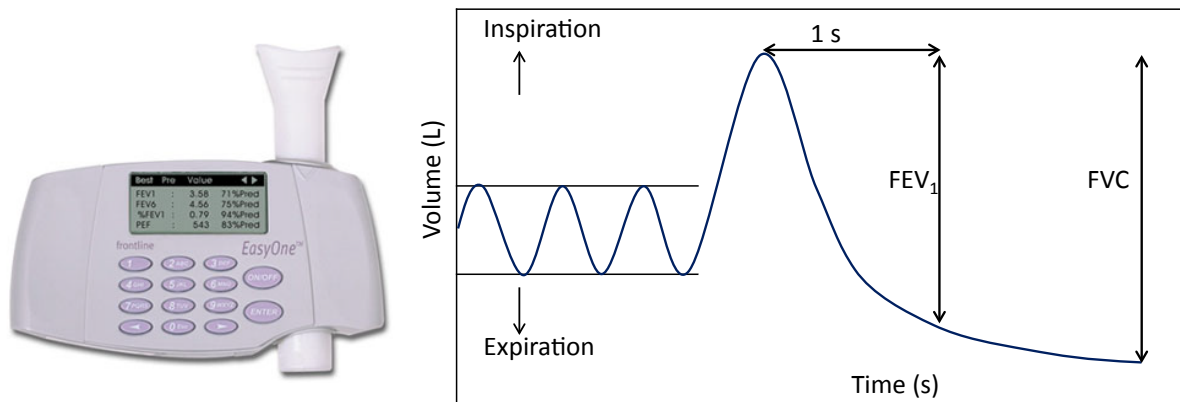


Figure 1.6: Handheld spirometer and volume-time airflow curve depicting  $FEV_1$  and FVC.  $FEV_1$  = forced expiratory volume in one second, FVC = forced vital capacity.



### 1.4.1.2 Plethysmography

Plethysmography is performed during a series of coached breathing manouvers in a closed system. This procedure provides a number of lung volume and capacity measurements [54]. The tidal volume (TV) is the amount of air inhaled and exhaled during normal breathing. The inspiratory reserve volume (IRV) is the volume of gas than can be maximally inhaled at the end of normal inspiration. The expiratory reserve volume (ERV) is the volume of gas the can maximally exhaled at the end of normal exhalation. The vital capacity (VC) is the maximum amount of air that can be expelled after a maximum inhalation, and can be calculated as  $IRV+TV+ERV$ . The residual volume (RV) is the amount of air that remains in the lung after a maximal expiration. The functional residual capacity (FRC) is the volume of gas remaining in the lung at the end of passive exhalation. The inspiratory capacity (IC) is the volume of air that can be maximally inhaled from exhalation of tidal breathing. The total lung capacity (TLC) is the volume of gas in the lung following a maximal inhalation. Figure 1.7 illustrates the measurements and relationships of these lung volumes.

The subject is seated upright in an air-sealed plethysmograph chamber and breaths normally through a mouthpiece with a shutter. At the end of normal expiration, the shutter closes the mouthpiece and the subject is instructed to make inhalation efforts, which expand the lung and decrease the gas volume in the chamber. The gas pressure in the box before and after the inhalation effort can be measured and the volume of the box is known. Following Boyle's law [55], the change in the lung volume (or the decrease of gas volume in the box) can be calculated. In the meantime, the pressure at the mouthpiece before and after the inhalation effort is measured, and with the calculated lung volume change, the resting lung volume FRC, can be derived. Similarly, the other static volumes can be obtained though maximal inhalation/exhalation, and normal inhalation/exhalation as well as the relationships between these volumes in Fig. 1.7.

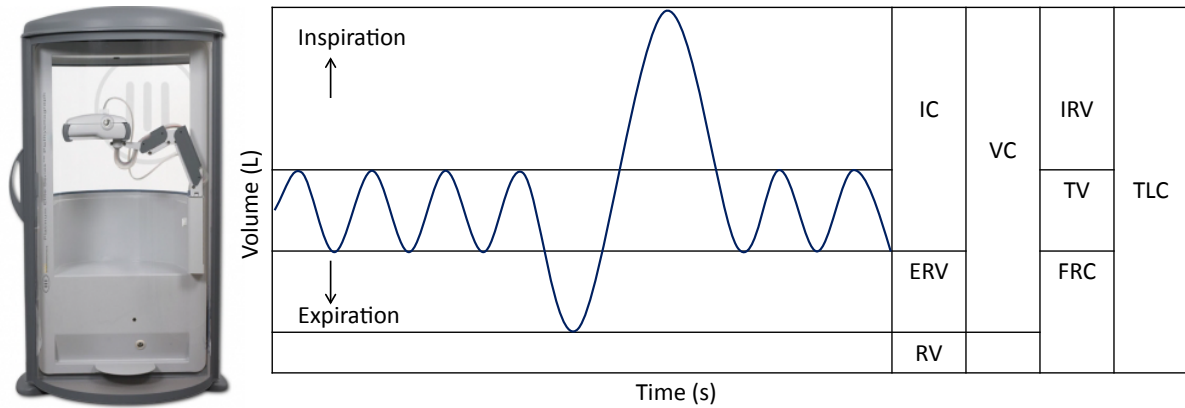


Figure 1.7: Body plethysmograph and measurements of lung volumes using a volume-time curve. Adapted from Wanger *et al.*, *European Respiratory Journal* (2005) [54].

IC = inspiratory capacity, ERV = expiratory reserve volume, RV = residual volume, VC = vital capacity, IRV = inspiratory reserve volume, TV = tidal volume, FRC = functional residual capacity, TLC = total lung capacity.

### 1.4.1.3 Diffusing Capacity

The diffusing capacity of the lung for carbon monoxide ( $DL_{CO}$ ) is an indirect measure of gas diffusion across the alveolar-capillary membranes. In the plethysmograph chamber, the subject is instructed to exhale to RV and then make a maximal inhalation to TLC by breathing in a gas mixture of helium (~10%), carbon monoxide (~0.2%) and room air. The subject is then instructed to hold his/her breath for ~10 s and exhale through a mouthpiece [56]. During this breath-hold, the carbon monoxide and helium diffuse across the alveolar membrane into the blood. The exhaled gas is collected with the gas volume exhaled at the beginning discarded (anatomic dead space) [56]. The remaining gas mixture is analysed to obtain the concentration of carbon monoxide and helium in comparison with that before the breath-hold. Therefore, the amount of carbon monoxide that diffuses into the pulmonary circulation can be estimated.

It should be noted that these PFT measurements require considerable patient efforts (potentially problematic for children and patients with severe lung disease), lack reproducibility and provide only global rather than regional measurements of pulmonary complications that are thought to be highly heterogeneous. Nevertheless, PFTs are routinely performed in clinics and remain the gold standard for clinical lung disease managements largely due to the low cost,

wide availability and the relative ease of use.

## **1.4.2 Lung Functional Decline**

### **1.4.2.1 Normal Aging**

The physiological changes of the lung during aging result in changes of clinical measurements of lung function including airflow, lung volumes and gas exchange. The seminal work by Fletcher and Peto in 1977 [57] provides the basis for our current understanding of lung function change during aging, as shown in Fig. 1.8. This study [57] shows that, starting from the age of 25, FEV<sub>1</sub> declines continuously at a rate of ~42 ml/year over a lifetime without the development of clinically significant airflow obstruction in most cases. Other studies have shown lung volume changes due to the effects of aging. For example, previous studies [30, 28, 31] observed increases in RV, RV/TLC and FRC and decreases in VC while TLC shows no significant change over time. The increase in RV (indicative of air trapping) and FRC is likely due to the increased chest wall rigidity and diminished lung elastic recoil [28]. TLC remains almost constant due to the balanced effects of decreased elastic recoil of the lung and increased elastic recoil of the chest wall [30, 28]. There is also increase in the anatomic deadspace that was thought due to calcification of the cartilage in large airways wall [58]. Regarding gas exchange, previous studies [31] demonstrated a decline in DL<sub>CO</sub> with age, and this is likely due to reduction of alveolar surface area, decreased density of lung capillaries and a decline in pulmonary capillary blood volume [28].

### **1.4.2.2 Obstructive Lung Disease**

The pathological changes (Sec. 1.3) involved in COPD result in pulmonary physiological abnormalities including mucous over-production, ciliary dysfunction, airflow obstruction, hyperinflation, gas exchange abnormalities, pulmonary hypertension and systemic effects [45]. Mucous hypersecretion associated with chronic bronchitis however, does not necessarily cause

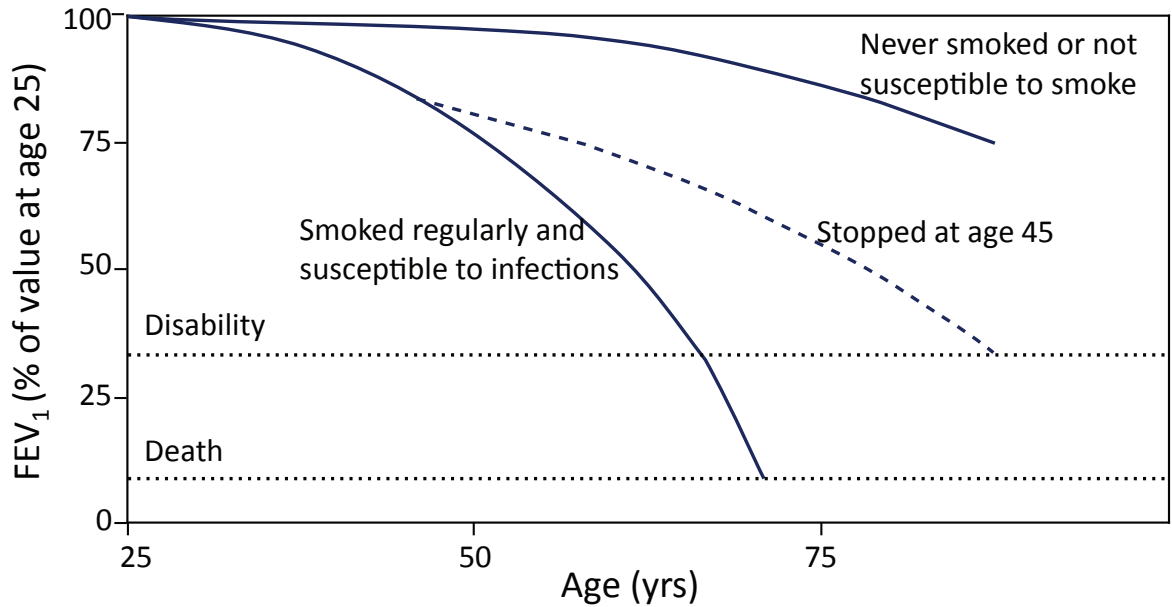


Figure 1.8: Normal lung function decline during aging in never smokers and accelerated lung function decline in regular smokers. However, following smoking cessation, lung function decline rates return to normal. Adapted from Fletcher *et al.* British Medical Journal (1977) [57].

airflow limitation. Ciliary dysfunction may result in difficulty in mucous expectoration. Small airway pathologies (i.e., mucus production, edema, airway fibrosis, airway smooth hyperplasia, loss of radial traction from alveoli) cause airway narrowing and reduced airway caliber, leading to increased airway resistance, reduced airflow and hyperinflation. The degraded physiological changes are reflected by reduced  $FEV_1$ , FVC and  $FEV_1/FVC$ . FVC is reduced and RV is increased because of premature airway closure during expiration at abnormally high lung volumes. Increased FRC, TLC and RV/TLC arise from hyperinflation due to the loss of lung elastic recoil. The barrel-shaped chest common in COPD subjects is due to lung hyperinflation and decreased lung compliance, which result in increased efforts required for breathing. Alveolar space enlargement, alveolar wall destruction and pulmonary capillary bed apoptosis result in decreased surface area for gas exchange (i.e., reduced  $DL_{CO}$  in advanced stages) and ventilation-perfusion mismatch. Gas exchange abnormalities and ventilation-perfusion mismatch results in hypoxia, hypercapnia and pulmonary hypertension due to hypoxic vaso-

constriction of pulmonary arteries. Severe COPD also involves severe systemic effects, i.e., cardiovascular disease. Clinically, a post-bronchodilator  $FEV_1/FVC < 70\%$  confirms the diagnosis of COPD and the severity is classified according to the Global Initiative for chronic Obstructive Lung Disease (GOLD) criteria [17] as shown in Table 1.1.

Table 1.1: Grading of COPD airflow limitation severity based on post-bronchodilator  $FEV_1$

GOLD stage	Severity	$FEV_1/FVC < 70\%$
GOLD I	Mild	$FEV_1\%_{pred} \geq 80\%$
GOLD II	Moderate	$50\% \leq FEV_1\%_{pred} < 80\%$
GOLD III	Severe	$30\% \leq FEV_1\%_{pred} < 50\%$
GOLD IV	Very severe	$FEV_1\%_{pred} < 30\%$

$FEV_1$  = Forced expiratory volume in one second, FVC = Forced vital capacity,  
 $\%_{pred}$  = Percent predicted value.

In asthma, the complex inflammation process causes airway smooth muscle hypertrophy, mucous gland hyperplasia, basement membrane thickening, and continuing cellular infiltration. The associated physiological changes, especially during an asthma attack, include changes of airflow and lung volumes. For example, expiratory flow is reduced as reflected by  $FEV_1$  and  $FEV_1/FVC$  due to increased airway obstruction. FVC is decreased and RV is increased because of airway closure during expiration. FRC and TLC are increased due to lung hyperinflation and  $RV/TLC$  is increased, indicative of gas trapping. In clinical management of asthma, it is important to assess asthma control and severity to evaluate patients and optimize the treatments. Asthma control is defined as the extent to which the manifestations of asthma are reduced by treatments, encompassing evaluation of current impairment and future risk [59]. According to the Global Initiative for Asthma 2017 [46], asthma control is categorized as either “well-controlled” or “poorly-controlled”. Asthma severity refers to the difficulty in controlling asthma with treatments [59] and can be classified as “mild”, “moderate” and “severe” [46].

## 1.5 Pulmonary Imaging and Imaging Biomarkers

### 1.5.1 Chest x-ray

X-rays were discovered by Wilhelm Röntgen in 1895 and very quickly translated to clinical applications across the world. Today, x-rays are widely used as a preeminent imaging technique of modern medicine [60]. X-rays are typically generated using an x-ray tube that converts electrical power to electromagnetic radiation. An x-ray tube is a vacuum container housing a tungsten filament, a cathode and an anode. When the filament is heated up by an electrical current, electrons with enough thermal energy escape from the metal atoms. A very high voltage (i.e., 30-150 kV) is applied between the cathode and the anode to accelerate the escaped electrons. The highly accelerated electrons strike the anode and the electron-anode atom collision generates heat and importantly produces x-rays through bremsstrahlung and characteristic emission. Bremsstrahlung is the process when the electrons interact with nuclei and the lost kinetic energy is emitted as x-ray photons with many energies. Characteristic emission is another way to generate x-ray photons through electron-electron collisions. The accelerated electrons collide with the inner orbital electrons of the anode metal atom. When the energetic electrons have enough energy, the inner orbital electrons are knocked off and the empty orbits are filled by electrons from higher energy orbits, releasing characteristic x-ray photons. When the generated x-ray photons pass through body tissue, a number of interactions happen. Coherent scattering occurs when low energy x-ray photons collide with tissue atoms, resulting in scattered photons without depositing energy to the tissue. Photoelectric effect occurs when the energy of x-ray photons is below  $\sim 25$  keV. The incoming photon interacts with an innermost orbital electron of the atom and the photon energy is completely absorbed, resulting in an escaped orbital electron that travels throughout the body tissue. When the energy of x-rays increases, Compton effect becomes predominant over photoelectric effect. The incident x-ray photons collide with outer orbital electron of tissue atom, transferring energy to eject the

electron from the atom and resulting in scattered photons with loss of directional information. The x-ray-tissue interactions result in removal of some of the photons, known as attenuation. Attenuation coefficient is a term that determines the average intensity of x-rays at a specific energy travelling through a specific material. Different tissues have different attenuation coefficients and result in different average x-ray intensities that are measured by an image receptor to generate a radiograph.

Chest x-ray is the most commonly used method to evaluate lung abnormalities because of the wide availability, low cost, fast image acquisition and low radiation dose. Posterior-anterior chest x-rays are performed in the upright position and the patients' hands are placed on the back of their hips with the elbows rolled slightly forward so that the scapulae are removed from the field of view [61]. Lateral projections are also commonly acquired with the patients' sagittal plane parallel to the film and arms folded over the head to eliminate the presence of their arms in the image [61]. When x-ray beams travel through the body, part of them are absorbed, termed as attenuation. Different tissues attenuate x-rays at different levels and this contributes to x-ray image contrast. For example, high attenuating structures such as bone absorb many x-rays and appear white while low attenuating tissues such as lung parenchyma absorb fewer x-rays thus appear black in the image. The typical dose associated with a chest x-ray is around 0.01 mSv, which is equivalent to approximately three days of background radiation [62]. The resulting images provide poor soft tissue contrast, superposition of different tissues onto each other and limited diagnostic information.

Chest radiographs have been used to detect a number of pulmonary complications of COPD and asthma. Chest radiographs are mostly useful for detecting COPD at advanced stages i.e., emphysema. The abnormal findings typically include enlarged lung volumes, increased anterior-posterior diameter of the chest, flattened diaphragm, reduced pulmonary vessels, thickened bronchial wall, increased retrosternal space and focal hyper-lucent areas [63, 41], as shown in Fig. 1.9. Radiographic abnormalities associated with asthma are generally subtle and mainly include enlarged lung volumes, increased lung lucency, thickened bronchial wall

and mild prominence of hilar vessels [41]. Although there are some conflicting views of the utility of chest radiograph for obstructive lung disease management [64, 65, 66, 67], it is valuable in excluding pneumonia or other complications [68].

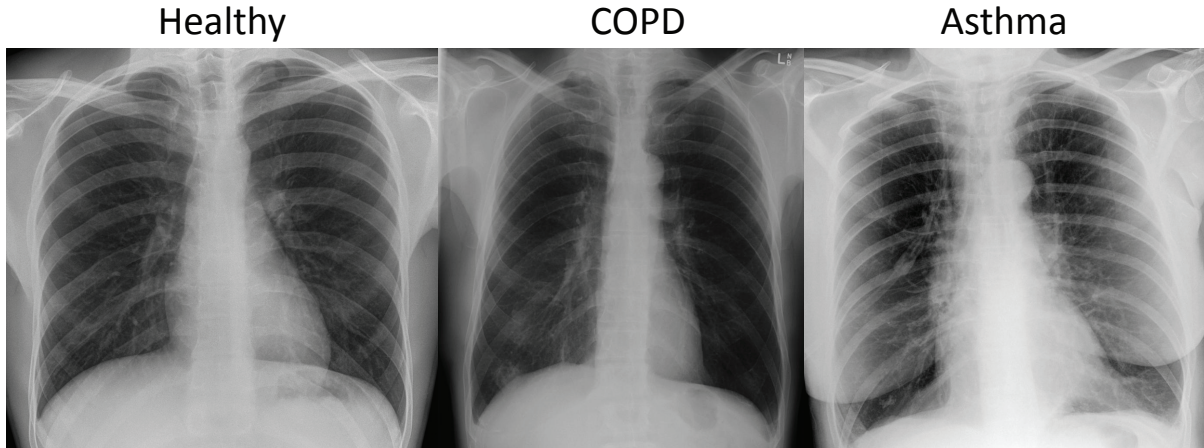


Figure 1.9: X-ray radiograph of a healthy, COPD and asthma subject. Healthy case courtesy of Dr. Ian Bickle, Radiopaedia.org, rID: 50318. COPD (predominantly emphysema) case from The Townsville Hospital, Radiopaedia.org, rID: 19446. The lung is hyper-inflated as evidenced by more than 10 posterior ribs, flattened diaphragm, narrowed mediastinum and regions of hyper-lucency that are indicative of emphysema. Asthma case courtesy of Dr. Ian Bickle, Radiopaedia.org, rID: 33470. Lung hyper-inflation is indicated by flattened diaphragm and more than 6 anterior or 10 posterior ribs at the lung diaphragm level.

## 1.5.2 X-ray Computed Tomography

Although widely used, there are a number of limitations associated with plain x-ray imaging including low image contrast and importantly, the inability to provide 3D visualization of anatomical structures. An x-ray-related technique, computed tomography (x-ray CT) was developed in the 1970s to overcome these limitations and has been widely used in clinics. X-ray CT employs elaborately organized x-ray sources and x-ray detectors to acquire a series of x-ray projections and provides cross-sectional visualization of the inside of objects through appropriate data manipulation. While several CT scanner designs are available, they typically integrate an x-ray source and an x-ray detector array with fixed relationship. A fan-shaped x-ray beam travels through body tissue and photon attenuation information of the tissue is measured by



the detector array. The x-ray source and detector array are rotated around the object and a number of projections are acquired for the current slice. Once complete, the x-ray source-detector is moved to the next slice and the whole procedures are repeated until the desired object is covered. The acquired x-ray attenuation information is then reconstructed to generate cross-sectional images. The resultant images are represented by matrices, where each element has a CT number (or Hounsfield unit (HU)) that is proportional to the actual voxel density and calculated by comparing the attenuation coefficient of the tissue to water:

$$HU = \frac{\mu_{tissue} - \mu_{water}}{\mu_{water}} \times 1000, \quad (1.1)$$

where  $\mu_{tissue}$  and  $\mu_{water}$  represent the attenuation coefficients of tissue and water, respectively. Soft tissue such as liver has a CT number around 30 - 50 HU, blood around 80 HU, bone around 1500 - 4000 HU, air around -1000 HU depending on pressure [69]. The radiation dose associated with a typical chest CT is  $\sim 8\text{mSv}$  [69], which is equivalent to  $\sim 3.6$  years natural background radiation or 400 chest x-rays [69]. Figure 1.10 shows chest CT of a healthy volunteer, COPD and asthma subject.

### 1.5.2.1 Lung Parenchyma Abnormalities

Chest CT has been routinely used to evaluate lung parenchyma and airway structural abnormalities in COPD patients. Emphysema is a pathophysiological subtype of COPD characterized by distal airspace enlargement due to alveoli destruction, leading to decreased lung parenchyma density. Emphysematous regions of the lung appear dark in chest CT, and this has been previously evaluated by comparing chest CT and post-mortem measurements [70]. Previous studies have demonstrated strong and significant correlations between chest CT gradings and pathological findings of emphysema. However, these grading methods were mainly based on visual inspection and introduced considerable intra- and inter-observer variability [71]. Later, computerized chest CT analysis methods were developed to provide quantitative information about

emphysema. One of the most commonly used methods separates emphysematous lung regions from normal tissue by identifying inspiration CT voxels with HU below -950 [72]. Another widely used method employs the lowest 15% of inspiration CT lung signal intensity histogram to identify emphysematous lung parenchyma [72] and this method is preferred for longitudinal evaluation of chest CT [72]. These automatic quantitative analysis results have demonstrated correlation with radiologists' interpretation [73], pulmonary function test results [74], macroscopic and microscopic pulmonary histology measurements [75, 76]. However, these single threshold-based measurements may not best approximate radiologists' interpretation preference [77]. Recently, another approach was developed to provide optimal emphysema classification using principle component analysis of whole lung and regional lung density histograms [77]. Other methods have been developed to cluster emphysema based on the size and distribution of emphysematous lesions [78]. The relationship between the total number of emphysema clusters and cluster sizes has been investigated for emphysema progression evaluation - fewer but larger emphysematous bullae indicates more severe emphysema [78].

### **1.5.2.2 Airway Disease**

Airway disease is another pathological feature associated with obstructive lung disease and chest CT has been used to evaluate airway abnormalities. High resolution CT provides a way to measure airway tree structure up to the fifth or sixth generation in 3D. Chest CT findings of airway abnormalities associated with obstructive lung disease include bronchiectasis, bronchial wall thickening, mucous plugging, atelectasis, and mosaic lung attenuation. Bronchiectasis exhibits localized, dilated airways and is usually associated with increased internal bronchial diameter than adjacent pulmonary arteries [41]. Bronchial wall thickening is usually present with bronchiectasis with thicker airway wall and the identification is largely subjective [41]. Several approaches have been developed to segment the airway tree including commercial implementations (Pulmonary Workstation V2.0, VIDA Diagnosis, Coralville, IA, USA). The segmented airways are quantified to provide airway dimensions such as bronchial wall thick-

ness, wall area, wall area percent and lumen area [79]. However, these analyses are limited to large airways while small airways (diameters <2 mm), which are the major sites of airflow obstruction in obstructive lung disease, cannot be directly assessed using CT due to spatial resolution limitations [72]. Previous studies [80] have shown that small airway obstructions resulted in prolonged time constants for lung filling and emptying, leading to gas trapping in obstructive lung disease. Therefore, small airway abnormalities can be indirectly assessed by quantifying expiration CT, where gas trapped regions exhibit low attenuation, i.e., mosaic attenuation pattern. The extent of gas trapping can be estimated by thresholding the expiratory CT using -856 HU [81] but emphysema-related hyperinflation cannot be differentiated. Other approaches quantify gas trapping due to small airway disease regardless of emphysema by calculating the relative volume change [82], mean lung signal ratio [83] and voxel-by-voxel signal intensity relationships [84] between inspiratory and expiratory CT.

In asthma patients, previous studies have shown that CT-derived gas-trapping and airflow limitation measurements were correlated with clinical measurements [85, 86, 87]. Other studies have shown that CT-derived air-trapping worsened following methacholine challenge [88, 89] and improved after bronchodilator treatment [88, 89, 90]. Further investigations demonstrated that CT-determined gap-trapping was associated with disease duration [91], asthma severity [86, 87, 91], and airway hyperresponsiveness [88, 87]. Regarding large airways, previous studies observed decreased bronchial wall area after salbutamol [89] and increased wall thickness [92] associated with airflow obstruction [92, 93] in asthmatics than healthy controls. Other studies [92] have shown greater bronchial wall thickness ratio and wall area percent in asthmatics with deficient airflow reversibility than those without.

In COPD patient, previous studies have shown that CT-derived emphysema measurements were inversely associated with exercise capacity [94, 95, 96], lung volumes and function [74, 97, 98], dyspnea and quality of life [99], exacerbation [100], histological measurements [75, 101] and radiologists' assessments [73, 102]. In addition, chest CT provides a way to differentiate subtypes of emphysema, i.e., centrilobular, panlobular, and paraseptal emphy-

sema, based on the regional and anatomical distributions of CT findings [103]. Regarding large airway abnormalities, previous studies have shown correlation between airway wall thickening and COPD symptoms [104], lung functional deficits [104, 105], exacerbation frequency [95, 100] and bronchodilator responsiveness [106]. For small airways, previous studies have demonstrated that CT measurements of gas trapping correlated well with spirometry measurements, exercise capacity, quality of life [107] and other imaging measurements of lung function [108].

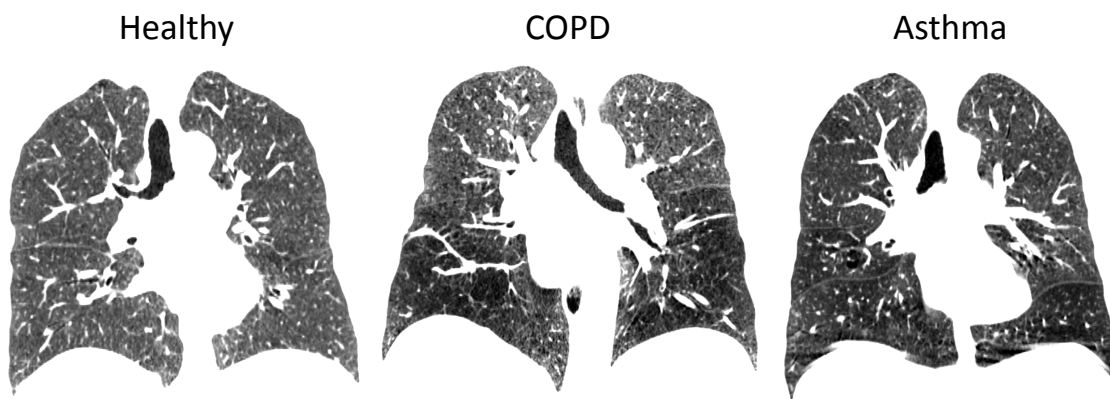


Figure 1.10: Representative CT images of a healthy, COPD and asthma subject.

In addition to a wealth of unique and quantitative pulmonary structural abnormality measurements, chest CT can also provide functional assessment of the lung in patients with COPD and asthma. Xenon-CT employs inhaled radiodense xenon gases to change the density of local lung region and airspaces that contain Xenon exhibit higher Hounsfield units indicating ventilation [109]. Dual energy CT provides another way of assessing lung function. Previous studies employed xenon-CT and dual-energy CT and observed ventilation, perfusion and ventilation/perfusion ratio that were correlated with pulmonary function measurements in COPD patients [110]. Other studies of asthmatics have shown that Xenon-CT ventilation defects were associated with worse spirometry measurements and thicker airway walls [111], which were increased and decreased following methacholine and salbutamol, respectively [112].

### 1.5.3 Nuclear Medicine

Nuclear medicine techniques such as single photon emission computed tomography (SPECT) and positron emission tomography (PET) utilize radioactive tracers, termed as radiopharmaceuticals, to acquire physiological function information. The radiopharmaceuticals are generated by bonding unstable radioactive atoms to pharmaceutically active molecules that are involved in certain physiological processes through injection, oral ingestion or inhalation. The bonded unstable radioactive atoms undergo radioactive decay to become more stable by spontaneously emitting particles and/or photons. For example in nuclear medicine imaging, technetium-99m ( $^{99m}\text{Tc}$ ), which is a commonly used radionuclide, undergoes isomeric transition into stable  $^{99}\text{Tc}$  and emits a  $\gamma$  photon. A  $\gamma$ -ray detector (also known as Anger camera) is placed around the patient to detect the emitted  $\gamma$  photons. The number and position of the emitted  $\gamma$  photons are acquired and used to generate physiologically-relevant patient information. A gamma camera selects  $\gamma$ -rays from a specific direction and converts the  $\gamma$ -rays' energy into visible light photons with a scintillation crystal, i.e., NaI. The generated visible photons are collected and converted by photosensors, i.e., photomultiplier tubes, into photoelectrons, which are then amplified to detectable electrical signals that are proportional to  $\gamma$ -rays's energy and encode spatial location information of the  $\gamma$ -rays. A computer system is then used to compile these signals, decode the location and intensity information and finally generate an image.

Similar to planar x-ray, a single static gamma camera only provides a 2D functional image without depth information. SPECT, similar to CT, can provide 3D tomographic images by rotating a gamma camera around the object or using multiple/ring gamma cameras to acquire a number of projections at different angles. Designed based on gamma cameras, SPECT shares some limitations as gamma cameras, including low spatial resolution, long scan time and inefficient use of radionuclides. Another related technique is PET that detects photon pairs rather than a single photon during radionuclide decay. PET employs radionuclides that undergo Beta+ decay with emission of positrons. The emitted positrons travel a short distance before interact-

ing with atomic electrons. This interaction results in annihilation of the positron-electron pairs and emission of two 0.511 MeV  $\gamma$  photons in opposite directions. These  $\gamma$ -ray pairs encode not only the spatial location information but also importantly the direction information of  $\gamma$  photons, which constitutes to higher sensitivity of PET over SPECT. The two  $\gamma$  photons are detected by two detector elements and the location of radionuclide Beta+ decay is restricted to that line, which is then sorted to construct a 3D image.

Nuclear medicine methods have been used to evaluate lung function including ventilation, perfusion and ventilation/perfusion ratio through inhalation or injection of radiotracers. Radioactive gases ( $^{133}\text{Xe}$ ,  $^{81m}\text{Kr}$ ), aerosols ( $^{99m}\text{Tc}$ -diethylenetriamine pentaacetate (DTPA)) and Technegas have been used for SPECT ventilation imaging through inhalation while  $^{99m}\text{Tc}$ -macroaggregates of albumin (MAA) are typically used for SPECT perfusion measurements via intravenous injection [113]. Regional distributions of the radiotracers are used to mark the physiological processes.  $^{133}\text{Xe}$  is the most traditional inhaled agent for SPECT ventilation imaging for assessments of regional lung volume and ventilation [114]. Although relatively inexpensive and readily available,  $^{133}\text{Xe}$  has a long half-life, low spatial resolution due to low energy and requires significant patient cooperation [115].  $^{81m}\text{Kr}$  has an optimal energy, short half-life and allows for spontaneous measurements of ventilation and perfusion. However,  $^{81m}\text{Kr}$  is extremely expensive with limited availability, and has critical requirements on generators, prohibiting its routine use [115]. More recently,  $^{99m}\text{Tc}$ -based radioactive aerosols have been used to evaluate regional ventilation as they are relatively inexpensive, easy to use and readily available [115]. However, a major concern is the size of the particles. For example, the large particles ( $>1 \mu\text{m}$ ), i.e.,  $^{99m}\text{Tc}$ -DTPA, result in hyperdeposition in the central airways with limited ventilation information [113] while small particles ( $<1 \mu\text{m}$ ), i.e., Technegas, lead to alveolar deposition with distortion due to alveolar-capillary clearance [113]. In general, Technegas is preferred due to homogeneous distribution and less focal deposition in both large and small airways [116]. SPECT perfusion images are typically acquired following intravenous injection of  $^{99m}\text{Tc}$ -MAA. The large size particles (10-150  $\mu\text{m}$ ) block the pulmonary arterial cir-

ulation, giving a relative measurement of regional blood flow. The radiation dose associated with a typical SPECT scan using  $^{99m}\text{Tc}$  for combined ventilation and perfusion is  $\sim 2\text{-}3$  mSv [113]. SPECT-derived asthma airway closure measurements have been correlated with clinical findings [117], and changes were observed following bronchoconstriction [118, 119] and associated with peripheral airways disease [119]. Regional ventilation and perfusion changes were observed following bronchodilator [118, 120], exercise [121], allergen challenge [122], and histamine inhalation [123, 124]. In COPD patients, SPECT-derived airway obstruction measurements have been correlated with lung function tests [125] and higher degree of airway obstruction was observed compared with healthy controls [126, 127]. SPECT ventilation/perfusion mismatching was observed in emphysema patients with superior sensitivity than CT [125, 128, 129] and was shown to be sensitive for early detection of obstructive lung disease [130, 131]. Different ventilation/perfusion matching patterns were observed in emphysema patients compared to healthy controls [128].

PET employs positron emitters to generate regional physiological measurements of the lung including ventilation, perfusion and cellular inflammation.  $^{13}\text{N}$  has been used for PET ventilation and perfusion [132] through inhalation or bolus injection. For example, through bolus injection,  $^{13}\text{N}$  delivered in the blood stream diffuses across the alveolar membrane and enters the lung due to its insolubility in blood or tissue. As a result, unventilated lung regions retain the tracer due to gas trapping while ventilated areas do not.  $^{18}\text{F}$ -fluorodeoxyglucose (FDG), an analogous glucose, is the most commonly used PET radiotracer due to high uptake in metabolically active cells, i.e., cancer. In asthma patients, PET has revealed poor lung ventilation [133] and systematically reduced regional perfusion [134] due to bronchoconstriction. Other studies have demonstrated the utility of using PET to quantify pulmonary neutrophilic [135] and eosinophilic [136] inflammation. Another study [137] observed correlation between lung tissue density and PET perfusion, ventilation/perfusion ratio measurements. In addition, high ventilation/perfusion ratio was observed in emphysema dominant obstructive lung disease while low ventilation/perfusion ratio tended to be more common in small airways disease. In COPD,

PET demonstrated significantly higher heterogeneity of perfusion and ventilation/perfusion ratio than healthy controls [138]. PET has demonstrated higher  $^{18}\text{F}$ -FDG uptake and increased neutrophilic inflammation correlated with disease severity [139]. PET ventilation/perfusion mismatch has demonstrated close correlation with the severity of gas exchange deficits measured using arterial partial pressure of oxygen [140].

Although promising, a number of limitations have restricted the routine use of nuclear medicine methods for pulmonary disease management including low image resolution and long image acquisition time for SPECT, and a need for a cyclotron and radiopharmaceutical formulation for PET.

#### 1.5.4 Pulmonary Magnetic Resonance Imaging

Magnetic resonance imaging (MRI) makes use of the nuclear properties of atoms [141, 142]. Nuclei of atoms with an odd number of protons and neutrons together generate spin and small magnetic moments along the spinning axis. Hydrogen ( $^1\text{H}$ ) nuclei of water (proton), provide commonly named protons, and this is the most commonly used nucleus for medical MRI due to its high concentrations (body tissues consist largely of water) and their strong magnetic moments. In the absence of an external magnetic field, these nuclear magnetic moments are randomly oriented in the body and the net macroscopic magnetic moment is zero. However, when placed in a strong external magnetic field  $\vec{B}_0$ , such as provided by the MR scanner, these magnetic moments align with  $\vec{B}_0$  either in parallel or anti-parallel direction, corresponding to lower and higher energy states, respectively. The magnetic field  $\vec{B}_0$  generates spin torque, which causes the spins to precess around  $\vec{B}_0$  at a specific nuclear frequency  $\omega$  (Larmor frequency, i.e.,  $\omega \approx 42.3 \text{ MHz/T}$  for  $^1\text{H}$ ). For tissues, the net magnetization  $\vec{M}$ , which is the product of the sum of the vector magnetic moments, is non-zero in  $\vec{B}_0$  direction. However, the net magnetization  $\vec{M}$  under the static external magnetic field  $\vec{B}_0$  cannot be detected macroscopically. In order to detect this signal, a radiofrequency (RF) pulse at the Larmor frequency with an energy that equals the energy difference between the two energy states is applied perpendicular to  $\vec{B}_0$ .



RF excitation results in a torque that tilts  $\vec{M}$  away from  $\vec{B}_0$  direction, generating a magnetization component  $\vec{M}'$  in the transverse plane rotating at the Larmor frequency. The rotating  $\vec{M}'$  in the transverse plane induces a change of magnetic flux through a receiver coil and therefore, generates a time-varying voltage at the Larmor frequency. The voltage in the receiver coil is the MRI signal that is detected and decays over time, which is called free induction decay. This free induction decay results from loss of coherence in the transverse component  $\vec{M}'$  due to local variations in the magnetic field and spin-spin interactions, called transverse relaxation (T2). The decay constant is termed T2\*, which is shorter than T2 due to local magnetic field inhomogeneities. The longitudinal component  $\vec{M}$  along  $\vec{B}_0$  also decays back to the low energy state due to interactions between spins and the surrounding environment, which is called longitudinal relaxation (T1). The MRI signal (or the receiver coil voltage) is determined by the  $^1\text{H}$  density in tissues, the main magnetic field strength, temperature, nuclear-specific magnetic properties, and relaxation time (different tissue have different relaxation time). To acquire different MRI signals from the different anatomical regions, it is necessary to spatially vary the magnetic field across the anatomy by incorporating three different magnetic field gradients (x, y, and z). Conventionally, the process of multi-slice 2D MRI signal acquisition consists of slice selection, frequency encoding and phase encoding procedures. The slice selection procedure (combination of the frequency offset RF pulse with z-gradient determining slice thickness) restricts signal responses from a region by selectively exciting the spins within a specific slice or plane exposed to a specific magnetic field. Within the selected slice, a phase encoding gradient or y-gradient selects the same phase line and the frequency encoding gradient or x-gradient is turned on while the receiver is triggered. Thus, MR signals at different locations along the frequency encoding direction with the same y-phase are detected. These x-y steps are repeated a number of times until all the signals from selected plane are acquired to generate an image.

### 1.5.4.1 $^1\text{H}$ MRI

MRI is an imaging method that provides excellent soft tissue contrast of the anatomy with high spatial resolution and no ionizing radiation. Despite these advantages, conventional  $^1\text{H}$  MRI of the lung has been technically challenging due to a number of reasons. The lung is largely an air-filled organ with typically  $\sim 800$  g lung tissue distributed over a  $\sim 4$ - $6$  L lung volume [143, 144]. Since MRI signal intensity is proportional to  $^1\text{H}$  density in the tissue, the low lung tissue density and low  $^1\text{H}$  atom density result in low MRI signal intensity. In addition, an adult lung consists of  $\sim 480$  million alveoli [25] and the countless air-tissue interfaces lead to local magnetic field inhomogeneities [145]. Since  $^1\text{H}$  spin precession frequency is determined by the local magnetic field, the  $^1\text{H}$  atoms at these air-tissue interfaces spin at different rates, leading to increased dephasing of the magnetization and signal decay. Furthermore, due to the relatively slow image acquisition speed, the respiratory and cardiac motion cause artifacts that further degrade MRI image quality. Because of these limitations, it was thought that conventional pulmonary  $^1\text{H}$  MRI provides limited information about the lung, although a number of studies have demonstrated its clinical utility. For example, previous studies of asthma anti-inflammatory treatments using conventional  $^1\text{H}$  MRI demonstrated different regional allergic reaction with different allergen doses. The MRI-based treatment response measurements corresponded to eosinophilic responses, suggesting the promising utility of MRI for asthma management [146]. Other studies of asthma employed multiple  $^1\text{H}$  MRI acquisitions to generate ventilation measurements that were correlated to pulmonary function tests [147] and noble gas MRI outcomes [148]. In COPD, previous studies observed inspiration-expiration  $^1\text{H}$  MRI lung signal intensity changes that were correlated with airflow obstruction measurements [149]. Another study has revealed inflammatory bronchial wall thickening, mucus secretion, emphysematous tissue loss, reduced blood volume in COPD using  $^1\text{H}$  MRI [150]. A recent study demonstrated lower  $^1\text{H}$  MRI lung signal intensities that were related to CT emphysema measurements and higher anterior-posterior signal intensity gradients in COPD patients compared to never-smokers [151].

Oxygen-enhanced MRI (OE-MRI) [152] was developed in the 1990s to provide regional pulmonary ventilation information using molecular O<sub>2</sub> as a contrast agent. Molecular O<sub>2</sub> contains two unpaired electrons in the outer shells and is weakly paramagnetic. The presence of O<sub>2</sub> will accelerate the longitudinal relaxation of protons in lung tissue depending in O<sub>2</sub> concentration [152]. Previous studies have shown that MRI oxygen enhancement measurements of COPD were correlated with lung diffusing capacity [153, 154], lung function measurements [153, 155], CT emphysema score [153] and disease stages [155]. In asthma, studies have shown different O<sub>2</sub> enhancement ratio across asthma severities and correlation with lung function measurements [156, 157, 158]. Another study demonstrated decreased oxygen transfer function after segmental allergen challenge and increased volume of lung tissue with prolonged relaxation times that were correlated with the percentage of eosinophils measurements [159].

Fourier decomposition of free-breathing pulmonary <sup>1</sup>H MRI (FDMRI) has been developed for visualization and quantification of lung ventilation and perfusion using conventional MRI systems [160]. FDMRI exploits fast acquisition and deformable registration of a series of free-breathing conventional pulmonary <sup>1</sup>H MRI without using exogenous contrast agents. In the spatially aligned images, MRI signal intensity oscillations over time can be decomposed using Fast Fourier Transforms to generate functional ventilation and perfusion maps [161]. In COPD, previous studies have shown that FD-derived lung ventilation measurements were correlated with <sup>3</sup>He MRI lung ventilation outcomes (with high spatial overlap) [162, 163], airway resistance [162] and CT emphysema score [162, 164]. However, limited work of using free-breathing <sup>1</sup>H MRI for asthma evaluation has been done so far. A pioneering study of lung disease including asthma explored <sup>1</sup>H MRI lung signal intensity changes during breathing as a surrogate measurement of lung function [147]. This study demonstrated excellent correlation between FDMRI-derived lung ventilation and pulmonary function measurements [147]. A recent study of asthma [165] demonstrated that FDMRI-derived ventilation defect measurements increased after methacholine challenge and decreased after salbutamol, and similar results were observed using <sup>3</sup>He MRI. Using the same technique, another study observed correlation be-

tween free-breathing  $^1\text{H}$  MRI ventilation and  $^3\text{He}$  MRI ventilation measurements and lower FDMRI ventilation outcomes in asthmatics compared to healthy volunteers [148].

As previously discussed, conventional  $^1\text{H}$  MRI of the lung is challenging due in part to low tissue density and magnetic susceptibility that result in fast MR signal decay. As a result, the lung appears as a black hole with limited structural information when conventional MR spin-echo pulse sequences are used. Ultra-short echo-time (UTE) MRI acquisition methods have been proposed to provide enhanced visualization of lung structure and function using conventional MRI systems. UTE MRI employs short echo-time (time between the end of the RF excitation to the beginning of data acquisition [166]) pulses to minimize signal decay and motion artifacts and maximize the visibility of lung parenchyma [145]. Recent studies have shown that UTE MRI provides enhanced visualization of pulmonary structures comparable to CT [167, 168]. Figure 1.11 shows UTE MR images for a healthy, COPD and asthma subject compared to conventional  $^1\text{H}$  MRI. In asthma, previous studies [169] have shown that UTE MRI lung static and dynamic signal intensities were lower than healthy volunteers, correlated with lung function and CT radiodensity measurements. In COPD, previous studies demonstrated significant correlations between lung function measurements and both CT and UTE MRI lung densities [170]. UTE MRI lung signal-intensity measurements were also correlated with CT emphysema measurements and lung function tests [171]. UTE MRI  $T_2^*$  values were lower for severe COPD than moderate COPD and were correlated with lung function measurements, and CT-based functional lung volumes [172].

#### **1.5.4.2 Inhaled Noble Gas MRI**

The challenges associated with conventional MRI of the lung can be overcome using inhaled gaseous contrast agents, i.e.,  $^3\text{He}$  and/or  $^{129}\text{Xe}$ , which permit direct visualization of MRI lung airspaces. However, the low spin density of  $^3\text{He}$  and  $^{129}\text{Xe}$  gases compared with solid tissue prohibits its MR detectability under thermal equilibrium polarization. Since MR signals are determined by spin polarization, one way to improve MR signals of the noble gases is through

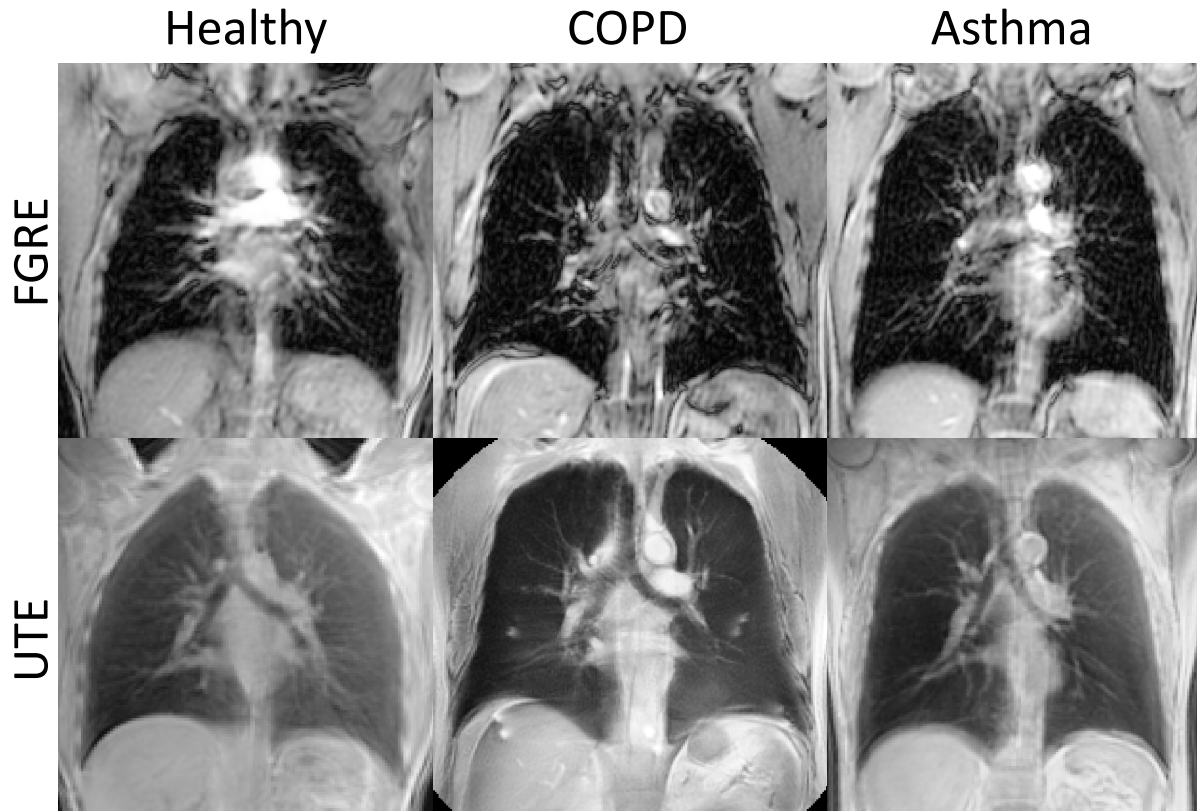


Figure 1.11: Representative conventional FGRE and UTE MR coronal images of a healthy, COPD and asthma subject. In conventional FGRE MRI, lung structural abnormalities inherent to obstructive lung disease cannot be visually distinguished due to low tissue and  $^1\text{H}$  density. In contrast, UTE MRI provides enhanced visualization of the lung with higher signal intensities and regions of low signal intensities are visible in obstructive lung disease compared to the healthy volunteer.

hyperpolarization to enhance the visibility of gases in a MR scanner. Hyperpolarization of noble gases with  $1/2$  spin is typically achieved through optical pumping of alkali metal vapour (i.e., Rb) and spin exchange between excited alkali atoms and noble gas nuclei [173]. The optical pumping technique involves a glass cell filled with a mixture of Rb vapour and noble gases placed in a small magnetic field. Circularly polarized laser light is used to excite the electrons of Rb atoms and through collisions, the polarized Rb electrons transfer angular momentum to noble gas nuclei. This process results in increased noble gas nuclear spin polarization up to 10,000 times higher than thermal polarization [174], suppressing the signals from other tissues. Although the initial investigation of noble gas MRI of the lung employed hyperpolarized

$^{129}\text{Xe}$ , the focus quickly shifted to hyperpolarized  $^3\text{He}$  MRI. This is mainly because  $^3\text{He}$  provides higher magnetic moments (hence higher gyromagnetic ratio of  $-32.3\text{ MHz/T}$  for  $^3\text{He}$  vs  $-11.8\text{ MHz/T}$  for  $^{129}\text{Xe}$ ) and higher achievable polarization level ( $\sim 50\%$  for  $^3\text{He}$  vs  $\sim 20\%$  for  $^{129}\text{Xe}$ ) [175]. Since 1996 when the first noble gas MRI of human lung was acquired [176], this technique was quickly adapted for a variety of lung disorders including asthma, COPD, cystic fibrosis and lung cancer. Importantly, previous studies have demonstrated the excellent safety [177] and tolerability [178] profile of this technique across a wide range of respiratory disorders. Recently, the area of noble gas lung MRI is transitioning back to  $^{129}\text{Xe}$  due to its higher natural abundance and lower cost compared to  $^3\text{He}$  as well as the advancements of hyperpolarization techniques.

Using this technique, two types of images including spin density and diffusion weighted images can be acquired to provide lung structural and functional information. Spin density images provide high resolution visualization of noble gas distribution in the lung and the MR signal intensities reflect regional gas abundance and ventilation upon inhalation. As shown in Fig. 1.12, homogeneous noble gas MR signals are observed in healthy lung suggesting that all regions of the lung are equally ventilated. In contrast, heterogeneous MR signals are observed in asthma and COPD lung indicating that lung regions with no or low signal intensities are poorly ventilated or not ventilated within the breath-hold procedure. Importantly, previous studies have shown highly reproducible noble gas MRI lung ventilation and ventilation defect measurements through short-term repeated scans [179, 180, 181] and consistence with other imaging modalities [182]. Initial investigation of noble gas MRI of the lung involved radiologists' visual interpretation [182, 183, 184], as well as manual [185, 186, 187], semi-automated [188, 189] and automated [190] segmentation of noble gas MR images. A number of metrics have been developed to quantify noble gas MRI including ventilation defect volume, ventilation volume, coefficient of variation of signal intensities, ventilation defect percent (VDP). Among these metrics, VDP is a widely used noble gas MRI biomarkers that is calculated by normalizing ventilation defect volume to the thoracic cavity [188]. To date, a number of investigations

have been performed to evaluate COPD and asthma static ventilation abnormalities using noble gas MRI. In asthma, previous studies [179, 191] observed increased number of  $^3\text{He}$  ventilation defects compared to healthy subjects. Similar observations were reported in children with asthma than those without [192]. Another study [183] demonstrated that in asthma, the number of  $^3\text{He}$  ventilation defects per slice was greater than controls, related to asthma severity and correlated with lung function measurements. Other investigations reported correlation between  $^3\text{He}$  VDP and airway resistance and dyspnea [193]. Greater  $^3\text{He}$  ventilation defects were also related to worse airflow obstruction, greater airways resistance, airway inflammation [194] and asthma control [195]. In addition, high spatial overlap was observed between  $^3\text{He}$  MRI ventilation defects and CT gas trapping measurements and lobar differences of  $^3\text{He}$  MRI ventilation levels were related to neutrophilic inflammation [196]. Regarding asthma treatment, previous studies have shown greater ventilation heterogeneity [197], and number and size [191, 193] of ventilation defects following methacholine and exercise challenge. Improvements of  $^3\text{He}$  ventilation were observed after bronchodilator [179, 198] with partial recovery [191, 193, 199]. In COPD, noble gas MRI VDP was correlated with lung function measurements [200], COPD exacerbations [201] and pulmonary emphysema measurements [202]. Importantly, previous studies [203] demonstrated improved  $^3\text{He}$  distribution after bronchodilator therapy regardless of changes of  $\text{FEV}_1$  in COPD.

Diffusion weighted noble gas MRI provides a way to quantify pulmonary microstructure by sensing the movements of inhaled gas atoms. Both  $^3\text{He}$  and  $^{129}\text{Xe}$  are highly diffusive and after inhalation, the diffusion of gas atoms due to random Brownian motion is restricted by the alveolar wall, bouncing back and forth within the airspace. Therefore, the “apparent” diffusion coefficient (ADC) during the diffusion time interval can be used to reflect the extent of alveolar restriction of gas atom movements, providing a surrogate measurement of airspace dimensions [204]. For example, increased ADC ( $\text{cm}^2/\text{s}$ ) values reflect enlarged airspace and these are valuable tools for evaluating lung structural changes, i.e., emphysema-related airspace enlargements. The majority of diffusion-weighted imaging for ADC involves  $^3\text{He}$ . However,

it is important to note that  $^{129}\text{Xe}$  provides added value of measuring transmembrane diffusion across the alveolar wall. Previous studies of  $^3\text{He}$  ADC measurements have demonstrated high reproducibility [205, 206] and strong correlation with histological measurements of airspace dimensions [52, 207]. In patients with COPD, studies have demonstrated elevated  $^3\text{He}$  and  $^{129}\text{Xe}$  ADC values compared to healthy volunteers [208, 186, 209], and correlations with age [210, 209, 200], pulmonary function tests [208, 209, 200], CT measurements of emphysema [210, 200], and gas trapping [108]. Another study [211] demonstrated that  $^3\text{He}$  ADC measurements were more sensitive to early or pre-clinical lung structure changes than pulmonary function measurements. Recently, investigations have shown decreased  $^3\text{He}$  ADC values in COPD patients treated with bronchodilators [212], suggesting a reduction of regional gas trapping. For asthma, limited work has been performed to investigate lung structure using diffusion weighted noble gas MRI. Some studies [213, 214] observed elevated ADC values in asthma compared to healthy volunteers while others [193] demonstrated no differences. Regarding asthma treatments, whole lung ADC was increased after methacholine challenge and decreased after salbutamol administration [193], and correlated with CT gas trapping measurements [214].

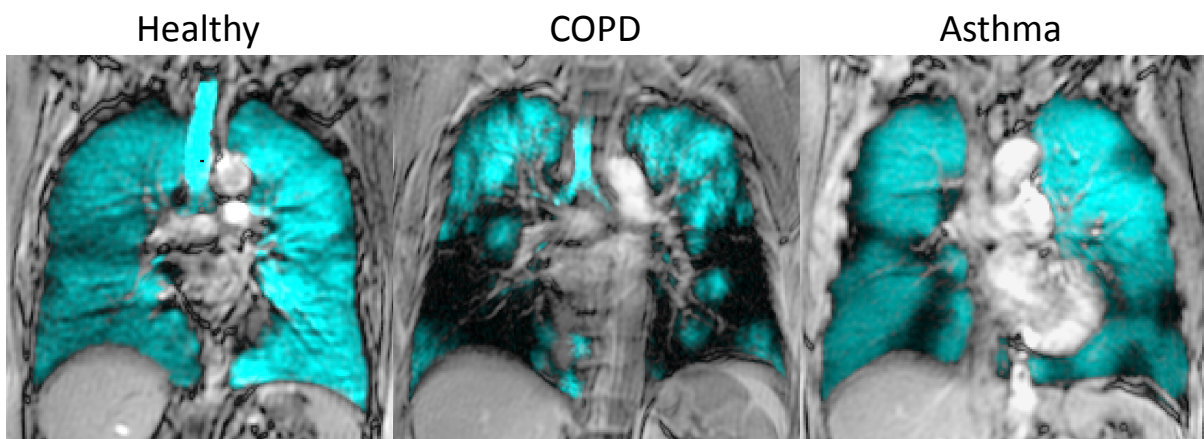


Figure 1.12: Representative co-registered hyperpolarized  $^3\text{He}$  (cyan) and  $^1\text{H}$  (gray) MR coronal images of a healthy, COPD and asthma subject. Homogeneous  $^3\text{He}$  MRI signal intensities are observed in the healthy while heterogeneous signal intensities are seen in obstructive lung disease.



## 1.6 Medical Image Segmentation, Registration and Evaluation Methods

### 1.6.1 Image Segmentation

Image segmentation is the process of partitioning an image  $I(x)$ ,  $x \in \Omega$ , into multiple regions or classes such that the pixels within each region or class share some common characteristics, i.e., signal intensity homogeneity [215, 216]. This thesis focuses on medical image segmentation, which plays a crucial role in medical imaging applications [217, 218, 219, 220] such as tumor or pathology localization, structure/function mapping, mass detection and quantification, medical image registration, surgical planning or simulation, and computer-aided diagnosis, to name just a few. With respect to pulmonary imaging, which is the focus of this work, lung segmentation is fundamentally required as a first step to quantify pulmonary structural-functional abnormalities and generate imaging biomarkers with the hope to facilitate the development of pulmonary medicine. In the following section, I will provide brief descriptions of the commonly-used medical image segmentation algorithms before I present the pulmonary MRI segmentation algorithms in Chapters 2–3.

### 1.6.2 Medical Image Segmentation Algorithms

#### 1.6.2.1 Thresholding

Thresholding is perhaps the simplest segmentation approach, with fast implementation and intuitive properties [221]. Thresholding is the procedure of determining a global threshold of some image features, i.e., signal intensities, to divide the feature space into the “foreground” and “background” regions. The “foreground” region represents the pixels with intensities that are greater than or equal to the threshold and the “background” region contains the pixels with intensities that are less than the threshold, resulting in “0-1” binary segmentation. Threshold-

ing segmentation is based on the assumption that the difference or contrast of image signal intensities from the “foreground” and “background” regions is high [218, 220]. Due the complexity of medical images, usually more than one threshold is determined to segment an object or multiple objects, which is called multi-thresholding segmentation [222]. Thresholds are usually generated interactively based on observers’ visual inspection, although automated methods exist [221] including the Otsu’s thresholding method [223].

Global thresholding considers image signal intensity information exclusively without taking into account the spatial relationship between pixels. In medical images, due to signal intensity inhomogeneity, imaging artifacts, various pathologies, and different levels of noise, global thresholding is usually not sufficient. For these reasons, variations of classical thresholding methods have been proposed including local/dynamic thresholding. These thresholding schemes were developed to account for foreground/background signal intensity variation. The basic idea is that the signal intensities may not be uniform across the whole image, but are relatively homogeneous within a local region. Therefore, local thresholds can be determined for different parts of the image [224] and these local segmentation can be merged to derive the global segmentation. In practice, different statistical methods are used to generate the local thresholds including mean, standard deviation, mean of the maximum or minimum values [225], and local gradient [226].

### 1.6.2.2 Region Growing

Region growing is an image segmentation technique aimed to extract a connected region of pixels with similar signal intensities [227]. In the simplest form, region growing requires a seed point or region that belongs to the target region for initialization. The algorithm then grows the current region by including more neighbouring pixels to the seeds under some similarity criterion [228]. A simple similarity metric is the absolute difference between a candidate pixel intensity  $f(x)$  and the current region’s mean signal intensity  $\mu_r$ , i.e.,  $S(x, r) = |f(x) - \mu_r|$ . This process is iterated until no more pixels can be added and the final “region” is obtained.

Another similar but fundamentally different algorithm is region splitting [229] instead of growing. This algorithm starts with an initial segmentation, i.e., the whole image, and recursively splits the regions that do not satisfy a uniform criterion into new regions that are more uniform, i.e., lower signal intensity variances. The splitting procedure is repeated on each of the new regions until no further splitting is needed. This process results in a number of small uniform regions, some of which are very homogeneous and can be merged. This leads to the split-and-merge algorithm, which is used to combine the small uniform regions and generate larger regions as the final segmentation [230, 231].

### 1.6.2.3 Watershed

Watershed is an image processing technique that employs the topography information in gray level images. This technique was originally developed by Digabel and Lantuejoul [232] and later adapted for image segmentation [233]. To appreciate this algorithm, one can consider a 2D image as a 3D topographic surface where the elevation at each pixel location is represented by the grayscale value. Such a representation leads to catchment basins that are analogous to regions to be extracted. Intuitively, a falling water drop will flow along the path with the steepest slope until it reaches a local minimum or basin. The water drops from pixels that trace to the same minimum are grouped to the same catchment basins, and the basin's boundaries are considered as watershed lines, resulting in the segmentation. This concept also applies to higher-dimensional images and images with multiple regions to be extracted.

In general, there are two types of approaches to find the watersheds of an image: 1) flooding approach, and 2) rainfalling approach. In the flooding approach, which is also called the immersion approach, holes are pierced at the local minima of the surface and water flows are injected through these holes to flood the respective catchment basins. If the water flow from one basin is about to meet the other, a wall or watershed line is built to separate the two water flows, and these watershed lines correspond to the boundaries of the regions in the image [234]. The rainfalling simulation, as the name suggests, flows water drops on image pixels along the

steepest paths until they reach a local minimum, which is labelled with a unique tag. The water drops from pixels that accumulate in the same local minima are considered as a group. Once all the pixels are related to a tagged local minima, image regions are identified and the segmentation is generated [233]. A number of efficient algorithms have been developed to find watersheds [235, 236].

#### 1.6.2.4 Classifiers

Classification algorithms seek to assign pre-defined class labels to a given sample set and are considered supervised processes. Classification and segmentation are closely related to each other as segmentation implies a classification and classification implicitly represents segmentation. Classification typically involves a training and a testing phase. In the training phase, unique and distinguishing properties of different classes are generated. In the following testing phase, samples are “recognized” and assigned a pre-defined class label based on generated characteristic properties. In the following section, a brief review of some commonly-used classifiers is provided.

***K*-nearest neighbours:** The *K*-nearest neighbour (*K*-NN) algorithm [237] is a simple and non-parametric classifier. The training process consists of storing the samples and the associated labels. The testing process measures the similarity between a query sample and the stored samples based on some distance metric, which is not necessarily the Euclidean distance (although it is commonly used). The *K* (i.e., a pre-defined integer) nearest neighbours from the stored samples are selected and the associated labels are used to generate a label for the query samples, i.e., through majority vote. This classifier requires minimal explicit training and all the training data is used for testing. As a result, the computation cost is high in terms of time and memory requirements. Although this algorithm enables multi-class classification, it is sensitive to “noise”.

**Support vector machines:** Support vector machine (SVM) [238] is a supervised linear classifier that aims to generate a hyperplane to separate the training samples. Such hyperplanes

are generated to maximize the distances between the nearest samples in the two classes, so that the risk of overall classification error is low. With the generated separating hyperplane, query points are then mapped to one side of the plane in the same space and the class labels are determined. Although SVM was initially designed as a two-class linear classifier, improvements [239] have been made for multi-class applications. In addition, a non-linear SVM classifier can be achieved by mapping the samples to a higher-dimensional kernel space such that they become linearly separable. Another advantage of SVM classifiers is that they provide robust classification and are relatively insensitive to noise or small sample sizes. In addition, SVM is represented by a convex optimization problem and the global optimum exists. However, there are a number of limitations associated with SVM including high computational burden during both the training and the testing phase, and the choice of kernel can be tricky [240].

**Maximum likelihood:** Maximum likelihood is a supervised classifier developed based on Bayes theorem. This algorithm aims to maximize the posterior probability  $p(i|w) = \frac{p(\omega|i)p(i)}{\sum_j p(\omega|j)p(j)}$ , which is interpreted as the probability of assigning a class label  $i$  to a sample  $\omega$  if  $p(i|w)$  is greater than any  $p(j|w)$  for class label  $i \neq j$ . The prior probability  $p(i)$  represents the relative frequency of the occurrence of class  $i$ , which can be estimated from the training samples. The class-dependent term  $p(\omega|i)$  represents the probability that a sample  $\omega$  appears in class  $i$ , which can be assumed to satisfy a parametric form, i.e., Gaussian distribution [241]. For a new sample, the posterior probability for each class is calculated and the label of the class with the highest probability is assigned to the sample, that is, the maximum likelihood. This classifier requires a large amount of samples for each class, and does not perform well with small class sizes. In addition, the training process is sensitive to pre-classification [220].

**Artificial neural network:** Artificial neural network (ANN) is an information processing system inspired by the neuron systems in human brain. This model was first designed in the 1940s [242] and later significantly improved [243]. An ANN consists of a large number of processing units that are called artificial neurons or nodes. These neurons or nodes are highly inter-connected to generate a complex network, where the connection weights are

tuned through learning or training processes. ANN represents a paradigm of machine learning and has been successfully applied to medical image processing, including segmentation and classification [244] especially with the emergence of deep learning. ANNs are data-driven self-adaptive classifiers and are very flexible in approximating the relationship between groups with high accuracy [245]. However, a major drawback of ANNs is that the learning process is slow and a large amount of computational power is required to generate reasonable outputs, as reported by a recent study by Google [246].

### 1.6.2.5 Clustering

Clustering aims to organize a set of samples into distinct groups called clusters such that samples within a cluster are similar to each other based on some specified measurements and dissimilar to samples in other clusters. Unlike classification, clustering does not rely on pre-defined groups or training and is also known as unsupervised classification. Due to this property, new patterns or features from large datasets can be discovered during the clustering procedure without requiring intensive or extensive background knowledge [247]. In the following section, I briefly review some representative clustering methods.

**K-means:** K-means [248] is a clustering algorithm that aims to partition a given dataset with  $N$  samples  $\{I_1(x), I_2(x) \dots I_N(x)\}$  into  $K$  clusters  $\{N_1(x), N_2(x) \dots N_K(x)\}$ , such that the cluster-wide dissimilarity is minimized, i.e., sum of squared differences from samples to the cluster mean. For example, the K-means clustering algorithm can be mathematically formulated as follows:

$$\arg \min_{\{N_1, N_2, \dots, N_K\}} \sum_{k=1}^K \sum_{j=1}^{|N_k|} \|I_j(x) - \mu_k\|^2, \quad (1.2)$$

where  $\mu_k$  represents the mean of cluster  $k$  and  $|N_k|$  indicates number of samples in the  $k^{\text{th}}$  cluster  $N_k$ . This problem Eq.(1.2) is computationally difficult, but local optimization-based algorithms exist. The most common K-means clustering algorithm employs an iterative implementation of two alternating steps: 1) clustering (assignment) and 2) mean calculation (update) [249]. The algorithm is started by defining a desired number of clusters  $K$  and assigning  $K$  arbitrary means

to each cluster. In the clustering (assignment) step, each sample is associated to the closest cluster based on the selected similarity measurement. In the mean re-calculation (update) step, the mean is re-computed for each cluster. These two steps are iterated until no more changes occur or a maximum number of iterations is reached.

It should be noted that this algorithm often leads to a local optimum and is sensitive to noise and initial cluster assignment [250]. Another drawback is that the number of clusters  $K$  needs to be pre-defined, although this can be overcome by adding an outer loop with increased computation complexity [251].

**Fuzzy C-means:** The Fuzzy C-means algorithm [252] is a generalized form of K-means clustering approach based on fuzzy set theory [253]. Instead of a hard (i.e.,  $\{0, 1\}$ ) assignment as in the traditional K-means, Fuzzy C-means allows soft (i.e.,  $[0, 1]$ ) assignment of each sample to a cluster by adding a weighting factor as follows:

$$\arg \min_{\{N_1, N_2, \dots, N_K\}} \sum_{k=1}^K \sum_{j=1}^{|N_k|} \omega_{k,j} * \|I_j(x) - \mu_k\|^2, \quad (1.3)$$

where  $\omega_{k,j} \in [0, 1]$  is pre-defined and represents the probability or weight of assigning sample  $j$  to cluster  $k$ . The numerical implementation of Fuzzy C-means is similar to the K-means approach except that the mean of cluster  $k$  is calculated in a weighted manner and the weight  $\omega_{k,j}$  is updated [252].

**Expectation Maximization:** Similar to the centroid and mean-based K-means [248] and Fuzzy C-means [252] clustering algorithms, the expectation maximization algorithm [254] employs the same clustering procedure with the assumption that the samples follow a mixture of Gaussian function. As reflected by the name, this algorithm involves an *expectation* stage and a *maximization* stage for each iteration to maximize the likelihood estimation of the samples. In the *expectation* stage, the posterior probability  $P(N_k|I_j(x); \phi)$  for assigning sample  $I_j(x)$  to cluster  $N_k$  is calculated based on a given statistical model  $\phi$ . In the *maximization* stage, the mean, sample distribution, and the coefficients of the mixture model are re-estimated using

the updated probability measurements. The two stages are iterated until convergence and the resulting “fuzzy” probabilities can be discretized to generate the final clusters. Due to different similarity measurements, this algorithm addresses sample inhomogeneity problem only to some extent. However, this algorithm is sensitive to initialization and the convergence rate is slow especially when dealing with high-dimensional data.

### 1.6.2.6 Deformable Models

Since their introduction [255], deformable models have attracted a great deal of attention in the area of object tracking/recognition, edge detection, image segmentation and modelling. In general, deformable models are closed parametric curves in 2D or surfaces in 3D that are able to expand or contract under the influence of internal, and external forces [256, 217, 219]. The internal forces are designed to keep the continuity of the curve or surface and the external forces are defined to fit the model to the desired object [256]. Depending on the representation of the curves and surfaces, deformable models can be divided into two categories: 1) parametric deformable models, and 2) geometric deformable models.

**Parametric deformable models:** Parametric deformable models, also known as active contours or snakes, represent contours/surfaces explicitly using parameterized formulations that can be solved under an energy minimization perspective. Let  $C$  denote a 2D contour embedded in an image  $I(x, y)$ ,  $\{x, y\} \in \Omega$ . The contour  $C$  is represented by a number of control points  $v(s) = (x(s), y(s))$ ,  $s \in [0, 1]$  in the normalized parameter domain with  $v(0)$  and  $v(1)$  representing the first and last control point, respectively. The energy of contour  $C = \{v(s) = (x(s), y(s)), s \in [0, 1]\}$  can be generally formulated as follows:

$$E(C) = E_{int} + E_{ext}. \quad (1.4)$$



The internal force  $E_{int}$  keeps the contour continuous and is defined as

$$E_{int} = \int_0^1 \left( \alpha(s) \left| \frac{\partial C}{\partial s} \right|^2 + \beta(s) \left| \frac{\partial^2 C}{\partial s^2} \right|^2 \right) ds, \quad (1.5)$$

where  $\alpha$  and  $\beta$  represent the weights of the two components. In Eq. (1.5), the first component controls the elasticity of the contour and the second term regulates the rigidity of the model.

The external force  $E_{ext}$  attracts the contour towards the desired object boundaries and is given by

$$E_{ext} = -\omega \int_0^1 |\nabla I(C(s))| ds, \quad (1.6)$$

where  $\omega$  provides the relative weight of the external force  $E_{ext}$  to the internal potential  $E_{int}$ .

The optimal contour  $C^*$  can be obtained by minimizing the object function Eq. (1.4) using an analytical gradient decent approach.

The parametric deformable models are capable of generating closed contours/surfaces directly with sub-pixel accuracy, incorporating a variety of constraints (i.e., gradient vector flow), *prior* knowledge, and are robust to image noise and boundary discontinuities. The model initialization can be performed manually or automatically, i.e., using the Hough transform and region-growing. However, it should be noted that such parametric deformable models are locally-optimized [257], and are sensitive to initialization and the initial contours are usually placed close to the object to generate reasonable results. Another drawback of these models is the associated difficulty of handling topological changes such as merging and splitting during contour evolution [258, 259].

**Geometric deformable models:** Geometric deformable models were developed based on level-set theories and are also known as level-set methods. As previously described [258], parametric deformable models have remarkable limitations in dealing with topology changes during curve/surface evolution because of the required parametrization procedure. The level-set method [258] was developed to address this problem by implicitly representing curves/surfaces with a level set of higher-dimensional function. These level set function employs geometric

measurements and are free from curve/surface parametrization. In other words, the level-set method implicitly evolves curves/surfaces by updating the level set function and therefore is able to handle topology changes during evolution.

Following the curve evolution theory [260], an evolving curve  $C(s, t)$  can be implicitly represented by a level set function  $\phi(x, y, t)$  at the zero level, i.e.,

$$\phi(C(s, t), t) = 0, \quad (1.7)$$

where  $t$  represents time. With an initial  $\phi$  at  $t = 0$ , it is possible to estimate  $\phi$  at any time  $t$  by differentiating the equation Eq. (1.7) with respect to  $t$ , i.e.,

$$\frac{\partial \phi}{\partial t} + \nabla \phi \frac{\partial C}{\partial t} = 0, \quad (1.8)$$

where  $\frac{\partial C}{\partial t}$  is the curve evolution speed along the normal direction dependent on local curvature  $k$ , i.e.,  $\frac{\partial C}{\partial t} = F \cdot \frac{\nabla \phi}{|\nabla \phi|}$ . The surface curvature  $k$  depends only on  $\phi$  and is defined as follows:

$$k = \frac{\phi_{xx}\phi_y^2 - 2\phi_x\phi_y\phi_{xy} + \phi_{yy}\phi_x^2}{(\phi_x^2 + \phi_y^2)^{3/2}}, \quad (1.9)$$

which can be calculated as previously described [258]. Thus, Eq. (1.8) can be re-written as

$$\frac{\partial \phi}{\partial t} + F \cdot |\nabla \phi| = 0. \quad (1.10)$$

Clearly, Eq. (1.10) determines the motion of  $\phi$ , which can be updated as follows:

$$\phi(t + \Delta t) = \phi(t) - \Delta t \cdot F |\nabla \phi|, \quad (1.11)$$

where  $\Delta t$  is the time step for evolution and the gradient  $|\nabla \phi|$  can be calculated using a finite difference method [258]. Depending on the applications, curvature, intensity gradient, shape, and contour position information can be incorporated to construct the speed function  $F$  to

generate desired results.

The level-set method [258] was later implemented by Cassels et al. [260] and Malladi et al. [261] for image segmentation and generated promising results. However, there are a number of limitations associated with these methods. For example, these methods involve solving partial differential equations and estimating second order derivatives and are therefore computationally expensive although fast implementations, i.e., narrow-band [262] and sparse-field [263] methods are available. In addition, there are limitations on the evolution step size for numerical stability and the convergence rate is slow. Importantly, level-set methods rely on local optimization techniques, are sensitive to initialization and generate only local minima.

### 1.6.2.7 Markov Random Fields

Markov Random Field (MRF) represent a joint probability distribution model and was first introduced to image processing in the 1980s [264]. For image segmentation, reconstruction and labelling, MRF provides a way to model the interactions between image pixels by introducing a series of hidden variables and representing the image as a graph [265]. Let  $G = \langle V, E \rangle$  denote a MRF graph for an image  $I(x)$ ,  $x \in \Omega$ , where  $V$  is the set of nodes or vertices representing the observations (i.e., signal intensities) of image pixels or superpixels,  $E$  is the set of undirected edges between adjacent nodes  $i$  and  $j$ ,  $\{i, j\} \in V$ . The hidden variables are associated with the pixels and the adjacent pixel-pixel interactions are encoded in a form of edge dependencies. For binary image segmentation, a hidden variable  $L_i$  for node  $i$  takes random value of “0” or “1” representing the desired background and foreground of the image, respectively. The resulting joint probability of such a graph can be formulated as follows:

$$P(L, I) = \prod_{i \in V} \Psi(L_i, I_i) \prod_{i, j \in V} \Phi(L_i, L_j). \quad (1.12)$$

In Eq. 1.12,  $\Psi(L_i, I_i)$  represents the association between the label and the observation for node  $i$ , i.e., the likelihood that node  $i$  belongs to label  $L_i$ ;  $\Phi(L_i, L_j)$  indicates the pixel-pixel interactions

encoded in the hidden variables for adjacent pixels  $i$  and  $j$ ,  $\{i, j\} \in V$ . Taking the *log* form of  $P(L, I)$  (Eq. 1.12) gives rise to

$$E(L, I) = \sum_{i \in V} \Psi(L_i, I_i) + \sum_{i, j \in V} \Phi(L_i, L_j), \quad (1.13)$$

The segmentation is then achieved by finding the maximum of the joint probability, which can be obtained using gradient descent, simulated annealing or iterated conditional modes. While MRF represents a powerful and elegant approach to complex data analysis, early-stage solvers are nevertheless computationally demanding.

### 1.6.2.8 Graph-cut Methods

By representing digital images as MRF graph  $G = \langle V, E \rangle$ , image segmentation can be viewed as a labeling problem - assigning labels from a finite label set  $L$  to each voxel under some optimal criterion constraints. The graph-based image segmentation problem can be formulated as finding a finite set of labels under some given objection function that measures either “goodness” or “badness” of a solution [266]. The optimal segmentation or label set, can be achieved by optimizing the formulated objective function through combinatorial optimization. For example, the “0-1” image segmentation problem can be solved by finding a *min-cut* over the image graph with minimal labeling cost and minimal segmentation surface area [266]. With appropriate graph design, the process of finding a *min-cut* that divides an image graph is actually equivalent to optimizing the objective function. Thanks to the max-flow/min-cut theories [267, 268], the min-cut problem can be further equivalently and efficiently solved through the associated max-flow formulation in a globally optimal manner. A number of max-flow algorithms have been proposed including the “augmenting paths” [267] and the “push-relabel” [269] algorithms.

Pioneered in the early 2000s by Boykov and Kolmogorov [270], graph-cut methods have been widely used in image segmentation and achieved tremendous success in medical applica-

tions. However, such discrete graph-cut methods are limited by metrication error, high memory load and computation burden [271]. Later, the discrete graph-cut methods were investigated in spatially continuous settings [272, 273, 274] to avoid the grid biases and achieve high computational efficiency with sub-voxel accuracy. A brief review of the discrete and continuous graph-based max-flow/min-cut is provided in Appendix A.

### 1.6.3 Segmentation Performance Evaluation

When an image is segmented, the “goodness” of the segmentation is quantitatively evaluated to determine the performance of the segmentation algorithm. Segmentation evaluation is typically performed by comparing algorithm outputs to ground truth, which is, however, usually not available. Physical and computational phantoms could serve as the ground truths, but there are inherent limitations [217]. Expert manual delineation of the objects of interest, although not always perfect, involves invaluable experiences and high-level human prior knowledge and is often used as a surrogate of such ground truths. I briefly describe the segmentation evaluation metrics, namely accuracy, reproducibility, and computational time as follows.

#### 1.6.3.1 Accuracy

Region-, volume-, and distance-based metrics are commonly employed to evaluate the similarity between algorithm and expert manual outputs.

Dice-similarity-coefficient (*DSC*) [275] is a commonly-used region-based metric to quantify the overlap ratio of algorithm segmentation with respect to reference standards. Let  $R_A$  and  $R_M$  denote the algorithm and manual segmentation of the same object, respectively. *DSC* is calculated as follows:

$$DSC = \frac{2(R_M \cap R_A)}{R_M + R_A} \times 100\% . \quad (1.14)$$

*DSC* ranges from 0% to 100%, representing no overlap to perfect overlap between two segmentation, respectively.

Volume-based metrics including volume error  $\delta V_E$ , absolute volume error  $|\delta V_E|$ , percent volume error  $\delta V_P$ , and absolute percent volume error  $|\delta V_P|$  measure the similarity of two segmentation in terms of the physical sizes. Let  $|R_A|$  and  $|R_M|$  be the sizes of the object generated from algorithm segmentation and expert manual delineation, respectively. Volume error  $\delta V_E$  and absolute volume error  $|\delta V_E|$  are calculated as follows:

$$\delta V_E = |R_A| - |R_M|, \quad |\delta V_E| = \left| |R_A| - |R_M| \right|. \quad (1.15)$$

Percent volume error  $\delta V_P$  and absolute percent volume error  $|\delta V_P|$  are calculated as follows:

$$\delta V_P = \frac{|R_A| - |R_M|}{|R_M|} \times 100\%, \quad |\delta V_P| = \left| \frac{|R_A| - |R_M|}{|R_M|} \right| \times 100\%. \quad (1.16)$$

Distance-based measurements evaluate the discrepancies between two contours in 2D and surfaces in 3D. Depending on the application, a number of different forms of distance measurements can be calculated. Manual segmentation as a contour (in 2D) or a surface (in 3D) is represented by a vertex set  $M = \{m_i | i = 1, \dots, K\}$  that consist of  $K$  vertices. Let  $d(m_i, \partial R_A)$  be the Euclidean distance from a vertex  $m_i$  to the algorithm surface  $\partial R_A$ . Root-mean-squared-error (*RMSE*) of the manual-algorithm surface distances is calculated as follows:

$$RMSE = \sqrt{\frac{1}{K} \sum_{i=1}^K d(m_i, \partial R_A)^2}, \quad (1.17)$$

mean absolute distance (*MAD*) is given as:

$$MAD = \frac{1}{K} \sum_{i=1}^K d(m_i, \partial R_A), \quad (1.18)$$

and maximum absolute distance (*MAXD*) follows:

$$MAXD = \max_{i \in \{1, \dots, K\}} \{d(m_i, \partial R_A)\}, \quad (1.19)$$

### 1.6.3.2 Reproducibility

For segmentation algorithms that involve user interaction, it is important to evaluate algorithm segmentation reproducibility to determine their clinical utility especially for longitudinal, cross-center and multi-observer studies. In addition, observers with less experience are involved for interactive algorithm segmentation to provide a worst case scenario for algorithm performance and simulate real-world applications. Both intra- and inter-observer reproducibility are evaluated using coefficient-of-variation (*CoV*), intra-class correlation coefficient (*ICC*) and smallest detectable differences (*SDD*).

*CoV* is calculated as the ratio of standard deviation (*SD*) over the mean:

$$CoV = \frac{SD}{Mean} \times 100\%. \quad (1.20)$$

Intra-*CoV* evaluates the measurement variability across repetitions and inter-*CoV* indicates the measurement variability between multiple observers. Intra- and inter-*ICC* measure the absolute agreements among repetitions and between observers. *SDD* provides an estimate of the minimum measurement change that can be detected at a given confidence level and is calculated as follows:

$$SDD = Z_{\alpha/2} \sqrt{2} \times SEM, \quad (1.21)$$

where  $Z_{\alpha/2}$  is the standard normal deviation corresponding to a probability  $\alpha$  (i.e.,  $\alpha = 0.05$ ,  $Z_{\alpha/2} = 1.96$ ), and *SEM* is the standard error of measurement [276].

### 1.6.3.3 Computation Time

Computation time consists of the time required for manual interaction, registration (if applicable) and computer-based implementation measured in the units of seconds or minutes.

### 1.6.4 Image Registration

Image registration is the process of finding a geometrical mapping (or transformation) to correspond points in two images [277], one is referred to as moving image and the other is fixed image. According to Maurer and Fitzpatrick [278], image registration is defined as “*the determination of a one-to-one mapping between the coordinates in one space and those in another such that points in the two spaces that correspond to the same anatomical points are mapped to each other*”. A registration algorithm consists of four major components [279]:

- Feature space – the type of information contained in images that can be used for image matching. Potential features include image signal intensities, geometric features such as curves/edges/shapes/surfaces, user-defined objects, reference points/landmarks, and hybrid features;
- Search space of transformation model – the type of geometric transformations that is used to warp the moving images. Depending on the nature of the object of interest, different transformation models are used for different registrations. For example, rigid transformation is suitable for bony and stiff structures like bone whereas deformable registration may be more appropriate for deformable tissues such as breast, lung and prostate;
- Similarity metric – measurements (depends on the choice of feature space) that rate the “goodness” of a matching and guide the next search. Commonly-used similarity measurements include but not limit to distance between landmarks/edges/shapes, sum of absolute differences, sum of squared differences, correlation coefficient, ratio image uniformity, mutual information, Fourier similarity of image signal intensities;
- Search strategy – how to derive the optimal transformation. Given a transformation model, the optimal transformation parameters that match two images can be computed either in closed-form (straightforward and fast) or through mathematical optimization (i.e., Gauss-Newton minimization, gradient descent, Levenberg-Marquardt, Powell’s,



and convex optimization methods) of the formulated multi-dimensional registration problems.

Medical image registration plays a vital role in a large number of clinical applications, including disease diagnosis, treatment planning, evaluation of surgical or radiotherapy procedures [280]. Regarding the goals of this thesis, multi-modality pulmonary image registration provides a way to combine valuable and complementary image findings from different sources for a better understanding of lung disease mechanisms and perhaps developing novel treatments. There are many registration algorithms and these algorithms can be categorized differently based on different criteria [277]. Here in this thesis, based on the nature of transformation, medical image registration algorithms can be grouped into: rigid, affine, elastic, deformable models (linear elastic, viscous fluid flow, diffusion models, curvature registration, diffeomorphic flow, optical flow and others) [281]. In the following section, I will provide a brief review of the commonly-used medical image registration methods before presenting the pulmonary CT-MRI registration work in Chapter 4. For simplicity, 2D images are used here but the concepts apply to 3D images.

## 1.6.5 Medical Image Registration Algorithms

### 1.6.5.1 Rigid Registration

Rigid transformation provides a point-point mapping model that preserves all distances, angles and lengths [277]. Registration problems involves rigid transformation are referred to as rigid registration that contains two components to optimize – rotation and translation. For example,

$$\begin{aligned}
 I' &= \begin{bmatrix} \cos(\theta) & -\sin(\theta) \\ \sin(\theta) & \cos(\theta) \end{bmatrix} \cdot I + \begin{bmatrix} t_x \\ t_y \end{bmatrix} \\
 &= R \cdot I + \mathbf{t};
 \end{aligned} \tag{1.22}$$

where  $R$  is a orthogonal rotation matrix with rotation angle of  $\theta$  around the axis perpendicular the image plane;  $\mathbf{t} = \{t_x, t_y\}^T$  defines the translations along  $x$  and  $y$  directions, respectively. Similarly, 3D rigid registration can be formulated by considering the rotation angle  $\theta$ , and the translation components in  $x, y$  and  $z$  axes.

Rigid-body registration is generally easy to optimize and is widely used to align bony and stiff structure such as bone and skull [282]. In many registration problems, rigid registration is employed to roughly align two images to account for large global misalignment that is difficult for local deformable registration to compensate [283].

### 1.6.5.2 Affine Registration

In many medical image registration applications, i.e., inter-patient registrations, intra-patient registrations, there are usually geometric distortions and rigid mappings are not sufficient to compensate for this. Affine registration provides a way to compensate most of the large-scale deformation [284] by adding a shearing and a scaling factor [285] to the rigid registration model (1.22) as follows:

$$\begin{aligned} I' &= \begin{bmatrix} a_{11} & a_{12} \\ a_{21} & a_{22} \end{bmatrix} \cdot I + \begin{bmatrix} t_x \\ t_y \end{bmatrix} \\ &= A \cdot I + \mathbf{t}, \end{aligned} \tag{1.23}$$

where there is no restriction on the elements in matrix  $A$ . In affine transformation model, angles or lengths are no longer preserved but parallel lines remain parallel after transformation. Affine registration is also usually performed to initialize and facilitate the following deformable registration [286]. It should be noted that affine transformation can be applied to sub-regions of images and these local affine mappings can be combined [287, 288] to compose the output registered images.

### 1.6.5.3 Deformable Registration

Deformable registration employs non-linear dense transformation or a spatially varying deformation model to map points in one image to points in another image [281]. For example, a point  $\mathbf{x}$  is mapped to another point  $\mathbf{x}' = f(\mathbf{x})$ , where  $f(\cdot)$  represents non-linear mapping function. A more comprehensive review of deformable registration is provided in [289, 281].

**Thin-place spline:** Thin-place spline (TPS) [290], or surface spline, is a popular deformable transformation model that has been widely used for deformable image registration. TPS can be appreciated as a thin plastic plate that passes through a number of sparse “knots” (control points) in the moving image while keeping the bending energy of the thin plates minimal [290, 291]. The generated transformation with low degree-of-freedom is used to estimate a much denser transformation to deform each point. TPS model contains an affine component to ensure that a solution exists for any configuration of control points [291] as follows:

$$\mathbf{x}' = f(\mathbf{x}) = A\mathbf{x} + t + \sum_{i=1}^N F_i r_i^2 \ln r_i^2, \quad (1.24)$$

where  $r_i = |x - x_i|$  is the Euclidean distance between  $x$  and  $x_i$ . The bending energy of TPS is given as follows:

$$E(f) = \int \int \left( \frac{\partial^2 f}{\partial x^2} \right)^2 + 2 \left( \frac{\partial^2 f}{\partial x \partial y} \right)^2 + \left( \frac{\partial^2 f}{\partial y^2} \right)^2 dx dy, \quad (1.25)$$

For image registration, one can combine the bending energy (1.25) with a similarity measurement, i.e., distance between the corresponding control points in two images, and closed-form solution can be readily achieved following previous studies [291]. A considerable advantage provided by TPS transformation is that the control points can be placed arbitrarily [292, 277] rather than regularly, as required by cubic B-spline.

**Free-form deformation:** Free-form deformation (FFD) [293] is another expressive and popular deformable transformation model and was pioneered by Rueckert *et al.* for breast MRI

registration [286]. The basic idea of FFD, based on B-splines [294], is to transform an object by deforming a grid of control points defined over the image domain. The transformation within a rectangle of control points is modeled by a number of univariate polynomial (or splines) defined only within that rectangle. The polynomial coefficients are chosen such that the derivatives up to the  $2^{nd}$  order are continuous, producing the “cubic splines”.

For a mesh of control points  $\phi_{i,j}$  ( $i$  and  $j$  are bounded by the size of the control point grid) with uniform spacing defined over the image, the transformation of the image is formulated as the tensor product of 1D cubic B-splines as follows:

$$T(x, y) = \sum_{l=0}^3 \sum_{m=0}^3 B_l(u) B_m(v) \phi_{i+l, j+m}, \quad (1.26)$$

where  $B_{l,m}(u)$  is a segment of the cubic B-spline with value of 0 for  $\{l, m\} \notin [-1, 2]$  [286]. This formulation reduces the effects from motion of remote control points and provide “local support” to the neighbourhood of the control point to capture local deformation. The resulting dense deformation controls the shape of the entire object and produces a smooth and continuous transformation with similar definition of bending energy (1.25).

As discussed above, a limitation of FFD is that it requires uniformly distributed control point while TPS utilizes arbitrarily-place control points. However, unlike TPS, FFD does not require solving as linear system to compute the deformation. In addition, TPS control points influence the whole deformation domain while FFD provides only “local support” around control points and can model the local deformation.

**Finite-element model:** Finite-element model (FEM) is a biomechanical/biophysical model that employs the anatomical and physiological properties of tissue to reliably estimate the deformation field [281]. FEM divides images into various tissues of interest and assigns them with tissue-specific material properties to constraint the deformation. This approach requires that the image domain is properly meshed, and the tissue/material properties are carefully defined, which is challenging due to our limited understanding. However, FEM provides im-

proved efficiency to generate deformation solution due to the limited search space. Another advantage of FEM is that it, under some physically meaningful constraints, permits incorporation of the dynamic behavior of tissues into registration [295], and is more suitable for intra-patient registration [281].

Other transformation models, i.e., elastic body, viscous fluid flow, diffusion, curvature, flows of diffeomorphisms, that depict the physical behavior of objects are also widely used for deformable medical image registration, as previously reviewed [281].

## 1.6.6 Registration Performance Evaluation

A number of metrics are commonly used to evaluate the performance of a registration, including corresponding point distance, alignment of objects of interest, and computational efficiency.

### 1.6.6.1 Accuracy

Registration accuracy is usually measured by calculating the distances between corresponding landmarks (termed as “targets” that are not used for registration). In rigid-body landmark-based registration, registration error stems from three parts [296]: 1) fiducial localization error (*FLE*) due to improper identification of fiducial targets, 2) target registration error (*TRE*) due to misalignment of corresponding landmarks, and, 3) fiducial registration error (*FRE*) due to the procedure of searching for the optimal transformation.

Let  $F_1 = \{f_1^i | i = 1, \dots, N\}$  and  $F_2 = \{f_2^i | i = 1, \dots, N\}$  be the set of  $N$  fiducials identified in the fixed image  $I_1(x)$  and the moving image  $I_2(x)$ , respectively. With the derived transformation  $T$ , *TRE* [296] for the  $N$  pairs of fiducials, calculated in the root-mean-squared form, is given as follows:

$$TRE = \sqrt{\frac{1}{N} \sum_{i=1}^N |f_1^i - f_2^i(T)|^2}, \quad (1.27)$$

where  $|f_1^i - f_2^i(T)|$  is the Euclidean distance between the  $i^{th}$ -pair of fiducials from  $I_1(x)$  and  $I_2(x)$  under the transformation  $T$ . Since *TRE* is calculated in a root-mean-squared form, it gives an

estimation of the standard deviation of the registration errors for all the targets.

*FLE* [296] provides a statistical measure of the registration error due to fiducial target localization variability. By comparing *FLE* with *TRE*, it is possible to determine if the fiducial identification procedure dominates *TRE* measurements. For registration accuracy evaluation, manual identification of multiple fiducial targets is usually performed by an experience expert on multiple occasions. *FLE* for the multi-occasion-multi-target identification procedure is determined as follows:

$$FLE = \sqrt{\frac{1}{N} \sum_{i=1}^N (\sigma_{i_x}^2 + \sigma_{i_y}^2 + \sigma_{i_z}^2)}, \quad (1.28)$$

where  $\sigma_{i_{x,y,z}}^2$  represent the variances of the locations in  $x$ ,  $y$  and  $z$  directions for the  $i^{\text{th}}$  fiducial in one image.

In landmark-based registration, *FRE*, in the root-mean-squared form, is a common measure of overall fiducial misalignment because the registration is invariably flawed to some degree by *FLE* [297]. For the  $K$ -pairs of corresponding landmarks  $X_1 = \{x_1^i \mid i = 1, \dots, K\}$  from  $I_1(x)$  and  $X_2 = \{x_2^i \mid i = 1, \dots, K\}$  from  $I_1(x)$  used for registration, *FRE* is calculated as follows:

$$FRE = \sqrt{\frac{1}{K} \sum_{i=1}^K |x_1^i - x_2^i(T)|^2}, \quad (1.29)$$

Additionally, other secondary metrics [298, 299] for registration performance evaluation include *DSC*, *RMSE*,  $\delta V_E$ ,  $\delta V_P$ ,  $|\delta V_E|$ , and  $|\delta V_P|$ , as defined in Sec. 1.6.3, given reliable segmentation of the object of interest.

### 1.6.6.2 Computational Efficiency

Computational efficiency, i.e., in terms of runtime, including pre-processing and user interactions (if applicable), is a commonly used metric to evaluate registration performance.

## 1.7 Thesis Objectives

Pulmonary imaging, including traditional pulmonary MRI, inhaled hyperpolarized noble gas MRI and pulmonary CT, provides the potential for sensitive and regional visualization and quantification of lung structural and functional abnormalities. Importantly, these imaging techniques provide unique biomarkers and tremendous insights into the pathophysiology of obstructive lung disease, offering the potential for a better understanding of pulmonary disease mechanisms and providing patient-relevant information for improved patient care. To facilitate research and clinical applications of these imaging techniques for large-scale, cross-center and longitudinal studies of lung disease, image processing and analysis tools that can provide clinically-acceptable and physiologically-relevant intermediate endpoints are urgently required. Therefore, the overarching objective of this thesis is to develop pulmonary image processing and analysis approaches that can be used to provide lung structure-function measurements with the accuracy, reproducibility and computational efficiency required to support research and clinical studies of lung disease.

In Chapter 2, our objective was to develop a pulmonary image processing pipeline to quantify inhaled hyperpolarized noble gas MRI ventilation information. I wanted to provide lung segmentation that is required for quantifying the associated noble gas MRI ventilation information with accuracy, reproducibility and workflow efficiency suitable for broad research and clinical translation. I wanted to generate lung segmentation in high agreement with expert manual segmentation and high reproducibility to minimize inter and intra-observer variability without requiring intensive training or special expertise. In addition, I wanted to develop image segmentation tools that are applicable across a wide range of disease and disease severities to maximize its clinical utility.

In Chapter 3, my objective was to develop a general pulmonary  $^1\text{H}$  MRI lung segmentation approach for lung structure-function measurements that can be achieved through advanced image processing and acquisition developments. While inhaled noble gas MRI provides promis-

ing potential for respiratory disease monitoring/evaluation, the widespread clinical translation is difficult because of requirements for specialized equipment (i.e., coil and polarizer) and limited accessibility to noble gases. With the recent developments in pulmonary  $^1\text{H}$  MRI techniques including traditional  $^1\text{H}$  MRI, Fourier-decomposition of free-breathing  $^1\text{H}$  MRI, multi-volume  $^1\text{H}$  MRI analysis and ultra-short echo-time MRI acquisition, there is the potential to provide lung structure-function measurements longitudinally and in response to treatments. To translate  $^1\text{H}$  MRI for clinical applications, robust lung segmentation is needed as a first step. Accordingly, I aimed to develop a  $^1\text{H}$  MRI lung multiregion segmentation approach for widespread, cross-centre and longitudinal clinical managements of respiratory disease, compare the spatial agreement between algorithm and manual segmentation, and evaluate the algorithm reproducibility as well as computational efficiency.

In Chapter 4, my objective was to develop an image processing pipeline to generate regional lung structure-function measurements using CT and noble gas MRI. CT provides tremendous insight into the structural basis, i.e., lung parenchyma and airways, of lung disease. However, CT provides only lung structural information and no information about how these structural changes impact lung function. By combining the structural information from CT and functional information using noble gas MRI, there is enormous opportunity to better understand pulmonary disease mechanisms and develop novel regional treatments for improved patient care. Accordingly, I aimed to develop a CT- $^3\text{He}$  MRI deformable registration approach with high registration accuracy. In addition, I wanted to integrate the developed CT- $^3\text{He}$  MRI registration approach into a fully automated image processing pipeline to generate regional and whole lung structure-function measurements in high agreement with a previously-validated method. Finally, I wanted to minimize observers' efforts when using our approach and improve the computational efficiency for efficient clinical workflow.

Finally, in Chapter 5 I reviewed the clinical problems and the unmet clinical needs. We summarized the work presented in Chapters 2–4 and reported the important findings. We then discussed the general and study specific limitations of this thesis. Finally, I provided an outline



of future work based on the knowledge generated by this work.

## Bibliography

- [1] GOLD Executive Committee et al. Global strategy for the diagnosis, management, and prevention of chronic obstructive pulmonary disease (updated 2013). *Available on <http://www.goldcopd.org>*, 2013.
- [2] World Health Organization. Chronic respiratory diseases: Burden of COPD. *<http://www.who.int/respiratory/copd/burden/en/>*.
- [3] World Health Organization. Chronic obstructive pulmonary disease (COPD) fact sheet. *<http://www.who.int/mediacentre/factsheets/fs315/en/>*, 2013.
- [4] World Health Organization. Global health observatory (GHO) data: Top 10 causes of death. *[http://www.who.int/gho/mortality\\_burden\\_disease/causes\\_death/top\\_10/en/](http://www.who.int/gho/mortality_burden_disease/causes_death/top_10/en/)*, 2015.
- [5] Global Asthma Network. The global asthma report 2014. *<http://www.globalasthmareport.org/burden/mortality.php>*, 2014.
- [6] Statistics Canada. Chronic obstructive pulmonary disease in Canadians, 2009 to 2011. *<http://www.statcan.gc.ca/pub/82-625-x/2012001/article/11709-eng.htm>*, 2011.
- [7] Shirley Bryan and Tanya Navaneelan. Deaths from chronic obstructive pulmonary disease in Canada, 1950 to 2011. *<http://www.statcan.gc.ca/pub/82-624-x/2015001/article/14246-eng.htm>*, 2015.
- [8] Canadian Institute of Health Information. Indicator: Chronic obstructive pulmonary disease (COPD) hospitalization for Canadians younger than age 75. *[https://www.cihi.ca/sites/default/files/document/cphi-tech-notes-copd\\_en.pdf](https://www.cihi.ca/sites/default/files/document/cphi-tech-notes-copd_en.pdf)*, 2008.
- [9] Statistics Canada. Asthma, 2014. *<http://www.statcan.gc.ca/pub/82-625-x/2015001/article/14179-eng.htm>*, 2014.

- [10] P Smetanin, D Stiff, C Briante, S Ahmad, L Wong, and A Ler. Life and economic impact of lung disease in Ontario: 2011 to 2041. *RiskAnalytica, on behalf of the Ontario Lung Association*, 2011.
- [11] Ontario Ministry of Finance. 2011 ontario budget: Chapter II: Ontario's economic outlook and fiscal plan section h: Details of ontarios finances. [http://www.fin.gov.on.ca/en/budget/ontariobudgets/2011/ch2h.html#c2\\_secH\\_table25](http://www.fin.gov.on.ca/en/budget/ontariobudgets/2011/ch2h.html#c2_secH_table25), 2011.
- [12] Canadian Institute for Health Information. *Health Indicators*, 2008.
- [13] Clare Gardiner, Merryn Gott, Sheila Payne, Neil Small, Sarah Barnes, David Halpin, Charlotte Ruse, and David Seamark. Exploring the care needs of patients with advanced COPD: an overview of the literature. *Respiratory medicine*, 104(2):159–165, 2010.
- [14] Kelly Chugg, Christopher Barton, Ral Antic, and Alan Crockett. The impact of alexithymia on asthma patient management and communication with health care providers: a pilot study. *Journal of Asthma*, 46(2):126–129, 2009.
- [15] N Nalina, M Sathish Chandra, et al. Assessment of quality of life in bronchial asthma patients. *International Journal of Medicine and Public Health*, 5(1):93–97, 2015.
- [16] Alvar Agusti, Peter MA Calverley, Bartolome Celli, Harvey O Coxson, Lisa D Edwards, David A Lomas, William MacNee, Bruce E Miller, Steve Rennard, Edwin K Silverman, et al. Characterisation of COPD heterogeneity in the ECLIPSE cohort. *Respiratory research*, 11(1):122, 2010.
- [17] Klaus F Rabe, Suzanne Hurd, Antonio Anzueto, Peter J Barnes, Sonia A Buist, Peter Calverley, Yoshinosuke Fukuchi, Christine Jenkins, Roberto Rodriguez-Roisin, Chris Van Weel, et al. Global strategy for the diagnosis, management, and prevention of chronic obstructive pulmonary disease: GOLD executive summary. *American journal of respiratory and critical care medicine*, 176(6):532–555, 2007.

- [18] Global Initiative for Chronic Obstructive Lung Disease. Global strategy for the diagnosis, management, and prevention of chronic obstructive pulmonary disease 2006. [http://www.who.int/respiratory/copd/GOLD\\_WR\\_06.pdf](http://www.who.int/respiratory/copd/GOLD_WR_06.pdf), 2006.
- [19] N Mittmann, L Kuramoto, SJ Seung, JM Haddon, C Bradley-Kennedy, and JM Fitzgerald. The cost of moderate and severe COPD exacerbations to the Canadian healthcare system. *Respiratory medicine*, 102(3):413–421, 2008.
- [20] A Sonia Buist. Similarities and differences between asthma and chronic obstructive pulmonary disease: treatment and early outcomes. *European respiratory journal*, 21(39 suppl):30s–35s, 2003.
- [21] Rodrigo Athanazio. Airway disease: similarities and differences between asthma, COPD and bronchiectasis. *Clinics*, 67(11):1335–1343, 2012.
- [22] Michael G Levitzky. *Pulmonary physiology*. McGraw-Hill Medical Publishing, 2003.
- [23] Weibel ER. Architecture of the human lung. use of quantitative methods establishes fundamental relations between size and number of lung structures. *Science (New York, NY)*, 137(3530):577–585, 1962.
- [24] John Burnard West. *Respiratory physiology: the essentials*. Lippincott Williams & Wilkins, 2012.
- [25] Matthias Ochs, Jens R Nyengaard, Anja Jung, Lars Knudsen, Marion Voigt, Thorsten Wahlers, Joachim Richter, and Hans Jørgen G Gundersen. The number of alveoli in the human lung. *American journal of respiratory and critical care medicine*, 169(1):120–124, 2004.
- [26] Erik Folch and Atul C Mehta. Airway interventions in the tracheobronchial tree. In *Seminars in respiratory and critical care medicine*, volume 29, pages 441–452. © Thieme Medical Publishers, 2008.

- [27] Adolph Fick. On liquid diffusion. *Journal of Membrane Science*, 100(1):33–38, 1995.
- [28] Jean-Paul Janssens, Jean-Claude Pache, and LP Nicod. Physiological changes in respiratory function associated with ageing. *European Respiratory Journal*, 13(1):197–205, 1999.
- [29] Robert O. Crapo. *The Aging Lung*. In *Pulmonary Disease in the Elderly Patient*. Editor: Donald A. Mahler, 1993.
- [30] James M Turner, Jere Mead, and Mary Ellen Wohl. Elasticity of human lungs in relation to age. *Journal of Applied Physiology*, 25(6):664–671, 1968.
- [31] Gulshan Sharma and James Goodwin. Effect of aging on respiratory system physiology and immunology. *Clinical interventions in aging*, 1(3):253, 2006.
- [32] Michael I Polkey, M Lou Harris, Philip D Hughes, CH Hamnegård, Declan Lyons, Malcolm Green, and John Moxham. The contractile properties of the elderly human diaphragm. *American journal of respiratory and critical care medicine*, 155(5):1560–1564, 1997.
- [33] Kenneth Tolep, Nancy Higgins, Stephen Muza, Gerard Criner, and STEVEN G Kelsen. Comparison of diaphragm strength between healthy adult elderly and young men. *American journal of respiratory and critical care medicine*, 152(2):677–682, 1995.
- [34] WM Wahba. Influence of aging on lung function-clinical significance of changes from age twenty. *Anesthesia & Analgesia*, 62(8):764–776, 1983.
- [35] Dennis E Niewoehner and Jerome Kleinerman. Morphologic basis of pulmonary resistance in the human lung and effects of aging. *Journal of applied physiology*, 36(4):412–418, 1974.
- [36] JR Edge, FJC Millard, Lynne Reid, and G Simon. The radiographic appearances of the

- chest in persons of advanced age. *The British journal of radiology*, 37(442):769–774, 1964.
- [37] Erik K Verbeken, Michel Cauberghs, Ingrid Mertens, Jacques Clement, Joseph M Lauweryns, and Karel P Van de Woestijne. The senile lung: comparison with normal and emphysematous lungs 1. structural aspects. *Chest*, 101(3):793–799, 1992.
- [38] Sundeep S Salvi and Peter J Barnes. Chronic obstructive pulmonary disease in non-smokers. *The lancet*, 374(9691):733–743, 2009.
- [39] Bo Lundbäck, Anne Lindberg, Maj Lindström, Eva Rönmark, Ann-Christin Jonsson, Elsy Jönsson, L-G Larsson, Staffan Andersson, Thomas Sandström, and Kjell Larsson. Not 15 but 50% of smokers develop COPD?report from the obstructive lung disease in Northern Sweden studies. *Respiratory medicine*, 97(2):115–122, 2003.
- [40] Gordon L Snider, Jerome Kleinerman, William M Thurlbeck, and Zakir H Bengali. The definition of emphysema: Report of a national heart, lung, and blood institute, division of lung diseases workshop, 1985.
- [41] W Richard Webb and Charles B Higgins. *Thoracic imaging: pulmonary and cardiovascular radiology*. Lippincott Williams & Wilkins, 2010.
- [42] James C Hogg, Peter T Macklem, and WM Thurlbeck. Site and nature of airway obstruction in chronic obstructive lung disease. *New England Journal of Medicine*, 278(25):1355–1360, 1968.
- [43] Steven D Shapiro and Edward P Ingenito. The pathogenesis of chronic obstructive pulmonary disease: advances in the past 100 years. *American Journal of Respiratory Cell and Molecular Biology*, 32(5):367–372, 2005.
- [44] William MacNee. Pathogenesis of chronic obstructive pulmonary disease. *Proceedings of the American Thoracic Society*, 2(4):258–266, 2005.

- [45] William MacNee. ABC of chronic obstructive pulmonary disease: pathology, pathogenesis, and pathophysiology. *BMJ: British Medical Journal*, 332(7551):1202, 2006.
- [46] Global Initiative for Asthma Report. Global strategy for asthma management and prevention (2017 update). <http://ginasthma.org/2017-gina-report-global-strategy-for-asthma-management-and-prevention/>, 2017.
- [47] WW Busse, HA Boushey, CA Camargo, D Evans, MB Foggs, SL Janson, et al. Expert panel report 3: Guidelines for the diagnosis and management of asthma. *Washington, DC: US Department of Health and Human Services, National Heart Lung and Blood Institute*, pages 1–417, 2007.
- [48] Nizar N Jarjour and Elizabeth AB Kelly. Pathogenesis of asthma. *Medical Clinics of North America*, 86(5):925–936, 2002.
- [49] Chris Corrigan. Mechanisms of asthma. *Medicine*, 36(4):177–180, 2008.
- [50] Peter J Barnes, Jeffrey M Drazen, Stephen I Rennard, and Neil C Thomson. *Asthma and COPD: basic mechanisms and clinical management*. Elsevier, 2009.
- [51] James C Hogg. Pathophysiology of airflow limitation in chronic obstructive pulmonary disease. *The Lancet*, 364(9435):709–721, 2004.
- [52] Jason C Woods, Cliff K Choong, Dmitriy A Yablonskiy, John Bentley, Jonathan Wong, John A Pierce, Joel D Cooper, Peter T Macklem, Mark S Conradi, and James C Hogg. Hyperpolarized  $^3\text{He}$  diffusion MRI and histology in pulmonary emphysema. *Magnetic resonance in medicine*, 56(6):1293–1300, 2006.
- [53] Martin R Miller, JATS Hankinson, V Brusasco, F Burgos, R Casaburi, A Coates, R Crapo, P Enright, CPM Van Der Grinten, P Gustafsson, et al. Standardisation of spirometry. *European respiratory journal*, 26(2):319–338, 2005.

- [54] J Wanger, JL Clausen, A Coates, OF Pedersen, V Brusasco, F Burgos, R Casaburi, R Crapo, P Enright, CPM Van Der Grinten, et al. Standardisation of the measurement of lung volumes. *European Respiratory Journal*, 26(3):511, 2005.
- [55] Jonathan Law and Richard Rennie. *A Dictionary of Physics*. OUP Oxford, 2015.
- [56] N Macintyre, RO Crapo, G Viegi, DC Johnson, CPM Van der Grinten, V Brusasco, F Burgos, R Casaburi, A Coates, P Enright, et al. Standardisation of the single-breath determination of carbon monoxide uptake in the lung. *European Respiratory Journal*, 26(4):720–735, 2005.
- [57] Charles Fletcher and Richard Peto. The natural history of chronic airflow obstruction. *Br Med J*, 1(6077):1645–1648, 1977.
- [58] Ronnie Ann Rosenthal, Michael E Zenilman, and Mark R Katlic. *Principles and practice of geriatric surgery*. Springer Science & Business Media, 2013.
- [59] Helen K Reddel, D Robin Taylor, Eric D Bateman, Louis-Philippe Boulet, Homer A Boushey, William W Busse, Thomas B Casale, Pascal Chanez, Paul L Enright, Peter G Gibson, et al. An official American Thoracic Society/European Respiratory Society statement: asthma control and exacerbations: standardizing endpoints for clinical asthma trials and clinical practice. *American journal of respiratory and critical care medicine*, 180(1):59–99, 2009.
- [60] Suzanne Amador Kane. *Introduction to physics in modern medicine*. Taylor & Francis, 2009.
- [61] Rita Joarde and Neil Crundwell. The normal chest X-ray: An approach to interpretation. In *Chest X-Ray in Clinical Practice*, pages 15–27. Springer, 2009.
- [62] David J Brenner and Eric J Hall. Computed tomography an increasing source of radiation exposure. *New England Journal of Medicine*, 357(22):2277–2284, 2007.

- [63] Sudhakar NJ Pipavath, Rodney A Schmidt, Julie E Takasugi, and J David Godwin. Chronic obstructive pulmonary disease: radiology-pathology correlation. *Journal of thoracic imaging*, 24(3):171–180, 2009.
- [64] Massimo Miniati, Erica Filippi, Fabio Falaschi, Laura Carrozzi, EN Milne, H Dirk Sostman, and Massimo Pistolesi. Radiologic evaluation of emphysema in patients with chronic obstructive pulmonary disease. chest radiography versus high resolution computed tomography. *American journal of respiratory and critical care medicine*, 151(5):1359–1367, 1995.
- [65] William Thurlbeck and George Simon. Radiographic appearance of the chest in emphysema. *American Journal of Roentgenology*, 130(3):429–440, 1978.
- [66] CJ Hodson and SE Trickey. Bronchial wall thickening in asthma. *Clinical Radiology*, 11(3):182–191, 1960.
- [67] Emily A DiMango, Herman Lubetsky, and John HM Austin. Assessment of bronchial wall thickening on posteroanterior chest radiographs in acute asthma. *Journal of Asthma*, 39(3):255–261, 2002.
- [68] Anke HW Bruns, Jan Jelrik Oosterheert, Mathias Prokop, Jan-Willem J Lammers, Eelko Hak, and Andy IM Hoepelman. Patterns of resolution of chest radiograph abnormalities in adults hospitalized with severe community-acquired pneumonia. *Clinical infectious diseases*, 45(8):983–991, 2007.
- [69] Rita Joarder and Neil Crundwell. *Chest X-ray in clinical practice*. Springer Science & Business Media, 2009.
- [70] Rosemary Coddington, SL Mera, PR Goddard, and JW Bradfield. Pathological evaluation of computed tomography images of lungs. *Journal of clinical pathology*, 35(5):536–540, 1982.



- [71] Kazuyoshi Kuwano, Kenichi Matsuba, Tohgo Ikeda, Junji Murakami, Akiteru Araki, Hiromu Nishitani, Teruyoshi Ishida, Kosei Yasumoto, and Nobuaki Shigematsu. The diagnosis of mild emphysema. *Am Rev Respir Dis*, 141:169–78, 1990.
- [72] Harvey O Coxson, John Mayo, Stephen Lam, Giles Santyr, Grace Parraga, and Don D Sin. New and current clinical imaging techniques to study chronic obstructive pulmonary disease. *American journal of respiratory and critical care medicine*, 180(7):588–597, 2009.
- [73] Alexander A Bankier, Viviane De Maertelaer, Caroline Keyzer, and Pierre Alain Gevenois. Pulmonary emphysema: Subjective visual grading versus objective quantification with macroscopic morphometry and thin-section CT densitometry. *Radiology*, 211(3):851–858, 1999.
- [74] Kyung J Park, Colleen J Bergin, and Jack L Clausen. Quantitation of emphysema with three-dimensional CT densitometry: Comparison with two-dimensional analysis, visual emphysema scores, and pulmonary function test results. *Radiology*, 211(2):541–547, 1999.
- [75] Pierre Alain Gevenois, Viviane De Maertelaer, Paul De Vuyst, Jacqueline Zanen, and Jean-Claude Yernault. Comparison of computed density and macroscopic morphometry in pulmonary emphysema. *American journal of respiratory and critical care medicine*, 152(2):653–657, 1995.
- [76] Pierre Alain Gevenois, Paul De Vuyst, Viviane De Maertelaer, Jacqueline Zanen, Daniele Jacobovitz, Manuel G Cosio, and Jean-Claude Yernault. Comparison of computed density and microscopic morphometry in pulmonary emphysema. *American journal of respiratory and critical care medicine*, 154(1):187–192, 1996.
- [77] Amir M Owrangi, Roya Etemad-Rezai, David G McCormack, Ian A Cunningham, and

Grace Parraga. Computed tomography density histogram analysis to evaluate pulmonary emphysema in ex-smokers. *Academic radiology*, 20(5):537–545, 2013.

- [78] Michiaki Mishima, Toyohiro Hirai, Harumi Itoh, Yasutaka Nakano, Hiroaki Sakai, Shigeo Muro, Koichi Nishimura, Yoshitaka Oku, Kazuo Chin, Motoharu Ohi, et al. Complexity of terminal airspace geometry assessed by lung computed tomography in normal subjects and patients with chronic obstructive pulmonary disease. *Proceedings of the National Academy of Sciences*, 96(16):8829–8834, 1999.
- [79] Harvey O Coxson. Quantitative computed tomography assessment of airway wall dimensions: current status and potential applications for phenotyping chronic obstructive pulmonary disease. *Proceedings of the American Thoracic Society*, 5(9):940–945, 2008.
- [80] Harvey O Coxson, Jonathon Leipsic, Grace Parraga, and Don D Sin. Using pulmonary imaging to move chronic obstructive pulmonary disease beyond FEV1. *American journal of respiratory and critical care medicine*, 190(2):135–144, 2014.
- [81] Jordan Alexander Zach, John D Newell Jr, Joyce Schroeder, James R Murphy, Douglas Curran-Everett, Eric A Hoffman, Philip M Westgate, MeiLan K Han, Edwin K Silverman, James D Crapo, et al. Quantitative CT of the lungs and airways in healthy non-smoking adults. *Investigative radiology*, 47(10):596, 2012.
- [82] Shin Matsuoka, Yasuyuki Kurihara, Kunihiro Yagihashi, Makoto Hoshino, Naoto Watanabe, and Yasuo Nakajima. Quantitative assessment of air trapping in chronic obstructive pulmonary disease using inspiratory and expiratory volumetric MDCT. *American Journal of Roentgenology*, 190(3):762–769, 2008.
- [83] Seiichirou Eda, Keishi Kubo, Keisaku Fujimoto, Yukinori Matsuzawa, Morie Sekiguchi, and Fumikazu Sakai. The relations between expiratory chest CT using helical CT and pulmonary function tests in emphysema. *American journal of respiratory and critical care medicine*, 155(4):1290–1294, 1997.

- [84] Craig J Galbán, Meilan K Han, Jennifer L Boes, Komal A Chughtai, Charles R Meyer, Timothy D Johnson, Stefanie Galbán, Alnawaz Rehemtulla, Ella A Kazerooni, Fernando J Martinez, et al. Computed tomography-based biomarker provides unique signature for diagnosis of COPD phenotypes and disease progression. *Nature medicine*, 18(11):1711–1715, 2012.
- [85] Kenneth B Newman, David A Lynch, Lee S Newman, Denise Ellegood, and John D Newell. Quantitative computed tomography detects air trapping due to asthma. *Chest*, 106(1):105–109, 1994.
- [86] F Mitsunobu, T Mifune, K Ashida, Y Hosaki, H Tsugeno, M Okamoto, S Harada, S Takata, and Y Tanizaki. Influence of age and disease severity on high resolution CT lung densitometry in asthma. *Thorax*, 56(11):851–856, 2001.
- [87] Tetsuya Ueda, Akio Niimi, Hisako Matsumoto, Masaya Takemura, Toyohiro Hirai, Masafumi Yamaguchi, Hirofumi Matsuoka, Makiko Jinnai, Shigeo Muro, Kazuo Chin, et al. Role of small airways in asthma: investigation using high-resolution computed tomography. *Journal of Allergy and Clinical Immunology*, 118(5):1019–1025, 2006.
- [88] Jonathan G Goldin, Michael F McNitt-Gray, Steven M Sorenson, Timothy D Johnson, Beth Dauphinee, Eric C Klerup, Donald P Tashkin, and Denise R Aberle. Airway hyperreactivity: assessment with helical thin-section CT. *Radiology*, 208(2):321–329, 1998.
- [89] Catherine Beigelman-Aubry, Andre Capderou, Philippe A Grenier, Christian Straus, Marie-Helene Becquemin, Thomas Similowski, and Marc Zelter. Mild intermittent asthma: CT assessment of bronchial cross-sectional area and lung attenuation at controlled lung volume 1. *Radiology*, 223(1):181–187, 2002.
- [90] José-Manuel Tunon-de Lara, François Laurent, Violaine Giraud, Thierry Perez, Bernard Aguilaniu, Houari Meziane, Armelle Basset-Merle, and Pascal Chanez. Air trapping

in mild and moderate asthma: effect of inhaled corticosteroids. *Journal of allergy and clinical immunology*, 119(3):583–590, 2007.

- [91] Ashley Busacker, John D Newell, Thomas Keefe, Eric A Hoffman, Janice Cook Granroth, Mario Castro, Sean Fain, and Sally Wenzel. A multivariate analysis of risk factors for the air-trapping asthmatic phenotype as measured by quantitative CT analysis. *CHEST Journal*, 135(1):48–56, 2009.
- [92] H Gono, K Fujimoto, S Kawakami, and K Kubo. Evaluation of airway wall thickness and air trapping by HRCT in asymptomatic asthma. *European Respiratory Journal*, 22(6):965–971, 2003.
- [93] F Mitsunobu, K Ashida, Y Hosaki, H Tsugeno, M Okamoto, N Nishida, T Nagata, S Takata, and Y Tanizaki. Decreased computed tomographic lung density during exacerbation of asthma. *European Respiratory Journal*, 22(1):106–112, 2003.
- [94] K Wakayama, N Kurihara, S Fujimoto, M Hata, and T Takeda. Relationship between exercise capacity and the severity of emphysema as determined by high resolution CT. *European Respiratory Journal*, 6(9):1362–1367, 1993.
- [95] MeiLan K Han, Brian Bartholmai, Lyrica X Liu, Susan Murray, Jeffrey L Curtis, Frank C Sciurba, Ella A Kazerooni, Bruce Thompson, Margaret Frederick, Daner Li, et al. Clinical significance of radiologic characterizations in COPD. *COPD: Journal of Chronic Obstructive Pulmonary Disease*, 6(6):459–467, 2009.
- [96] Alejandro A Diaz, Brian Bartholmai, Raúl San José Estépar, James Ross, Shin Matsumoto, Tsuneo Yamashiro, Hiroto Hatabu, John J Reilly, Edwin K Silverman, and George R Washko. Relationship of emphysema and airway disease assessed by CT to exercise capacity in COPD. *Respiratory medicine*, 104(8):1145–1151, 2010.
- [97] Pierre Alain Gevenois, Paul De Vuyst, Marieme Sy, Pietro Scillia, Laurent Chaminade,

- Viviane De Maertelaer, Jacqueline Zanen, and Jean-Claude Yernault. Pulmonary emphysema: quantitative CT during expiration. *Radiology*, 199(3):825–829, 1996.
- [98] Joyce D Schroeder, Alexander S McKenzie, Jordan A Zach, Carla G Wilson, Douglas Curran-Everett, Douglas S Stinson, John D Newell Jr, and David A Lynch. Relationships between airflow obstruction and quantitative CT measurements of emphysema, air trapping, and airways in subjects with and without chronic obstructive pulmonary disease. *American Journal of Roentgenology*, 201(3):W460–W470, 2013.
- [99] Peter J Castaldi, Raúl San José Estépar, Carlos S Mendoza, Craig P Hersh, Nan Laird, James D Crapo, David A Lynch, Edwin K Silverman, and George R Washko. Distinct quantitative computed tomography emphysema patterns are associated with physiology and function in smokers. *American journal of respiratory and critical care medicine*, 188(9):1083–1090, 2013.
- [100] MeiLan K Han, Ella A Kazerooni, David A Lynch, Lyrica X Liu, Susan Murray, Jeffrey L Curtis, Gerard J Criner, Victor Kim, Russell P Bowler, Nicola A Hanania, et al. Chronic obstructive pulmonary disease exacerbations in the COPDGen study: associated radiologic phenotypes. *Radiology*, 261(1):274–282, 2011.
- [101] Harvey O Coxson, Robert M Rogers, Kenneth P Whittall, Yulia D'yachkova, Peter D Pare, Frank C Sciurba, and James C Hogg. A quantification of the lung surface area in emphysema using computed tomography. *American journal of respiratory and critical care medicine*, 159(3):851–856, 1999.
- [102] Hester A Gietema, Nestor L Müller, Paola V Nasute Fauerbach, Sanjay Sharma, Lisa D Edwards, Pat G Camp, Harvey O Coxson, Evaluation of COPD Longitudinally to Identify Predictive Surrogate Endpoints (ECLIPSE) investigators, et al. Quantifying the extent of emphysema:: Factors associated with radiologists estimations and quantita-

- tive indices of emphysema severity using the ECLIPSE cohort. *Academic radiology*, 18(6):661–671, 2011.
- [103] David A Lynch, John HM Austin, James C Hogg, Philippe A Grenier, Hans-Ulrich Kauczor, Alexander A Bankier, R Graham Barr, Thomas V Colby, Jeffrey R Galvin, Pierre Alain Gevenois, et al. CT-definable subtypes of chronic obstructive pulmonary disease: a statement of the fleischner society. *Radiology*, 277(1):192–205, 2015.
- [104] Thomas B Grydeland, Asger Dirksen, Harvey O Coxson, Tomas ML Eagan, Einar Thorsen, Sreekumar G Pillai, Sanjay Sharma, Geir Egil Eide, Amund Gulsvik, and Per S Bakke. Quantitative computed tomography measures of emphysema and airway wall thickness are related to respiratory symptoms. *American journal of respiratory and critical care medicine*, 181(4):353–359, 2010.
- [105] Yasutaka Nakano, Shigeo Muro, Hiroaki Sakai, Toyohiro Hirai, Kazuo Chin, Mitsuhiro Tsukino, Koichi Nishimura, Harumi Itoh, Peter D Paré, James C Hogg, et al. Computed tomographic measurements of airway dimensions and emphysema in smokers: correlation with lung function. *American journal of respiratory and critical care medicine*, 162(3):1102–1108, 2000.
- [106] Victor Kim, Parag Desai, John D Newell, Barry J Make, George R Washko, Edwin K Silverman, James D Crapo, Surya P Bhatt, and Gerard J Criner. Airway wall thickness is increased in COPD patients with bronchodilator responsiveness. *Respiratory research*, 15(1):84, 2014.
- [107] Craig P Hersh, George R Washko, Raúl San José Estépar, Sharon Lutz, Paul J Friedman, MeiLan K Han, John E Hokanson, Philip F Judy, David A Lynch, Barry J Make, et al. Paired inspiratory-expiratory chest CT scans to assess for small airways disease in COPD. *Respiratory research*, 14(1):42, 2013.
- [108] Dante PI Capaldi, Nanxi Zha, Fumin Guo, Damien Pike, David G McCormack, Mi-

- randa Kirby, and Grace Parraga. Pulmonary imaging biomarkers of gas trapping and emphysema in COPD:  $^3\text{He}$  MR imaging and CT parametric response maps. *Radiology*, 279(2):597–608, 2016.
- [109] David MF Murphy, John T Nicewicz, Salvatore M Zabbatino, and Roger A Moore. Local pulmonary ventilation using nonradioactive xenon-enhanced ultrafast computed tomography. *Chest*, 96(4):799–804, 1989.
- [110] Hye Jeon Hwang, Joon Beom Seo, Sang Min Lee, Namkug Kim, Sang Young Oh, Jae Seung Lee, Sei Won Lee, and Yeon-Mok Oh. Assessment of regional xenon ventilation, perfusion, and ventilation-perfusion mismatch using dual-energy computed tomography in chronic obstructive pulmonary disease patients. *Investigative radiology*, 51(5):306–315, 2016.
- [111] Eun Jin Chae, Joon Beom Seo, Jeongjin Lee, Namkug Kim, Hyun Woo Goo, Hyun Joo Lee, Choong Wook Lee, Seung Won Ra, Yeon-Mok Oh, and You Sook Cho. Xenon ventilation imaging using dual-energy computed tomography in asthmatics: initial experience. *Investigative radiology*, 45(6):354–361, 2010.
- [112] Jae-Woo Jung, Jae-Woo Kwon, Tae-Wan Kim, So-Hee Lee, Kyung-Mook Kim, Hye-Ryun Kang, Heung-Woo Park, Chang-Hyun Lee, Jin-Mo Goo, Kyung-Up Min, et al. New insight into the assessment of asthma using xenon ventilation computed tomography. *Annals of Allergy, Asthma & Immunology*, 111(2):90–95, 2013.
- [113] Johan Petersson, Alejandro Sánchez-Crespo, Stig A Larsson, and Margareta Mure. Physiological imaging of the lung: single-photon-emission computed tomography (SPECT). *Journal of applied physiology*, 102(1):468–476, 2007.
- [114] Kazuyoshi Suga, Kazuya Nishigauchi, Norihiko Kume, Shinji Koike, Katsuyuki Takano, Osamu Tokuda, Tsuneo Matsumoto, and Naofumi Matsunaga. Dynamic pul-

- monary SPECT of xenon-133 gas washout. *Journal of Nuclear Medicine*, 37(5):807–814, 1996.
- [115] Paul C Hanson. Ventilation scintigraphy. *Journal of nuclear medicine technology*, 15(4):193–197, 1987.
- [116] Marika Bajc, JB Neilly, M Miniati, C Schuemichen, M Meignan, and Björn Jonson. Eanm guidelines for ventilation/perfusion scintigraphy. *European journal of nuclear medicine and molecular imaging*, 36(8):1356–1370, 2009.
- [117] Gregory G King, Stefan Eberl, Cheryl M Salome, Steven R Meikle, and Ann J Woolcock. Airway closure measured by a technegas bolus and SPECT. *American journal of respiratory and critical care medicine*, 155(2):682–688, 1997.
- [118] Ludwig A Engel, L Landau, L Taussig, RR Martin, and G Sybrecht. Influence of bronchomotor tone on regional ventilation distribution at residual volume. *Journal of applied physiology*, 40(3):411–416, 1976.
- [119] Catherine E Farrow, Cheryl M Salome, Benjamin E Harris, Dale L Bailey, Elizabeth Bailey, Norbert Berend, Iven H Young, and Gregory G King. Airway closure on imaging relates to airway hyperresponsiveness and peripheral airway disease in asthma. *Journal of Applied Physiology*, 113(6):958–966, 2012.
- [120] AR Sovijärvi, L Pöyhönen, L Kellomäki, and Antero Muittari. Effects of acute and long-term bronchodilator treatment on regional lung function in asthma assessed with krypton-81m and technetium-99m-labelled macroaggregates. *Thorax*, 37(7):516–520, 1982.
- [121] T Munkner and A Bundgaard. Regional V/Q changes in asthmatics after exercise. *European journal of respiratory diseases. Supplement*, 143:62–66, 1985.



- [122] T Munkner and A Bundgaard. Regional V/Q changes in asthmatics after antigen inhalation. *European journal of respiratory diseases. Supplement*, 143:44–47, 1985.
- [123] H Clague, D Ahmad, MJ Chamberlain, WK Morgan, and S Vinitzki. Histamine bronchial challenge: effect on regional ventilation and aerosol deposition. *Thorax*, 38(9):668–675, 1983.
- [124] T Munkner and A Bundgaard. Regional V/Q changes in asthmatics after histamine inhalation. *European journal of respiratory diseases. Supplement*, 143:22–27, 1985.
- [125] Katashi Satoh, Satoru Nakano, Masatada Tanabe, Yoshihiro Nishiyama, Kazue Takahashi, T Kobayashi, Naomi Honjo, Mayumi Sasaki, Jiro Fujita, and Hiroki Okada. A clinical comparison between technegas SPECT, CT, and pulmonary function tests in patients with emphysema. *Radiation medicine*, 15(5):277–282, 1996.
- [126] Jonas Jögi, Marie Ekberg, Björn Jonson, Gracijela Bozovic, and Marika Bajc. Ventilation/perfusion spect in chronic obstructive pulmonary disease: an evaluation by reference to symptoms, spirometric lung function and emphysema, as assessed with HRCT. *European journal of nuclear medicine and molecular imaging*, 38(7):1344–1352, 2011.
- [127] Marika Bajc, Hanna Markstad, Linnea Jarenbäck, Ellen Tufvesson, Leif Bjermer, and Jonas Jögi. Grading obstructive lung disease using tomographic pulmonary scintigraphy in patients with chronic obstructive pulmonary disease (COPD) and long-term smokers. *Annals of nuclear medicine*, 29(1):91–99, 2015.
- [128] Kazuyoshi Suga, Yasuhiko Kawakami, Hiroaki Koike, Hideyuki Iwanaga, Osamu Tokuda, Munemasa Okada, and Naofumi Matsunaga. Lung ventilation–perfusion imbalance in pulmonary emphysema: assessment with automated V/Q quotient SPECT. *Annals of nuclear medicine*, 24(4):269–277, 2010.
- [129] Kazuyoshi Suga, Hideyuki Iwanaga, Osamu Tokuda, Munemasa Okada, and Naofumi

- Matsunaga. Intrabullous ventilation in pulmonary emphysema: assessment with dynamic xenon-133 gas SPECT. *Nuclear medicine communications*, 33(4):371–378, 2012.
- [130] George V Taplin, Donald P Tashkin, Sawtantra K Chopra, Osvaldo E Anselmi, Dennis Elam, Barry Calvarese, Anne Coulson, Roger Detels, and Stanley N Rokaw. Early detection of chronic obstructive pulmonary disease using radionuclide lung-imaging procedures. *Chest*, 71(5):567–575, 1977.
- [131] Abhimanyu Garg, PG Gopinath, JN Pande, and JS Guleria. Role of radio-aerosol and perfusion lung imaging in early detection of chronic obstructive lung disease. *European Journal of Nuclear Medicine and Molecular Imaging*, 8(4):167–171, 1983.
- [132] Michio Senda, Kiyoshi Murata, Harumi Itoh, Yoshiharu Yonekura, and Kanji Torizuka. Quantitative evaluation of regional pulmonary ventilation using PET and nitrogen-13 gas. *Journal of nuclear medicine: official publication, Society of Nuclear Medicine*, 27(2):268–273, 1986.
- [133] Jose G Venegas, Tilo Winkler, Guido Musch, Marcos F Vidal Melo, Dominick Layfield, Nora Tgavalekos, Alan J Fischman, Ronald J Callahan, Giacomo Bellani, and R Scott Harris. Self-organized patchiness in asthma as a prelude to catastrophic shifts. *Nature*, 434(7034):777–782, 2005.
- [134] R Scott Harris, Tilo Winkler, Nora Tgavalekos, Guido Musch, Marcos F Vidal Melo, Tobias Schroeder, Yuchiao Chang, and José G Venegas. Regional pulmonary perfusion, inflation, and ventilation defects in bronchoconstricted patients with asthma. *American journal of respiratory and critical care medicine*, 174(3):245–253, 2006.
- [135] Delphine L Chen and Daniel P Schuster. Imaging pulmonary inflammation with positron emission tomography: a biomarker for drug development. *Molecular pharmaceuticals*, 3(5):488–495, 2006.

- [136] R Scott Harris, José G Venegas, Chanikarn Wongviriyawong, Tilo Winkler, Mamary Kone, Guido Musch, Marcos F Vidal Melo, Nicolas de Prost, Daniel L Hamilos, Roshi Afshar, et al. 18F-FDG uptake rate is a biomarker of eosinophilic inflammation and airway response in asthma. *Journal of Nuclear Medicine*, 52(11):1713–1720, 2011.
- [137] LH Brudin, CG Rhodes, SO Valind, PD Buckingham, T Jones, and JM Hughes. Regional structure-function correlations in chronic obstructive lung disease measured with positron emission tomography. *Thorax*, 47(11):914–921, 1992.
- [138] Marcos F Vidal Melo, Tilo Winkler, R Scott Harris, Guido Musch, Reginald E Greene, and Jose G Venegas. Spatial heterogeneity of lung perfusion assessed with 13N PET as a vascular biomarker in chronic obstructive pulmonary disease. *Journal of Nuclear Medicine*, 51(1):57–65, 2010.
- [139] Deepak R Subramanian, Lee Jenkins, Ross Edgar, Nabil Quraishi, Robert A Stockley, and David G Parr. Assessment of pulmonary neutrophilic inflammation in emphysema by quantitative positron emission tomography. *American journal of respiratory and critical care medicine*, 186(11):1125–1132, 2012.
- [140] Marcos F Vidal Melo, Dominick Layfield, R Scott Harris, Kevin O'Neill, Guido Musch, Torsten Richter, Tilo Winkler, Alan J Fischman, and Jose G Venegas. Quantification of regional ventilation-perfusion ratios with PET. *Journal of Nuclear Medicine*, 44(12):1982–1991, 2003.
- [141] Felix Bloch. Nuclear induction. *Physical review*, 70(7-8):460, 1946.
- [142] Nicolaas Bloembergen, Edward Mills Purcell, and Robert V Pound. Relaxation effects in nuclear magnetic resonance absorption. *Physical review*, 73(7):679, 1948.
- [143] KH Albertine. Structural organization and quantitative morphology of the lung. *Application of magnetic resonance to the study of lung. Futura, Armonk, New York, USA*, pages 73–114, 1996.

- [144] Hans-Ulrich Kauczor. MRI of the lung. 2009.
- [145] Colleen J Bergin, Gary M Glover, and John Pauly. Magnetic resonance imaging of lung parenchyma. *Journal of thoracic imaging*, 8(1):12–17, 1993.
- [146] Jens Vogel-Claussen, Julius Renne, Jan Hinrichs, Christian Schönfeld, Marcel Gutberlet, Frank Schaumann, Carla Winkler, Cornelia Faulenbach, Norbert Krug, Frank K Wacker, et al. Quantification of pulmonary inflammation after segmental allergen challenge using turbo-inversion recovery-magnitude magnetic resonance imaging. *American journal of respiratory and critical care medicine*, 189(6):650–657, 2014.
- [147] Maren Zapke, Hans-Georg Topf, Martin Zenker, Rainer Kuth, Michael Deimling, Peter Kreisler, Manfred Rauh, Christophe Chedf’hotel, Bernhard Geiger, and Thomas Rupprecht. Magnetic resonance lung function—a breakthrough for lung imaging and functional assessment? a phantom study and clinical trial. *Respiratory research*, 7(1):106, 2006.
- [148] Francesca Pennati, James D Quirk, Dmitriy A Yablonskiy, Mario Castro, Andrea Aliverti, and Jason C Woods. Assessment of regional lung function with multivolume 1H MR imaging in health and obstructive lung disease: Comparison with 3He MR imaging. *Radiology*, 273(2):580–590, 2014.
- [149] Tae Iwasawa, Hiroshi Takahashi, Takashi Ogura, Akira Asakura, Toshiyuki Gotoh, Sei-ichiro Kagei, Jun-ichi Nishimura, Makoto Obara, and Tomio Inoue. Correlation of lung parenchymal mr signal intensity with pulmonary function tests and quantitative computed tomography (CT) evaluation: a pilot study. *Journal of Magnetic Resonance Imaging*, 26(6):1530–1536, 2007.
- [150] Julia Ley-Zaporozhan, Sebastian Ley, and Hans-Ulrich Kauczor. Proton MRI in COPD. *COPD: Journal of Chronic Obstructive Pulmonary Disease*, 4(1):55–65, 2007.

- [151] Amir M Owрани, Jian X Wang, Andrew Wheatley, David G McCormack, and Grace Parraga. Quantitative 1H and hyperpolarized 3He magnetic resonance imaging: Comparison in chronic obstructive pulmonary disease and healthy never-smokers. *European journal of radiology*, 83(1):64–72, 2014.
- [152] Robert R Edelman, Hiroto Hatabu, Eiji Tadamura, Wei Li, and Potthumarthi V Prasad. Noninvasive assessment of regional ventilation in the human lung using oxygen-enhanced magnetic resonance imaging. *Nature medicine*, 2(11):1236–1239, 1996.
- [153] Yoshiharu Ohno, Hiroto Hatabu, Daisuke Takenaka, Shuji Adachi, Marc Van Cauteren, and Kazuro Sugimura. Oxygen-enhanced MR ventilation imaging of the lung: preliminary clinical experience in 25 subjects. *American Journal of Roentgenology*, 177(1):185–194, 2001.
- [154] Yoshiharu Ohno, Hiroto Hatabu, Daisuke Takenaka, Marc Van Cauteren, Masahiko Fujii, and Kazuro Sugimura. Dynamic oxygen-enhanced MRI reflects diffusing capacity of the lung. *Magnetic resonance in medicine*, 47(6):1139–1144, 2002.
- [155] Yoshiharu Ohno, Tae Iwasawa, Joom Beom Seo, Hisanobu Koyama, Hiroshi Takahashi, Yeon-Mok Oh, Yoshihiro Nishimura, and Kazuro Sugimura. Oxygen-enhanced magnetic resonance imaging versus computed tomography: multicenter study for clinical stage classification of smoking-related chronic obstructive pulmonary disease. *American journal of respiratory and critical care medicine*, 177(10):1095–1102, 2008.
- [156] Yoshiharu Ohno, Hisanobu Koyama, Keiko Matsumoto, Yumiko Onishi, Munenobu Nogami, Daisuke Takenaka, Sumiaki Matsumoto, and Kazuro Sugimura. Oxygen-enhanced MRI vs. quantitatively assessed thin-section CT: pulmonary functional loss assessment and clinical stage classification of asthmatics. *European journal of radiology*, 77(1):85–91, 2011.
- [157] Yoshiharu Ohno, Mizuho Nishio, Hisanobu Koyama, Shinichiro Seki, Takeshi

- Yoshikawa, Sumiaki Matsumoto, Makoto Obara, Marc van Cauteren, and Kazuro Sugimura. Asthma: comparison of dynamic oxygen-enhanced MR imaging and quantitative thin-section CT for evaluation of clinical treatment. *Radiology*, 273(3):907–916, 2014.
- [158] Wei-Juan Zhang, Robert M Niven, Simon S Young, Yu-Zhen Liu, Geoffrey JM Parker, and Josephine H Naish. Dynamic oxygen-enhanced magnetic resonance imaging of the lung in asthmaintial experience. *European journal of radiology*, 84(2):318–326, 2015.
- [159] Julius Renne, Jan Hinrichs, Christian Schönfeld, Marcel Gutberlet, Carla Winkler, Cornelia Faulenbach, Peter Jakob, Frank Schaumann, Norbert Krug, Frank Wacker, et al. Noninvasive quantification of airway inflammation following segmental allergen challenge with functional MR imaging: a proof of concept study. *Radiology*, 274(1):267–275, 2014.
- [160] Grzegorz Bauman, Michael Puderbach, Michael Deimling, Vladimir Jellus, Christophe Chefd’hotel, Julien Dinkel, Christian Hintze, Hans-Ulrich Kauczor, and Lothar R Schad. Non-contrast-enhanced perfusion and ventilation assessment of the human lung by means of fourier decomposition in proton MRI. *Magnetic resonance in medicine*, 62(3):656–664, 2009.
- [161] Grzegorz Bauman, Ulf Lützen, Mathias Ullrich, Thomas Gaass, Julien Dinkel, Gunnar Elke, Patrick Meybohm, Inéz Frerichs, Beata Hoffmann, Jan Borggreffe, et al. Pulmonary functional imaging: qualitative comparison of fourier decomposition MR imaging with SPECT/CT in porcine lung. *Radiology*, 260(2):551–559, 2011.
- [162] Dante PI Capaldi, Khadija Sheikh, Fumin Guo, Sarah Svenningsen, Roya Etemad-Rezai, Harvey O Coxson, Jonathon A Leipsic, David G McCormack, and Grace Parraga. Free-breathing pulmonary 1H and hyperpolarized 3He MRI: comparison in COPD and bronchiectasis. *Academic radiology*, 22(3):320–329, 2015.
- [163] Fumin Guo, Dante PI Capaldi, Di C Robert, Aaron Fenster, and Grace Parraga. Registra-

- tion pipeline for pulmonary free-breathing 1H MRI ventilation measurements. In *SPIE Medical Imaging*, pages 10137–10137. International Society for Optics and Photonics, 2017.
- [164] Andreas Voskresbenzev, Marcel Gutberlet, Till F Kaireit, Frank Wacker, and Jens Vogel-Claussen. Low-pass imaging of dynamic acquisitions (LIDA) with a group-oriented registration (GOREG) for proton mr imaging of lung ventilation. *Magnetic Resonance in Medicine*, 2016.
- [165] Dante P Capaldi, Khadija Sheikh, Sarah Svenningsen, Miranda Kirby, Harvey Coxson, David G McCormack, and Grace Parraga. Measurement of asthma treatment response using free-breathing 1H ventilation MRI. In *A19. GETTING POLARIZED: MR IMAGING IN OBSTRUCTIVE LUNG DISEASE*, pages A1055–A1055. Am Thoracic Soc, 2016.
- [166] Damian J Tyler, Matthew D Robson, R Mark Henkelman, Ian R Young, and Graeme M Bydder. Magnetic resonance imaging with ultrashort TE (UTE) pulse sequences: technical considerations. *Journal of Magnetic Resonance Imaging*, 25(2):279–289, 2007.
- [167] Gaël Dournes, Fanny Menut, Julie Macey, Michaël Fayon, Jean-François Chateil, Marjorie Salel, Olivier Corneloup, Michel Montaudon, Patrick Berger, and François Laurent. Lung morphology assessment of cystic fibrosis using MRI with ultra-short echo time at submillimeter spatial resolution. *European radiology*, 26(11):3811–3820, 2016.
- [168] Yoshiharu Ohno, Hisanobu Koyama, Takeshi Yoshikawa, Shinichiro Seki, Daisuke Takenaka, Masao Yui, Aiming Lu, Mitsue Miyazaki, and Kazuro Sugimura. Pulmonary high-resolution ultrashort TE MR imaging: Comparison with thin-section standard-and low-dose computed tomography for the assessment of pulmonary parenchyma diseases. *Journal of Magnetic Resonance Imaging*, 43(2):512–532, 2016.
- [169] Khadija Sheikh, Fumin Guo, Dante PI Capaldi, Alexei Ouriadov, Rachel L Eddy, Sarah

- Svenningsen, and Grace Parraga. Ultrashort echo time MRI biomarkers of asthma. *Journal of Magnetic Resonance Imaging*, 2016.
- [170] David J Roach, Yannick Cr emillieux, Suraj D Serai, Robert P Thomen, Hui Wang, Yuan-shu Zou, Rhonda D Szczesniak, Sadia Benzaquen, and Jason C Woods. Morphological and quantitative evaluation of emphysema in chronic obstructive pulmonary disease patients: A comparative study of MRI with CT. *Journal of Magnetic Resonance Imaging*, 44(6):1656–1663, 2016.
- [171] Weijing Ma, Khadija Sheikh, Sarah Svenningsen, Damien Pike, Fumin Guo, Roya Etemad-Rezai, Jonathan Leipsic, Harvey O Coxson, David G McCormack, and Grace Parraga. Ultra-short echo-time pulmonary MRI: Evaluation and reproducibility in COPD subjects with and without bronchiectasis. *Journal of Magnetic Resonance Imaging*, 41(5):1465–1474, 2015.
- [172] Yoshiharu Ohno, Hisanobu Koyama, Takeshi Yoshikawa, Keiko Matsumoto, Masaya Takahashi, Marc Van Cauteren, and Kazuro Sugimura. T2\* measurements of 3-T MRI with ultrashort TEs: capabilities of pulmonary function assessment and clinical stage classification in smokers. *American Journal of Roentgenology*, 197(2):W279–W285, 2011.
- [173] W Happer, E Miron, S Schaefer, D Schreiber, WA Van Wijngaarden, and X Zeng. Polarization of the nuclear spins of noble-gas atoms by spin exchange with optically pumped alkali-metal atoms. *Physical Review A*, 29(6):3092, 1984.
- [174] MS Albert, GD Cates, B Driehuys, W Happer, B Saam, CS Springer, and A Wishnia. Biological magnetic resonance imaging using laser-polarized  $^{129}\text{Xe}$ . 1994.
- [175] Arvind K Venkatesh, Adelaide X Zhang, Joey Mansour, Lyubov Kubatina, Chang-Hyun Oh, Gregory Blasche, M Selim  n l , Dilip Balamore, Ferenc A Jolesz, Bennett B Gold-



- berg, et al. MRI of the lung gas-space at very low-field using hyperpolarized noble gases. *Magnetic resonance imaging*, 21(7):773–776, 2003.
- [176] Hans-Ulrich Kauczor, Dirk Hofmann, Karl-Friedrich Kreitner, Helge Nilgens, Reinhard Surkau, Wemer Heil, Andreas Potthast, Michael V Knopp, Ernst W Otten, and Manfred Thelen. Normal and abnormal pulmonary ventilation: visualization at hyperpolarized He-3 MR imaging. *Radiology*, 201(2):564–568, 1996.
- [177] Barbara A Lutey, Stephen S Lefrak, Jason C Woods, Tariq Tanoli, James D Quirk, Adil Bashir, Dmitriy A Yablonskiy, Mark S Conradi, Seth T Bartel, Thomas K Pilgram, et al. Hyperpolarized 3He MR imaging: Physiologic monitoring observations and safety considerations in 100 consecutive subjects. *Radiology*, 248(2):655–661, 2008.
- [178] Yajur Shukla, Andrew Wheatley, Miranda Kirby, Sarah Svenningsen, Adam Farag, Giles E Santyr, Nigel AM Paterson, David G McCormack, and Grace Parraga. Hyperpolarized 129Xe magnetic resonance imaging: tolerability in healthy volunteers and subjects with pulmonary disease. *Academic radiology*, 19(8):941–951, 2012.
- [179] Talissa A Altes, Patrick L Powers, Jack Knight-Scott, Gary Rakes, Thomas AE Platts-Mills, Eduard E de Lange, Bennett A Alford, John P Mugler, and James R Brookeman. Hyperpolarized 3He MR lung ventilation imaging in asthmatics: preliminary findings. *Journal of Magnetic Resonance Imaging*, 13(3):378–384, 2001.
- [180] Lindsay Mathew, Andrea Evans, Alexei Ouriadov, Roya Etemad-Rezai, Robert Fogel, Giles Santyr, David G McCormack, and Grace Parraga. Hyperpolarized 3He magnetic resonance imaging of chronic obstructive pulmonary disease: reproducibility at 3.0 Tesla. *Academic radiology*, 15(10):1298–1311, 2008.
- [181] Grace Parraga, Lindsay Mathew, Roya Etemad-Rezai, David G McCormack, and Giles E Santyr. Hyperpolarized 3He magnetic resonance imaging of ventilation de-

- fects in healthy elderly volunteers: initial findings at 3.0 Tesla. *Academic radiology*, 15(6):776–785, 2008.
- [182] Talissa A Altes, Patrice K Rehm, Frank Harrell, Michael Salerno, Thomas M Daniel, and Eduard E de Lange. Ventilation imaging of the lung: Comparison of hyperpolarized helium-3 MR imaging with Xe-133 scintigraphy. *Academic radiology*, 11(7):729–734, 2004.
- [183] Eduard E de Lange, Talissa A Altes, James T Patrie, John D Gaare, Jeffrey J Knake, John P Mugler, and Thomas A Platts-Mills. Evaluation of asthma with hyperpolarized helium-3 MRI: correlation with clinical severity and spirometry. *CHEST Journal*, 130(4):1055–1062, 2006.
- [184] Eduard E de Lange, Talissa A Altes, James T Patrie, Jaywant Parmar, James R Brooke-man, John P Mugler, and Thomas AE Platts-Mills. The variability of regional airflow obstruction within the lungs of patients with asthma: assessment with hyperpolarized helium-3 magnetic resonance imaging. *Journal of Allergy and Clinical Immunology*, 119(5):1072–1078, 2007.
- [185] Neil Woodhouse, Jim M Wild, Martyn NJ Paley, Stanislaw Fichelle, Zead Said, Andrew J Swift, and Edwin JR van Beek. Combined helium-3/proton magnetic resonance imaging measurement of ventilated lung volumes in smokers compared to never-smokers. *Journal of magnetic resonance imaging*, 21(4):365–369, 2005.
- [186] Grace Parraga, Alexei Ouriadov, Andrea Evans, Shayna McKay, Wilfred W Lam, Aaron Fenster, Roya Etemad-Rezai, David McCormack, and Giles Santyr. Hyperpolarized  $^3\text{He}$  ventilation defects and apparent diffusion coefficients in chronic obstructive pulmonary disease: preliminary results at 3.0 Tesla. *Investigative radiology*, 42(6):384–391, 2007.
- [187] Miranda Kirby, Lindsay Mathew, Andrew Wheatley, Giles E Santyr, David G McCor-

- mack, and Grace Parraga. Chronic obstructive pulmonary disease: longitudinal hyperpolarized  $^3\text{He}$  MR imaging. *Radiology*, 256(1):280–289, 2010.
- [188] Miranda Kirby, Mohammadreza Heydarian, Sarah Svenningsen, Andrew Wheatley, David G McCormack, Roya Etemad-Rezai, and Grace Parraga. Hyperpolarized  $^3\text{He}$  magnetic resonance functional imaging semiautomated segmentation. *Academic radiology*, 19(2):141–152, 2012.
- [189] Wei Zha, David J Niles, Stanley J Kruger, Bernard J Dardzinski, Robert V Cadman, David G Mummy, Scott K Nagle, and Sean B Fain. Semiautomated ventilation defect quantification in exercise-induced bronchoconstriction using hyperpolarized helium-3 magnetic resonance imaging: a repeatability study. *Academic radiology*, 23(9):1104–1114, 2016.
- [190] Nicholas J Tustison, Brian B Avants, Lucia Flors, Talissa A Altes, Eduard E de Lange, John P Mugler, and James C Gee. Ventilation-based segmentation of the lungs using hyperpolarized  $^3\text{He}$  MRI. *Journal of Magnetic Resonance Imaging*, 34(4):831–841, 2011.
- [191] Saba Samee, Talissa Altes, Patrick Powers, Eduard E de Lange, Jack Knight-Scott, Gary Rakes, John P Mugler III, Jonathan M Ciambotti, Bennet A Alford, James R Brooker, et al. Imaging the lungs in asthmatic patients by using hyperpolarized helium-3 magnetic resonance: assessment of response to methacholine and exercise challenge. *Journal of Allergy and Clinical Immunology*, 111(6):1205–1211, 2003.
- [192] Robert V Cadman, Robert F Lemanske, Michael D Evans, Daniel J Jackson, James E Gern, Ronald L Sorkness, and Sean B Fain. Pulmonary  $^3\text{He}$  magnetic resonance imaging of childhood asthma. *Journal of Allergy and Clinical Immunology*, 131(2):369–376, 2013.
- [193] Stephen Costella, Miranda Kirby, Geoffrey N Maksym, David G McCormack, Nigel AM

- Paterson, and Grace Parraga. Regional pulmonary response to a methacholine challenge using hyperpolarized  $^3\text{He}$  magnetic resonance imaging. *Respirology*, 17(8):1237–1246, 2012.
- [194] Sarah Svenningsen, Miranda Kirby, Danielle Starr, Harvey O Coxson, Nigel AM Paterson, David G McCormack, and Grace Parraga. What are ventilation defects in asthma? *Thorax*, pages thoraxjnl–2013, 2013.
- [195] Sarah Svenningsen, Parameswaran Nair, Fumin Guo, David G McCormack, and Grace Parraga. Is ventilation heterogeneity related to asthma control? *European Respiratory Journal*, pages ERJ–00393, 2016.
- [196] Sean B Fain, Guillermo Gonzalez-Fernandez, Eric T Peterson, Michael D Evans, Ronald L Sorkness, Nizar N Jarjour, William W Busse, and Janet E Kuhlman. Evaluation of structure-function relationships in asthma using multidetector CT and hyperpolarized  $\text{He-3}$  MRI. *Academic radiology*, 15(6):753–762, 2008.
- [197] Yang-Sheng Tzeng, Kenneth Lutchen, and Mitchell Albert. The difference in ventilation heterogeneity between asthmatic and healthy subjects quantified using hyperpolarized  $^3\text{He}$  MRI. *Journal of Applied Physiology*, 106(3):813–822, 2009.
- [198] Sarah Svenningsen, Miranda Kirby, Danielle Starr, Del Leary, Andrew Wheatley, Geoffrey N Maksym, David G McCormack, and Grace Parraga. Hyperpolarized  $^3\text{He}$  and  $^{129}\text{Xe}$  MRI: differences in asthma before bronchodilation. *Journal of Magnetic Resonance Imaging*, 38(6):1521–1530, 2013.
- [199] Stanley J Kruger, David J Niles, Bernard Dardzinski, Amy Harman, Nizar N Jarjour, Marcella Ruddy, Scott K Nagle, Christopher J Francois, Ronald L Sorkness, Ryan M Burton, et al. Hyperpolarized helium-3 MRI of exercise-induced bronchoconstriction during challenge and therapy. *Journal of Magnetic Resonance Imaging*, 39(5):1230–1237, 2014.

- [200] Miranda Kirby, Sarah Svenningsen, Amir Owrangi, Andrew Wheatley, Adam Farag, Alexei Ouriadov, Giles E Santyr, Roya Etemad-Rezai, Harvey O Coxson, David G McCormack, et al. Hyperpolarized  $^3\text{He}$  and  $^{129}\text{Xe}$  MR imaging in healthy volunteers and patients with chronic obstructive pulmonary disease. *Radiology*, 265(2):600–610, 2012.
- [201] Miranda Kirby, Nikhil Kanhere, Roya Etemad-Rezai, David G McCormack, and Grace Parraga. Hyperpolarized helium-3 magnetic resonance imaging of chronic obstructive pulmonary disease exacerbation. *Journal of Magnetic Resonance Imaging*, 37(5):1223–1227, 2013.
- [202] Miranda Kirby, Sarah Svenningsen, Nikhil Kanhere, Amir Owrangi, Andrew Wheatley, Harvey O Coxson, Giles E Santyr, Nigel AM Paterson, David G McCormack, and Grace Parraga. Pulmonary ventilation visualized using hyperpolarized helium-3 and xenon-129 magnetic resonance imaging: differences in COPD and relationship to emphysema. *Journal of Applied Physiology*, 114(6):707–715, 2013.
- [203] Miranda Kirby, Lindsay Mathew, Mohammadreza Heydarian, Roya Etemad-Rezai, David G McCormack, and Grace Parraga. Chronic obstructive pulmonary disease: quantification of bronchodilator effects by using hyperpolarized He MR imaging. *Radiology*, 261(1):283–292, 2011.
- [204] Brian T Saam, Dmitriy A Yablonskiy, Vikram D Kodibagkar, Jason C Leawoods, David S Gierada, Joel D Cooper, Stephen S Lefrak, and Mark S Conradi. MR imaging of diffusion of  $^3\text{He}$  gas in healthy and diseased lungs. *Magnetic resonance in medicine*, 44(2):174–179, 2000.
- [205] Andreas E Morbach, Klaus K Gast, Jörg Schmiedeskamp, Anja Dahmen, Annette Herweling, Claus P Heussel, Hans-Ulrich Kauczor, and Wolfgang G Schreiber. Diffusion-weighted MRI of the lung with hyperpolarized helium-3: a study of reproducibility. *Journal of Magnetic Resonance Imaging*, 21(6):765–774, 2005.

- [206] Sandra Diaz, Ingrid Casselbrant, Eeva Piitulainen, Goran Pettersson, Peter Magnusson, Barry Peterson, Per Wollmer, Peter Leander, Olle Ekberg, and Per Akeson. Hyperpolarized  $^3\text{He}$  apparent diffusion coefficient MRI of the lung: reproducibility and volume dependency in healthy volunteers and patients with emphysema. *Journal of Magnetic Resonance Imaging*, 27(4):763–770, 2008.
- [207] Robert P Thomen, James D Quirk, David Roach, Tiffany Egan-Rojas, Kai Ruppert, Roger D Yusen, Talissa A Altes, Dmitriy A Yablonskiy, and Jason C Woods. Direct comparison of  $^{129}\text{Xe}$  diffusion measurements with quantitative histology in human lungs. *Magnetic resonance in medicine*, 2016.
- [208] Michael Salerno, Eduard E de Lange, Talissa A Altes, Jonathon D Truwit, James R Brookeman, and John P Mugler. Emphysema: hyperpolarized helium-3 diffusion MR imaging of the lungs compared with spirometric indexes initial experiences. *Radiology*, 222(1):252–260, 2002.
- [209] S Sivaram Kaushik, Zackary I Cleveland, Gary P Cofer, Gregory Metz, Denise Beaver, John Nouls, Monica Kraft, William Auffermann, Jan Wolber, H Page McAdams, et al. Diffusion-weighted hyperpolarized  $^{129}\text{Xe}$  MRI in healthy volunteers and subjects with chronic obstructive pulmonary disease. *Magnetic resonance in medicine*, 65(4):1154–1165, 2011.
- [210] Sean B Fain, Talissa A Altes, Shilpa R Panth, Michael D Evans, Barnaby Waters, John P Mugler, Frank R Korosec, Thomas M Grist, Mike Silverman, Michael Salerno, et al. Detection of age-dependent changes in healthy adult lungs with diffusion-weighted  $^3\text{He}$  MRI. *Academic radiology*, 12(11):1385–1393, 2005.
- [211] Chengbo Wang, John P Mugler, Eduard E Lange, James T Patrie, Jaime F Mata, and Talissa A Altes. Lung injury induced by secondhand smoke exposure detected

- with hyperpolarized helium-3 diffusion MR. *Journal of Magnetic Resonance Imaging*, 39(1):77–84, 2014.
- [212] Miranda Kirby, Mohammadreza Heydarian, Andrew Wheatley, David G McCormack, and Grace Parraga. Evaluating bronchodilator effects in chronic obstructive pulmonary disease using diffusion-weighted hyperpolarized helium-3 magnetic resonance imaging. *Journal of applied physiology*, 112(4):651–657, 2012.
- [213] Chengbo Wang, Talissa A Altes, John P Mugler, G Wilson Miller, Kai Ruppert, Jaime F Mata, Gordon D Cates, Larry Borish, and Eduard E de Lange. Assessment of the lung microstructure in patients with asthma using hyperpolarized <sup>3</sup>He diffusion mri at two time scales: comparison with healthy subjects and patients with COPD. *Journal of Magnetic Resonance Imaging*, 28(1):80–88, 2008.
- [214] Sherif Gonem, Steven Hardy, Niels Buhl, Ruth Hartley, Marcia Soares, Richard Kay, Rino Costanza, Per Gustafsson, Christopher E Brightling, John Owers-Bradley, et al. Characterization of acinar airspace involvement in asthmatic patients by using inert gas washout and hyperpolarized 3-helium magnetic resonance. *Journal of Allergy and Clinical Immunology*, 137(2):417–425, 2016.
- [215] Nikhil R Pal and Sankar K Pal. A review on image segmentation techniques. *Pattern recognition*, 26(9):1277–1294, 1993.
- [216] Azriel Rosenfeld. *Digital picture processing*. Academic press, 1976.
- [217] Dzung L Pham, Chenyang Xu, and Jerry L Prince. Current methods in medical image segmentation. *Annual review of biomedical engineering*, 2(1):315–337, 2000.
- [218] Koon-Pong Wong. Medical image segmentation: methods and applications in functional imaging. In *Handbook of biomedical image analysis*, pages 111–182. Springer, 2005.

- [219] Ahmed Elnakib, Georgy Gimelfarb, Jasjit S Suri, and Ayman El-Baz. Medical image segmentation: A brief survey. In *Multi Modality State-of-the-Art Medical Image Segmentation and Registration Methodologies*, pages 1–39. Springer, 2011.
- [220] Alireza Norouzi, Mohd Shafry Mohd Rahim, Ayman Altameem, Tanzila Saba, Abdolvahab Ehsani Rad, Amjad Rehman, and Mueen Uddin. Medical image segmentation methods, algorithms, and applications. *IETE Technical Review*, 31(3):199–213, 2014.
- [221] Prasanna K Sahoo, Sakc Soltani, and Andrew KC Wong. A survey of thresholding techniques. *Computer vision, graphics, and image processing*, 41(2):233–260, 1988.
- [222] Siddharth Arora, Jayadev Acharya, Amit Verma, and Prasanta K Panigrahi. Multilevel thresholding for image segmentation through a fast statistical recursive algorithm. *Pattern Recognition Letters*, 29(2):119–125, 2008.
- [223] Nobuyuki Otsu. A threshold selection method from gray-level histograms. *Automatica*, 11(285-296):23–27, 1975.
- [224] CK Chow and T Kaneko. Automatic boundary detection of the left ventricle from cineangiograms. *Computers and biomedical research*, 5(4):388–410, 1972.
- [225] Kenneth R Castleman. *Digital image processing*. Prentice Hall, Upper Saddle River, NJ, 1996.
- [226] Josef Kittler, John Illingworth, and J Föglein. Threshold selection based on a simple image statistic. *Computer vision, graphics, and image processing*, 30(2):125–147, 1985.
- [227] Steven W Zucker. Region growing: Childhood and adolescence. *Computer graphics and image processing*, 5(3):382–399, 1976.
- [228] Rafael C Gonzalez and Richard E Woods. Image processing. *Digital image processing*, 2, 2007.



- [229] Robert M Haralick and Linda G Shapiro. Image segmentation techniques. *Computer vision, graphics, and image processing*, 29(1):100–132, 1985.
- [230] Steven L Horowitz and Theodosios Pavlidis. Picture segmentation by a tree traversal algorithm. *Journal of the ACM (JACM)*, 23(2):368–388, 1976.
- [231] Theodosios Pavlidis and Y-T Liow. Integrating region growing and edge detection. *IEEE Transactions on Pattern Analysis and Machine Intelligence*, 12(3):225–233, 1990.
- [232] H Digabel and C Lantuejoul. Iterative algorithms. *Proceedings of the 2nd European Symposium Quantitative Analysis of Microstructures in Material Science, Biology and Medicine*, pages 85–89, 1978.
- [233] Serge Beucher and Christian Lantuéjoul. Use of watersheds in contour detection. 1979.
- [234] Pierre Soille and Luc M Vincent. Determining watersheds in digital pictures via flooding simulations. In *Lausanne-DL tentative*, pages 240–250. International Society for Optics and Photonics, 1990.
- [235] Luc Vincent and Pierre Soille. Watersheds in digital spaces: an efficient algorithm based on immersion simulations. *IEEE transactions on pattern analysis and machine intelligence*, 13(6):583–598, 1991.
- [236] Serge Beucher and Fernand Meyer. The morphological approach to segmentation: the watershed transformation. *Optical Engineering-New York-Marcel Dekker Incorporated*, 34:433–433, 1992.
- [237] Vicent Caselles, Ron Kimmel, and Guillermo Sapiro. Geodesic active contours. *International journal of computer vision*, 22(1):61–79, 1997.
- [238] Corinna Cortes and Vladimir Vapnik. Support-vector networks. *Machine learning*, 20(3):273–297, 1995.

- [239] Chih-Wei Hsu and Chih-Jen Lin. A comparison of methods for multiclass support vector machines. *IEEE transactions on Neural Networks*, 13(2):415–425, 2002.
- [240] Laura Auria and Rouslan A Moro. Support vector machines (SVM) as a technique for solvency analysis. 2008.
- [241] Paul L Rosin and Joviša Žunić. Measuring rectilinearity. *Computer Vision and Image Understanding*, 99(2):175–188, 2005.
- [242] Warren S McCulloch and Walter Pitts. A logical calculus of the ideas immanent in nervous activity. *The bulletin of mathematical biophysics*, 5(4):115–133, 1943.
- [243] Frank Rosenblatt. The perceptron: A probabilistic model for information storage and organization in the brain. *Psychological review*, 65(6):386, 1958.
- [244] Erol Gelenbe, Yutao Feng, and K Ranga R Krishnan. Neural network methods for volumetric magnetic resonance imaging of the human brain. *Proceedings of the IEEE*, 84(10):1488–1496, 1996.
- [245] P Smitha, L Shaji, and MG Mini. A review of medical image classification techniques. In *International conference on VLSI, Communication & Intrumnataiom*, pages 34–38, 2011.
- [246] Quoc V Le. Building high-level features using large scale unsupervised learning. In *Acoustics, Speech and Signal Processing (ICASSP), 2013 IEEE International Conference on*, pages 8595–8598. IEEE, 2013.
- [247] T Velmurugan and T Santhanam. Computational complexity between K-means and K-medoids clustering algorithms for normal and uniform distributions of data points. *Journal of computer science*, 6(3):363, 2010.
- [248] James MacQueen et al. Some methods for classification and analysis of multivariate

- observations. In *Proceedings of the fifth Berkeley symposium on mathematical statistics and probability*, volume 1, pages 281–297. Oakland, CA, USA., 1967.
- [249] Guy Barrett Coleman and Harry C Andrews. Image segmentation by clustering. *Proceedings of the IEEE*, 67(5):773–785, 1979.
- [250] Sami Ayramo Tommi Karkkainen. Introduction to partitioning-based clustering methods with a robust example. 2006.
- [251] Greg Hamerly. Making k-means even faster. In *Proceedings of the 2010 SIAM international conference on data mining*, pages 130–140. SIAM, 2010.
- [252] James C Bezdek, Robert Ehrlich, and William Full. FCM: The fuzzy c-means clustering algorithm. *Computers & Geosciences*, 10(2-3):191–203, 1984.
- [253] Lotfi A Zadeh. Fuzzy sets. *Information and control*, 8(3):338–353, 1965.
- [254] Arthur P Dempster, Nan M Laird, and Donald B Rubin. Maximum likelihood from incomplete data via the EM algorithm. *Journal of the royal statistical society. Series B (methodological)*, pages 1–38, 1977.
- [255] Michael Kass, Andrew Witkin, and Demetri Terzopoulos. Snakes: Active contour models. *International journal of computer vision*, 1(4):321–331, 1988.
- [256] Tim McInerney and Demetri Terzopoulos. Deformable models in medical image analysis: a survey. *Medical image analysis*, 1(2):91–108, 1996.
- [257] Isaac Cohen, Laurent D Cohen, and Nicholas Ayache. Using deformable surfaces to segment 3-D images and infer differential structures. *CVGIP: Image understanding*, 56(2):242–263, 1992.
- [258] Stanley Osher and James A Sethian. Fronts propagating with curvature-dependent speed: algorithms based on hamilton-jacobi formulations. *Journal of computational physics*, 79(1):12–49, 1988.

- [259] Chenyang Xu, Dzung L Pham, and Jerry L Prince. Image segmentation using deformable models. *Handbook of medical imaging*, 2:129–174, 2000.
- [260] Vicent Caselles, Francine Catté, Tomeu Coll, and Françoise Dibos. A geometric model for active contours in image processing. *Numerische mathematik*, 66(1):1–31, 1993.
- [261] Ravi Malladi, James A Sethian, and Baba C Vemuri. Shape modeling with front propagation: A level set approach. *IEEE transactions on pattern analysis and machine intelligence*, 17(2):158–175, 1995.
- [262] David Adalsteinsson and James A Sethian. A fast level set method for propagating interfaces. *Journal of computational physics*, 118(2):269–277, 1995.
- [263] Ross T Whitaker. A level-set approach to 3D reconstruction from range data. *International journal of computer vision*, 29(3):203–231, 1998.
- [264] Stuart Geman and Donald Geman. Stochastic relaxation, gibbs distributions, and the Bayesian restoration of images. *IEEE Transactions on pattern analysis and machine intelligence*, (6):721–741, 1984.
- [265] Andrew Blake, Pushmeet Kohli, and Carsten Rother. *Markov random fields for vision and image processing*. MIT Press, 2011.
- [266] Yuri Y Boykov and M-P Jolly. Interactive graph cuts for optimal boundary & region segmentation of objects in ND images. In *Computer Vision, 2001. ICCV 2001. Proceedings. Eighth IEEE International Conference on*, volume 1, pages 105–112. IEEE, 2001.
- [267] LR Ford and DR Fulkerson. *Flows in networks* princeton university press. *Princeton, New Jersey*, 276, 1962.
- [268] Peter Elias, Amiel Feinstein, and Claude Shannon. A note on the maximum flow through a network. *IRE Transactions on Information Theory*, 2(4):117–119, 1956.

- [269] Andrew V Goldberg and Robert E Tarjan. A new approach to the maximum-flow problem. *Journal of the ACM (JACM)*, 35(4):921–940, 1988.
- [270] Yuri Boykov and Vladimir Kolmogorov. An experimental comparison of min-cut/max-flow algorithms for energy minimization in vision. *Pattern Analysis and Machine Intelligence, IEEE Transactions on*, 26(9):1124–1137, 2004.
- [271] Thomas Pock, Antonin Chambolle, Daniel Cremers, and Horst Bischof. A convex relaxation approach for computing minimal partitions. In *Computer Vision and Pattern Recognition, 2009. CVPR 2009. IEEE Conference on*, pages 810–817. IEEE, 2009.
- [272] Gilbert Strang. Maximal flow through a domain. *Mathematical Programming*, 26(2):123–143, 1983.
- [273] Jing Yuan, Egil Bae, and Xue-Cheng Tai. A study on continuous max-flow and min-cut approaches. In *Computer Vision and Pattern Recognition (CVPR), 2010 IEEE Conference on*, pages 2217–2224. IEEE, 2010.
- [274] Jing Yuan, Egil Bae, Xue-Cheng Tai, and Yuri Boykov. A continuous max-flow approach to potts model. *Computer Vision–ECCV 2010*, pages 379–392, 2010.
- [275] Lee R Dice. Measures of the amount of ecologic association between species. *Ecology*, 26(3):297–302, 1945.
- [276] Michael Eliasziw, S Lorraine Young, M Gail Woodbury, and Karen Fryday-Field. Statistical methodology for the concurrent assessment of interrater and intrarater reliability: using goniometric measurements as an example. *Physical therapy*, 74(8):777–788, 1994.
- [277] Milan Sonka and J Michael Fitzpatrick. Handbook of medical imaging (volume 2, medical image processing and analysis). SPIE- The international society for optical engineering, 2000.

- [278] Calvin R Maurer and J Michael Fitzpatrick. A review of medical image registration. *Interactive image-guided neurosurgery*, 17, 1993.
- [279] Lisa Gottesfeld Brown. A survey of image registration techniques. *ACM computing surveys (CSUR)*, 24(4):325–376, 1992.
- [280] Roumen Kountchev and Kazumi Nakamatsu. *Advances in Reasoning-Based Image Processing Intelligent Systems: Conventional and Intelligent Paradigms*, volume 29. Springer Science & Business Media, 2012.
- [281] Aristeidis Sotiras, Christos Davatzikos, and Nikos Paragios. Deformable medical image registration: A survey. *IEEE transactions on medical imaging*, 32(7):1153–1190, 2013.
- [282] Alexis Roche, Xavier Pennec, Michael Rudolph, DP Auer, Grégoire Malandain, Sébastien Ourselin, Ludwig M Auer, and Nicholas Ayache. Generalized correlation ratio for rigid registration of 3d ultrasound with mr images. In *International Conference on Medical Image Computing and Computer-Assisted Intervention*, pages 567–577. Springer, 2000.
- [283] Carlos Oscar Sánchez Sorzano, Philippe Thévenaz, and Michael Unser. Elastic registration of biological images using vector-spline regularization. *IEEE Transactions on Biomedical Engineering*, 52(4):652–663, 2005.
- [284] Wolfgang Wein, Shelby Brunke, Ali Khamene, Matthew R Callstrom, and Nassir Navab. Automatic ct-ultrasound registration for diagnostic imaging and image-guided intervention. *Medical image analysis*, 12(5):577–585, 2008.
- [285] Torsten Butz and Jean-Philippe Thiran. Affine registration with feature space mutual information. In *Medical Image Computing and Computer-Assisted Intervention—MICCAI 2001*, pages 549–556. Springer, 2001.

- [286] Daniel Rueckert, Luke I Sonoda, Carmel Hayes, Derek LG Hill, Martin O Leach, and David J Hawkes. Nonrigid registration using free-form deformations: application to breast mr images. *IEEE transactions on medical imaging*, 18(8):712–721, 1999.
- [287] Alain Pitiot, Eric Bardinet, Paul M Thompson, and Grégoire Malandain. Piecewise affine registration of biological images for volume reconstruction. *Medical image analysis*, 10(3):465–483, 2006.
- [288] Xiahai Zhuang, Kawal S Rhode, Reza S Razavi, David J Hawkes, and Sebastien Ourselin. A registration-based propagation framework for automatic whole heart segmentation of cardiac MRI. *IEEE transactions on medical imaging*, 29(9):1612–1625, 2010.
- [289] Mark Holden. A review of geometric transformations for nonrigid body registration. *IEEE transactions on medical imaging*, 27(1):111–128, 2008.
- [290] Fred L. Bookstein. Principal warps: Thin-plate splines and the decomposition of deformations. *IEEE Transactions on pattern analysis and machine intelligence*, 11(6):567–585, 1989.
- [291] Serge Belongie, Jitendra Malik, and Jan Puzicha. Shape matching and object recognition using shape contexts. *IEEE transactions on pattern analysis and machine intelligence*, 24(4):509–522, 2002.
- [292] Sergey Osechinskiy and Frithjof Kruggel. Slice-to-volume nonrigid registration of histological sections to MR images of the human brain. *Anatomy Research International*, 2011, 2010.
- [293] Thomas W Sederberg and Scott R Parry. Free-form deformation of solid geometric models. *ACM SIGGRAPH computer graphics*, 20(4):151–160, 1986.

- [294] Seungyong Lee, George Wolberg, and Sung Yong Shin. Scattered data interpolation with multilevel B-splines. *IEEE transactions on visualization and computer graphics*, 3(3):228–244, 1997.
- [295] Enzo Ferrante and Nikos Paragios. Slice-to-volume medical image registration: A survey. *Medical Image Analysis*, 39:101–123, 2017.
- [296] J Michael Fitzpatrick, Jay B West, and Calvin R Maurer. Predicting error in rigid-body point-based registration. *IEEE transactions on medical imaging*, 17(5):694–702, 1998.
- [297] J Michael Fitzpatrick. Fiducial registration error and target registration error are uncorrelated. In *Proc SPIE*, volume 7261, pages 726102–12, 2009.
- [298] Aditya Bharatha, Masanori Hirose, Nobuhiko Hata, Simon K Warfield, Matthieu Ferrant, Kelly H Zou, Eduardo Suarez-Santana, Juan Ruiz-Alzola, Anthony D’amico, Robert A Cormack, et al. Evaluation of three-dimensional finite element-based deformable registration of pre-and intraoperative prostate imaging. *Medical physics*, 28(12):2551–2560, 2001.
- [299] Haytham Elhawary, Sota Oguro, Kemal Tuncali, Paul R Morrison, Servet Tatli, Paul B Shyn, Stuart G Silverman, and Nobuhiko Hata. Multimodality non-rigid image registration for planning, targeting and monitoring during CT-guided percutaneous liver tumor cryoablation. *Academic radiology*, 17(11):1334–1344, 2010.



## Chapter 2

# Globally Optimal Co-Segmentation of Three-Dimensional Pulmonary $^1\text{H}$ and Hyperpolarized $^3\text{He}$ MRI with Spatial Consistence Prior

*Previous methods for noble gas ( $^3\text{He}/^{129}\text{Xe}$ ) MRI structural-functional information quantification involve many low level and labourious user interactions, introduce high observer variability and require significant amount of runtime. Here we developed and evaluated an automated lung segmentation using the valuable and complementary information from both  $^1\text{H}$  and  $^3\text{He}$  and the  $^1\text{H}$ - $^3\text{He}$  co-segmentation problem was solved using convex optimization techniques.*

*The contents of this chapter were previously published in Medical Image Analysis: F Guo, J Yuan, M Rajchl, S Svenningsen, DPI Capaldi, K Sheikh, A Fenster and G Parraga. Globally optimal co-segmentation of three-dimensional pulmonary  $^1\text{H}$  and hyperpolarized  $^3\text{He}$  MRI with spatial consistence prior. Medical image analysis 23.1 (2015): 43-55. Permission to reproduce this article was granted by Elsevier and is provided in Appendix G.*

### 2.1 Introduction

According to World Health Organization, 64 million adults have been diagnosed worldwide with chronic obstructive pulmonary disease (COPD) [1]. Recent studies reported that  $\sim 10\%$  of

adults aged 40 years and older have clinically relevant COPD [2], but a minority have a clinical diagnosis and are undergoing treatment [3].

With the recent emergence of functional pulmonary imaging approaches using inhaled hyperpolarized  $^3\text{He}/^{129}\text{Xe}$  magnetic resonance imaging (MRI), there is now the potential to provide regional information about lung structure and function, allowing for COPD patient monitoring over time and in response to therapy [4, 5]. To quantify and analyze regional pulmonary function, lung segmentation of the fused structural information from  $^1\text{H}$  MRI and functional information from  $^3\text{He}$  MRI is required. In subjects with respiratory disease,  $^3\text{He}$  MRI provides visual evidence of ventilation heterogeneity - characteristic regions of signal void that cannot be easily quantified and normalized [6] because these images provide little anatomical information. On the other hand, segmentation of the lung from  $^1\text{H}$  MRI is also particularly challenging due to poor image quality stemming from low proton density, magnetic susceptibility and motion artifacts [7, 8], resulting in ghost contours of the chest wall, partial volume effects and indistinguishable gray levels with surrounding tissues [9, 10, 11, 12].

Previous work showed that both structural and functional information can be derived from images and provide complementary information that segmentation methods can exploit [13, 14, 15]. For example,  $^1\text{H}$  MRI has poorly defined edges around the mediastinum where the heart and hilar structures move during breath-hold imaging. In contrast, and as shown in Fig. 2.1,  $^3\text{He}$  MRI has poorly defined edges on the lung periphery, where ventilation defects are commonly present. Here we identified a way to perform lung segmentation by exploring image features of both  $^1\text{H}$  and  $^3\text{He}$  images and propose a way to simultaneously extract the lung from the two input three-dimensional (3D) images.

### 2.1.1 Previous Studies

Previous work [16, 9] showed that pulmonary MRI segmentation is more complex than pulmonary CT approaches, mainly because of the low proton and tissue density in pulmonary MR images as compared to tissue contrast provided by CT. Approaches for extracting the lung from

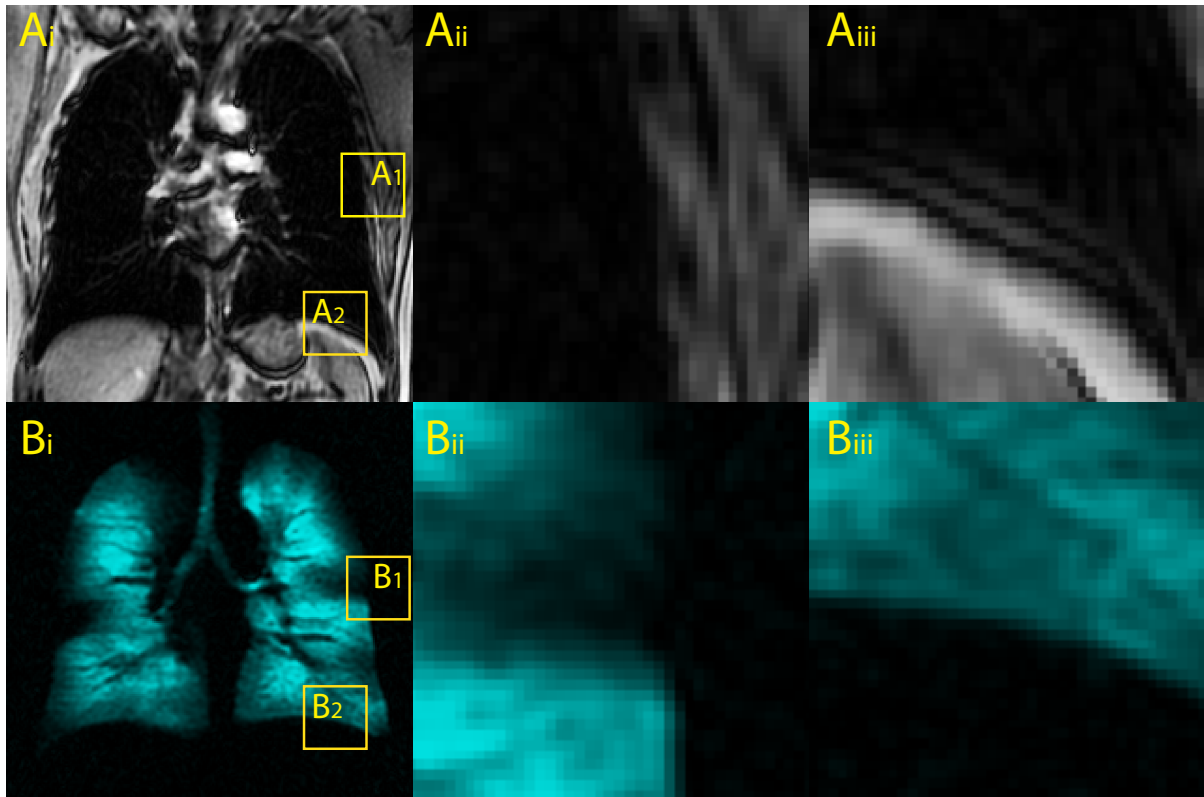


Figure 2.1: Complementary edge information in  $^1\text{H}$  and  $^3\text{He}$  MRI.  $A_i$ )  $^1\text{H}$  MRI coronal slice with inset box  $A_1$  shown expanded in  $A_{ii}$ ) and  $A_2$  shown expanded in  $A_{iii}$ ).  $B_i$ )  $^3\text{He}$  MRI coronal slice with inset box  $B_1$  shown expanded in  $B_{ii}$ ) and  $B_2$  shown expanded in  $B_{iii}$ ).

pulmonary MRI have been developed mainly based on grey level thresholding, active contour and modelling methods.

For  $^1\text{H}$  MRI lung segmentation, a multi-step automatic method that used histogram-based thresholding and morphological operations was developed [12]. In another attempt, a model-matching method was used to segment the lung by registering individual images to a lung model created from manually segmented training dataset [17]. Another approach combined supervised neural network classifier and parametric active contour techniques [18]. Merging of multiple parametric active contours within homogeneous regions [19] was also piloted to automatically segment the lung. Finally, lung was segmented using a modified geometric snake model that integrated gradient flow forces and region constraints provided by a Fuzzy C-means clustering method [9].

With respect to  $^3\text{He}$  MRI lung segmentation, thresholding [20, 21] and a statistical model-based method [22] using principle component analysis were developed. A 2D semi-automated segmentation approach using registered pulmonary  $^1\text{H}$ - $^3\text{He}$  MR images was proposed [23] consisting of k-means clustering of  $^3\text{He}$  MRI, region growing of  $^1\text{H}$  MRI and landmark-based  $^1\text{H}$ - $^3\text{He}$  registration.

While these approaches have provided promising results, some limitations still remain that need to be tackled including improved algorithm performance and efficient workflow translation. For example, some of these approaches required substantial runtime [17, 23] while others were restricted to certain region of interest [19] or dependent on robust grey level thresholding [20, 12, 21]. Finally, other approaches required a substantial amount of user interaction [23], extensive training and frequent updating with careful expert manual segmentation [18, 22].

### 2.1.2 Contributions

To address some of the limitations of the current approaches, here we introduce a convex optimization based co-segmentation approach that exploits image features from both  $^1\text{H}$  and  $^3\text{He}$  MRI for lung segmentation. We summarize our main contributions as follows:

- We present a global optimization based approach to jointly segment pulmonary  $^1\text{H}$  and  $^3\text{He}$  MRI, and demonstrate that the global and exact optimum of the complicated combinatorial optimization problem can be achieved through convex relaxation.
- We propose a *coupled continuous max-flow* model and prove its duality to the studied convex relaxed co-segmentation formulation. With the help of the *coupled continuous max-flow* formulation, we show that the original complicated optimization problem can be equivalently solved under a primal and dual perspective, which avoids tackling the challenging optimization problem directly.
- We derive an efficient numerical algorithm based on the proposed *coupled continuous max-flow* formulation using a modern duality-augmented algorithmic scheme, namely

the *coupled continuous max-flow* algorithm, which is implemented on a GPU to achieve high performance in numerics.

Recently, a graph-cut based method was developed to segment CT (anatomical) and PET (functional) images simultaneously over two discrete graphs by enforcing an inter-surface context cost [24]. This approach made use of image information from both modalities and incorporated the introduced context cost to achieve spatial consistency. It is well known that such discrete graph-cut methods can yield excellent performance [25]. However, these discrete optimization based approaches are limited by grid bias or metrication error [26, 27]. Although these errors can be reduced by increasing the number of neighboring nodes [26] or applying high order clique [28], extra memory and computational load are required [29]. Our proposed approach is fundamentally distinct from previous work in that the image co-segmentation problem was formulated and studied in spatially continuous settings, and globally optimized under a convex relaxation perspective. Compared with discrete graph optimization based methods, the proposed convex optimization based approach successfully avoids metrication errors [26, 27] and substantially improves segmentation accuracy, while providing great numerical advantages with much lower memory load and higher computational efficiency [30, 31]. Recently, a different joint segmentation approach [32] was developed to simultaneously segment the whole gland ( $\mathcal{R}_{WG}$ ) and the central gland ( $\mathcal{R}_{CG}$ ) in a single 3D prostate MR image. This previous approach also employed a coupled continuous max-flow model and convex optimization techniques. However, our method employed a graph-based approach as opposed to the level-set/contour evaluation based method. In addition, our approach incorporated the spatial consistency between the  $^1\text{H}$  lung  $\mathcal{R}_L^1$  and  $^3\text{He}$  lung  $\mathcal{R}_L^2$ , (i.e.,  $\mathcal{R}_L^1 \approx \mathcal{R}_L^2$ ), as opposed to the inter-contour relationship, (i.e.,  $\mathcal{R}_{CG} \subset \mathcal{R}_{WG}$ ), resulting in a different flow configuration and different optimization scheme.

## 2.2 Methods

We introduce an image *co-segmentation model* in the spatially continuous settings to jointly segment the lung from input 3D  $^1\text{H}$  and  $^3\text{He}$  MRI pairs. We demonstrate that the proposed *spatially continuous co-segmentation model* can be globally optimized by means of convex relaxation. In other words, the globally optimal lung masks can be obtained simultaneously by solving a convex relaxation formulation, which is much simpler in theory and numerical computation than the original combinatorial optimization formulation, i.e., the proposed *spatially continuous co-segmentation model*. In addition, we present a *coupled continuous max-flow formulation* and demonstrate its equivalence to the convex relaxed co-segmentation model through primal and dual analysis. The introduced *coupled continuous max-flow formulation* allows us to directly derive an efficient duality-based algorithm to the studied *spatially continuous co-segmentation model*. The derived algorithm can be easily implemented using parallel computation architectures to achieve high computation performance.

### 2.2.1 Spatially Continuous Co-Segmentation Model

Given a  $^1\text{H}$  MR image  $I_1(x)$  and a  $^3\text{He}$  MR image  $I_2(x)$ ,  $x \in \Omega$ , that are appropriately co-registered, we propose to simultaneously segment both images into the lung, i.e.,  $\mathcal{R}_L^1$  and  $\mathcal{R}_L^2$ , and the associated complementary background, i.e.,  $\mathcal{R}_B^1$  and  $\mathcal{R}_B^2$ , while imposing the spatial consistency between the two segmented lung  $\mathcal{R}_L^1$  and  $\mathcal{R}_L^2$ .

#### 2.2.1.1 Continuous Min-Cut Formulations

In this work, we focus on a spatially continuous convex optimization approach, which, due to its computational efficiency, substantially decreases runtime for 3D image segmentation. Additionally, the continuous optimization based approach is able to avoid metrication error introduced by discrete graph-based approaches [26, 27], which, although can be improved with more neighbouring nodes or high order cliques, extra memory and computation power

are required [29]. We refer readers to Appendix A for comparison of the two categories of algorithms.

Let  $u_i(x) \in \{0, 1\}$ ,  $i \in \{1, 2\}$ , be the indicator or labelling function of the corresponding region  $\mathcal{R}_L^i$ , such that

$$u_i(x) = \begin{cases} 1, & \text{where } x \in \mathcal{R}_L^i \\ 0, & \text{otherwise} \end{cases}.$$

In view of the continuous min-cut model (A.1), the segmentation of each image  $I_1(x)$  and  $I_2(x)$  can be achieved by minimizing the *continuous min-cut* energy:

$$E_i(u_i) = \left\{ \int_{\Omega} (1 - u_i) D_s^i(x) dx + \int_{\Omega} u_i D_t^i(x) dx \right\} + \int_{\Omega} \omega_i(x) |\nabla u_i| dx, \quad i \in \{1, 2\}, \quad (2.1)$$

where  $D_t^i(x)$  and  $D_s^i(x)$ ,  $i \in \{1, 2\}$ , represent the labelling cost function *w.r.t.* the lung  $\mathcal{R}_L^i$  and the background  $\mathcal{R}_B^i$ , respectively. In addition, the boundary weight function  $\omega_i(x) \geq 0$ ,  $i \in \{1, 2\}$ , in (2.1) is non-negative, and the associated total-variation function in (2.1) properly encodes the weighted total area of the segmented lung  $\mathcal{R}_L^i$  in 3D.

### 2.2.1.2 Spatial Consistency Prior

Upon observation of the  $^1\text{H}$  and  $^3\text{He}$  MR images, there is signal intensity overlap between lung  $\mathcal{R}_L^1$  and  $\mathcal{R}_L^2$  in the two spatially aligned MR images. For example, for healthy subjects without ventilation defects, there are regions of diminished signal intensity in  $^1\text{H}$  MR images and enhanced signal intensity in  $^3\text{He}$  images. For patients with disease, there are also regions of diminished signal intensity in  $^1\text{H}$  MR images and both diminished and greater signal intensities in  $^3\text{He}$  images. Instead of exploiting the “binary” diminished-to-enhanced signal intensities, we utilized a “relaxed” correlation where diminished signal intensity in  $^1\text{H}$  MRI lung can be mapped to both enhanced and diminished signal intensity in  $^3\text{He}$  MRI lung, the extent of which was controlled or weighted to facilitate segmentation. For example, in terms of the cost function, the sampled ventilation defect voxels within  $^3\text{He}$  images had a greater probability (or

lower cost) of being assigned a foreground label, compared with the zero or lower probability (higher cost) in the case of “binary” signal intensity mapping correlations. While the lung boundary information in  $^3\text{He}$  images might also be influenced by the edges between ventilation and ventilation defect regions within the lung, we would like to emphasize that the associated  $^1\text{H}$  image signal intensity information as well as the regularization terms could interact to minimize this effect. Therefore, we exploited this information by enforcing a spatial similarity between the two extracted lung ( $\mathcal{R}_L^1$  and  $\mathcal{R}_L^2$ ) as a constraint and then penalizing the differences of the two lung  $\mathcal{R}_L^1$  and  $\mathcal{R}_L^2$  such that

$$E_3(u_1, u_2) = \int_{\Omega} |u_1 - u_2| dx. \quad (2.2)$$

To take advantage of image information from the two modalities, we present a *continuous co-segmentation formulation* by coupling the spatial similarity (2.2) to the two independent segmentation (2.1) such that

$$\min_{u_{1,2}(x) \in \{0,1\}} E_1(u_1) + E_2(u_2) + \beta E_3(u_1, u_2), \quad (2.3)$$

where  $\beta > 0$  weights the contribution of the spatial dissimilarity of the two lung to the total continuous min-cut energy. By denoting the inner product of two function, i.e.,  $h(x)$  and  $g(x)$ , as  $\langle h, g \rangle = \int h(x)g(x) dx$ , the above optimization problem (2.3) can be rewritten as follows:

$$\begin{aligned} \min_{u_{1,2}(x) \in \{0,1\}} & \langle 1 - u_1, D_s^1 \rangle + \langle u_1, D_t^1 \rangle + \int_{\Omega} \omega_1(x) |\nabla u_1| dx + \\ & \langle 1 - u_2, D_s^2 \rangle + \langle u_2, D_t^2 \rangle + \int_{\Omega} \omega_2(x) |\nabla u_2| dx + \beta \int_{\Omega} |u_1 - u_2| dx, \end{aligned} \quad (2.4)$$

where the energy function contains two independent continuous min-cut segmentation problems (2.1) *w.r.t.* the two lung  $\mathcal{R}_L^1$  and  $\mathcal{R}_L^2$  and the spatial regional similarity *prior* (2.2).



### 2.2.2 Convex Relaxed Co-Segmentation Model

Given the highly non-smooth total-variation and absolute volume difference terms, the above binary-constrained optimization problem (2.4) results in a very challenging combinatorial optimization problem. Based on the recently developed convex relaxation techniques [33], the challenging non-convex optimization problem (2.4) can be solved globally and exactly by means of convex relaxation, i.e., the convex relaxed formulation of (2.4) as follows:

$$\begin{aligned} \min_{u_{1,2}(x) \in [0,1]} & \langle 1 - u_1, D_s^1 \rangle + \langle u_1, D_t^1 \rangle + \int_{\Omega} \omega_1(x) |\nabla u_1| dx + \\ & \langle 1 - u_2, D_s^2 \rangle + \langle u_2, D_t^2 \rangle + \int_{\Omega} \omega_2(x) |\nabla u_2| dx + \beta \int_{\Omega} |u_1 - u_2| dx, \end{aligned} \quad (2.5)$$

where the voxel-wise binary constraints  $u_{1,2}(x) \in \{0, 1\}$  in (2.4) are relaxed to the respective convex intervals  $u_{1,2}(x) \in [0, 1]$ . Clearly, (2.5) gives rise to a convex optimization problem, which can be optimized globally.

In the following sections, we show the *convex relaxed co-segmentation formulation* (2.5) also solves the original binary-constrained co-segmentation problem (2.4) exactly.

## 2.3 Coupled Continuous Max-Flow Approach

We present a coupled continuous max-flow model and show that it is mathematically equivalent to the studied convex relaxed co-segmentation problem (2.5). Moreover, we demonstrate that the introduced combinatorial optimization problem (2.4), the continuous co-segmentation model, can be solved exactly.

### 2.3.1 Coupled Continuous Max-Flow Model

The coupled flow-maximization setup was configured by combining two independent standard flow-maximization graphs and these independent elements were previously developed and described [34]. The original contribution of the current approach is that an extra flow  $r(x)$  was

introduced to link the two independent graphs, which, at a first glance, looks similar to but quite different from previous studies about joint segmentation of MRI femoral lumen and outer wall with a “nesting” layout constraint [35]. Figure 2.2 shows a schematic diagram of the coupled flow-maximization configuration.

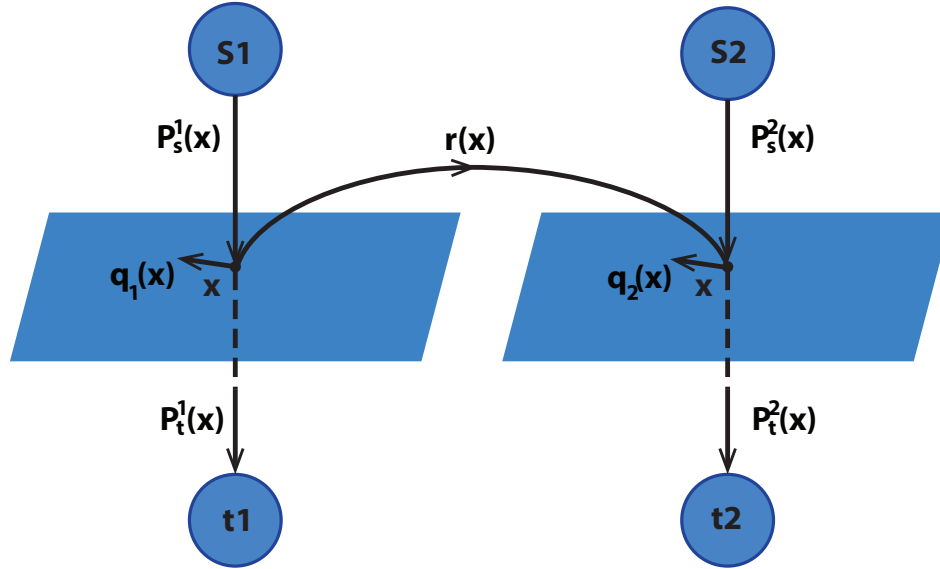


Figure 2.2: Coupled flow-maximization settings. For two image domains  $\Omega_i$ ,  $i \in \{1, 2\}$ , two source terminals  $s_i$  and two sink terminals  $t_i$  were linked to each pixel  $x \in \Omega_i$ . The source flow  $p_s^i(x)$  was directed from  $s_i$  and the sink flow  $p_t^i(x)$  was directed to  $t_i$  along with a spatial flow  $q_i(x)$  around each  $x$ . An extra flow  $r(x)$  was also directed from  $x \in \Omega_1$  to the same position in  $\Omega_2$ .

- We employed two copies  $\Omega_1$  and  $\Omega_2$  of the image domain  $\Omega$  *w.r.t.* the two continuous min-cut graphs, respectively; we added a source terminal  $s_i$  and a sink terminal  $t_i$  to the image domain  $\Omega_i$ ,  $i \in \{1, 2\}$ . We linked  $s_i$  to each pixel  $x \in \Omega_i$ , along which a source flow  $p_s^i(x)$  was directed. Similarly, we linked each  $x \in \Omega_i$  to  $t_i$ , along which a sink flow  $p_t^i(x)$  was directed. Moreover, within  $\Omega_i$ , a spatial flow  $q_i(x)$  around each pixel  $x \in \Omega_i$  was specified.
- At each pixel  $x \in \Omega_1$ , there was an extra link to the same position  $x \in \Omega_2$  and describing an additional flow  $r(x)$ .

Following the flow configuration demonstrated in Fig. 2.2, we formulate the *coupled continuous max-flow model* by maximizing the total flow that is allowed to send from the two source terminals  $s_1$  and  $s_2$ :

$$\max_{p_s^{1,2}, p_t^{1,2}, q_{1,2}, r} \int_{\Omega} p_s^1 dx + \int_{\Omega} p_s^2 dx, \quad (2.6)$$

subject to the following constraints of the flow function:

- For the two source flow fields  $p_s^{1,2}(x)$  and each pixel  $x \in \Omega_{1,2}$ , we defined the respective flow capacity constraints such that

$$p_s^1(x) \leq D_s^1(x), \quad p_s^2(x) \leq D_s^2(x). \quad (2.7)$$

- For the two sink flow fields  $p_t^{1,2}(x)$  and each pixel  $x \in \Omega_{1,2}$ , the respective flow capacity constraints are given by

$$p_t^1(x) \leq D_t^1(x), \quad p_t^2(x) \leq D_t^2(x). \quad (2.8)$$

- For the two spatial flows  $q_{1,2}(x)$  and each pixel  $x \in \Omega_{1,2}$ , the flow capacity constraints are defined as

$$|q_1(x)| \leq \omega_1(x), \quad |q_2(x)| \leq \omega_2(x). \quad (2.9)$$

- The extra coupled flow field  $r(x)$  is constrained by

$$|r(x)| \leq \beta. \quad (2.10)$$

- In addition to the flow capacity constraints, for  $\forall x \in \Omega_1$ , the flow fields  $(p_s^1(x), p_t^1(x), q_1(x))$ ,

$r(x)$ ) are balanced, i.e., the flow conservation constraint, such that

$$F_1(x) := \operatorname{div} q_1(x) + p_t^1(x) - p_s^1(x) + r(x) = 0; \quad (2.11)$$

for  $\forall x \in \Omega_2$ , the flow fields  $(p_s^2(x), p_t^2(x), q_2(x), r(x))$  are balanced such that

$$F_2(x) := \operatorname{div} q_2(x) + p_t^2(x) - p_s^2(x) - r(x) = 0. \quad (2.12)$$

### 2.3.2 Duality and Exactness of Convex Relaxation

The *coupled continuous max-flow model* (2.6) maximizes the linear total-flow function subject to the flow capacity and conservation constraints (2.7) - (2.12). Now we prove the equivalence between the proposed *coupled continuous max-flow model* (2.6) and *convex relaxed co-segmentation formulation* (2.5) under the primal and dual perspective of convex optimization, i.e.,

**Proposition 1** *The proposed coupled continuous max-flow model (2.6) is equivalent or dual to the convex relaxed co-segmentation formulation (2.5) such that*

$$(2.6) \iff (2.5).$$

The proof follows variational facts: we introduce the multiplier function  $u_1(x)$  and  $u_2(x)$  to the two flow conservation conditions (2.11) and (2.12), respectively. Therefore, we have the following primal-dual optimization formulation, which is equivalent to (2.6):

$$\min_{u_{1,2}} \max_{p_s, p_t, q, r} \int_{\Omega} p_s^1 dx + \int_{\Omega} p_s^2 dx + \int_{\Omega} u_1(x) F_1(x) dx + \int_{\Omega} u_2(x) F_2(x) dx, \quad (2.13)$$

subject to the flow capacity constraints (2.7) - (2.10). Given the definitions of function (2.11) and (2.12), the primal-dual optimization problem (2.13), after re-organizing the function terms,

finally amounts to the optimization problem such that:

$$\begin{aligned} \min_{u_{1,2}} \max_{p_s, p_t, q, r} & \int_{\Omega} (1 - u_1) p_s^1 dx + \int_{\Omega} u_1 p_t^1 dx + \\ & \int_{\Omega} (1 - u_2) p_s^2 dx + \int_{\Omega} u_2 p_t^2 dx + \\ & \int_{\Omega} u_1 \operatorname{div} q_1 dx + \int_{\Omega} u_2 \operatorname{div} q_2 dx + \int_{\Omega} (u_1 - u_2) r dx \end{aligned} \quad (2.14)$$

subject to the flow capacity constraints (2.7) - (2.10).

Similar to the work previously described [34], maximizing the energy (2.14) over the flow function  $p_s^{1,2}(x)$ ,  $p_t^{1,2}(x)$ ,  $q_{1,2}(x)$  and  $r(x)$ , subject to the respective flow capacities (2.7) - (2.10), results in the *convex relaxed co-segmentation formulation* (2.5). As a result, the duality or equivalence between (2.6) and (2.5) is proven such that

$$(2.6) \iff (2.13) \text{ or } (2.14) \iff (2.5).$$

With the help of the *coupled continuous max-flow formulation* (2.6) and proposition 3, we can also simply threshold the global optimum  $u_{1,2}^*(x) \in [0, 1]$  of the convex relaxed co-segmentation problem (2.5) by any  $\gamma \in (0, 1]$  to generate global binary optimum of (2.4). The proof follows the similar analytical procedures given by [34] and the fact that thresholding of (A.8) does not change the sign of  $u_1^*(x) - u_2^*(x)$  for  $\forall x \in \Omega$ , i.e., if  $u_1^*(x) - u_2^*(x) \geq 0$ , then  $u_1^\gamma(x) - u_2^\gamma(x) \geq 0$ ; if  $u_1^*(x) - u_2^*(x) \leq 0$ , then  $u_1^\gamma(x) - u_2^\gamma(x) \leq 0$ .

### 2.3.3 Coupled Continuous Max-Flow Algorithm

Observing the primal-dual formulation (2.13) and proposition 1, it is obvious that the optimal labelling function  $u_{1,2}(x)$  of the convex relaxed co-segmentation problem (2.5) can be computed by the optimal multipliers of its equivalent primal-dual problem (2.13) alternatively, which is the essential idea of the *coupled continuous max-flow algorithm* proposed in this section. We show that such a coupled flow-maximization based numerical scheme successfully

avoids tackling the non-smooth total-variation and absolute function terms in the proposed co-segmentation problem (2.4) by means of simple projection steps, and results in efficient convergence.

In view of the primal-dual formulation (2.13), where the energy function is just the Lagrangian function of the *coupled continuous max-flow model* (2.6), we define its augmented Lagrangian function as follows:

$$L_c(u, p_s, p_t, q, r) = \int_{\Omega} p_s^1 dx + \int_{\Omega} p_s^2 dx + \int_{\Omega} u_1 F_1 dx + \int_{\Omega} u_2 F_2 dx - \frac{c}{2} \|F_1\|^2 - \frac{c}{2} \|F_2\|^2, \quad (2.15)$$

where  $c > 0$ .

By means of the augmented Lagrangian algorithm [36, 37], we propose the *coupled continuous max-flow algorithm* using an augmented optimization scheme. This scheme splits the optimization problem into sub-flow-maximization problems exploiting independent flow variables, thus it can be independently optimized at each  $k$ -th iteration as follows:

1. Maximize  $L_c(u, p_s, p_t, q, r)$  over  $|q_1(x)| \leq \omega_1(x)$  by fixing the other variables, which gives

$$q_1^{k+1} = \arg \max_{|q_1(x)| \leq \omega_1(x)} -\frac{c}{2} \|\text{div } q_1 - T_1^k\|^2,$$

where  $T_1^k = (p_s^1)^k - (p_t^1)^k - r^k + (u_1)^k/c$ . It can be implemented by the one-step gradient-projection:

$$q_1^{k+1} = \text{Proj}_{|q_1(x)| \leq \omega_1(x)}(q_1^k + \alpha \nabla(\text{div } q_1^k - T_1^k)). \quad (2.16)$$

We refer the well-known Chambolle's scheme [38] for its detailed implementation.

2. Maximize  $L_c(u, p_s, p_t, q, r)$  over  $p_s^1(x) \leq D_s^1(x)$  by fixing the other variables, which gives

$$(p_s^1)^{k+1} = \arg \max_{p_s^1(x) \leq D_s^1(x)} \int_{\Omega} p_s^1 dx - \frac{c}{2} \|p_s^1 - G_1^k\|^2,$$

where  $G_1^k = \operatorname{div} q_1^{k+1} + (p_t^1)^k + r^k - (u_1)^k/c$ . It can be solved exactly by:

$$(p_s^1)^{k+1} = \min(G_1^k + 1/c, D_s^1). \quad (2.17)$$

3. Maximize  $L_c(u, p_s, p_t, q, r)$  over  $p_t^1(x) \leq D_t^1(x)$  by fixing the other variables, which gives

$$(p_t^1)^{k+1} = \arg \max_{p_t^1(x) \leq D_t^1(x)} -\frac{c}{2} \|p_t^1 + H_1^k\|^2,$$

where  $H_1^k = \operatorname{div} q_1^{k+1} - (p_s^1)^{k+1} + r^k - (u_1)^k/c$ . It can be solved exactly by:

$$(p_t^1)^{k+1} = \min(-H_1^k, D_t^1). \quad (2.18)$$

4. Following the similar steps as (1)-(3), we maximize  $L_c(u, p_s, p_t, q, r)$  over the flow fields  $(q_2, p_s^2, p_t^2)$ , and compute the new values of  $q_2^{k+1}$ ,  $(p_s^2)^{k+1}$  and  $(p_t^2)^{k+1}$ .

5. Maximize  $L_c(u, p_s, p_t, q, r)$  over the coupled flow field  $|r(x)| \leq \beta$  by fixing the other variables, which gives

$$r^{k+1} = \arg \max_{|r(x)| \leq \beta} -\frac{c}{2} \|r + J_1^k\|^2 - \frac{c}{2} \|r - J_2^k\|^2,$$

where  $J_1^k = \operatorname{div} q_1^{k+1} - (p_s^1)^{k+1} + (p_t^1)^{k+1} - (u_1)^k/c$  and  $J_2^k = \operatorname{div} q_2^{k+1} - (p_s^2)^{k+1} + (p_t^2)^{k+1} - (u_2)^k/c$ .

It can be computed exactly by

$$r^{k+1} = (J_2^k - J_1^k)/2. \quad (2.19)$$

6. Update the labelling function  $u_i^{k+1}(x)$ ,  $i \in \{1, 2\}$ , by

$$u_i^{k+1}(x) = u_i^k(x) - c F_i^{k+1}(x), \quad (2.20)$$

where, by observing (2.11) and (2.12), the function  $F_i^{k+1}(x)$ ,  $i \in \{1, 2\}$ , are computed as below:

$$F_1^{k+1} = \text{div } q_1^{k+1} - (p_s^1)^{k+1} + (p_t^1)^{k+1} + r^{k+1}$$

and

$$F_2^{k+1} = \text{div } q_2^{k+1} - (p_s^2)^{k+1} + (p_t^2)^{k+1} - r^{k+1}.$$

7. Let  $k = k + 1$  and repeat the above steps until convergence.

At each iteration, the two labelling function  $u_1(x)$  and  $u_2(x)$  are changed by the values  $cF_1(x)$  and  $cF_2(x)$  respectively. Hence, we evaluate the average total labelling change per each pixel:

$$\frac{c \left( \int_{\Omega} |F_1| dx + \int_{\Omega} |F_2| dx \right)}{|\Omega|} \leq \delta,$$

where  $|\Omega|$  stands for the total image volume in the unit of voxels and  $\delta > 0$  is the convergence criterion. In this paper, we set  $\delta$  to  $10^{-4}$  for convergence measurements.

The proposed *coupled continuous max-flow algorithm* was implemented using a parallel computing platform (GPGPU), which significantly accelerated the numerical computation.

## 2.4 Experiments

### 2.4.1 Study Subjects

In total, 25 ex-smokers were evaluated including five asymptomatic ex-smokers (ES) and twenty COPD ex-smokers who provided written informed consent to a study protocol approved by Health Canada and a local research ethics board (Appendix H). COPD subjects with a clinical diagnosis were classified according to the Global Initiative for chronic Obstructive Lung Disease (GOLD) criteria as previously described [39]. Subject demographic characteristics are provided in Table 2.1.



Table 2.1: Subject demographic and pulmonary function measurements

	ES/GOLD U	GOLD I/II	GOLD III/IV
Mean(SD)	(n = 9)	(n = 8)	(n = 8)
Age yrs	67(11)	76(6)	71(9)
Male n	3	5	6
BMI kg.m <sup>-2</sup>	28(5)	28(5)	26(4)
Pack yrs	32(14)	38(17)	66(41)
FEV <sub>1</sub> % <sub>pred</sub>	87(23)	72(16)	30(8)
FVC% <sub>pred</sub>	85(24)	96(6)	64(15)
FEV <sub>1</sub> /FVC	78(7)	53(11)	34(4)
TLC% <sub>pred</sub>	101(14)	109(10)	119(14)
RV/TLC	48(11)	41(15)	64(8)
DL <sub>co</sub> % <sub>pred</sub>	74(26)	48(16)	37(9)
VDP(%)	8(4)	18(10)	28(3)

BMI = Body mass index, FEV<sub>1</sub> = Forced expiratory volume in one second, FVC = Forced vital capacity, TLC = Total lung capacity, RV = Residual volume, DL<sub>co</sub> = Diffusing capacity for carbon monoxide, %<sub>pred</sub> = Percent predicted value, VDP= Ventilation defect percent [23].

## 2.4.2 MRI

MRI was performed using a whole-body 3.0 Tesla Discovery MR750 MRI system (General Electric Health Care [GEHC], Milwaukee, WI, USA) with broadband imaging capability [40]. Subjects were instructed to inhale a gas mixture from a 1.0 L Tedlar bag (Jensen Inert Products, Coral Springs, FL, USA) from functional residual capacity (FRC) and image acquisition was performed in coronal plane with a breath-hold maneuver.

For <sup>1</sup>H MRI acquisitions, subjects were scanned in breath-hold inspiration after inhaling 1.0 L medical grade nitrogen (N<sub>2</sub>) (Spectra Gases, Alpha, NJ, USA) from functional residual capacity (FRC). Conventional <sup>1</sup>H MRI was acquired using an eight-channel, transmit/receive whole-body radiofrequency (RF) coil (127 MHz, maximum excitation power 8.0 kW delivered by a narrow-band RF power amplifier, GEHC, Milwaukee, WI, USA), and a 2D multi-slice fast gradient-recalled echo sequence (12 s acquisition time, repetition time (TR) = 4.3 ms, echo time (TE) = 1.2 ms, flip angle = 20°, field of view (FOV) = 40 cm×40 cm, bandwidth = 25 kHz, matrix = 128 (phase encoding) × 80 (frequency encoding), 14–17 slices, slice thickness

= 15 mm, 0 mm gap), as previously described [41]. Auto shimming was used for  $^1\text{H}$  MRI acquisitions (chest region) for the centre slice. The maximum magnetic field gradient strength was 5 G/cm for x,y and z gradients and image distortion compensation was enabled by default. Images were reconstructed from original k-space data using Fourier transforms with Matlab R2013a (The Mathworks Inc., Natick, MA, USA).

For  $^3\text{He}$  MRI acquisition, subjects were instructed to inhale 1.0 L hyperpolarized  $^3\text{He}$  (30-40% polarization, 5 ml/kg of body weight) diluted with medical grade ( $\text{N}_2$ ) (Spectra Gases, Alpha, NJ, USA) from FRC. Static ventilation images were acquired using a single-channel, rigid, linear birdcage transmit/receive elliptical chest coil (Rapid Biomedical, Wuerzburg, Germany, 97.3 MHz, maximum excitation power 3.2 kW delivered by an AMT 3T90 broad-band RF power amplifier (GEHC, Milwaukee, WI, USA)), and a 2D multi-slice fast gradient-recalled echo sequence (10 s acquisition time, TR = 3.8 ms, TE = 1.0 ms, flip angle =  $7^\circ$ , FOV = 40 cm $\times$ 40 cm, bandwidth = 49 kHz, matrix = 128 (phase encoding)  $\times$  80 (frequency encoding), 14–17 sections, slice thickness = 15 mm, 0 mm gap), as previously described [41]. Due to hardware limitation, we used previously determined  $^1\text{H}$  MRI shimming settings for all hyperpolarized gas MRI acquisitions (chest region) for the centre slice. The maximum magnetic field gradient strength was 5 G/cm for for x,y and z gradients and no image distortion compensation was used. Images were reconstructed from original k-space data using Fourier transforms with Matlab R2013a (The Mathworks Inc., Natick, MA, USA).

### 2.4.3 Segmentation Pipeline

The main components of the proposed segmentation pipeline are shown in Fig. 2.3, including image resampling,  $^3\text{He}$  to  $^1\text{H}$  MRI rigid registration, user seeding of representative regions to generate the respective probability density functions (PDF) and max-flow computation with spatial consistency constraint. Here we describe the pipeline in detail.

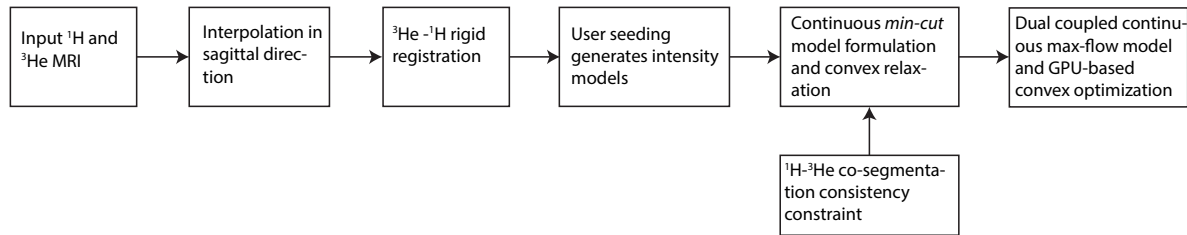


Figure 2.3: Block diagram of the proposed co-segmentation pipeline.

### 2.4.3.1 Pre-processing

The voxel sizes of the original  $^1\text{H}$  and  $^3\text{He}$  MR images were  $3.125 \times 3.125 \times 15 \text{ mm}^3$ . We resampled the original images into approximately isotropic voxels with a size of  $\sim 3 \times 3 \times 3 \text{ mm}^3$  to ensure that the classical 3D total-variational function regularizes along the three directions equally. Prior to segmentation, all  $^3\text{He}$  images were rigidly registered to the associated  $^1\text{H}$  MRI to compensate for potential patient movement during image acquisition procedure. For this purpose we employed a block-matching approach [42] implemented within the *NiftyReg* package [43] using default parameters.

### 2.4.3.2 User Interaction

The proposed algorithm was implemented in Matlab R2013a (The Mathworks Inc., Natick, MA, USA) with a graphical user interface (GUI). The sole user interaction involved was sampling the lung tissue and the background on a single  $^1\text{H}$  and  $^3\text{He}$  MR slices in coronal plane using a 2D brush tool (see Fig. 2.4). Specifically, we selected the coronal slice where the trachea is most obvious or where it is challenging to separate the trachea from the lung cavity, such as when the trachea attaches the lung parenchyma. For normal images, we simply cut the main bronchi to separate it from the lung cavity. In the case of intensity overlap between the bronchi and the lung, we placed seeds on the trachea and/or the main bronchi to ensure that they were separated. The sampled voxels were used: 1) to estimate the PDF of the image intensities for both the lung and the background; 2) as hard constraints, i.e., resulting in minimum

and maximum cost for the object and background labels, respectively, as previously described [44].

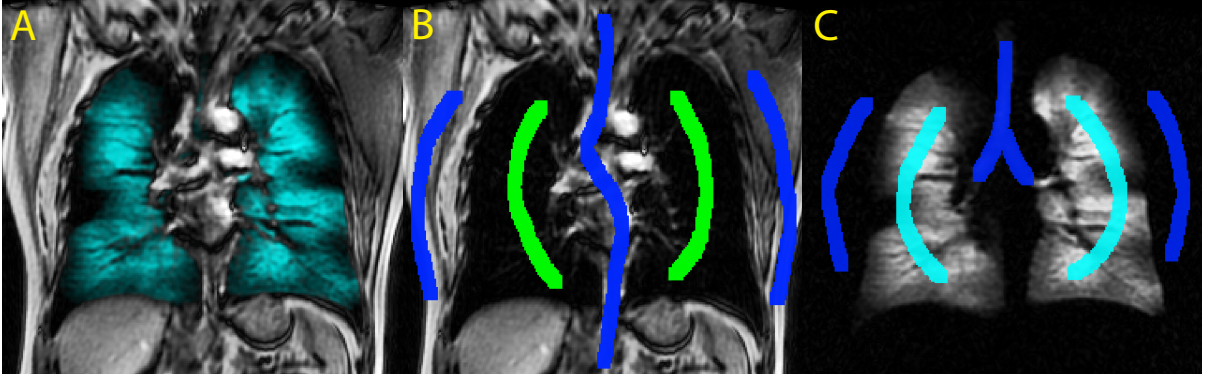


Figure 2.4: User seeds on co-registered  $^3\text{He}$  and  $^1\text{H}$  MRI. A) Combined view of  $^3\text{He}$  (cyan) and  $^1\text{H}$  MRI (grayscale). B) User-defined seeds on  $^1\text{H}$  MRI. C) User-defined seeds on  $^3\text{He}$  MRI.

### 2.4.3.3 Optimization

All computation was performed on a Linux desktop (CentOS 6.5) with 16 G RAM and an Intel(R) Core (TM) i7-3770 CPU running at 3.4 GHz and a GeForce GTX680 GPU (NVIDIA Corp., Santa Clara, CA, USA). Users were asked to place lung and background seeds as shown in Fig. 2.4. Data terms  $D_{s,t}^1$  and  $D_{s,t}^2$  in (2.1) were computed for the  $^1\text{H}$  and  $^3\text{He}$  MR images, respectively. The data terms are designed following a previous method [45], as the cost of assigning a background and foreground label to a voxel  $x$ , such that

$$D_{s,t}^i(x) = -\log h_{s,t}(I_i(x)), \quad i \in \{1, 2\}, \quad (2.21)$$

where  $h_s(I_i(x))$  and  $h_t(I_i(x))$  are the PDF for the background and the lung, respectively. Furthermore, the edge weight function  $\omega_{1,2}(x)$  in (2.5), which penalizes the image gradients such that the segmentation results would be more likely to converge at strong image boundaries, was given as:  $\omega_k(x) = \lambda_1^k + \lambda_2^k \exp(-\lambda_3^k |\nabla I_i(x)|^2)$ ,  $k \in \{1, 2\}$ , where  $\lambda_{1,2,3}^k \geq 0$  can be adjusted by users according to the results. For the duration of the experiments, all parameters were adjusted

heuristically on another three subjects not included in the experiments. Table 2.2 contains all segmentation parameters used in the experiments.

Table 2.2: Parameters for  $^1\text{H}$ - $^3\text{He}$  co-segmentation and  $^1\text{H}$  MRI single segmentation

Parameters	Co-segmentation		Single segmentation
	$^1\text{H}$ MRI	$^3\text{He}$ MRI	$^1\text{H}$ MRI
$\lambda_1$	0.1	0.04	0.15
$\lambda_2$	2.5	0.2	5
$\lambda_3$	90	30	40
$\beta$	1.5		0

See Sec. 2.4.3.3 and (2.4) for the definition of these parameters.

## 2.4.4 Evaluation Methods

The performance of the proposed algorithm was evaluated against manual segmentation performed by an expert observer (SS), who has more than 4 years-experience in pulmonary  $^1\text{H}$  MRI segmentation. Algorithm results were compared with manual outcomes using a mix of region-, volume- and distance-based metrics.

### 2.4.4.1 Region-based Metric

We calculated the Dice-similarity-coefficient ( $DSC$ ) to measure the overlap ratio of manual and algorithm-generated lung masks as follows:

$$DSC = \frac{2(R_M \cap R_A)}{R_M + R_A}, \quad (2.22)$$

where  $R_M$  and  $R_A$  represent the lung masks generated by manual and algorithm segmentation of the same subject, respectively.

### 2.4.4.2 Volume-based Metrics

Let  $V_A$  and  $V_M$  be the lung volumes generated from our algorithm and manual segmentation of the same subject, respectively. Volume accuracy was calculated using total volume error  $\delta V_E$ :

$$\delta V_E = (V_A - V_M), \quad (2.23)$$

and percent volume error  $\delta V_P$ :

$$\delta V_P = \frac{V_A - V_M}{V_M} \times 100\%. \quad (2.24)$$

Absolute total and percent volume errors  $|\delta V_E|$  (2.23) and  $|\delta V_P|$  (2.24) were also computed for direct variance measurements. Univariate relationships of algorithm and manually-generated lung volumes were determined using linear regression ( $r^2$ ) and Pearson correlation coefficients ( $r$ ) with GraphPad Prism version 6.00 (GraphPad Software, San Diego, CA, USA).

### 2.4.4.3 Distance-based Metrics

We also employed root-mean-squared-error (*RMSE*) and maximum absolute distance (*MAXD*) of the two sets of lung surface vertices to measure the agreement of lung surfaces. We denote the manual lung surface  $M$  as a set of vertices  $\{m_i : i = 1, \dots, K\}$  and algorithm lung surface  $A$  as  $\{a_i : i = 1, \dots, N\}$ , where  $K$  and  $N$  are the number of vertices that comprise the manual and algorithm lung surfaces, respectively. Let  $d(m_i, A)$  be the Euclidean distance from a vertex  $m_i$  to the surface  $A$ . *RMSE* and *MAXD* were calculated as follows:

$$RMSE = \sqrt{\frac{1}{K} \sum_{i=1}^K d(m_i, A)^2} \quad (2.25)$$

$$MAXD = \max_{i \in [1, K]} \{d(m_i, A)\}. \quad (2.26)$$

The overall performance of the proposed algorithm in terms of the above metrics was determined by averaging the  $DSC$ ,  $RMSE$ ,  $MAXD$ ,  $\delta V_E$ ,  $\delta V_P$ ,  $|\delta V_E|$  and  $|\delta V_P|$  for each subgroup as well as the entire dataset. In addition, we recorded the runtime for each subject, including pre-processing, user interaction and the following max-flow optimization. We also compared the runtime required by the CPU and GPU-based implementation of the max-flow optimization procedure and reported the mean runtime for all subjects in the dataset.

### 2.4.5 Comparison to Single Modality Segmentation

We assessed the effectiveness of incorporating multi-channel image information by comparing  $^1\text{H}$ - $^3\text{He}$  co-segmentation results with single  $^1\text{H}$  MRI segmentation. For the two comparative algorithms, we optimized the parameters (Table 2.2) independently on the same training subjects. The two methods used exactly identical initializations except the weighting parameter  $\beta$  in (2.5) was set to 1.5 for joint segmentation and 0 for single  $^1\text{H}$  MRI segmentation. The results from the two algorithm segmentation were reported for all the evaluation metrics:  $DSC$ ,  $RMSE$ ,  $MAXD$ ,  $\delta V_E$ ,  $\delta V_P$ ,  $|\delta V_E|$  and  $|\delta V_P|$ .

Paired  $t$ -tests were used to compare the performance of the two algorithms. Normality of data was determined using Shapiro-Wilk tests and when significant, the Mann-Whitney U test for nonparametric data was performed using Statistical Package for the Social Sciences (SPSS version 22, SPSS Inc, Chicago, IL, USA). In addition, a one-way analysis of variance (ANOVA) was performed for statistical comparison of the differences (single  $^1\text{H}$  and joint  $^1\text{H}$ - $^3\text{He}$  segmentation) between the three subgroups. All results were considered significant when the probability of making a type I error was less than 5% ( $p < 0.05$ ).

### 2.4.6 Sensitivity to $^1\text{H}$ - $^3\text{He}$ MRI Registration Error

The proposed co-segmentation algorithm employs complementary features from both  $^1\text{H}$  and  $^3\text{He}$  images, thus requiring them to be properly aligned. To test its robustness to  $^1\text{H}$ - $^3\text{He}$  MRI registration accuracy, which is usually difficult to achieve, we added artificial registration error

to the resultant rigid  $^3\text{He}$ - $^1\text{H}$  MRI transformation. Following [24], we added  $\pm 10\%$  rotation and  $\pm 10\%$  translation perturbation (signs were randomly chosen) to the obtained transformation matrix in the three directions independently for all the subjects, resulting in additional six sets of data with artificially perturbed  $^3\text{He}$ - $^1\text{H}$  rigid registration. We re-calculated all the metrics and compared them with the results before those artificial errors were added.

### 2.4.7 Operator Variability

Our algorithm is near-automated except for the user seeding step. To estimate the segmentation variability, we calculated inter- and intra-operator variability by applying our algorithm to the whole dataset independently randomized for two observers. The two observers performed algorithm segmentation five times [46] on five different days separated by at least 24 hours each to minimize memory bias with independent initializations.

We computed the coefficient-of-variation (*CoV*, calculated as  $\frac{SD}{Mean} * 100\%$ ) and intra-class correlation coefficient (*ICC*) for *DSC* and *RMSE* to evaluate the precision of the algorithm. Intra-*CoV* measures the variability of five repetitions with respect to the mean for a single operator, while inter-*CoV* measures the variability of the repeated measurements between multiple users. *ICC* measures the absolute agreement of different repetitions by computing the proportion of variance between them and was determined using SPSS. In addition, the 95% confidence intervals (*CI*) for *CoV* and *ICC* were also determined.

## 2.5 Results

### 2.5.1 3D Co-Segmentation: Representative Results

Figure 2.5 shows representative co-segmentation results for a COPD GOLD II subject (57 yr male,  $FEV_1 = 72\%_{pred}$ ,  $FEV_1/FVC = 62\%$ ). The associated  $^3\text{He}$  images are shown in Fig. 2.4A and 2.4C. Figure 2.5A shows the segmented anterior to posterior lung slices and Fig.



2.4B shows the segmented lung rendered in 3D.

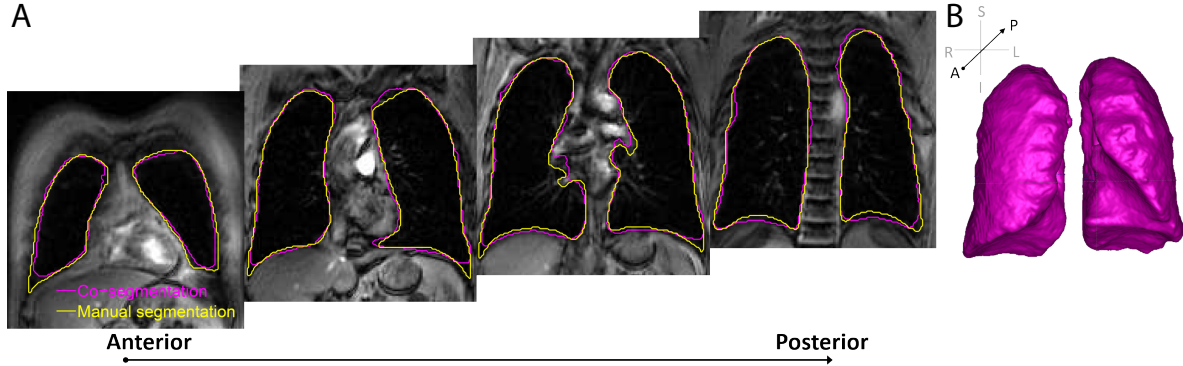


Figure 2.5: Representative algorithm co-segmentation for a single COPD subject. A) Three-dimensional co-segmentation results are shown for two-dimensional anterior to posterior slices. B) Co-segmented whole lung volume rendered result. (Yellow: manual segmentation, purple: co-segmentation.  $DSC = 94.3\%$ ,  $RMS E = 3.4$  mm,  $\delta V_E = 0.15$  L,  $\delta V_P = 2.3\%$ )

## 2.5.2 Comparison to Manual Segmentation

The performance of the proposed *coupled continuous max-flow* approach for segmenting the entire database is shown in Table 2.3 and 2.5. The co-segmentation method yielded a mean  $DSC$  of 91.0% for all the subjects. The mean  $DSC$  for the ES/GOLD U, GOLD I/II and GOLD III/IV groups were 90.3%, 91.0% and 91.7%, respectively. For the whole database, the overall  $DSC$  ranged from 78.1% (one subject with very low SNR) to 94.6%. We also observed low  $SD < 4\%$ .

The  $RMSE$  and  $SD$  for all the subjects were 4.3 mm and 0.7 mm, respectively, which are equal to  $\sim 1.4$  and 0.2 times the voxel width (3.125 mm isotropic voxel size). The mean  $RMSE$  ranged from 4.0 mm to 4.5 mm and  $SD$  from 0.5 mm to 0.7 mm for all the subgroups. We observed a slightly increasing trend of  $RMSE$  from ES/GOLD U to GOLD III/IV groups. The mean  $MAXD$  was 21.4 mm and we observed comparable  $MAXD$  for the three groups.

The overall mean  $|\delta V_P|$  was 8.8% and the mean  $|\delta V_E|$  was 0.42 L, compared with the whole lung volume with a typical value of  $\sim 5$ -8 L. In addition, we observed an increasing trend in the generated absolute volume and its percentage errors from ES/GOLD U to GOLD III/IV

Table 2.3: Group-by-group comparison of  $^1\text{H}$  segmentation and  $^1\text{H}$ - $^3\text{He}$  co-segmentation. \* $p < 0.05$ 

	ES/GOLD U (n = 9)		GOLD I/II (n = 8)		GOLD III/IV (n = 8)		p-value			
	$^1\text{H}$ MRI	$^1\text{H}$ - $^3\text{He}$ MRI	Difference	$^1\text{H}$ MRI	$^1\text{H}$ - $^3\text{He}$ MRI	Difference		$^1\text{H}$ MRI	$^1\text{H}$ - $^3\text{He}$ MRI	Difference
<i>DSC</i> (%)	89.2±2.3	90.3±3.9*	-1.1±3.5	88.8±1.9	91.0±1.7*	-2.2±1.8	90.0±1.7	91.7±1.8*	-1.7±1.9	0.015
<i>RMS E</i> (mm)	5.3±1.0	4.0±0.7*	1.3±1.0	5.7±0.6	4.3±0.5*	1.4±0.6	5.6±0.9	4.5±0.7*	1.1±0.7	0.017
<i>MAXD</i> (mm)	25.5±5.7	21.4±6.3*	4.1±5.1	26.4±3.6	21.5±3.2*	4.9±4.1	26.6±6.3	21.5±5.1*	5.1±7.0	0.487
$ \delta V_E $ (L)	0.57±0.28	0.25±0.19*	0.32±0.29	0.72±0.24	0.39±0.30*	0.33±0.33	0.84±0.39	0.64±0.30*	0.20±0.33	0.013
$ \delta V_P $ (%)	13.7±6.3	6.3±4.9*	7.5±6.1	15.7±5.9	8.4±6.5*	7.3±7.3	15.4±7.0	11.9±6.2*	3.4±5.6	<0.0001
$\delta V_E$ (L)	0.57±0.29	-0.05±0.30*	0.61±0.44	0.72±0.24	0.26±0.41*	0.46±0.36	0.77±0.51	0.64±0.30*	0.13±0.43	<0.0001
$\delta V_P$ (%)	13.7±6.5	-0.9±7.9*	14.6±10.9	15.7±5.9	5.8±8.8*	9.8±7.7	14.3±9.0	11.9±6.2*	2.3±7.3	<0.0001

DSC: Dice-similarity-coefficient; RMSE: Root-mean-squared-error; MAXD: Maximum absolute distance;  $\delta V_E$ : Volume error;  $\delta V_P$ : Percent volume error;  $|\delta V_E|$ : Absolute volume error;  $|\delta V_P|$ : Absolute percent volume error.

Table 2.4: Evaluation of  $^3\text{He}$ - $^1\text{H}$  registration accuracy on algorithm performance

	<i>DSC</i> (%)	<i>RMS E</i> (mm)	<i>MAXD</i> (mm)	$ \delta V_E $ (L)	$ \delta V_P $ (%)	$\delta V_E$ (L)	$\delta V_P$ (%)
±10% <i>Rot.x err.</i>	90.97±2.75	4.27±0.71	21.44±5.05	0.42±0.31	8.75±6.29	0.27±0.44	5.35±9.36
±10% <i>Rot.y err.</i>	90.98±2.74	4.27±0.71	21.44±5.01	0.42±0.31	8.74±6.29	0.27±0.44	5.38±9.33
±10% <i>Rot.z err.</i>	90.98±2.75	4.27±0.71	21.44±5.07	0.42±0.31	8.73±6.28	0.27±0.44	5.35±9.34
±10% <i>Trans.x err.</i>	90.98±2.75	4.27±0.71	21.41±5.05	0.42±0.31	8.74±6.30	0.27±0.44	5.35±9.37
±10% <i>Trans.y err.</i>	90.99±2.75	4.27±0.71	21.42±5.07	0.42±0.31	8.70±6.28	0.27±0.44	5.36±9.31
±10% <i>Trans.z err.</i>	90.97±2.75	4.27±0.71	21.50±5.01	0.42±0.31	8.75±6.29	0.27±0.44	5.36±9.36
Mean	90.98±2.74	4.27±0.71	21.44±5.03	0.42±0.31	8.74±6.28	0.27±0.44	5.36±9.33

*Rot.x, y, z err.*: artificial rotation error added to the base  $^3\text{He}$ - $^1\text{H}$  registration in  $x, y, z$  directions, respectively; *Trans.x, y, z err.*: artificial translation error added to the base  $^3\text{He}$ - $^1\text{H}$  registration in  $x, y, z$  directions, respectively.

DSC: Dice-similarity-coefficient; RMSE: Root-mean-squared-error; MAXD: Maximum absolute distance;  $\delta V_E$ : Volume error;  $\delta V_P$ : Percent volume error;  $|\delta V_E|$ : Absolute volume error;  $|\delta V_P|$ : Absolute percent volume error.

Table 2.5: Co-segmentation and single  $^1\text{H}$  MRI segmentation performance.  $*p < 0.0001$ 

Segmentation	$^1\text{H}$ MRI	$^1\text{H}$ - $^3\text{He}$ MRI
<i>DS C</i> (%)	89.3±2.0	<b>91.0±2.8*</b>
<i>RMS E</i> (mm)	5.5±0.9	<b>4.3±0.7*</b>
<i>MAX D</i> (mm)	26.1±5.3	<b>21.4±5.1*</b>
$ \delta V_E $ (L)	0.70±0.33	<b>0.42±0.31*</b>
$ \delta V_P $ (%)	14.9±6.4	<b>8.8±6.3*</b>
$\delta V_E$ (L)	0.68±0.37	<b>0.27±0.44*</b>
$\delta V_P$ (%)	14.5±7.2	<b>5.4 ±9.4*</b>

groups. The obtained volume errors were on average of 0.27 L or 5.4%, suggesting slightly higher lung volumes generated by the proposed method.

The Pearson correlation coefficients and the 95% *CI* for algorithm and manually-generated lung volumes were also calculated for each group and the whole dataset, as shown in Table 2.6. The algorithm-generated lung volumes for subgroups and the whole dataset were significantly correlated with manual reference standard ( $r$ : 0.90–0.94,  $p < 0.0001$ ) (see Table 2.6 and Fig. 2.6A). In addition, Bland-Altman analysis, shown in Fig. 2.6B, showed a bias of 0.27 L for algorithm-generated lung volumes.

Table 2.6: Relationship of algorithm and manually-generated lung volumes by subject subgroup

	ES/GOLD U (n = 9)	GOLD I/II (n = 8)	GOLD III/IV (n = 8)	All (n = 25)
Pearson $r$	0.94	0.90	0.92	0.94
95% <i>CI</i>	0.92 - 0.96	0.85 - 0.94	0.87 - 0.95	0.92 - 0.95
$p$ -value	<0.0001	<0.0001	<0.0001	<0.0001

We also performed expert manual segmentation on multiple occasions and these were used as the reference standard, and evaluated manual segmentation variability using a one-way ANOVA. Specifically, the same expert (SS) manually segmented the same 25 subjects on three occasions separated by at least 48 hours, resulting in three sets of algorithm segmentation results (Round1-3), shown in Table 2.7. As shown in Table 2.7, there were no significant differences for the multiple expert manual segmentation results ( $p > 0.05$ ). Additionally, we altered the co-segmentation parameters  $\lambda_{1,2,3}$  (for  $^1\text{H}$  MRI),  $\lambda_{1,2,3}$  (for  $^3\text{He}$  MRI) and  $\beta$ , as shown in

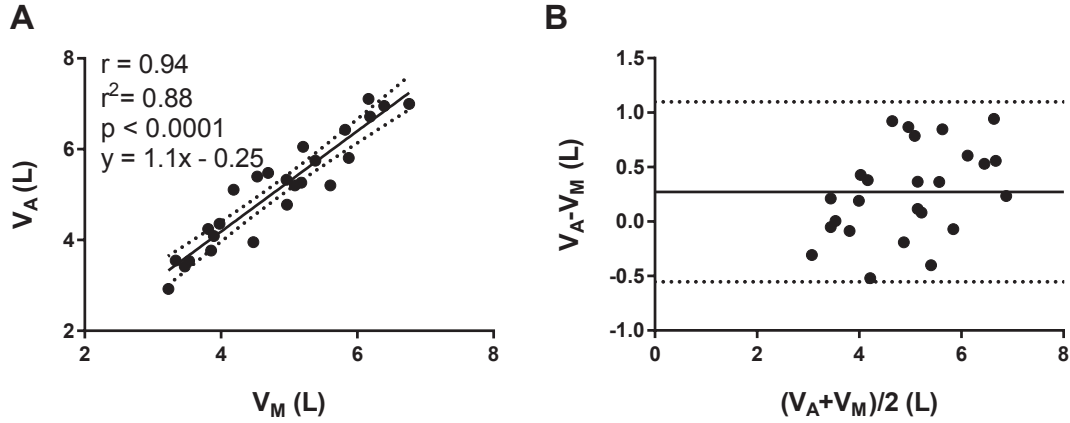


Figure 2.6: Relationship and agreement of algorithm- ( $V_A$ ) and manually- ( $V_M$ ) generated lung volumes. A) Linear correlation of algorithm- and manually-generated lung volumes. B) Bland-Altman plots of algorithm- and manually-generated lung volumes, *solid line* indicates the mean difference and *dotted lines* represent the 95% limits of agreement.

Table 2.2, by  $\pm 40\%$ ,  $\pm 15\%$ ,  $\pm 10\%$ ,  $\pm 40\%$ ,  $\pm 50\%$ ,  $\pm 30\%$  and  $\pm 25\%$ , respectively, and applied the algorithm to a random round of initialization by one user. We altered one parameter at a time while keeping the others fixed and measured the change of  $DSC$  ( $\Delta DSC$ ). We obtained  $\Delta DSC$  of 0.14%, 0.09%, 0.06%, 0.09%, 0.02%, 0.03% and 0.02% for the above parameter changes, respectively.

Table 2.7: Impact of manual segmentation: co-segmentation results based on three rounds of manual segmentation

Segmentation	Round1	Round2	Round3	p-value
$DSC$ (%)	91.0 $\pm$ 2.8	91.1 $\pm$ 2.6	91.2 $\pm$ 2.6	0.73
$RMSE$ (mm)	4.3 $\pm$ 0.7	4.2 $\pm$ 0.7	4.2 $\pm$ 0.6	0.35
$MAXD$ (mm)	21.4 $\pm$ 5.1	21.6 $\pm$ 4.9	21.4 $\pm$ 5.4	0.79
$ \delta V_E $ (L)	0.42 $\pm$ 0.31	0.40 $\pm$ 0.29	0.36 $\pm$ 0.26	0.07
$ \delta V_P $ (%)	8.8 $\pm$ 6.3	8.3 $\pm$ 5.9	7.5 $\pm$ 5.3	0.06
$\delta V_E$ (L)	0.27 $\pm$ 0.44	0.22 $\pm$ 0.44	0.20 $\pm$ 0.40	0.22
$\delta V_P$ (%)	5.4 $\pm$ 9.4	4.2 $\pm$ 9.2	4.0 $\pm$ 8.3	0.21

### 2.5.3 Comparison to Single Modality Segmentation

Comparative results of the proposed  $^1\text{H}$ - $^3\text{He}$  MRI co-segmentation method and single  $^1\text{H}$  MRI segmentation for each subgroup and the whole group are shown in Table 2.3 and 2.5, respectively. The co-segmentation yielded significantly different accuracy measurements than segmentation that employed only  $^1\text{H}$  MRI information (see Table 2.3 and 2.5, all  $p < 0.05$ ). For example, the mean  $DSC$  and  $RMSE$  for co-segmentation were  $91.0 \pm 2.8\%$  and  $4.3 \pm 0.7$  mm, respectively, compared with  $89.3 \pm 2.0\%$  and  $5.5 \pm 0.9$  mm from single  $^1\text{H}$  MRI segmentation. ANOVA results show that the differences between single and co-segmentation for the three subgroups are significantly different (except in terms of  $MAXD$ ). For example, we calculated  $\delta V_P$  of 14.6%, 9.8% and 2.3% for ES/GOLD U, GOLD I/II and GOLD III/IV groups, respectively.  $\delta V_E$  follows the same trend.

Both segmentation methods yielded positive total and percent volume errors, suggesting a systematically greater lung volumes for algorithm segmentation. However, this effect was less obvious in the proposed co-segmentation method. Representative cases are shown in Fig. 2.5A, where  $^1\text{H}$  MRI segmentation presents leakage in the superior lung area and we observed that the co-segmentation-generated boundaries are closer to the manual reference standard.

### 2.5.4 Influence of $^1\text{H}$ - $^3\text{He}$ MRI Registration on Co-Segmentation

Co-segmentation results with artificial registration errors added to the base  $^1\text{H}$ - $^3\text{He}$  transformation matrix are shown in Table 2.4. Small differences were observed for the additional six sets of results compared with base co-segmentation outcomes, none of which were significantly different. In addition, small differences were observed between the six sets of results. These results suggest that the proposed algorithm is robust to certain  $^3\text{He}$ - $^1\text{H}$  registration error.

### 2.5.5 Operator Variability

Quantitative assessment of algorithm segmentation variability is shown in Table 2.8. As can be seen, the *CoV* are small and the *ICC* are high. For example, for Observer1, we obtained for *DSC*: *CoV* of 0.6% and *ICC* of 0.975, for *RMSE*: *CoV* of 3.7% and *ICC* of 0.985. In addition, the absolute agreement between the two observers was also high with a small variance, i.e., inter- *CoV* and *ICC* for *DSC* were 0.7% and 0.990, respectively.

Table 2.8: Intra and inter-observer variability

	Observer1	Observer2	Inter-observer
<i>DSC</i> (%)	90.8±2.6	91.1±2.9	91.0±2.8
<i>CoV</i> (%)	0.6	0.6	0.7
<i>ICC</i>	0.975	0.992	0.990
<i>RMSE</i> (mm)	4.4±0.8	4.2±0.7	4.3±0.7
<i>CoV</i> (%)	3.6	4.8	5.1
<i>ICC</i>	0.985	0.977	0.988

### 2.5.6 Computation Time

Initialization of our approach included rigid registration  $^3\text{He}$  and  $^1\text{H}$  MRI and user interactions in the form of placing seeds on the object and background for the two images using a Matlab GUI. The mean time required for initialization was approximately 20 s, including  $\sim 15$  s for  $^1\text{H}$  and  $^3\text{He}$  MRI registration and less than 5s for user seeding. Table 2.9 compares the runtime for manual, CPU and GPU-based implementation of the co-segmentation method.

Table 2.9: Time required for manual segmentation and partial runtime (s) for co-segmentation algorithm

Segmentation	Manual	CPU-based	GPU-based
Rigid registration	N/A	$\sim 15$	$\sim 15$
User seeding	N/A	$\sim 5$	$\sim 5$
Max-flow optimization	N/A	$\sim 40$	$\sim 5$
Total	$\sim 1000$	$\sim 60$	$\sim 25$

## 2.6 Discussion

We developed an approach to segmenting the lung from both  $^1\text{H}$  and  $^3\text{He}$  MR images by properly imposing the spatial consistency between the lung of two input MR images, which generated a spatially continuous co-segmentation model. We studied the challenging combinatorial optimization problem of the proposed continuous co-segmentation model by means of convex relaxation, for which we introduced a convex dual formulation, namely the coupled continuous max-flow model, and derived a coupled continuous max-flow algorithm based on a multiplier augmented scheme. We showed that the convex relaxed optimization model solves the original combinatorial optimization problem globally and exactly, and is much simpler to optimize in mathematics. Experimental results demonstrated that the proposed approach achieved great advantages in terms of high accuracy, low user interaction and variability, high computational efficiency and robustness to inaccurate  $^1\text{H}$ - $^3\text{He}$  MRI registration.

### 2.6.1 Accuracy

Comparing co-segmentation with expert manual segmentation, the proposed method agreed with manual results and yielded comparable performance for patient groups with progressive disease states. For example, *DSC* for all subgroups were greater than 90% with small *SD*. We observed slightly higher to lower accuracy in terms of mean *RMSE* and volume errors from ES/GOLD U to GOLD III/IV groups. This might be explained by the fact that  $^3\text{He}$  images become more and more incomplete with the progression of pulmonary disease severity, thus providing less useful information for the co-segmentation algorithm, resulting in degradation of the segmentation accuracy. Due to the nature of the proposed co-segmentation algorithm, which incorporates useful features from both images, the more complete the images are, the more useful image information they provide and hence the more accurate the results would be. The obtained results from the proposed algorithm demonstrated the correlation of  $^3\text{He}$ -derived lung function and that measured according to the GOLD criterion. In fact, this relation was

investigated by [20], suggesting that our results are in agreement.

*RMSE* and *MAXD* report the surface agreement between algorithm and manual lung segmentation. The mean *RMSE* ranged from 4.0 mm to 4.5 mm for all groups with an overall mean of 4.3 mm for the whole patient group. Considering the  $3 \times 3 \times 3 \text{ mm}^3$  voxels, the *RMSE* was less than 1.5 times in-plane voxel width. The surface agreement for each group followed a similar trend as *DSC*, and the same reason above applies. We observed that the main surface disagreement occurs in the regions where both high curvature structures from  $^1\text{H}$  MRI and insufficient functional information from  $^3\text{He}$  images are present. For example, the costophrenic presents high curvature in  $^1\text{H}$  MRI (Fig. 2.4B) and less information from  $^3\text{He}$  images (Fig. 2.4A), resulting in under-segmentation shown in Fig. 2.5A. However, the true edges could also be successfully segmented in regions with strong features from both images, even with weak boundaries or high curvatures (see the cardiac notch in Fig. 2.5A).

The volume errors and their percentages as well as the absolute values were relatively low (Table 2.5). The overall positive  $\delta V_E$  and  $\delta V_P$  indicate a systematic lung volume difference of 0.27 L between algorithm and expert manual segmentation. Considering that a typical lung volume is 5–8 L, these errors are likely clinically acceptable. In addition, we observed that the major volume difference occurred at the most posterior and/or anterior slices, where there is little image information contained and the image quality is generally poor. Because these regions are so difficult to segment manually, it is not clear that more user interaction (i.e., more seeds in these regions) will be helpful. We anticipate that, by removing these most posterior and/or anterior slices, the differences in the algorithm and manually-generated volumes would decrease significantly. It is also important to note that these slices typically make a small contribution to the total volume and therefore their removal may be clinically acceptable.

We evaluated manual observer segmentation variability and these results show that on the basis of three rounds of segmentation (Table 2.7), there were no significant differences and this reproducibility was used as the reference for algorithm performance evaluation. In addition, the small variation of *DSC* ( $\Delta DSC$ ) suggests that  $\lambda_{1,2,3}$  and  $\beta$  in Table 2.2 are not sensitive to



co-segmentation results.

### 2.6.2 Co-Segmentation vs Single Segmentation

The proposed co-segmentation algorithm enforced the spatial consistency between the two lung and thus generated results similar to the manual reference standard. The results from the proposed co-segmentation approach and single segmentation are provided in Table 2.3 and 2.5. These data suggests significant improvements in accuracy ( $p < 0.05$ ) for the co-segmentation approach. This may stem from the incorporation of image information from multiple channels that facilitated localizing the true boundaries that are not available using either channel alone. In this study,  $^3\text{He}$  information was used in a complementary fashion to assist  $^1\text{H}$  segmentation especially in challenging regions (i.e., the hilum and mediastinum), that are plagued by image artifacts stemming from cardiac movement and blood flow. On the other hand for  $^3\text{He}$  MRI, the hilum and mediastinum is relatively easily segmented because the boundaries are very clear given that there is no  $^3\text{He}$  signal in the heart. Even in COPD subjects with peripheral ventilation defects,  $^3\text{He}$  information in the hilum and mediastinum contributed to  $^1\text{H}$  MRI segmentation improvements. In fact, we investigated the region-specific influence of  $^3\text{He}$  information by placing a bounding box over the mediastinum/hilum region in the centre slices (in the coronal plane) in  $^1\text{H}$  MRI. The same bounding box was then mapped to  $^1\text{H}$  MRI manual segmentation,  $^1\text{H}$ - $^3\text{He}$  co-segmentation as well as  $^1\text{H}$  MRI single segmentation masks. We calculated  $DSC$  inside and outside the bounding box for both co-segmentation and single  $^1\text{H}$  MRI segmentation, resulting in four sets of  $DSC$ s ( $DSC_{co}^{in}$ ,  $DSC_H^{in}$ ,  $DSC_{co}^{out}$ , and  $DSC_H^{out}$ ). These data was used to determine the regional improvements and showed an overall improvement of  $\sim 1.5\%$  inside the bounding box and  $\sim 0.2\%$  outside the bounding box in terms of  $DSC$  (data not shown). In addition, the improvement inside the bounding box was significantly greater ( $p < 0.05$ ) than that outside the bounding box, and this is consistent with the notion of greater  $^3\text{He}$  MRI segmentation influence in the mediastinum/hilum region.

We also recognize that with disease progression (i.e., more numerous and larger functional

defects), there might be “confounding” lung boundaries when using the proposed approach. Therefore here, we weighted the contribution of  $^1\text{H}$  MRI segmentation energy (E1, (2.1)),  $^3\text{He}$  MRI segmentation energy (E2, (2.1)) and the dissimilarity term (E3, (2.2)) to the total energy (2.3) so that we can properly make use of  $^3\text{He}$  image features to facilitate but not degrade the segmentation. In fact, our measurements showed that E1, E2 and E3 account for  $81.07\pm 0.28\%$ ,  $18.86\pm 0.29\%$  and  $0.06\pm 0.06\%$  of the total energy, respectively, which means that  $^3\text{He}$  segmentation, as expected was complementary, did not dominate. Additionally, this “confounding” effect can be controlled in a few ways: 1) for user interaction with high level prior knowledge applied on  $^3\text{He}$  images, we not only place seeds on ventilated regions but also on defect regions; 2) the soft constraint parameter  $\beta$  in (2.3) can be learned and adjusted to ensure the dissimilarity of two segmented lung volumes, which means that the segmented lung from  $^1\text{H}$  and  $^3\text{He}$  images can be different. Similarly, the weight of E1, E2 and E3 to the total energy can also be learned and adjusted; 3) we can also penalize the difference between  $^1\text{H}$  and weighted  $^3\text{He}$  segmentation based on  $^3\text{He}$  image signal intensity, which will be in our future work. In fact, our experiments exploited patient subgroups with wide range of disease states. The mean ventilation defect percent measured using the method previously described by [23] was 8%, 18% and 28%, respectively. Although the improvement in segmentation decreased in the patients subgroups with more severe functional defects, which is expected, they are significant. This provides evidence to support the use of functional information for  $^1\text{H}$  MRI segmentation.

### 2.6.3 Influence of Pre-Registration for Co-Segmentation

The proposed co-segmentation requires that the two input images are properly aligned. However, registration itself is usually problematic. Moreover, acceptable registration often accompanies high computation cost, resulting in lower efficiency, especially when high resolution images are being generated. In fact, the  $^3\text{He}$ - $^1\text{H}$  MRI registration in this study is particularly challenging and few investigations have been contributed. The proposed approach, using the

default settings for the simple rigid registration provided by *NiftyReg*, aims to compensate for patient movement during image acquisition and avoids distortion introduced by affine or deformable registration approaches. We want to emphasize that the proposed approach does not require accurate registration as a prerequisite (see Table 2.4 for details). This is reflected in the soft constraint (2.2) that tolerates while penalizes the differences between individual segmentation, and the strength can be adjusted.

### 2.6.4 Reproducibility

The proposed method was highly reproducible in terms of *DSC* and *RMSE* (see Table 2.8 for details). The *CoV* of *DSC* within and between users were low ( $< 0.7\%$ ), suggesting the robustness toward the operator-specific biases. The *ICC* for all measurements were high, i.e.,  $> 0.975$ , indicating high absolute agreement between multiple measurements. Since our algorithm is not fully automated, the reproducibility is of great importance especially for multi-center and longitudinal clinical trials. The results in Table 2.8 indicate low user variability and high agreement between different repetitions, users and initializations, suggesting that our algorithm is robust to repetitions and easy to use, and requiring less expertise and workload for radiologists, compared with manual segmentation.

### 2.6.5 Runtime

The proposed algorithm was implemented using non-optimized Matlab code. The GPU-based implementation required  $\sim 25$  s to segment a pair of input  $^1\text{H}$  and  $^3\text{He}$  images, from which  $\sim 5$  s (20%) was used for computing the co-segmentation on GPU and the remaining 80% was used for  $^1\text{H}$ - $^3\text{He}$  image registration ( $\sim 60\%$ ) and user initialization ( $\sim 20\%$ ). The efficiency of our algorithm can be further improved, for example, using optimized Matlab built-in function, advanced C/C++ language, etc.. We want to emphasize that the runtime for the GPU-implemented algorithm can also be further improved by employing more advanced hardware, i.e., modern CPU and GPU, which are now economically available. In addition,  $\sim 60\%$  of the

time was spent on  $^1\text{H}$ - $^3\text{He}$  MRI rigid registration [42], which is inherently parallelable, thus improvement of the overall computation efficiency is possible. Currently, our approach requires very little observer interaction in order to improve speed and workflow. However, because both precision and accuracy are important for clinical applications, we want to emphasize that further user interaction involving high level prior knowledge, which may increase the time for image processing, might be useful to improve the performance.

### 2.6.6 Comparison to Previous Studies

$^1\text{H}$  MRI lung segmentation was previously reviewed [47] and typically, region, edge and model-based methods were used and validated. There are a number of limitations related to these methods that have motivated our work. For example, while most MRI is now acquired in 3D, these methods were often performed using two dimensional slices. However, nearly a generation ago, a 3D model-based method [17] was also developed, although boundary differences ( $\sim 10$  mm) and runtime (2–20 min) were substantial and not compatible with efficient clinical workflow. Over a decade ago, merging of multiple snakes method [19] was developed and showed that both smooth and sharp edges were preserved, but this was restricted to homogeneous regions in 2D. Another approach that incorporated grey level thresholding and morphological operations [12] achieved an average Jaccard index of about 0.82. Unfortunately however, because of intrinsic physiological and hardware variability [48], MR images cannot be processed based exclusively on signal intensities. The combined neural network and active contour method [18] also required extensive training and updating with careful expert manual segmentation. The template-based method [22] was highly novel and used unbiased shape/intensity template construction, statistical lung shape descriptions and level set segmentation in 3D. Although promising, performance was not reported. We developed the proposed algorithm to try to address the limitations of these previous approaches.

## 2.7 Conclusion

We developed a global optimization based approach to jointly segment the lung cavity from pulmonary  $^1\text{H}$  and  $^3\text{He}$  MRI. We evaluated the performance of the proposed approach on a clinical dataset of 25 subjects across a wide range of COPD GOLD stages. Experimental results showed that the proposed approach made efficient use of useful image features from multiple imaging channels and provided high computational efficiency, good agreement with expert manual segmentation and high reproducibility with low user interaction. Therefore, our approach might be suitable for evaluation of lung diseases using multi-modality imaging components, providing the potential for a better understanding of the bio-mechanical and physiological abnormalities in subjects with respiratory disease.

## Bibliography

- [1] Colin D Mathers, Doris Ma Fat, and JT Boerma. *The global burden of disease: 2004 update*. World Health Organization, 2008.
- [2] A Sonia Buist, Mary Ann McBurnie, William M Vollmer, Suzanne Gillespie, Peter Burney, David M Mannino, Ana Menezes, Sean D Sullivan, Todd A Lee, Kevin B Weiss, et al. International variation in the prevalence of COPD (the BOLD study): a population-based prevalence study. *The Lancet*, 370(9589):741–750, 2007.
- [3] Michal Bednarek, Janusz Maciejewski, Maria Wozniak, Pawel Kuca, and Jan Zielinski. Prevalence, severity and underdiagnosis of COPD in the primary care setting. *Thorax*, 63(5):402–407, 2008.
- [4] Sean Fain, Mark L Schiebler, David G McCormack, and Grace Parraga. Imaging of lung function using hyperpolarized helium-3 magnetic resonance imaging: Review of current

- and emerging translational methods and applications. *Journal of Magnetic Resonance Imaging*, 32(6):1398–1408, 2010.
- [5] Brett A Simon, David W Kaczka, Alexander A Bankier, and Grace Parraga. What can computed tomography and magnetic resonance imaging tell us about ventilation? *Journal of Applied Physiology*, 113(4):647–657, 2012.
- [6] Miranda Kirby, Lindsay Mathew, Mohammadreza Heydarian, Roya Etemad-Rezai, David G McCormack, and Grace Parraga. Chronic obstructive pulmonary disease: quantification of bronchodilator effects by using hyperpolarized  $^3\text{He}$  MR imaging. *Radiology*, 261(1):283–292, 2011.
- [7] CJ Bergin, JM Pauly, and A Macovski. Lung parenchyma: projection reconstruction MR imaging. *Radiology*, 179(3):777–781, 1991.
- [8] Colleen J Bergin, Gary M Glover, and John Pauly. Magnetic resonance imaging of lung parenchyma. *Journal of thoracic imaging*, 8(1):12–17, 1993.
- [9] Alireza Osareh and Bitra Shadgar. A segmentation method of lung cavities using region aided geometric snakes. *Journal of medical systems*, 34(4):419–433, 2010.
- [10] Renato Seiji Tavares, André Kubagawa Sato, M de Sales Guerra Tsuzuki, Toshiyuki Gotoh, Seiichiro Kagei, and Tae Iwasawa. Temporal segmentation of lung region MR image sequences using hough transform. In *Engineering in Medicine and Biology Society (EMBC), 2010 Annual International Conference of the IEEE*, pages 4789–4792. IEEE, 2010.
- [11] Renato Seiji Tavares, José Miguel Manzanares Chirinos, Leonardo Ishida Abe, Toshiyuki Gotoh, Seiichiro Kagei, Tae Iwasawa, and M de Sales Guerra Tsuzuki. Temporal segmentation of lung region from MRI sequences using multiple active contours. In *Engineering in Medicine and Biology Society, EMBC, 2011 Annual International Conference of the IEEE*, pages 7985–7988. IEEE, 2011.

- [12] William F Sensakovic, Samuel G Armato III, Adam Starkey, and Philip Caligiuri. Automated lung segmentation of diseased and artifact-corrupted magnetic resonance sections. *Medical physics*, 33:3085, 2006.
- [13] Heinz-Peter W Schlemmer, Bernd J Pichler, Matthias Schmand, Ziad Burbar, Christian Michel, Ralf Ladebeck, Kirstin Jattke, David Townsend, Claude Nahmias, Pradeep K Jacob, et al. Simultaneous MR/PET imaging of the human brain: Feasibility study1. *Radiology*, 248(3):1028–1035, 2008.
- [14] Alun J Lucas, Robert C Hawkes, Pedro Guerra, Richard E Ansorge, Robert E Nutt, John C Clark, Tim D Fryer, and T Adrian Carpenter. Development of a combined micro PET-MR system. In *Nuclear Science Symposium Conference Record, 2006. IEEE*, volume 4, pages 2345–2348. IEEE, 2006.
- [15] Ora Israel, Maya Mor, Diana Gaitini, Zohar Keidar, Luda Guralnik, Ahuva Engel, Alex Frenkel, Rachel Bar-Shalom, and Abraham Kuten. Combined functional and structural evaluation of cancer patients with a hybrid camera-based PET/CT system using 18f-fdg. *Journal of Nuclear Medicine*, 43(9):1129–1136, 2002.
- [16] LP Clarke, RP Velthuisen, MA Camacho, JJ Heine, M Vaidyanathan, LO Hall, RW Thatcher, and ML Silbiger. MRI segmentation: methods and applications. *Magnetic resonance imaging*, 13(3):343–368, 1995.
- [17] Boudewijn P. F. Lelieveldt, Rob J van der Geest, M Ramze Rezaee, Johan G. Bosch, and Johan H. C. Reiber. Anatomical model matching with fuzzy implicit surfaces for segmentation of thoracic volume scans. *Medical Imaging, IEEE Transactions on*, 18(3):218–230, 1999.
- [18] Ian Middleton and Robert I Damper. Segmentation of magnetic resonance images using a combination of neural networks and active contour models. *Medical engineering & physics*, 26(1):71–86, 2004.

- [19] Nilanjan Ray, Scott T. Acton, Talissa Altes, Eduard E. De Lange, James R. Brookeman, and S. T. Acton. Merging parametric active contours within homogeneous image regions for MRI-based lung segmentation. *IEEE Transactions on Medical Imaging*, 22:189–199, 2003.
- [20] Neil Woodhouse, Jim M Wild, Martyn NJ Paley, Stanislaw Fichelle, Zead Said, Andrew J Swift, and Edwin JR van Beek. Combined helium-3/proton magnetic resonance imaging measurement of ventilated lung volumes in smokers compared to never-smokers. *Journal of magnetic resonance imaging*, 21(4):365–369, 2005.
- [21] Nicholas J Tustison, Talissa A Altes, Gang Song, Eduard E de Lange, John P Mugler, and James C Gee. Feature analysis of hyperpolarized helium-3 pulmonary MRI: A study of asthmatics versus nonasthmatics. *Magnetic Resonance in Medicine*, 63(6):1448–1455, 2010.
- [22] Nicholas J Tustison, Brian B Avants, Lucia Flors, Talissa A Altes, Eduard E de Lange, John P Mugler, and James C Gee. Ventilation-based segmentation of the lungs using hyperpolarized  $^3\text{He}$  MRI. *Journal of Magnetic Resonance Imaging*, 34(4):831–841, 2011.
- [23] Miranda Kirby, Mohammadreza Heydarian, Sarah Svenningsen, Andrew Wheatley, David G McCormack, Roya Etemad-Rezai, and Grace Parraga. Hyperpolarized  $^3\text{He}$  magnetic resonance functional imaging semiautomated segmentation. *Academic radiology*, 19(2):141–152, 2012.
- [24] Q. Song, J. Bai, D. Han, S. Bhatia, W. Sun, W. Rockey, J. E. Bayouth, J. M. Buatti, and X. Wu. Optimal co-segmentation of tumor in PET-CT images with context information. *IEEE Trans Med Imaging*, 32(9):1685–1697, Sep 2013.
- [25] Yuri Boykov and Vladimir Kolmogorov. An experimental comparison of min-cut/max-flow algorithms for energy minimization in vision. *Pattern Analysis and Machine Intelligence, IEEE Transactions on*, 26(9):1124–1137, 2004.



- [26] Yuri Boykov and Vladimir Kolmogorov. Computing geodesics and minimal surfaces via graph cuts. In *Computer Vision, 2003. Proceedings. Ninth IEEE International Conference on*, pages 26–33. IEEE, 2003.
- [27] Thomas Pock, Antonin Chambolle, Daniel Cremers, and Horst Bischof. A convex relaxation approach for computing minimal partitions. In *Computer Vision and Pattern Recognition, 2009. CVPR 2009. IEEE Conference on*, pages 810–817. IEEE, 2009.
- [28] Pushmeet Kohli, M Pawan Kumar, and Philip HS Torr.  $P^3$  & beyond: Move making algorithms for solving higher order functions. *Pattern Analysis and Machine Intelligence, IEEE Transactions on*, 31(9):1645–1656, 2009.
- [29] Maria Klodt, Thomas Schoenemann, Kalin Kolev, Marek Schikora, and Daniel Cremers. An experimental comparison of discrete and continuous shape optimization methods. In *Computer Vision–ECCV 2008*, pages 332–345. Springer, 2008.
- [30] Claudia Nieuwenhuis, Eno Töppe, and Daniel Cremers. A survey and comparison of discrete and continuous multi-label optimization approaches for the potts model. *International journal of computer vision*, 104(3):223–240, 2013.
- [31] Cyrus Nambakhsh, Jing Yuan, Kumaradevan Punithakumar, Aashish Goela, Martin Rajchl, Terry M Peters, and Ismail Ben Ayed. Left ventricle segmentation in MRI via convex relaxed distribution matching. *Medical image analysis*, 17(8):1010–1024, 2013.
- [32] Jing Yuan, Eranga Ukwatta, Wu Qiu, Martin Rajchl, Yue Sun, Xue-Cheng Tai, and Aaron Fenster. Jointly segmenting prostate zones in 3D MRIs by globally optimized coupled level-sets. In *Energy Minimization Methods in Computer Vision and Pattern Recognition*, pages 12–25. Springer, 2013.
- [33] Tony F Chan, Selim Esedoglu, and Mila Nikolova. Algorithms for finding global minimizers of image segmentation and denoising models. *SIAM Journal on Applied Mathematics*, 66(5):1632–1648, 2006.

- [34] Jing Yuan, Egil Bae, and Xue-Cheng Tai. A study on continuous max-flow and min-cut approaches. In *Computer Vision and Pattern Recognition (CVPR), 2010 IEEE Conference on*, pages 2217–2224. IEEE, 2010.
- [35] Eranga Ukwatta, Jing Yuan, Wu Qiu, Martin Rajchl, Bernard Chiu, Shadi Shavakh, Jianrong Xu, and Aaron Fenster. Joint segmentation of 3D femoral lumen and outer wall surfaces from MR images. In *International Conference on Medical Image Computing and Computer-Assisted Intervention*, pages 534–541. Springer, 2013.
- [36] D. P. Bertsekas. *Nonlinear Programming*. Athena Scientific, September 1999.
- [37] Jing Yuan, Egil Bae, Xue-Cheng Tai, and Yuri Boykov. A spatially continuous max-flow and min-cut framework for binary labeling problems. *Numerische Mathematik*, 126(3):559–587, 2014.
- [38] Antonin Chambolle. An algorithm for total variation minimization and applications. *Journal of Mathematical imaging and vision*, 20(1-2):89–97, 2004.
- [39] Klaus F Rabe, Suzanne Hurd, Antonio Anzueto, Peter J Barnes, Sonia A Buist, Peter Calverley, Yoshinosuke Fukuchi, Christine Jenkins, Roberto Rodriguez-Roisin, Chris van Weel, et al. Global strategy for the diagnosis, management, and prevention of chronic obstructive pulmonary disease: GOLD executive summary. *American journal of respiratory and critical care medicine*, 176(6):532–555, 2007.
- [40] Grace Parraga, Alexei Ouriadov, Andrea Evans, Shayna McKay, Wilfred W Lam, Aaron Fenster, Roya Etemad-Rezai, David McCormack, and Giles Santyr. Hyperpolarized  $^3\text{He}$  ventilation defects and apparent diffusion coefficients in chronic obstructive pulmonary disease: preliminary results at 3.0 tesla. *Investigative radiology*, 42(6):384–391, 2007.
- [41] Miranda Kirby, Sarah Svenningsen, Amir Owrangi, Andrew Wheatley, Adam Farag, Alexei Ouriadov, Giles E Santyr, Roya Etemad-Rezai, Harvey O Coxson, David G Mc-

- Cormack, et al. Hyperpolarized  $^3\text{He}$  and  $^{129}\text{Xe}$  MR imaging in healthy volunteers and patients with chronic obstructive pulmonary disease. *Radiology*, 265(2):600–610, 2012.
- [42] Sébastien Ourselin, Alexis Roche, Gérard Subsol, Xavier Pennec, and Nicholas Ayache. Reconstructing a 3D structure from serial histological sections. *Image and vision computing*, 19(1):25–31, 2001.
- [43] Marc Modat, Gerard R Ridgway, Zeike A Taylor, Manja Lehmann, Josephine Barnes, David J Hawkes, Nick C Fox, and Sébastien Ourselin. Fast free-form deformation using graphics processing units. *Computer methods and programs in biomedicine*, 98(3):278–284, 2010.
- [44] Eranga Ukwatta, Jing Yuan, Martin Rajchl, Wu Qiu, David Tessier, and Aaron Fenster. 3-D carotid multi-region MRI segmentation by globally optimal evolution of coupled surfaces. *Medical Imaging, IEEE Transactions on*, 32(4):770–785, 2013.
- [45] Yuri Y Boykov and M-P Jolly. Interactive graph cuts for optimal boundary & region segmentation of objects in ND images. In *Computer Vision, 2001. ICCV 2001. Proceedings. Eighth IEEE International Conference on*, volume 1, pages 105–112. IEEE, 2001.
- [46] SD Walter, M Eliasziw, and A Donner. Sample size and optimal designs for reliability studies. *Statistics in medicine*, 17(1):101–110, 1998.
- [47] William F Sensakovic and Samuel G Armato III. Magnetic resonance imaging of the lung: automated segmentation methods. In *General Methods and Overviews, Lung Carcinoma and Prostate Carcinoma*, pages 219–234. Springer, 2008.
- [48] Philip J Robinson and Louis Kreel. Pulmonary tissue attenuation with computed tomography: comparison of inspiration and expiration scans. *Journal of computer assisted tomography*, 3(6):740–hyhen, 1979.

## Chapter 3

# Anatomical Pulmonary Magnetic Resonance Imaging Segmentation for Regional Structure-Function Measurements of Asthma

*<sup>1</sup>H (free-breathing and ultra-short echo-time) MRI provides new hopes for lung disease care but lung segmentation is generally required for <sup>1</sup>H MR image analysis and quantification of the derived structural-functional information. Here we developed and evaluated a segmentation approach that treated the left and right lung separately and integrated the prior knowledge about the relative size of the two lung to facilitate <sup>1</sup>H MRI lung segmentation.*

*The contents of this chapter were previously published in Medical Physics: F Guo, S Svenningsen, RL Eddy, DPI Capaldi, K Sheikh, A Fenster and G Parraga. Anatomical pulmonary magnetic resonance imaging segmentation for regional structure-function measurements of asthma. Medical physics 43.6 (2016): 2911-2926. Permission to reproduce this article was granted by John Wiley and Sons and is provided in Appendix G.*

### 3.1 Introduction

Asthma is a common chronic respiratory disease that affects ~300 million people worldwide and this is estimated to increase to ~400 million by 2025 [1]. Currently, spirometry mea-

surements are widely-used for asthma diagnosis and for monitoring disease progression and response to treatment [2]. Recently, pulmonary imaging measurements have shown that the pathophysiological characteristics of asthma are regionally heterogeneous [3, 4]. This is important because current clinical measurements like the forced expiratory volume in 1 s (FEV<sub>1</sub>) provide a global lung function measurements without regard to regional differences. It is perhaps for this reason that FEV<sub>1</sub> is weakly predictive of treatment response, disease progression and patient outcomes in obstructive lung disease [5].

Pulmonary imaging methods, including x-ray computed tomography (CT) [6, 7, 8], nuclear medicine [9, 10], and magnetic resonance imaging (MRI) [11, 12] have been developed as non-invasive ways to visualize the structural and functional abnormalities in asthma. In contrast to x-ray CT and nuclear medicine methods, MRI, including conventional <sup>1</sup>H MRI, noble gas [12, 13]/oxygen enhanced [14] MRI, Fourier Decomposition (FD) [15, 16, 17] and short/ultra-short echo-time (UTE) MRI [18], provides quantitative, sensitive and regional lung structure and function without the risk that stems from ionizing radiation. Therefore, pulmonary MRI is suitable for intensive, serial and longitudinal studies of asthma.

Anatomical <sup>1</sup>H MRI may be combined with inhaled hyperpolarized noble gas (<sup>3</sup>He and <sup>129</sup>Xe) MRI [11] to quantify regional ventilation abnormalities and these measurements depend on image registration and segmentation techniques [19]. <sup>1</sup>H MRI has also been used to generate biomarkers of segmental inflammatory response after allergen challenge in asthma [20] and to evaluate regional ventilation using image registration [21] and multi-volume MRI techniques[22].

To quantitatively measure the pulmonary structure and function using MRI, segmentation of the thoracic cavity needs to be optimized because this is the first step required. However, as shown in Fig. 3.1, lung segmentation remains challenging due to low tissue and proton density, magnetic susceptibility and inherent motion artifacts [18] that result in poorly defined edges and non-uniformly distributed intensities. In the context of an algorithm pipeline for MRI structure-function biomarker measurements, we think that shape *prior*, including equiva-

lence of topologies, volume/area, dynamic shape priors, size, covariance and other high order moment constraints may be helpful for improving segmentation performance [23, 24]. Therefore, here we developed a new way to rapidly segment pulmonary  $^1\text{H}$  MRI using a convex optimization-based approach that incorporates the left-to-right lung volume proportion as a constraint for simultaneous left and right lung segmentation. We think that the developed segmentation approach is an important step for widespread clinical translation of pulmonary  $^1\text{H}$  MRI.

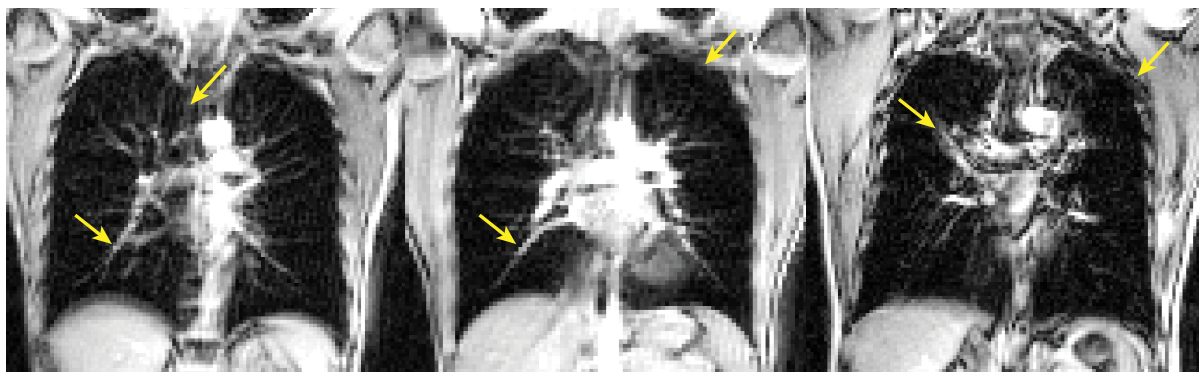


Figure 3.1: Pulmonary  $^1\text{H}$  MRI segmentation challenges. Centre coronal  $^1\text{H}$  MRI slices for three asthma participants with yellow arrows showing representative weak edges and protruding structures.

## 3.2 Materials and Methods

### 3.2.1 Study Subjects and Data Acquisition

Twenty participants including 15 severe poorly-controlled and five mild-to-moderate well-controlled asthmatics provided written informed consent to a protocol that was approved by Health Canada and a local research ethics board (Appendix H). Spirometry and plethysmography were performed using whole-body plethysmography (MedGraphics Corporation, St. Paul, MN, USA) according to the American Thoracic Society guidelines [25].

MR imaging was performed on a whole body 3.0 Tesla MR750 system with broadband

imaging capability (Excite 12.0, GE Healthcare, Milwaukee, WI, USA). Subjects were positioned supine and coronal images were acquired during a breath-hold of 1.0 L medical grade nitrogen ( $N_2$ ) inhaled from a Tedlar bag (Jensen Inert Products, Coral Springs, FL, USA) from functional residual capacity (FRC). Conventional  $^1H$  MRI was performed using an eight-channel, transmit/receive whole-body radiofrequency (RF) coil (127 MHz, maximum excitation power 8.0 kW delivered by a narrow-band RF power amplifier, GEHC, Milwaukee, WI, USA), and a 2D multi-slice fast gradient-recalled echo sequence (FGRE) [26] ( $\sim 10$  s acquisition time, 4.3 ms repetition time, 1.2 ms echo time,  $20^\circ$  flip angle,  $40\text{ cm} \times 40\text{ cm}$  field of view, 25 kHz bandwidth,  $128$  (phase encoding)  $\times 80$  (frequency encoding) matrix, 14–17 slices and 15 mm slice thickness, 0 gap). Auto shimming was used for  $^1H$  MRI acquisitions (chest region) for the centre slice. The maximum magnetic field gradient strength was 5 G/cm for x,y and z gradients and image distortion compensation was enabled by default. Images were reconstructed from original k-space data using Fourier transforms with Matlab R2013a (The Mathworks Inc., Natick, MA, USA).

### 3.2.2 Pulmonary $^1H$ MRI Multi-Region Segmentation with Volume Proportion Prior

We derived a volume proportion preserved Potts model, which is approximated by means of convex relaxation and further represented by a dual volume proportion preserved max-flow model. The derived max-flow model encodes the volume proportion *prior* and leads to a linear programming problem subject to convex and linear equality constraints. Here we describe the algorithm in detail as follows:

#### 3.2.2.1 A Volume Proportion Preserved Potts Model & Convex Relaxation

We denote  $I(x) \in \mathcal{Z}$ ,  $x \in \Omega$ , as a three-dimensional (3D) pulmonary  $^1H$  MR image, where  $\mathcal{Z}$  is the image intensity set,  $\Omega$  is the image domain and  $x$  represents a voxel. We aim to segment the image  $I(x)$  into three mutually disjoint regions: the left lung  $\mathcal{R}_{ll}$ , the right lung  $\mathcal{R}_{rl}$  and the

background  $\mathcal{R}_b$  with the following region layout:

$$\begin{aligned}\Omega &= \mathcal{R}_{ll} \cup \mathcal{R}_{rl} \cup \mathcal{R}_b, \\ \mathcal{R}_{ll} \cap \mathcal{R}_{rl} &= \emptyset, \mathcal{R}_{rl} \cap \mathcal{R}_b = \emptyset, \mathcal{R}_{ll} \cap \mathcal{R}_b = \emptyset.\end{aligned}\tag{3.1}$$

Here we focus on the proportion *prior*, the relative size of the left lung to right lung for pulmonary <sup>1</sup>H MRI segmentation. Such proportion *prior* was previously investigated and demonstrated significant improvements, i.e., accuracy/stability, on natural image sequences [27]. Here, we exploit the proportion *prior* we developed based on the augmented Lagrangian algorithm for the optimization problem. This is important because previous studies have shown that there is a relationship between the left and right lung volumes. Specifically, the study of a group of 78 subjects [28] showed that the right lung was  $\sim 1.13$  times larger than the left lung. Another investigation [29] of lung volumes at different breathing levels showed that the right lung volume was  $\sim 1.1 - 1.18$  times greater than the left lung. In a recent study [30], 99 subjects ranging in physical and physiological conditions were examined and the left lung was shown to be smaller than the right lung by a factor in the range of 1.12 to 1.22 with a mean of 1.18. Additionally, we segmented and validated a separate dataset of 15 randomly selected CT images (acquired at the same lung volume as their associated <sup>1</sup>H MR scans) using Pulmonary Workstation 2.0 (VIDA Diagnosis Inc., Coralville, IA, USA) and observed  $1.16 \pm 0.05$  times smaller left lung than the right lung. Based on these observations, we choose a left-to-right lung volume ratio of 1/1.15 for this study. Therefore, we propose to incorporate the left-to-right lung volume proportion *prior* to assist locating the left lung  $\mathcal{R}_{ll}$  and the right lung  $\mathcal{R}_{rl}$  by penalizing the following function:

$$\alpha \left| |\mathcal{R}_{ll}| - \gamma |\mathcal{R}_{rl}| \right|,\tag{3.2}$$

where  $|\mathcal{R}_{ll}|$  and  $|\mathcal{R}_{rl}|$  represent the volume sizes of the left and right lung, respectively.  $\gamma > 0$  represents the target ratio ( $\sim 1.15$ ) of  $|\mathcal{R}_{ll}|$  and  $|\mathcal{R}_{rl}|$  and  $\alpha > 0$  denotes the soft constraint to



the dissimilarity between the target and measured left-to-right lung volume ratio. Clearly, the introduced volume proportion *prior* (3.2) enforces the measured volume ratio  $|\mathcal{R}_{ll}| / |\mathcal{R}_{rl}|$  to be close to  $\gamma$ , i.e.,  $|\mathcal{R}_{ll}| / |\mathcal{R}_{rl}| \sim \gamma$ .

The Potts model [31] provides a way to segment an image into  $n$  mutually disjoint sub-regions  $\{\mathcal{R}_i : i = 1 \dots n\}$  with minimal labeling cost and surface area in the continuous settings. Using this approach, each voxel is assigned a cost that represents the probability of being assigned a label associated with that region. Here we use the probability density function (PDF)  $\pi_i(\mathcal{I}(x))$ ,  $i \in L = \{ll, rl, b\}$ , to generate the cost  $\rho_i(x)$  for each  $x$  by taking the the log-likelihoods of the respective PDF [32], i.e.,  $\rho_i(x) = -\log(\pi_i(\mathcal{I}(x)))$ ,  $i \in L$ . As such, we propose to segment the left and right lung from the given image  $\mathcal{I}(x)$  by minimizing the total labeling cost while achieving a “tight” total surface area for all the segmentation regions, together with minimizing the difference between the measured and target volume proportion (3.2) as follows

$$\min_{\mathcal{R}_{ll,rl,b}} \sum_{i \in L} \int_{\mathcal{R}_i} \rho_i(x) dx + \sum_{i \in L} \int_{\partial \mathcal{R}_i} ds + \alpha \left| |\mathcal{R}_{ll}| - \gamma |\mathcal{R}_{rl}| \right|, \quad (3.3)$$

subject to the disjoint region layout constraint (3.1).  $\alpha > 0$  weights the contribution of volume proportion difference to the total energy (3.3). In this paper, we call (3.3) the *volume-proportion preserved Potts model*.

Let  $\xi_i(x)$ ,  $i \in L$ , be the characteristic function for the corresponding region  $\mathcal{R}_i$ , such that  $\xi_i(x) = 1$  for  $x \in \mathcal{R}_i$  and 0 otherwise. Accordingly, the region layout (3.1) can be formulated as  $\sum_{i \in L} \xi_i(x) = 1$ ,  $\forall x \in \Omega$ , and the volume proportion constraint (3.2) can be written as

$$\alpha \left| \int_{\Omega} \xi_{ll} dx - \gamma \int_{\Omega} \xi_{rl} dx \right|. \quad (3.4)$$

Therefore, the *volume-proportion preserved Potts model* (3.3) is actually equal to:

$$\min_{\xi_i(x) \in \{0,1\}} \sum_{i \in L} \left\{ \langle \xi_i, \rho_i \rangle + \int_{\Omega} g(x) |\nabla \xi_i| dx \right\} + \alpha \left| \int_{\Omega} \xi_{ll} dx - \gamma \int_{\Omega} \xi_{rl} dx \right|, \quad (3.5)$$

subject to the labeling constraints  $\sum_{i \in L} \xi_i(x) = 1, \forall x \in \Omega$ .  $g(x) \geq 0$  weights the total-variation function  $|\nabla \xi_i|$  and  $\int_{\Omega} g(x) |\nabla \xi_i| dx$  measures the weighted total surface area for each region  $\mathcal{R}_i$ ,  $i \in L$ , which is equivalent to  $\int_{\partial \mathcal{R}_i} ds$  in (3.3).

However, the proposed *volume-proportion preserved Potts model* (3.5) is challenging to optimize because of the non-convex binary representation  $\xi_i(x), i \in L$ , non-smooth total-variation function, and the absolute function term. Previous studies [33, 34] provide a way to approximate the original optimization problem through convex relaxation, i.e.,

$$\min_{\xi_i(x) \in [0,1]} \sum_{i \in L} \left\{ \langle \xi_i, \rho_i \rangle + \int_{\Omega} g(x) |\nabla \xi_i| dx \right\} + \alpha \left| \int_{\Omega} \xi_{ll} dx - \gamma \int_{\Omega} \xi_{rl} dx \right|, \quad (3.6)$$

subject to the linear equality constraint  $\sum_{i \in L} \xi_i(x) = 1, \forall x \in \Omega$ . The binary function  $\xi_i(x) \in \{0, 1\}, i \in L$ , in (3.5) is relaxed to take values in the continuous set  $\xi_i(x) \in [0, 1]$  in (3.6), resulting in the *convex relaxed volume-proportion preserved Potts model*. In the convex domain, mature and robust optimization theories are readily available, and thus the approximated problem (3.6) becomes easier to solve mathematically.

### 3.2.2.2 A Dual Bounded Continuous Max-Flow Model

Here we introduce a continuous max-flow approach that is dual to the *convex relaxed volume-proportion preserved Potts model* (3.6) to solve the optimization problem (3.6).

Based on the conventional continuous max-flow configurations for the classical *Potts model* [31], we configure the proposed continuous max-flow model associated with (3.6) as shown in Fig. 3.2A.

- We added two terminals, the source  $s$  and the sink  $t$  to the flow graph. We put three copies  $\Omega_{ll}$ ,  $\Omega_{rl}$  and  $\Omega_b$  of the image domain  $\Omega$  corresponding to the left lung, right lung and the background in parallel.
- We linked the source terminal  $s$  to the same position  $x$  in  $\Omega_i, i \in L$ , along which an unconstrained flow  $p_s(x)$  was defined; we linked each voxel  $x$  in  $\Omega_i, i \in L$ , to the sink

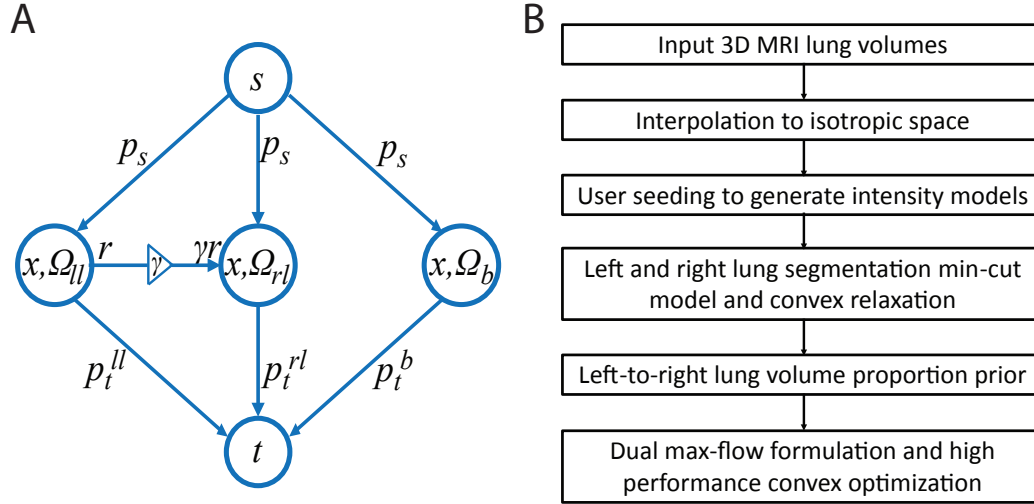


Figure 3.2: The volume-proportion preserved approach and pipeline for pulmonary  $^1\text{H}$  MRI multi-region segmentation. A) Max-flow configuration for the volume-proportion preserved Potts model. B) Pipeline for volume-proportion preserved multi-region  $^1\text{H}$  MRI segmentation.

terminal  $t$ , along which a sink flow  $p_t^i(x), i \in L$ , was directed; moreover, within each  $\Omega_i, i \in L$ , a spatial flow  $q^i(x)$  was specified at  $x$ .

- Additionally, an extra constraint flow  $r(x)$  was directed from  $\Omega_{ll}$ , and amplified by  $\gamma$  to the same position in  $\Omega_{rl}$ .

Note that, the source flow  $p_s(x)$  is the same for  $x \in \Omega_i, i \in L$ , the sink flow fields  $p_t^i(x)$  may be different and the spatial flow fields  $q^i(x)$  may also be different from each  $i$ . Based on the above specified continuous flow “network”, we propose the *volume-proportion preserved continuous max-flow model*, which maximizes the total flow that is allowed to send from the source  $s$ , i.e.,

$$\max_{p_s, p_t, q, r} \int_{\Omega} p_s(x) dx \quad (3.7)$$

which implicitly encodes the volume proportion *prior* subject to:

- *Flow capacity constraints*: The sink flows  $p_t^i(x)$ , the spatial flows  $q^i(x)$  and  $r(x), i \in L$ , suffice:

$$p_t^i(x) \leq \rho_i(x), \quad |q^i(x)| \leq g(x), \quad |r| \leq \alpha; \quad (3.8)$$

- *Flow conservation constraints:* We introduce a residual flow  $p_w^i$ ,  $i \in L$ , to the above flow configurations. Obviously, the total flow vanishes at each  $x$ ,  $\forall x \in \Omega_b$ ,

$$(\operatorname{div} q^b - p_s + p_t^b)(x) = -p_w^b(x) = 0; \quad (3.9)$$

the total flow does not vanish at  $x$ ,  $\forall x \in \Omega_{ll}$ , i.e.,

$$(\operatorname{div} q^{ll} - p_s + p_t^{ll})(x) = -p_w^{ll}(x) = -r; \quad (3.10)$$

the total flow does not vanish at  $x$ ,  $\forall x \in \Omega_{rl}$ , i.e.,

$$(\operatorname{div} q^{rl} - p_s + p_t^{rl})(x) = -p_w^{rl}(x) = \gamma r. \quad (3.11)$$

Clearly, the proposed *volume-proportion preserved continuous max-flow model* (3.7) is different from the classical *continuous max-flow model* [31] in that: the flow residue vanishes at each voxel  $x \in \Omega_b$ ; the flow residue does not vanish at each  $x \in \Omega_{ll}$ , but equals to a constant  $-r$  in the range of  $[-\alpha, \alpha]$ ; the flow residue does not vanish at each  $x \in \Omega_{rl}$ , but equals to a constant  $\gamma r$  in the range of  $[-\gamma\alpha, \gamma\alpha]$ .

We can also prove that the *volume-proportion preserved continuous max-flow model* (3.7) is dual/equivalent to the *convex relaxed volume-proportion preserved Potts model* (3.6). The proof is provide in the Appendix D.

### 3.2.2.3 An Efficient Numerical Solver to The Volume Proportion Preserved Max-Flow Model

Direct optimization of (3.6) is challenging due to the nonlinear and non-smooth terms involved. Through variational analysis we demonstrate that, instead of dealing with the minimization problem (3.6), we can alternatively convert the min-cut problem into its dual flow-maximization form (3.7), a linear programming problem with simple convex and linear con-

constraints. The model (B.4) provides the Lagrangian form of (3.7) with the linear equality constraints (B.1), (B.2), and, (B.3) multiplied by the characteristic function  $\xi_i(x)$ ,  $i \in L$ . Hence, by the theory of augmented multiplier algorithms [35], we can derive an efficient numerical solver to the *volume proportion preserved max-flow model* (3.7). In our implementation, we split the overall optimization problem into a series of simpler sub-problems that can be parallelized within each step. The details of the numerical implementation are provided in Appendix C.

### 3.2.3 Algorithm Implementation

Figure 3.2B shows the main components of the proposed segmentation approach with more details described as follows. Prior to segmentation, we resampled the original FGRE MR images into  $3 \times 3 \times 3$  mm isotropic space using the *Convert3D* command line tools [36] to ensure equal total variation regularization along the three directions. We then loaded the resampled images for graphical view using *ITK-SNAP* [36]. We used the two-dimensional (2D) brush tool to sample the left lung, right lung and the background on a single coronal plane. The coronal slice was chosen when the segmentation was deemed challenging visually, i.e., when the trachea attaches to the lung, prominent protruding structures, weak separation between the left and the right lung, etc.. These user inputs provide the appearance models or the probability density function for respective regions for the algorithm, and importantly incorporate high level knowledge to supervise the segmentation. These sampled voxel set  $S_i(x)$ ,  $i \in \{ll, rl, b\}$ , were used to estimate the respective PDFs  $\pi_i$  following  $\pi_i(z) = \frac{\int_{S_i} K(z-I(x)) dx}{A(S_i)}$ ,  $\forall z \in \mathcal{Z}$ , where  $z$  is the intensity bin and  $A(S_i)$  denotes the size of region  $S_i$ .  $K(x)$  represents the Gaussian kernel function in the form of  $\frac{1}{\sqrt{2\pi\sigma^2}} \exp(-x^2/2\sigma^2)$ , where  $\sigma$  is the kernel width. Figure 3.3 shows three different examples of user seeds and the respective probability density function. Note that the one-voxel wide thin seeds in the top panel of Fig. 3.3 were only used to illustrate the seeding procedure and we used four-voxel wide brushes for our algorithm implementation. We chose four-voxel wide seeds because: 1) the trachea and the tissue between left/right lower lobes, which are challenging to segment, has a similar size and the four-voxel wide brush

can sufficiently sample these regions with less user interaction/variability and saves time; 2) the four-voxel wide seeds can generate intensity models that are more likely to characterize the signal intensities in the lung, and, 3) the algorithm can benefit as the seeds that encode human prior knowledge influence the segmentation of their neighbouring regions. The derived probability density function were then used to generate the labeling cost  $\rho_i$  in (3.3) following [32]. In addition, these seeded regions incorporate high level human knowledge about the object of interest and therefore were hard-constrained to their own labels and excluded from other labels. Such operation offers the flexibility to tackle especially suspicious situations and can be readily and easily implemented in the proposed framework, i.e.,  $\rho_i(x) = 0$ ,  $\rho_j(x) = +\infty$ ,  $\forall x \in S_i$ , where  $\forall i, j \in L, i \neq j$ .

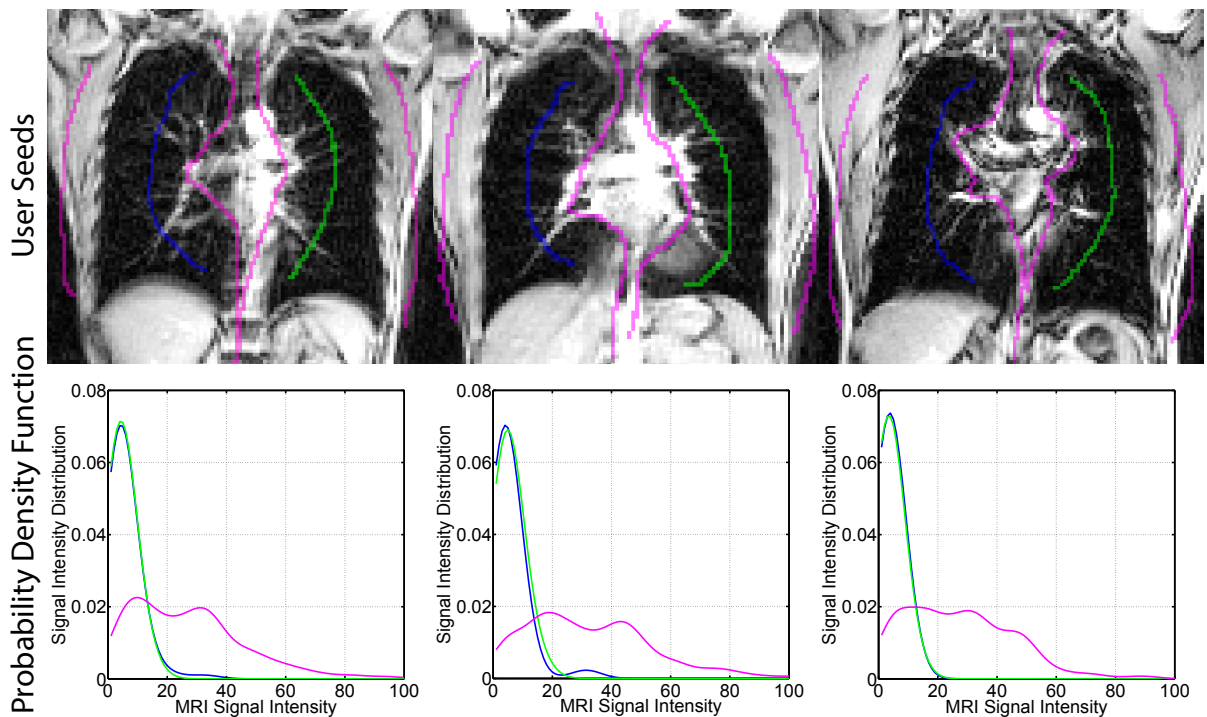


Figure 3.3: Representative user seeds and the generated probability density function for algorithm segmentation for three asthmatic subjects. Top panel: Green, blue and purple lines represent user seeds on the left and right lung and image background. Bottom panel: Corresponding MRI signal intensity distributions shown in colour as demonstrated in the middle panel images.

The surface weight function  $g(x)$  in (3.5) was designed based on image edge information,

i.e.,  $g(x) = \lambda_1 + \lambda_2 * \exp(-\lambda_3 * |\nabla I(x)|)$ , where  $\lambda_{1,2,3} \geq 0$  are scales. We optimized these parameters on a separate training dataset of five asthma subjects and kept them constant throughout the experiments, i.e.,  $\lambda_{1,2,3} = 0.05, 1.0$  and  $80$ , respectively;  $\alpha$  in (3.2) was chosen to be  $0.2$ . With the constructed data  $\rho_i(x)$  and regularization  $g(x)$  terms, we implicitly encoded the left-to-right lung volume proportion *prior* in the max-flow model (3.7). The associated augmented optimization algorithm was parallelized on a graphics card for speed-up.

The algorithm was implemented on a Linux desktop (CentOS 6.5, 16 G RAM) with a CPU (Intel(R) i7-3770, 3.40 GHz) and a GPU (GeForce, GTX 680, NVIDIA Corp., Santa Clara, CA, USA) to parallelize the convex optimizer. The label cost  $\rho_i(x)$ ,  $x \in L = \{ll, rl, b\}$ , and the regularization term  $g(x)$  were calculated on the CPU with Matlab R2013a (The Mathworks Inc., Natick, MA, USA) and the convex optimization was implemented on the GPU with CUDA (CUDA, NVIDIA Corp., Santa Clara, CA, USA). The CPU provides the calculated data and regularization terms to the GPU and the GPU performs parallel implementation of the numerical solver following Appendix C with single precision. We used single precision calculations for algorithm implementation and observed convergence within 300 iterations and convergence error  $< 10^{-4}$ , similar as shown previously [37].

### 3.2.4 Evaluation Methods

Algorithm segmentation was performed by two newly-trained graduate students (blinded to independently randomized dataset) five times each on five different days [38]. We used newly trained graduate students in order to provide a very conservative estimate of algorithm performance. For example, for manual segmentation, observer training and expertise are always required and here this was performed by an expert observer. The two newly trained graduate students who performed algorithm segmentation provided a worst case scenario for algorithm performance and better simulated real-world use in clinical trials at different sites where observer training is often not monitored or controlled. Algorithm segmentation accuracy was evaluated by comparing algorithm outputs to manual reference standard using Dice-similarity-coefficient

(*DSC*), root-mean-squared-error (*RMSE*) of the Euclidean surface distance (the shortest distance from a vertex in the manual surface to the algorithm-generated surface), absolute volume error ( $|\delta V_E|$ ) and absolute percent volume error ( $|\delta V_P|$ , for region-, surface- and volume-based similarity measurements). Manual segmentation was also performed by an expert observer (SS, five years experience in <sup>1</sup>H MRI segmentation) five times on five consecutive days and these were used as five sets of reference standards for algorithm segmentation to compare with. Each of the 10 sets (five for each observer) of algorithm outputs were compared to the multiple manual reference standard, resulting in 10 sets (five for each observer) of algorithm segmentation accuracy measurements. Instead of using multiple reference segmentation, it is also possible to employ simultaneous truth and performance level estimation [39] to estimate a single mean reference standard from multiple reference segmentation. We evaluated all the measurements independently because it helps the reader better understand how each and every measurement was derived and this provides excellent statistical power to detect significant differences. We also reported the mean runtime for the GPU-implemented multi-observer algorithm segmentation to evaluate computational time, and calculated *DSC*, *RMSE*,  $|\delta V_E|$  and  $|\delta V_P|$  for the left (L), right (R) and whole (W) lung. The overall algorithm accuracy was obtained by taking the mean of the 10 sets (five for each observer) of algorithm accuracy measurements for the two observers, which were also used to evaluate algorithm segmentation reproducibility. Both intra- and inter-observer algorithm segmentation variability were evaluated by calculating the coefficient-of-variation (*CoV*) and intra-class correlation coefficient (*ICC*) of the *DSC* and *RMSE* for the L, R and whole lung. *CoV* (calculated as the standard deviation divided by the mean) was used to evaluate the variability among repeated measurements, and *ICC* measures the reliability or the absolute agreement between repeated measurements. We also calculated the smallest detectable difference (*SDD*) [40] of individual and whole lung volumes, which also reflects measurement uncertainty as follows:

$$SDD = Z_{\alpha/2} \sqrt{2} * SEM, \quad (3.12)$$



where  $SEM$  is the standard error of measurement,  $Z_{\alpha/2}$  is determined from the standard normal distribution and corresponds to the chance of mistakenly concluding that change has occurred when it has not (i.e.,  $\alpha = 0.05$  and  $Z_{\alpha/2} = 1.96$ ).

In addition, we compared the multi-region segmentation results with two-region segmentation [41] outcomes. Specifically, the two approaches took the same user initializations as inputs and the two sets of whole lung segmentation were compared with the same expert manual segmentation. The correlation between algorithm and manually-generated lung volumes was measured using Pearson correlation coefficients ( $r$ ) and Bland-Altman analysis with GraphPad Prism version 6.02 (GraphPad Software Inc, San Diego, CA, USA). Two-way random-effects intra-class correlation coefficient ( $ICC$ ) to measure the absolute agreement within and between observers was determined using Statistical Package for the Social Science (SPSS version 23, SPSS Inc., Chicago, IL, USA). Intra- and inter- coefficient-of-variation ( $CoV$ ) were also determined. Both intra- and inter- $ICC$  and  $CoV$  were calculated in terms of  $DSC$  and  $RMSE$ . For paired t-tests, Shapiro- Wilk normality tests were first performed and when the data did not satisfy normal distribution, non-parametric Mann-Whitney U-tests were performed using SPSS. Results were considered significant when the probability of two-tailed type I error was less than 5% ( $p < 0.05$ ). All comparisons were performed for the L, R and whole lung.

## 3.3 Results

### 3.3.1 Subject Demographics

Table 3.1 provides a summary of the demographic characteristics of five mild-to-moderate well-controlled (2 males/3 females,  $28 \pm 6$  years) and 15 severe, poorly-controlled (5 males/10 females,  $47 \pm 13$  years) asthmatics. For the well-controlled subgroup, mean  $FEV_1$  was  $86 \pm 9\%_{pred}$  (range = 73–96% $_{pred}$ ),  $FEV_1/FVC$  was  $83 \pm 7\%$  (range = 75–93%), FRC was  $2.2 \pm 0.6$  L (range = 1.4–2.8 L), and total lung capacity (TLC) was  $5.5 \pm 1.2$  L (range = 4.4–7.1 L). For the severe, poorly-controlled subgroup, mean  $FEV_1$  was  $72 \pm 27\%_{pred}$  (range = 35–115% $_{pred}$ ),  $FEV_1/FVC$

was  $66\pm 17\%$  (range = 37–94%), FRC was  $2.9\pm 0.9$  L (range = 1.5–4.8 L), and TLC was  $5.6\pm 1.6$  L (range = 4.0–9.1 L).

Table 3.1: Subject demographics and pulmonary function measurements

Parameter	All (n = 20)	Well-controlled asthma (n = 5)	Severe, poorly controlled asthma (n = 15)
Mean( $\pm$ SD)			
Age (yr)	42(14)	28(6)	47(13)
Male (n)	7	2	5
BMI ( $\text{kg}\cdot\text{m}^{-2}$ )	28(6)	25(6)	29(6)
FEV <sub>1</sub> ( $\%_{pred}$ )	76(24)	86(9)	72(27)
FVC ( $\%_{pred}$ )	87(16)	88(6)	86(18)
FEV <sub>1</sub> /FVC (%)	70(17)	83(7)	66(17)
IC ( $\%_{pred}$ )	103(24)	108(9)	101(28)
FRC (L)	2.7(0.9)	2.2(0.6)	2.9(0.9)
TLC (L)	5.6(1.4)	5.5(1.2)	5.6(1.6)
TLC ( $\%_{pred}$ )	96(12)	97(8)	96(13)
RV/TLC (%)	34(11)	26(6)	37(11)

Note: BMI = body mass index, FEV<sub>1</sub> = forced expiratory volume in one second, FVC = forced vital capacity, FRC = functional residual capacity, IC = inspiratory capacity, TLC = total lung capacity, RV: residual volume,  $\%_{pred}$ : percent predicted value.

### 3.3.2 Algorithm and Manual Segmentation Measurement Reproducibility

Figure 3.4 shows representative manual and algorithm segmentation results in the coronal, sagittal and axial view as well as 3D rendered lung volumes for the right and left lung. Manual and algorithm segmentation variability for each subject is also provided in Table 3.2. For manual segmentation, the smallest detectable difference for lung volumes were 0.11 L, 0.12 L and 0.22 L for the left, right and whole lung, respectively. In addition, one-way analysis of variance (ANOVA) showed that there was no significant difference between the five sets of manually measured lung volumes ( $p = 0.98$  for L, R, and W). The smallest detectable difference for lung volumes generated using the algorithm was 0.10 L for the left, 0.14 L for the right and 0.24 L for whole lung. Table 3.3 shows that the inter-observer *CoV* for *DSC* between the two observers were 0.5%, 0.6% and 0.5% for the left lung, right lung and whole lung, respectively.

Similarly, the inter-observer *ICC* for *DSC* were 0.99, 0.91 and 0.97 for the L, R and whole lung respectively and there were very similar results for *RMSE*. Table 3.4 provides the *DSC*, *RMSE* for the repeated algorithm segmentation for the two observers.

Table 3.2: Algorithm and manual segmentation reproducibility

Subject	Mean lung volumes five rounds repeated measurement mean(SD)					
	Manual segmentation			Algorithm segmentation		
	<i>L</i>	<i>R</i>	<i>W</i>	<i>L</i> *	<i>R</i> *	<i>W</i> *
S1	1.57(0.02)	1.68(0.05)	3.25(0.07)	1.57(0.00)	1.77(0.01)	3.34(0.01)
S2	2.02(0.03)	2.30(0.03)	4.32(0.07)	1.72(0.07)	2.00(0.12)	3.72(0.18)
S3	1.87(0.03)	2.09(0.11)	3.96(0.14)	1.91(0.02)	2.24(0.03)	4.15(0.05)
S4	1.34(0.03)	1.62(0.02)	2.97(0.05)	1.25(0.03)	1.48(0.03)	2.73(0.06)
S5	1.55(0.04)	1.77(0.04)	3.32(0.07)	1.59(0.01)	1.85(0.02)	3.44(0.03)
S6	1.57(0.04)	1.98(0.06)	3.55(0.10)	1.56(0.01)	1.95(0.01)	3.51(0.02)
S7	1.33(0.05)	1.61(0.02)	2.94(0.06)	1.33(0.02)	1.60(0.04)	2.93(0.06)
S8	2.77(0.06)	2.96(0.05)	5.73(0.10)	2.76(0.04)	3.00(0.06)	5.76(0.09)
S9	1.97(0.02)	2.19(0.02)	4.16(0.03)	2.05(0.04)	2.36(0.05)	4.41(0.08)
S10	1.79(0.03)	1.99(0.04)	3.78(0.06)	1.67(0.03)	1.89(0.07)	3.56(0.09)
S11	2.36(0.06)	2.89(0.03)	5.25(0.08)	2.39(0.03)	2.99(0.08)	5.38(0.09)
S12	1.87(0.03)	2.19(0.04)	4.06(0.07)	1.94(0.04)	2.26(0.05)	4.20(0.09)
S13	1.45(0.02)	1.79(0.01)	3.23(0.03)	1.39(0.06)	1.74(0.06)	3.13(0.12)
S14	1.95(0.06)	2.62(0.05)	4.57(0.10)	2.29(0.01)	2.73(0.03)	5.02(0.03)
S15	1.40(0.03)	1.68(0.03)	3.08(0.06)	1.46(0.01)	1.76(0.01)	3.22(0.01)
S16	1.98(0.03)	2.29(0.02)	4.27(0.05)	2.16(0.06)	2.55(0.07)	4.71(0.12)
S17	1.54(0.01)	1.74(0.03)	3.28(0.05)	1.45(0.03)	1.68(0.02)	3.13(0.06)
S18	1.56(0.07)	1.79(0.04)	3.34(0.10)	1.56(0.07)	1.79(0.07)	3.35(0.13)
S19	1.76(0.02)	2.10(0.03)	3.85(0.05)	1.80(0.04)	2.16(0.05)	3.96(0.08)
S20	2.19(0.05)	2.64(0.06)	4.83(0.11)	2.08(0.02)	2.45(0.02)	4.53(0.04)
<i>SDD</i>	0.11	0.12	0.22	0.10	0.14	0.24

L = left lung, R = right lung, W = whole lung volume.

\*No significant difference between manual and algorithm measurements of left ( $p = 0.6$ ), right ( $p = 0.2$ ) and whole lung ( $p = 0.35$ ) volumes. *SDD*=smallest detectable difference.

### 3.3.3 Multi-region Segmentation and Parameter Sensitivity

In Fig. 3.5, three-region versus two region segmentation are directly compared and paired t- tests showed significant differences when the three-region method was used. For example, *RMSE* decreased by 0.8 mm (or ~17%) ( $p < 0.0001$ ) and absolute volume error decreased by 0.17 L (or ~43%) ( $p < 0.0001$ ) using the three-region approach. In addition, as shown in Fig.

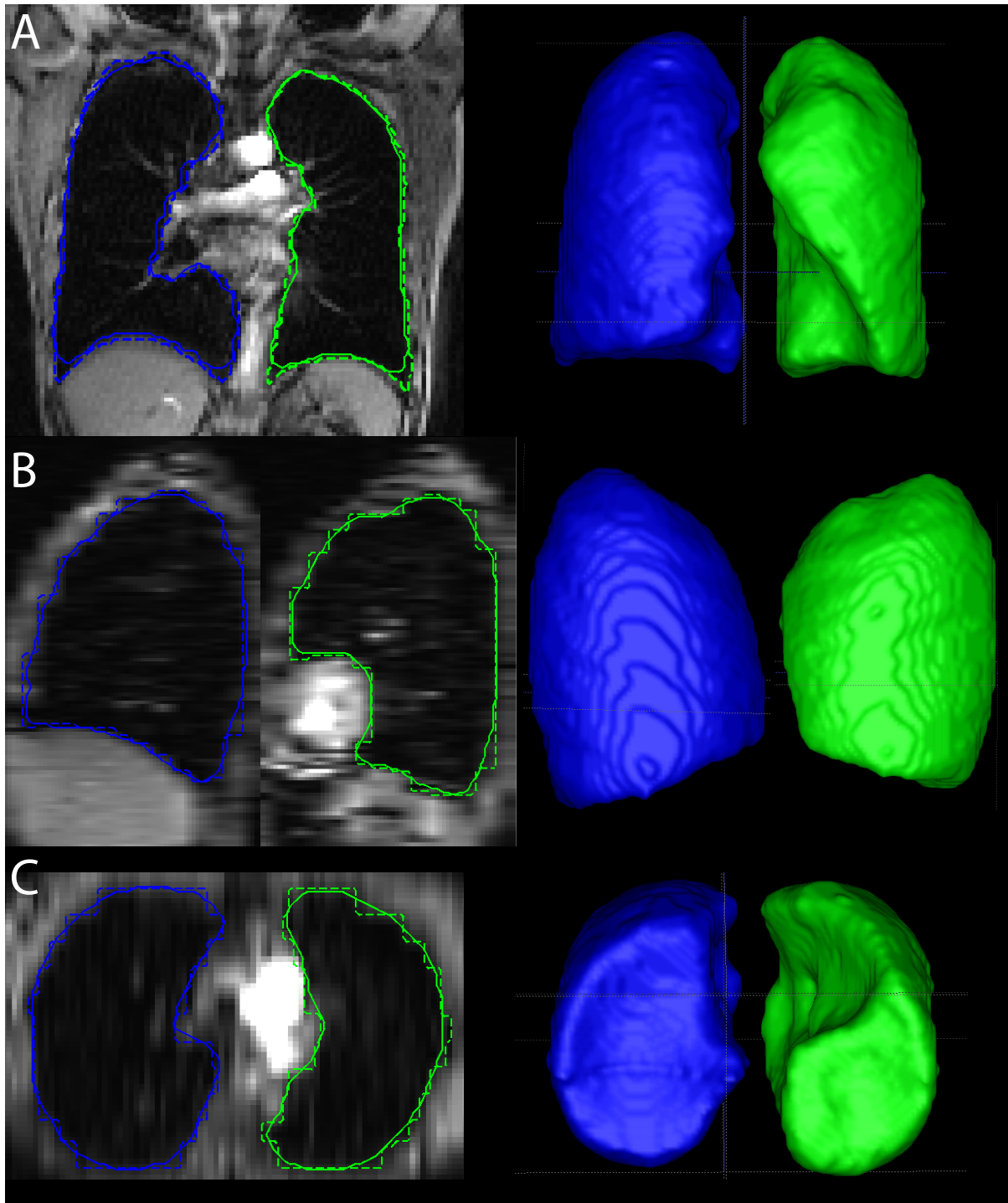


Figure 3.4: Representative  $^1\text{H}$  MRI left (green) and right (blue) lung segmentation results. Solid and dashed lines represent algorithm and manual segmentation, respectively. A) 2D and 3D coronal view of the lung contours and the rendered left and right lung volumes. B) 2D and 3D sagittal view of the lung boundaries and the rendered lung volumes. C) 2D and 3D axial view of the lung contours and the rendered individual lung volumes.

Table 3.3: Dice-similarity-coefficient and *RMSE* reproducibility

	Coefficient-of-variation (%)			Intra-class correlation coefficient		
	Left	Right	Whole	Left	Right	Whole
	Dice-similarity-coefficient					
Observer1	0.3	0.5	0.4	0.99	0.98	0.99
Observer2	0.2	0.4	0.3	0.99	0.98	0.99
Interobserver	0.5	0.6	0.5	0.99	0.91	0.97
	Root-mean-squared-error					
Observer1	3	4	3	0.99	0.98	0.99
Observer2	3	3	3	0.99	0.99	0.99
Interobserver	4	4	4	0.97	0.93	0.96

Table 3.4: Dice-similarity-coefficient and root-mean-squared-error for algorithm segmentation within and between observers

	Dice-similarity-coefficient (%)			Root-mean-squared-error (mm)		
	Left	Right	Whole	Left	Right	Whole
Observer1	90.7(4.0)	91.5(3.4)	91.1(3.5)	4.1(1.1)	4.1(0.8)	4.1(0.8)
Observer2	91.1(3.9)	91.7(3.3)	91.4(3.5)	4.0(1.2)	3.9(0.8)	3.9(0.8)
Interobserver	90.9(2.8)	91.6(1.8)	91.3(2.1)	4.1(1.2)	4.0(0.8)	4.0(0.8)

3.6, results are shown when the parameters ,  $\lambda_{1,2,3}$  and  $\alpha$  are altered by -15%, -10%, -5%, 0%, 5%, 10%, 15% of base values.

### 3.3.4 Relationship and Agreement of Manual and Algorithm Lung Volumes

Pearson correlation coefficients for algorithm and manual lung volumes provided in Fig. 3.7 show strong and significant correlations for algorithm with expert manual measurements ( $r^2$ : 0.89 - 0.91,  $p < 0.0001$ ). As shown using Bland-Altman analysis in Fig. 3.7, the algorithm yielded systematically greater left, right and whole lung volumes (with biases of 0.02 L, 0.04 L and 0.06 L, respectively), but there was no significant difference ( $p = 0.6, 0.2$  and  $0.35$ ) for the left, right and whole lung, respectively (Table 3.2). We also compared algorithm and plethysmography FRC+1 whole lung volumes in Fig. 3.7E) and F) and this showed a relatively strong correlation ( $r = 0.75$ ,  $r^2 = 0.56$ ,  $p = 0.0002$ ) between the two sets of lung volumes. Table

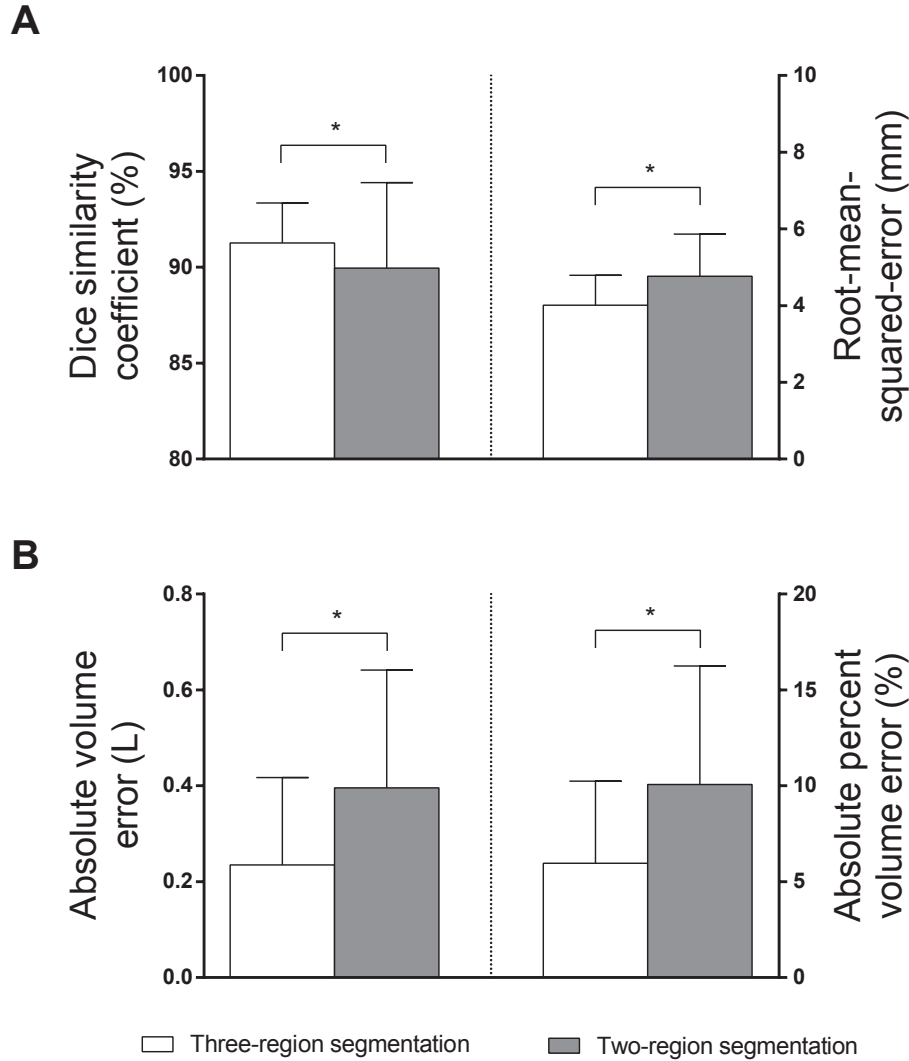


Figure 3.5: Comparison of two and three-region segmentation approach. A) Whole lung Dice-similarity-coefficient and  $RMSE$ , and, B) absolute volume error and absolute percent volume error for the three-region (white) and two-region (gray) segmentation approaches. Values are means for all subjects and error bars are  $SD$ .  $*p < 0.0001$ .

3.5 provides the  $DSC$ ,  $RMSE$  as well as absolute and percent volume error using the repeated manual segmentation measurements as the reference standard.  $DSC$  ranged from 79% to 95% for the left lung (mean  $91 \pm 3\%$ ) and 84% to 94% (mean  $92 \pm 2\%$ ) for the right lung. Similarly, mean  $RMSE$  were  $4 \pm 1$  mm for the left lung and  $4 \pm 1$  mm for the right lung along with a  $4 \pm 1$  mm surface distance error for the whole lung. The absolute and percent volume errors were

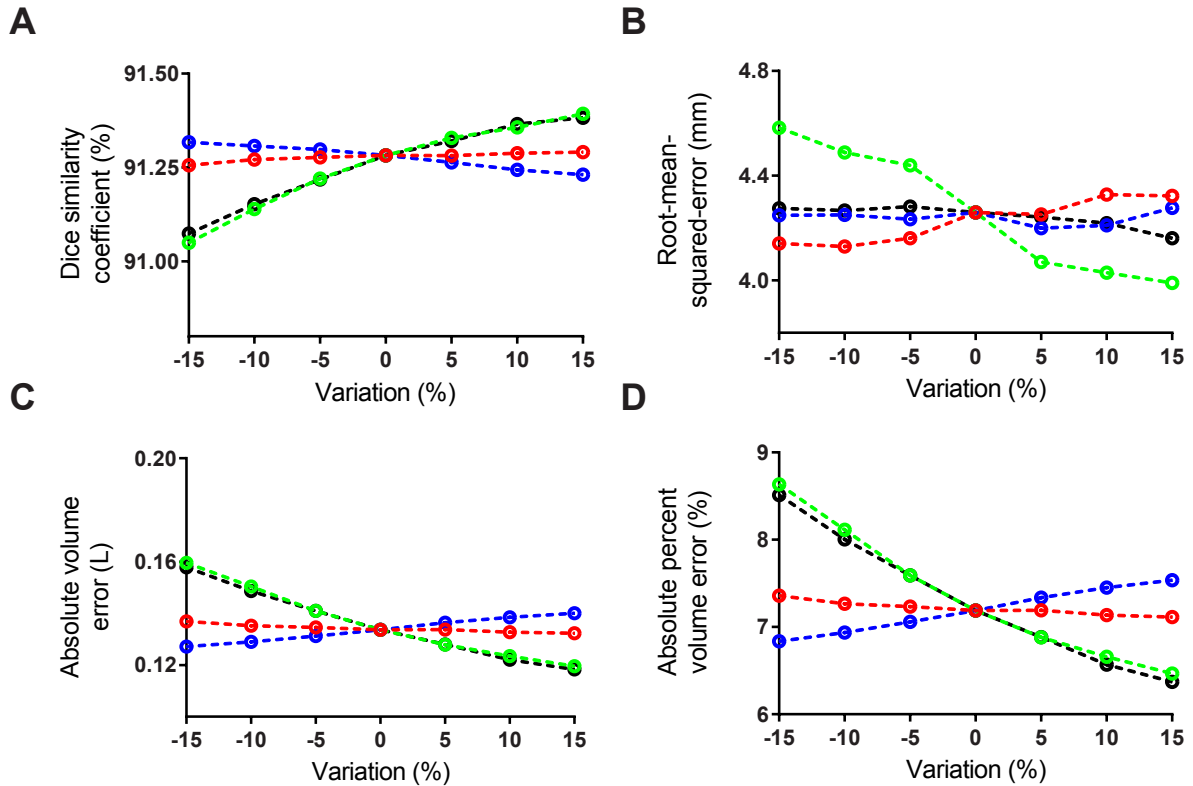


Figure 3.6: Algorithm segmentation parameter sensitivity tests. The optimized parameters ( $\alpha$ : red,  $\lambda_1$ : green,  $\lambda_2$ : blue,  $\lambda_3$ : black ) were changed by -15% ~ 15% and the algorithm segmentation accuracy results are shown in terms of A) *DSC*, B) *RMSE*, C) absolute volume error, and D) absolute percent volume error for the left lung.

0.11 L (6%) for the left lung, 0.13 L (6%) for the right lung, and 0.23 L (6.0%) for whole lung. There was significantly different *DSC* ( $p < 0.0001$ ) and *RMSE* ( $p < 0.0001$ ) for the right lung compared with the left lung.

### 3.3.5 Computation Time

We evaluated algorithm computation time by averaging the runtime for two observers who performed segmentations for all 20 subjects on five different occasions on five consecutive days. The GPU-based implementation required  $3.4 \pm 0.6$  s for convex max-flow optimization in addition to  $6.0 \pm 1.4$  s for user initialization, resulting in a total runtime of approximately 9 s for each segmentation (data not shown). This compares to roughly 30 minutes for manual

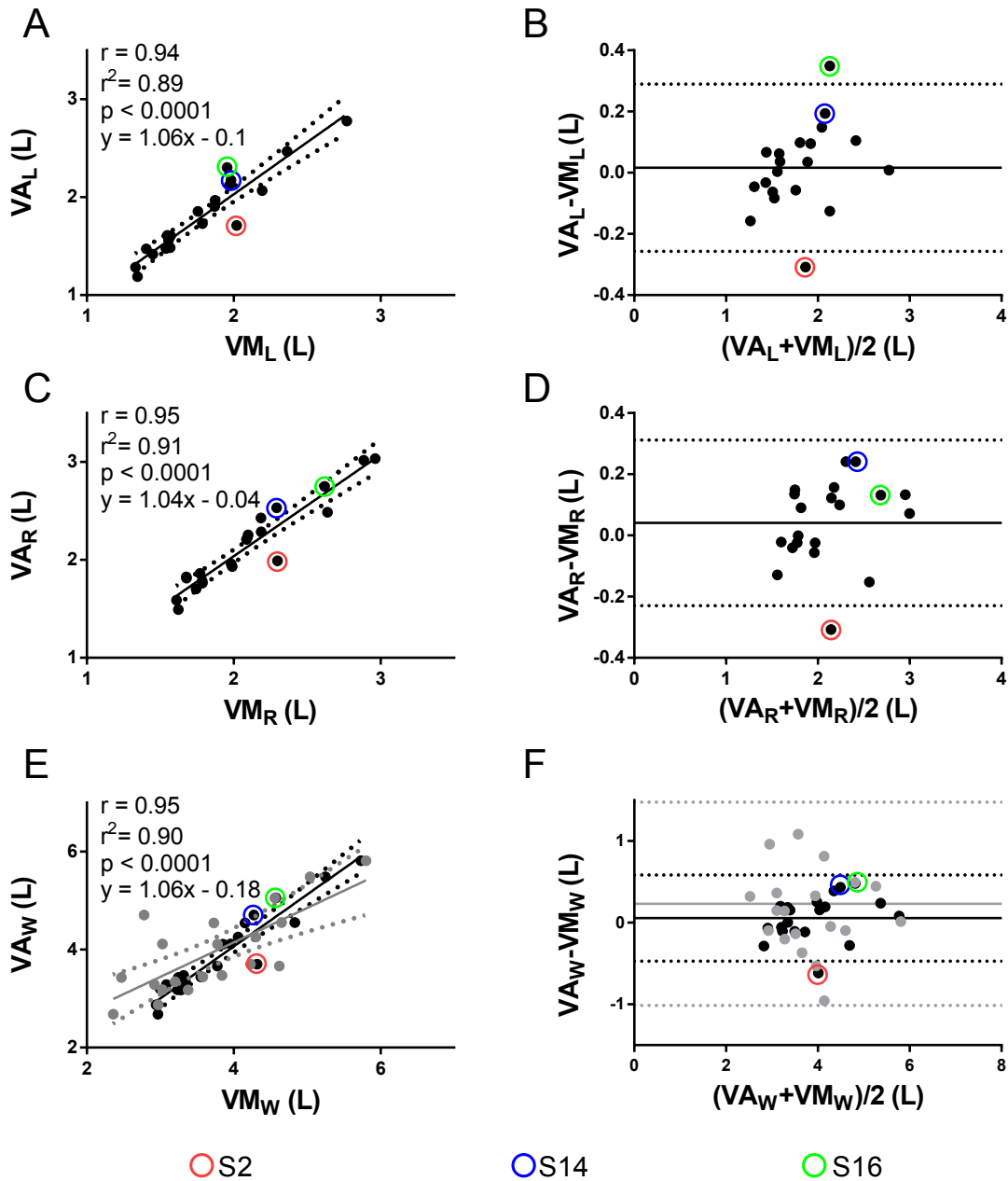


Figure 3.7: Relationships and Agreement for algorithm- and manually-generated Lung volumes. Black dots show linear regression for algorithm- and manually-generated A) left ( $VA_L$  and  $VM_L$ ), C) right ( $VA_R$  and  $VM_R$ ), and, E) whole ( $VA_W$  and  $VM_W$ ) lung volumes. Bland-Altman analysis of agreement is shown for B) left ( $VA_L$  and  $VM_L$ ), D) right ( $VA_R$  and  $VM_R$ ), and, F) whole ( $VA_W$  and  $VM_W$ ) lung. Dotted lines indicate the upper and lower limits and solid lines represent the biases. Coloured circles identify three algorithm to manual lung volume outliers corresponding to S2 (red), S14 (blue) and S16 (green) in Table 2. Gray dots in E) and F) represent the linear correlation ( $r = 0.75$ ,  $p = 0.0002$ ,  $y = 0.7x + 1.33$ ) and Bland-Altman plots for algorithm and plethysmography measured (FRC+1L) lung volume.



measurements and 15 minutes for semi-automated segmentation results previously reported [19].

Table 3.5: Expert manual segmentation variability for five rounds (R1-R5): mean(SD). (n = 20)

		Round1	Round2	Round3	Round4	Round5	Mean	p*
<i>DSC</i> (%)	L	90.8(2.8)	91.0(2.9)	91.0(2.8)	90.9(2.8)	90.9(2.7)	90.9(2.8)	0.92
	R	91.5(1.8)	91.4(1.8)	91.7(1.8)	91.5(1.9)	91.7(1.9)	91.6(1.8)	0.66
	W	91.2(2.1)	91.3(2.1)	91.4(2.1)	91.2(2.0)	91.3(2.1)	91.3(2.1)	0.85
<i>RMSE</i> (mm)	L	4.1(1.2)	4.0(1.2)	4.0(1.2)	4.1(1.2)	4.1(1.2)	4.1(1.2)	0.98
	R	4.0(0.7)	4.1(0.8)	4.0(0.8)	4.0(0.8)	4.0(0.8)	4.0(0.8)	0.88
	W	4.0(0.8)	4.0(0.8)	4.0(0.8)	4.0(0.8)	4.0(0.8)	4.0(0.8)	0.99
$ \delta V_E $ (L)	L	0.12(0.09)	0.11(0.10)	0.11(0.10)	0.11(0.10)	0.12(0.11)	0.11(0.10)	0.87
	R	0.12(0.10)	0.13(0.09)	0.12(0.10)	0.13(0.10)	0.12(0.09)	0.13(0.09)	0.65
	W	0.23(0.18)	0.24(0.18)	0.23(0.19)	0.23(0.18)	0.24(0.19)	0.23(0.18)	0.92
$ \delta V_P $ (%)	L	6.4(4.8)	6.3(5.1)	6.0(5.0)	6.0(5.0)	6.5(5.7)	6.2(5.1)	0.88
	R	5.5(4.2)	6.5(4.4)	5.8(4.2)	6.1(4.6)	5.9(4.2)	6.0(4.3)	0.23
	W	5.8(4.2)	6.3(4.2)	5.7(4.3)	5.9(4.2)	6.0(4.5)	6.0(4.3)	0.71

\*p-value was determined using an ANOVA.

### 3.4 Discussion

Although manual image segmentation is always an option, it is generally labour-intensive, time-consuming, and prone to intra- and inter-observer variability [42]. More importantly, manual segmentation methods inherently restrict translation to large-scale clinical and research studies. In recognition of this and the potential for pulmonary  $^1\text{H}$  MRI structure-function information to help clinically manage patients with asthma, we developed a multi-region segmentation method for volumetric lung measurements. As a way to improve  $^1\text{H}$  MRI segmentation, we exploited the inherent left-to-right lung volume proportion prior and dual optimization techniques and demonstrated: 1) excellent agreement with expert manual segmentation, 2) clinically-acceptable reproducibility, and 3) rapid implementation that is consistent with clinical and research requirements.

The proposed algorithm yielded lung volumes, *DSC*, *RMSE* and volume errors that showed excellent agreement with expert manual segmentation results. The algorithm-generated lung

surfaces also agreed with expert manual delineations (4 mm *RMSE* or 1.3 times in-plane voxel width) and considering that a typical lung volume is 3–6 L, the mean absolute whole lung volume errors (0.2 L/6%) are clinically-acceptable as they are similar to those of pulmonary function tests. The *CoV* and *ICC* ( $\geq 0.91$ ) also reflected excellent agreement within and between observers. Furthermore, the *SDD* (0.10 L, 0.14 L and 0.24 L) were comparable with those of expert observer with 5 years segmentation experience. We also observed *DSC* and *RMSE* that were different for the left and right lung; these differences, while not large, were significant and may stem from severe motion artifacts and shape changes in the left lung around the heart (i.e., the thin and elongated shape of the cardiophrenic angle), which, although small, poses extreme challenges for algorithm segmentation.

We tested our approach on a dataset of mild-to-moderate and severe, poorly-controlled asthma patients, and demonstrated some potential for use in a broad range of asthma patients. This is important because in respiratory diseases such as asthma and chronic obstructive pulmonary disease there are changes to the thoracic cavity shape and size concomitant with disease progression. This also provides an opportunity to test the algorithm in outlier cases such as Subjects 2, 14 and 16 in whom there was the lowest agreement with manual measurements. For Subject 2 the weakened agreement may have stemmed from the bright pulmonary vessels, that by virtue of the regularization term resulted in the algorithm converged at these strong edges. This issue may be mitigated by weighting the regularization term or alternatively, by adding more correcting seeds. In fact, after additional correcting seeds were added (227 voxels/54% more for the left lung and 191 voxels/43% more for the right lung) using the brush tool, whole lung re-segmentation was improved with *DSC* = 90%, *RMSE* = 4.8 mm and volume errors of 0.11 L and 2.6%. Two other outliers indicated by green and blue circles likely stemmed from very poor image quality that resulted in weak edges especially in the periphery and anterior regions, making them challenging to segment manually and algorithmically. Such issues may be addressed using correcting seeds or by employing more advanced data terms.

We segmented the left and right lung separately, resulting in a multi-region segmentation

approach that was superior to two-label segmentation. The two-region segmentation method [41] treats the left and right lung as a whole and the regularization term controls the segmentation to achieve a tight total surface. In inflated lung, i.e., functional residual capacity + 1L, there is usually weak separation between the two lung especially in the posterior and anterior regions, where the background and foreground signal intensities overlap substantially. Using the two-region segmentation method, the background regions that poorly separate the two lung are likely to be segmented as the lung to maintain a minimum surface, leading to lower segmentation accuracy in these regions. By regularizing the two lung separately, the left and right lung will not be influenced by the other and each will achieve its own minimum independently. As a result, the total regularization cost may or may not be greater than that obtained using the two-region segmentation method but leakage in these suspicious regions can be improved, and this was confirmed by the comparison between the three-region and two-region segmentation methods (all  $p < 0.0001$ ), as shown in Fig. 3.5. Although promising, the segmentation, especially for the left lung, is still problematic due to motion artifacts of the beating heart. By incorporating the left-to-right lung volume proportion *prior*, we, for the first time, “relate” the left and right lung to each other for  $^1\text{H}$  MRI lung segmentation. As a result, the left lung segmentation will likely be improved by the right lung because it is generally relatively easier to segment. In fact, we observed that, compared with the three-region segmentation method (without the volume proportion *prior*), the proposed method achieved 1.3% (left lung) and 0.6% (right lung) increase in *DSC*, 3.1% (left lung) and 0.9% (right lung) decrease for absolute volume percent error ( $|\delta V_p|$ ). In addition, we observed that, although the differences for segmentation accuracy for the two three-region segmentation methods are small, there is substantial decrease in *SD* for *DSC* for proposed method, suggesting that the proposed left-to-right lung volume proportion *prior* might improve the segmentation reproducibility. In summary, the three-region segmentation method (without volume proportion *prior*) directly separates the two lung and improves leakage between the left and right lung compared with the two-region method. This provides a way for more regional lung structure-function measurements, i.e., individual left and right lung

(even lobar or segmental with the developments of <sup>1</sup>H MRI techniques) vs whole lung evaluation. In addition, the two lung may be independently used to facilitate pulmonary <sup>1</sup>H MRI applications that involve challenging image processing. For example, free-breathing and/or multi-volume <sup>1</sup>H MRI whole lung registration is challenging because of the large deformation, and previous studies [43] have shown that lung image registration can be improved by treating the two lung separately. The proposed volume proportion *prior*, for the first time, relates the two lung, improves left lung segmentation and decreases segmentation variation. This speaks to the advantages of the proposed volume proportion preserved three-region segmentation approach. It is important to note that the proportion prior that we used is only one of many different approaches. As previously described [27], it is also possible to use proportion distribution *prior*. Another straightforward approach is to constrain the ratio between the two lung within a range, i.e.,  $\frac{\int_{\Omega} \xi_{ll} dx}{\int_{\Omega} \xi_{rl} dx} \in [\gamma_l, \gamma_u]$ , where  $\gamma_l$  and  $\gamma_u$  are the lower and upper bounds of the ratio, respectively. This form of constraint can be further rewritten as two restrictions:  $\gamma_l \int_{\Omega} \xi_{rl} dx - \int_{\Omega} \xi_{ll} dx \leq 0$  and  $\int_{\Omega} \xi_{ll} dx - \gamma_u \int_{\Omega} \xi_{rl} dx \leq 0$ , which can be incorporated by a different max-flow/min-cut model. Due to the variability of left-to-right lung volume ratio and the presence of various pathologies, it might be appropriate to constrain the measured left-to-right lung proportion within a pre-determined range. This incorporation of the proportion *prior* might be beneficial for this situation. In other words, the left-to-right lung proportion distribution, once determined, could be exploited to address the non-uniform distribution of the left-to-right lung volume proportion.

Although this segmentation approach employed diminished user interaction with high reproducibility, we must acknowledge a number of limitations. We used an intensity appearance model to build the data terms for the energy function, and it will be necessary to investigate more advanced data term formulations such as intensity distribution matching, distance constraints [44], segmentation moments [45]. In addition, other information such as textures [46, 47] may be useful for improved segmentation performance. The proposed approach is not fully automated, and this is also a shortcoming. Advanced and automated segmentation meth-

ods have also been applied to very challenging tasks including whole heart segmentation [48]. In addition, atlas and multi-atlas- based segmentation [36, 49] has also been used to automate these processes but there is a compromise between work flow efficiency and computational burden and possibly other potential sources of error. In addition, the proposed approach was only tested on conventional fast spoiled gradient echo (FGRE) MR pulse sequences. In future, we will compare algorithm performance using other image acquisition pulse sequences including ultra-short echo time methods that improve signal and contrast. Furthermore, a lung cavity segmentation gold standard is not available, and so we used multiple manual segmentation as the reference. We also used resampled isotropic images as previously suggested [36] to ensure equal regularization in all three directions; it was also possible to independently regularize the total variation term for anisotropic images. We also want to emphasize that it is possible to acquire isotropic images, and we are in the process of optimizing image acquisition methods to generate these. It is also worth noting that in this study MRI was acquired with patients inhaling an anoxic  $N_2$  breath-hold and not room air which is approximately 80%  $N_2$ . For this reason, we do not expect significant differences in contrast or segmentation precision when room air is used as contrast. Importantly, our proposed approach assumed a constant ratio between the left and right lung and this is a limitation for certain pathologies (i.e., tumors, severe cystic fibrosis, and congenital diaphragmatic hernia), which significantly weaken or even contradict the assumption and thus this method must be optimized for these cases. In these special cases, we can decrease the weight of the proportion *prior* or even remove the constraint in order to achieve a segmentation that is acceptable. We have not evaluated this algorithm on MRI acquired at full inhalation or full exhalation and it is worth noting that MRI of fully-emptied lung typically show high contrast pulmonary vessels that makes segmentation complex. To address this, tubular filters and optimized data terms for the energy model may be helpful and will be exploited in future. Next steps include  $^1H$  to  $^{129}Xe$  MRI co-registration - both acquired at FRC+1 L as well as  $^1H$  MRI tidal breathing (FRC+~1L) co-segmentation, both of which will be used to generate ventilation measurements. In our current implementa-

tion, we employed straightforward probability density functions to generate the cost  $\rho_i(x)$  by considering the intensity information ( $I(x)$ ) only. However, other spatial information, i.e., the geometry of the neighbourhood of  $x$  ( $G_N(x)$ ), might be beneficial for improved segmentation performance, as previously demonstrated [50]. In this case, we can design the cost as vector  $\rho_i(x) = \{I(x), G_N(x)\}$ , leading to segmentation in higher dimensions.

While this approach is not automatic, it does provide some opportunity for observer interactions which can be beneficial [32, 36] in some circumstances although methods [51] have been proposed to fulfill object recognition for automated image segmentation. In our implementation, we introduced “clues” to assist the algorithm in segmenting challenging regions. For example, seeds placed on the protruding major vessels, and regions with severe artifacts were immediately segmented as background. In order to improve the segmentation of these structures, for this task, we used one slice that encompassed the majority of these challenges, rather than a slice at random. User seeding provides important information of the foreground and background and it is important to note that when the seeding slice number was varied by  $\pm 3$ , there was no significant difference in segmentation results. We also tested seeding using two different and newly-trained undergraduate students who had no previous experience in  $^1\text{H}$  MRI segmentation. They performed algorithm segmentation of an additional 25 patients with chronic obstructive pulmonary disease three times each (on three different days) with a coefficient of variation of 0.5% and 3% for both *DSC* and *RMSE*, respectively. This speaks to the relatively small influence of seeding variation on algorithm segmentation results. We also note for the reviewer that a previous study [52] showed that the probability density function generated from sampled voxels provided a global and statistical description of the object of interest that was more appropriate than the commonly used Gaussian mixture of intensities or appearances. Indeed, our approach may represent an appropriate compromise between reproducibility and accuracy.

The GPU-based implementation required  $\sim 10$  s to segment each image, while manual and semi-automated approaches take about 15 min with substantial observer interactions. We also

want to emphasize that currently we are in the process of optimizing the code using advanced C/C++ language and an improved parallelization scheme in the numerical solver to enhance computational efficiency. The proposed approach significantly outperformed manual methods in terms of time and this bodes well for implementation in large-scale, multi-centre applications. As currently implemented, the lung may be segmented with very little user interaction but with good agreement with the manual reference standard. However, as we transition to clinical applications, challenging anatomic regions can be better segmented at the cost of slightly lower computational efficiency.

To directly and quantitatively compare our method with previous efforts requires that different datasets, evaluation metrics and ground truths are considered. The multi-step approach [53] is sensitive to initial model placement and there were substantial boundary differences ( $\sim 10$  mm) and computational cost (2–20 min). Merging of multiple snakes [54] was also piloted to segment pulmonary  $^1\text{H}$  MRI in 2D but this was highly dependent on edge information and restricted to homogeneous regions, which is challenging in pulmonary  $^1\text{H}$  MRI. An active contour method [55] was also previously developed using a neural network classifier but this required intensive training and frequent updating of the neural network. Another approach [56] used a region-aided geometric snake model combined with gradient information and a Fuzzy C-means clustering method which was prone to local minima and accumulated segmentation error from slice to slice. The hybrid approach [57] incorporated grey-level thresholding, regional shape descriptors, and morphological operations and a similar approach [58] used histogram thresholding, region growing and morphological operations to segment the left and right lung in 3D. However, pulmonary  $^1\text{H}$  MRI segmentation is extremely challenging and previous studies [55, 56] have shown that optimum MRI segmentation cannot be achieved using this information exclusively. In another attempt [59], the lung was segmented by deforming two meshes and this resulted in  $> 20\%$  volume errors and efficiency comparable to manual approaches. Statistical methods were also developed to segment 3D  $^1\text{H}$  MRI by exploiting voxel-wise correlation coefficients [60] and this required 1.4 s to segment a 3D dataset

with a spatial overlap ratio of  $\sim 0.7 \pm 0.1$ . An atlas-based approach [61] was also developed and while accurate, this required numerous registrations and label fusion (30 min) to generate target segmentation. Other recent methods rely on complementary functional pulmonary MRI information through convex optimization techniques [37], region-growing and substantial amount of time for user editing [19] with relatively low reproducibility. Compared to these methods, the propose approach demonstrated the necessary and sufficient precision, computational efficiency and accuracy required for research and clinical studies.

### 3.5 Conclusion

$^1\text{H}$  MRI has the potential to provide high resolution structural and functional information of the asthmatic lung. Here we developed and evaluated a multi-region segmentation approach that incorporates the left-to-right lung volume proportion *prior* as a first step in a segmentation and registration pipeline urgently needed for quantifying lung structure-function in asthma. We demonstrated algorithm accuracy with respect to manual measurements as well as the necessary and sufficient reproducibility and speed required for large-scale, multi-centre and clinical applications.

### Bibliography

- [1] Matthew Masoli, Denise Fabian, Shaun Holt, and Richard Beasley. The global burden of asthma: executive summary of the gina dissemination committee report. *Allergy*, 59(5):469–478, 2004.
- [2] William W Busse. Asthma diagnosis and treatment: filling in the information gaps. *Journal of allergy and clinical immunology*, 128(4):740–750, 2011.
- [3] Eduard E de Lange, Talissa A Altes, James T Patrie, John D Gaare, Jeffrey J Knake, John P Mugler, and Thomas A Platts-Mills. Evaluation of asthma with hyperpolar-



- ized helium-3 MRI: correlation with clinical severity and spirometry. *CHEST Journal*, 130(4):1055–1062, 2006.
- [4] Lisa Campana, Jennifer Kenyon, Sanaz Zhalehdoust-Sani, Yang-Sheng Tzeng, Yanping Sun, Mitchell Albert, and Kenneth R Lutchen. Probing airway conditions governing ventilation defects in asthma via hyperpolarized MRI image functional modeling. *Journal of Applied Physiology*, 106(4):1293–1300, 2009.
- [5] Isa Cerveri, Angelo G Corsico, Simone Accordini, Rosanna Niniano, Elena Ansaldo, Josep M Antó, Nino Künzli, Christer Janson, Jordi Sunyer, Deborah Jarvis, et al. Underestimation of airflow obstruction among young adults using  $FEV1/FVC < 70\%$  as a fixed cut-off: a longitudinal evaluation of clinical and functional outcomes. *Thorax*, 2008.
- [6] Kai Ding, Kunlin Cao, Matthew K Fuld, Kaifang Du, Gary E Christensen, Eric A Hoffman, and Joseph M Reinhardt. Comparison of image registration based measures of regional lung ventilation from dynamic spiral CT with Xe-CT. *Medical physics*, 39(8):5084–5098, 2012.
- [7] P Grenier, I Mourey-Gerosa, K Benali, MW Brauner, AN Leung, S Lenoir, MP Cordeau, and B Mazoyer. Abnormalities of the airways and lung parenchyma in asthmatics: CT observations in 50 patients and inter-and intraobserver variability. *European radiology*, 6(2):199–206, 1996.
- [8] Kai Ding, Kunlin Cao, Wilson Miller, Gary Christensen, Joseph Reinhardt, Stanley Benedict, Bruce Libby, and Ke Sheng. Correlation of measures of regional lung ventilation from 4DCT vs. hyperpolarized helium-3 MR. In *SPIE Medical Imaging*, pages 83171E–83171E. International Society for Optics and Photonics, 2012.
- [9] Gregory G King, Stefan Eberl, Cheryl M Salome, Iven H Young, and Ann J Woolcock. Differences in airway closure between normal and asthmatic subjects measured

with single-photon emission computed tomography and technegas. *American journal of respiratory and critical care medicine*, 158(6):1900–1906, 1998.

- [10] Gregory G King, Stefan Eberl, Cheryl M Salome, Steven R Meikle, and Ann J Woolcock. Airway closure measured by a technegas bolus and spect. *American journal of respiratory and critical care medicine*, 155(2):682–688, 1997.
- [11] H. O. Coxson, J. Leipsic, G. Parraga, and D. D. Sin. Using pulmonary imaging to move chronic obstructive pulmonary disease beyond FEV1. *Am J Respir Crit Care Med*, 190(2):135–44, 2014.
- [12] Sean Fain, Mark L Schiebler, David G McCormack, and Grace Parraga. Imaging of lung function using hyperpolarized helium-3 magnetic resonance imaging: Review of current and emerging translational methods and applications. *Journal of Magnetic Resonance Imaging*, 32(6):1398–1408, 2010.
- [13] Kai Ding, W Miller, Kunlin Cao, G Christensen, J Reinhardt, S Benedict, B Libby, and K Sheng. Quantification of regional lung ventilation from tagged hyperpolarized helium-3 MRI. In *2011 IEEE International Symposium on Biomedical Imaging: From Nano to Macro*, pages 1074–1077. IEEE, 2011.
- [14] Shin Matsuoka, Andetta R Hunsaker, Ritu R Gill, Francine L Jacobson, Yoshiharu Ohno, Samuel Patz, and Hiroto Hatabu. Functional MR imaging of the lung. *Magnetic resonance imaging clinics of North America*, 16(2):275–289, 2008.
- [15] Grzegorz Bauman, Michael Puderbach, Michael Deimling, Vladimir Jellus, Christophe Ched'hotel, Julien Dinkel, Christian Hintze, Hans-Ulrich Kauczor, and Lothar R Schad. Non-contrast-enhanced perfusion and ventilation assessment of the human lung by means of fourier decomposition in proton MRI. *Magnetic Resonance in Medicine*, 62(3):656–664, 2009.

- [16] Åsmund Kjørstad, Dominique MR Corteville, Andre Fischer, Thomas Henzler, Gerald Schmid-Bindert, Frank G Zöllner, and Lothar R Schad. Quantitative lung perfusion evaluation using fourier decomposition perfusion MRI. *Magnetic resonance in medicine*, 72(2):558–562, 2014.
- [17] Åsmund Kjørstad, Dominique MR Corteville, Thomas Henzler, Gerald Schmid-Bindert, Erlend Hodneland, Frank G Zöllner, and Lothar R Schad. Quantitative lung ventilation using fourier decomposition MRI; comparison and initial study. *Magnetic Resonance Materials in Physics, Biology and Medicine*, 27(6):467–476, 2014.
- [18] CJ Bergin, JM Pauly, and A Macovski. Lung parenchyma: projection reconstruction MR imaging. *Radiology*, 179(3):777–781, 1991.
- [19] Miranda Kirby, Mohammadreza Heydarian, Sarah Svenningsen, Andrew Wheatley, David G. McCormack, Roya Etemad-Rezai, and Grace Parraga. Hyperpolarized  $^3\text{He}$  magnetic resonance functional imaging semiautomated segmentation. *Academic Radiology*, November 2011.
- [20] Jens Vogel-Claussen, Julius Renne, Jan Hinrichs, Christian Schönfeld, Marcel Gutberlet, Frank Schaumann, Carla Winkler, Cornelia Faulenbach, Norbert Krug, Frank K Wacker, et al. Quantification of pulmonary inflammation after segmental allergen challenge using turbo-inversion recovery-magnitude magnetic resonance imaging. *American journal of respiratory and critical care medicine*, 189(6):650–657, 2014.
- [21] Maren Zapke, Hans-Georg Topf, Martin Zenker, Rainer Kuth, Michael Deimling, Peter Kreisler, Manfred Rauh, Christophe Chefd’hotel, Bernhard Geiger, and Thomas Rupprecht. Magnetic resonance lung function—a breakthrough for lung imaging and functional assessment? a phantom study and clinical trial. *Respir Res*, 7:106, 2006.
- [22] Francesca Pennati, James D Quirk, Dmitriy A Yablonskiy, Mario Castro, Andrea Aliverti, and Jason C Woods. Assessment of regional lung function with multivolume 1H

MR imaging in health and obstructive lung disease: Comparison with  $^3\text{He}$  MR imaging. *Radiology*, 2014.

- [23] Daniel Cremers, Mikael Rousson, and Rachid Deriche. A review of statistical approaches to level set segmentation: integrating color, texture, motion and shape. *International journal of computer vision*, 72(2):195–215, 2007.
- [24] Tobias Heimann and Hans-Peter Meinzer. Statistical shape models for 3D medical image segmentation: A review. *Medical image analysis*, 13(4):543–563, 2009.
- [25] Martin R Miller, JATS Hankinson, V Brusasco, F Burgos, R Casaburi, A Coates, R Crapo, P Enright, CP Van der Grinten, P Gustafsson, et al. Standardisation of spirometry. *Eur Respir J*, 26(2):319–38, 2005.
- [26] Miranda Kirby, Sarah Svenningsen, Amir Owrangi, Andrew Wheatley, Adam Farag, Alexei Ouriadov, Giles E Santyr, Roya Etemad-Rezai, Harvey O Coxson, David G McCormack, et al. Hyperpolarized  $^3\text{He}$  and  $^{129}\text{Xe}$  MR imaging in healthy volunteers and patients with chronic obstructive pulmonary disease. *Radiology*, 265(2):600–610, 2012.
- [27] Claudia Nieuwenhuis, Evgeny Strelakovski, and Daniel Cremers. Proportion priors for image sequence segmentation. In *Computer Vision (ICCV), 2013 IEEE International Conference on*, pages 2328–2335. IEEE, 2013.
- [28] WILLIAM M Thurlbeck. Post-mortem lung volumes. *Thorax*, 34(6):735–739, 1979.
- [29] B Johansen, O Bjørtuft, and J Boe. Static lung volumes in healthy subjects assessed by helium dilution during occlusion of one mainstem bronchus. *Thorax*, 48(4):381–384, 1993.
- [30] Eun Mi Chun, Seung Woo Suh, Hitesh N Modi, Eun Young Kang, Seok Joo Hong, and Hae-Ryong Song. The change in ratio of convex and concave lung volume in adolescent idiopathic scoliosis: a 3D CT scan based cross sectional study of effect of severity of curve

- on convex and concave lung volumes in 99 cases. *European Spine Journal*, 17(2):224–229, 2008.
- [31] Jing Yuan, Egil Bae, Xue-Cheng Tai, and Yuri Boykov. A continuous max-flow approach to potts model. In *Computer Vision—ECCV 2010*, pages 379–392. Springer, 2010.
- [32] Yuri Y Boykov and M-P Jolly. Interactive graph cuts for optimal boundary & region segmentation of objects in ND images. In *Computer Vision, 2001. ICCV 2001. Proceedings. Eighth IEEE International Conference on*, volume 1, pages 105–112. IEEE, 2001.
- [33] Tony F Chan, Selim Esedoglu, and Mila Nikolova. Algorithms for finding global minimizers of image segmentation and denoising models. *SIAM journal on applied mathematics*, 66(5):1632–1648, 2006.
- [34] Jan Lellmann, Jörg Kappes, Jing Yuan, Florian Becker, and Christoph Schnörr. Convex multi-class image labeling by simplex-constrained total variation. In *Scale Space and Variational Methods in Computer Vision*, pages 150–162. Springer, 2009.
- [35] Dimitri P Bertsekas. *Nonlinear programming*. 1999.
- [36] Paul A Yushkevich, Joseph Piven, Heather Cody Hazlett, Rachel Gimpel Smith, Sean Ho, James C Gee, and Guido Gerig. User-guided 3D active contour segmentation of anatomical structures: significantly improved efficiency and reliability. *Neuroimage*, 31(3):1116–1128, 2006.
- [37] Fumin Guo, Jing Yuan, Martin Rajchl, Sarah Svenningsen, Dante PI Capaldi, Khadija Sheikh, Aaron Fenster, and Grace Parraga. Globally optimal co-segmentation of three-dimensional pulmonary 1H and hyperpolarized 3He MRI with spatial consistence prior. *Medical Image Analysis*, 2015.
- [38] SD Walter, M Eliasziw, and A Donner. Sample size and optimal designs for reliability studies. *Statistics in medicine*, 17(1):101–110, 1998.

- [39] Simon K Warfield, Kelly H Zou, and William M Wells. Simultaneous truth and performance level estimation (staple): an algorithm for the validation of image segmentation. *IEEE transactions on medical imaging*, 23(7):903–921, 2004.
- [40] Michael Eliasziw, S Lorraine Young, M Gail Woodbury, and Karen Fryday-Field. Statistical methodology for the concurrent assessment of interrater and intrarater reliability: using goniometric measurements as an example. *Physical Therapy*, 74(8):777–788, 1994.
- [41] Jing Yuan, Egil Bae, and Xue-Cheng Tai. A study on continuous max-flow and min-cut approaches. In *Computer Vision and Pattern Recognition (CVPR), 2010 IEEE Conference on*, pages 2217–2224. IEEE, 2010.
- [42] Miranda Kirby. Pulmonary structure and function in chronic obstructive pulmonary disease evaluated using hyperpolarized noble gas magnetic resonance imaging. 2013.
- [43] Fumin Guo, Damien Pike, Sarah Svenningsen, Harvey O Coxson, John J Drozd, Jing Yuan, Aaron Fenster, and Grace Parraga. Development and application of pulmonary structure-function registration methods: towards pulmonary image-guidance tools for improved airway targeted therapies and outcomes. In *SPIE Medical Imaging*, pages 90380Y–90380Y. International Society for Optics and Photonics, 2014.
- [44] Lena Gorelick, Frank R Schmidt, Yuri Boykov, Andrew Delong, and Aaron Ward. Segmentation with non-linear regional constraints via line-search cuts. In *Computer Vision–ECCV 2012*, pages 583–597. Springer, 2012.
- [45] Maria Klodt and Daniel Cremers. A convex framework for image segmentation with moment constraints. In *Computer Vision (ICCV), 2011 IEEE International Conference on*, pages 2236–2243. IEEE, 2011.
- [46] Jitendra Malik, Serge Belongie, Thomas Leung, and Jianbo Shi. Contour and texture analysis for image segmentation. *International journal of computer vision*, 43(1):7–27, 2001.

- [47] Nikos Paragios and Rachid Deriche. Geodesic active regions and level set methods for supervised texture segmentation. *International Journal of Computer Vision*, 46(3):223–247, 2002.
- [48] Xiahai Zhuang. Challenges and methodologies of fully automatic whole heart segmentation: a review. *Journal of healthcare engineering*, 4(3):371–408, 2013.
- [49] Xiahai Zhuang, Wenjia Bai, Jingjing Song, Songhua Zhan, Xiaohua Qian, Wenzhe Shi, Yanyun Lian, and Daniel Rueckert. Multiatlas whole heart segmentation of CT data using conditional entropy for atlas ranking and selection. *Medical physics*, 42(7):3822–3833, 2015.
- [50] Lihi Zelnik-Manor and Pietro Perona. Self-tuning spectral clustering. 2005.
- [51] Anelia Angelova and Shenghuo Zhu. Efficient object detection and segmentation for fine-grained recognition. In *Computer Vision and Pattern Recognition (CVPR), 2013 IEEE Conference on*, pages 811–818. IEEE, 2013.
- [52] Andrew Delong, Lena Gorelick, Frank R Schmidt, Olga Veksler, and Yuri Boykov. Interactive segmentation with super-labels. In *Energy Minimization Methods in Computer Vision and Pattern Recognition*, pages 147–162. Springer, 2011.
- [53] Boudewijn P. F. Lelieveldt, Rob J van der Geest, M Ramze Rezaee, Johan G. Bosch, and Johan H. C. Reiber. Anatomical model matching with fuzzy implicit surfaces for segmentation of thoracic volume scans. *Medical Imaging, IEEE Transactions on*, 18(3):218–230, 1999.
- [54] Nilanjan Ray, Scott T. Acton, Talissa Altes, Eduard E. De Lange, James R. Brookeman, and S. T. Acton. Merging parametric active contours within homogeneous image regions for MRI-based lung segmentation. *IEEE Transactions on Medical Imaging*, 22:189–199, 2003.

- [55] Ian Middleton and Robert I Damper. Segmentation of magnetic resonance images using a combination of neural networks and active contour models. *Medical engineering & physics*, 26(1):71–86, 2004.
- [56] Alireza Osareh and Bita Shadgar. A segmentation method of lung cavities using region aided geometric snakes. *Journal of medical systems*, 34(4):419–433, 2010.
- [57] William F Sensakovic, Samuel G Armato III, Adam Starkey, and Philip Caligiuri. Automated lung segmentation of diseased and artifact-corrupted magnetic resonance sections. *Medical physics*, 33:3085, 2006.
- [58] Peter Kohlmann, Jan Strehlow, Betram Jobst, Stefan Krass, Jan-Martin Kuhnigk, Angela Anjorin, Oliver Sedlacek, Sebastian Ley, Hans-Ulrich Kauczor, and Mark Oliver Wielpütz. Automatic lung segmentation method for MRI-based lung perfusion studies of patients with chronic obstructive pulmonary disease. *International journal of computer assisted radiology and surgery*, pages 1–15, 2014.
- [59] Thomas Böttger, Tobias Kunert, Hans P Meinzer, and Ivo Wolf. Application of a new segmentation tool based on interactive simplex meshes to cardiac images and pulmonary MRI data. *Academic radiology*, 14(3):319–329, 2007.
- [60] Frank G Zöllner, Markus Daab, Meike Weidner, Verena Sommer, Katrin Zahn, Thomas Schaible, Gerald Weisser, Stefan O Schoenberg, K Wolfgang Neff, and Lothar R Schad. Semi-automatic lung segmentation of DCE-MRI data sets of 2-year old children after congenital diaphragmatic hernia repair: Initial results. *Magnetic resonance imaging*, 33(10):1345–1349, 2015.
- [61] Nicholas J Tustison, Kun Qing, Chengbo Wang, Talissa A Altes, and John P Mugler. Atlas-based estimation of lung and lobar anatomy in proton MRI. *Magnetic resonance in medicine*, 2015.



## Chapter 4

# Thoracic CT-MRI Co-Registration for Regional Pulmonary Structure-Function Measurements of Obstructive Lung Disease

*COPD and asthma are spatially and temporally heterogeneous disease and it is important to identify the exact location of lung structural-functional abnormalities. Here we developed and evaluated a deformable registration approach that employed the valuable information from  $^1\text{H}$  MRI to assist the target CT- $^3\text{He}$  MRI registration and an automated regional lung structure-function measurement pipeline for regional evaluation of obstructive lung disease.*

*The contents of this chapter were previously published in Medical Image Analysis: F Guo, S Svenningsen, M Kirby, DPI Capaldi, K Sheikh, A Fenster and G Parraga. Thoracic CT-MRI co-registration for regional pulmonary structure-function measurements of obstructive lung disease. Medical Physics 44.5 (2017): 1718-1733. Permission to reproduce this article was granted by John Wiley and Sons and is provided in Appendix G.*

### 4.1 Introduction

Chronic obstructive pulmonary disease (COPD) [1] and asthma [2] represent a staggering burden on patients, their caregivers and the health-care system worldwide. A major goal of COPD

and asthma research is to regionally understand disease mechanisms, provide a way to predict disease progression and measure response to therapies. In this regard, pulmonary imaging methods, including x-ray computed tomography (CT) [3], nuclear medicine methods [4], and magnetic resonance imaging (MRI) [5, 6], provide regional measurements of pulmonary structural-functional abnormalities. Hyperpolarized noble gas (<sup>3</sup>He/<sup>129</sup>Xe) MRI is emerging as a way to provide airway/airspace structure and physiological function that is complementary to CT. Importantly, noble gas MRI allows for visualization of pulmonary functional abnormalities and how they change overtime or in response to therapy [7] with high spatial and temporal resolution. By combining the structural information from CT and functional information from noble gas MRI, there is enormous potential to better understand pulmonary disease mechanisms and develop treatments for improved patient outcomes, i.e., lung volume reduction surgery [8], airway stent and valve placement in COPD [9] and airway-targeted bronchial thermoplasty in asthma [10].

To facilitate regional evaluation of pulmonary structure-function relationships and to assist in the development of novel regional therapies, fusion of anatomical CT and physiological noble gas MRI information is required. Therefore, our objective was to develop a clinically practical and physiologically relevant image analysis pipeline incorporating CT-noble gas MRI registration for regional evaluation of pulmonary measurements. CT-MRI registration is challenging due to a number of reasons. For example, the lung is a highly deformable organ [11], and the image quality is influenced by breathing and cardiac motion [6]. Furthermore, inconsistent breath-hold lung volumes during image acquisition between CT and MRI scans and geometric distortions associated with different image acquisition methods also pose challenges.

Previously, <sup>3</sup>He MRI was co-registered with CT using rigid [12] and affine [13] methods based on manually identified fiducial markers. The rigid registration method [12] was also optimized [14] and automated by registering CT to <sup>1</sup>H MRI [15], which was acquired simultaneously to <sup>3</sup>He MRI. Another approach [16] involved CT-<sup>3</sup>He MRI affine registration for the left and right lung using manual control points. A similar approach [17] was devel-

oped to match the manually identified lung shapes for CT and  $^1\text{H}$  MRI for CT- $^3\text{He}$  MRI registration by assuming that the  $^1\text{H}$  and  $^3\text{He}$  images were inherently registered; this approach [17] was automated by registering both CT and  $^3\text{He}$  MRI to  $^1\text{H}$  MRI [18] using *NiftyReg* (<http://cmictig.cs.ucl.ac.uk/wiki/index.php/NiftyReg>) affine and deformable registration tools [19]. Similarly,  $^1\text{H}$  and  $^3\text{He}$  MRI were directly and indirectly registered to CT [20] using the affine and deformable registration tools provided by *Advanced Normalization Tools (ANTs)*, (<http://stnava.github.io/ANTs/>) [21]. It is important to note that although promising, none of these previous approaches are being used in research or clinical workflows due to a number of limitations. For example, some methods [12, 16, 13, 17] involved substantial user interaction or required special expertise to identify image features, while the others [14, 17] relied on single-breath image acquisition techniques. While individual CT- $^1\text{H}$ ,  $^3\text{He}$ - $^1\text{H}$  and/or CT- $^3\text{He}$  MRI registration approaches [18, 20] were previously evaluated, the potential of image information from multiple imaging methods was not fully exploited. By incorporating image information from multiple methods [22, 23, 24, 25, 26, 27], we propose to register CT to sequentially acquired  $^1\text{H}$  and noble gas MRI simultaneously using a consistency *prior* (i.e., the similarity of the displacement field from individual CT- $^1\text{H}$  and CT-noble gas MRI registration). Therefore, here, we describe a way to co-register CT and  $^3\text{He}$  MRI by using  $^1\text{H}$  MRI (Fig. 4.1A) in a coupled manner and by solving the optimization problem through convex optimization joint CT- $^1\text{H}/^3\text{He}$  MRI deformable registration.

## 4.2 Materials and Methods

### 4.2.1 Study Subjects and Image Acquisition

Thirty-five patients including 15 severe, poorly-controlled asthma and 20 COPD patients provided written informed consent to a study protocol approved by Health Canada and a local research ethics board (Appendix H). COPD subjects with a clinical diagnosis were classified according to the Global Initiative for chronic Obstructive Lung Disease (GOLD) criteria [28],

and the asthma patients were classified as severe and poorly-controlled according to the Global Initiative of Asthma (GINA) treatment step criteria [29].

For <sup>1</sup>H MRI acquisitions, subjects were scanned in breath-hold inspiration after inhaling 1.0 L medical grade nitrogen (N<sub>2</sub>) (Spectra Gases, Alpha, NJ, USA) from functional residual capacity (FRC). MRI was acquired at 3.0 Tesla (Discovery MR750, General Electric Health Care [GEHC], Milwaukee, WI, USA) as previously described [30]. Subjects were instructed to inhale a gas mixture from a 1.0 L Tedlar bag (Jensen Inert Products, Coral Springs, FL, USA) from functional residual capacity (FRC+1) and images were acquired at inspiration breath-hold. <sup>1</sup>H MRI was performed using an eight-channel, transmit/receive whole-body radiofrequency (RF) coil (127 MHz, maximum excitation power 8.0 kW delivered by a narrow-band RF power amplifier, GEHC, Milwaukee, WI, USA), and a 2D multi-slice fast gradient-recalled echo sequence with patients holding their breath at 1.0 L of medical grade nitrogen (N<sub>2</sub>) (12 s acquisition time, repetition time/echo time/flip angle = 4.3 ms/1.2 ms/20°; field-of-view = 40 cm×40 cm; bandwidth = 25 kHz; matrix = 128 (phase encoding) × 80 (frequency encoding); 14–17 coronal slices, 15 mm slice thickness, 0 gap, 62.5% partial-echo percent). Auto shimming was used for <sup>1</sup>H MRI acquisitions (chest region) for the centre slice. The maximum magnetic field gradient strength was 5 G/cm for x,y and z gradients and image distortion compensation was enabled by default. Images were reconstructed from original k-space data using Fourier transforms with Matlab R2013a (The Mathworks Inc., Natick, MA, USA).

Hyperpolarized <sup>3</sup>He MRI was enabled using a single-channel, rigid, linear birdcage transmit/receive elliptical chest coil (Rapid Biomedical, Wuerzburg, Germany, 97.3 MHz, maximum excitation power 3.2 kW delivered by an AMT 3T90 broad-band RF power amplifier (GEHC, Milwaukee, WI, USA)). A turn-key system (HeliSpin, Polarean Inc., Durham, NC, USA) was used to polarize <sup>3</sup>He gas to 30-40% and doses of 5 ml/kg body weight were administered to 1.0 L Tedlar bags diluted by N<sub>2</sub>. <sup>3</sup>He static ventilation images were acquired using a 2D multi-slice fast gradient-recalled echo sequence (10 s acquisition, repetition time/echo time/flip angle = 3.8 ms/1.0 ms/7°; field-of-view = 40 cm×40 cm; bandwidth = 49 kHz; ma-

trix = 128 (phase encoding)  $\times$  80 (frequency encoding); 14–17 coronal slices, 15 mm slice thickness, 0 gap, 62.5% partial-echo percent). Due to hardware limitation, we used previously determined  $^1\text{H}$  shimming settings for all hyperpolarized gas MRI acquisitions (chest region) for the centre slice. The maximum magnetic field gradient strength was 5 G/cm for for x,y and z gradients and no image distortion compensation was used. Images were reconstructed from original k-space data using Fourier transforms with Matlab R2013a (The Mathworks Inc., Natick, MA, USA).

CT was performed on a 64-slice Lightspeed VCT scanner (GEHC, Milwaukee, WI, USA). A spiral acquisition of the entire lung from apex to base was performed with subjects in breath-hold after inhaling 1.0 L  $\text{N}_2$  from a Tedlar bag (detector configuration:  $64 \times 0.625$  mm collimation, 120 kVp, 100 effective mA, 500 ms tube rotation time, 1.0 pitch, 25-30 cm $\times$ 36 cm $\times$ 36 cm field-of-view). Data was reconstructed to a slice thickness of 1.25 mm and in-plane voxel size of  $\sim 0.7 \times 0.7$  mm<sup>2</sup> using a standard convolution kernel, as previously described [30].

### 4.2.2 Overview

Figure 4.1A shows representative CT,  $^1\text{H}$  and  $^3\text{He}$  MRI for an asthma and COPD patient. Figure 4.1B provides a schematic of a CT structure- $^3\text{He}$  MRI function measurements pipeline. While some of the main components in Fig. 4.1B were previously explored [18], here we describe a way to jointly register CT to spatially aligned  $^1\text{H}$  and  $^3\text{He}$  MRI for the target CT- $^3\text{He}$  MRI registration. Briefly, as shown in Fig. 4.1B,  $^1\text{H}$ ,  $^3\text{He}$  MRI and CT images were entered into the pipeline as inputs.  $^3\text{He}$  MRI was first registered to the associated  $^1\text{H}$  MRI using a rigid registration method that employed a block matching algorithm [31] followed by a deformable step that used B-spline free-form deformation techniques [32]. The same rigid registration method was used to initialize CT- $^1\text{H}$  MRI registration. With the transformed  $^3\text{He}$  and CT images, we proposed a deformable registration approach to simultaneously register CT to  $^1\text{H}$  and  $^3\text{He}$  MRI by coupling the displacement field from the independent CT- $^1\text{H}$  and CT- $^3\text{He}$  MRI registrations.

<sup>3</sup>He MR images were segmented to generate ventilation defect volumes using a hierarchical K-means clustering approach [33]. CT lobes and airway trees were generated using Pulmonary Workstation 2.0 (VIDA Diagnosis Inc., Coralville, IA, USA) and the labeled airway trees were used to identify lung segments, which were deformed using the CT-<sup>1</sup>H MRI rigid transformation and CT-<sup>3</sup>He MRI displacement field. Whole lung and segmental <sup>3</sup>He MRI ventilation defect percent (VDP) were calculated by normalizing the volumes of <sup>3</sup>He ventilation defects to the spatially matched CT whole lung and lung segments.

#### 4.2.2.1 CT-<sup>1</sup>H/<sup>3</sup>He MRI Registration with Consistent Displacement

Given two three-dimensional (3D) images  $I_1(x)$  and  $I_2(x)$ ,  $x \in \Omega$ , to be registered, the optimal displacement field  $\vec{\phi}(x) = [\phi^x(x), \phi^y(x), \phi^z(x)]^T$  that corresponds to directions  $D = \{x, y, z\}$  can be achieved by optimizing the objective function:

$$\min_{\vec{\phi}(x)} S(I_1(x), I_2(x); \vec{\phi}(x)) + \alpha \cdot R(\vec{\phi}(x)), \quad (4.1)$$

where  $S(I_1(x), I_2(x); \vec{\phi}(x))$  represents the similarity measurements that quantify the level of alignment between  $I_1(x)$  and  $I_2(x)$  under the displacement field  $\vec{\phi}(x)$ .  $R(\vec{\phi}(x))$  is the regularization term that tackles the optimization problem [34] to generate smooth displacement field  $\vec{\phi}(x)$  and the smoothness measurement is weighted by  $\alpha \geq 0$ .

We denote  $I_{CT}(x)$ ,  $I_H(x)$  and  $I_{He}(x)$  as the CT, <sup>1</sup>H and <sup>3</sup>He MRI of a subject, respectively. With the help of (4.1), CT to <sup>1</sup>H MRI deformable registration can be formulated as:

$$\min_{\vec{\phi}_1} E_1(\vec{\phi}_1) = S(I_H(x), I_{CT}(x); \vec{\phi}_1) + \alpha_1 \cdot R(\vec{\phi}_1). \quad (4.2)$$

Similarly, CT to <sup>3</sup>He MRI registration can be achieved through:

$$\min_{\vec{\phi}_2} E_2(\vec{\phi}_2) = S(I_{He}(x), I_{CT}(x); \vec{\phi}_2) + \alpha_2 \cdot R(\vec{\phi}_2). \quad (4.3)$$

In general, optimization-based image registration consists of three main components – a

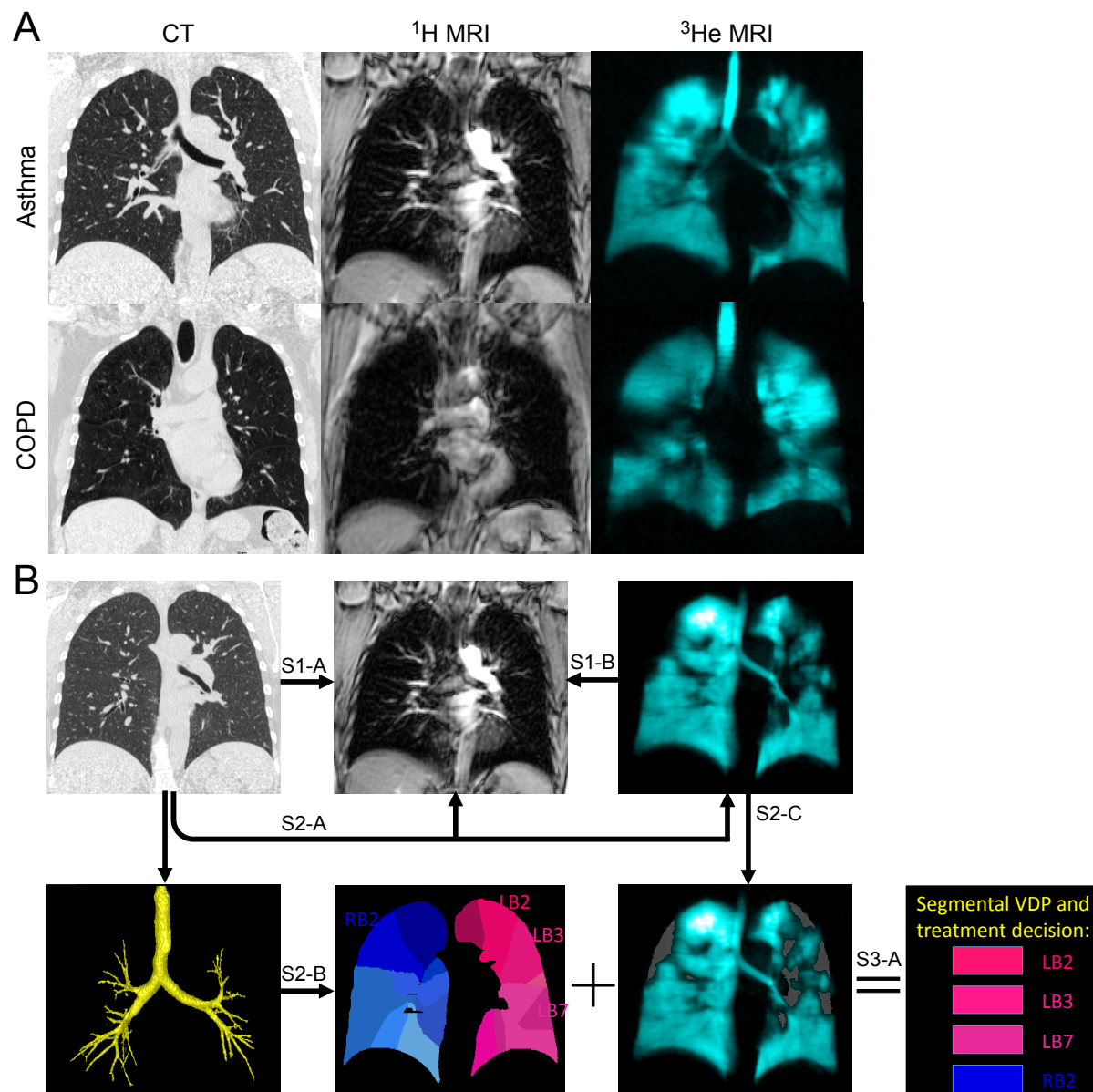


Figure 4.1: Representative CT,  $^1\text{H}/^3\text{He}$  MR images, and the proposed CT- $^3\text{He}$  MRI structure-function measurements workflow. A) CT,  $^1\text{H}$  and  $^3\text{He}$  MR images of an asthma and a COPD patient. B) CT- $^3\text{He}$  MRI structure-function measurements workflow in three steps (S1, S2 and S3). S1-A) CT to  $^1\text{H}$  MRI rigid registration. S1-B)  $^3\text{He}$  to  $^1\text{H}$  MRI rigid and deformable registration. S2-A) Joint CT- $^1\text{H}$  and CT- $^3\text{He}$  MRI deformable registration. S2-B) CT lung segments generation using segmented airways. S2-C)  $^3\text{He}$  MRI ventilation and defects segmentation. S3-A) Segmental  $^3\text{He}$  MRI VDP calculation.

similarity measurement, a transformation model and an optimization scheme, as comprehensively reviewed [26]. Here we employ the *self similarity context* (SSC) [35] as an image repre-

resentation for cross-modality image registration and the similarity between two images can be obtained by measuring the similarity of their representations, i.e., sum of absolute difference (*SAD*) of the *SSC*. As previously described [35], *SSC* defines a vector for each voxel  $x$  as:

$$SSC(x) = \exp\left(-\frac{SSD(p, q; x)}{\sigma^2}\right), \quad (p, q) \in \mathcal{N}_x, \quad (4.4)$$

where  $\mathcal{N}_x$  is the neighbourhood of  $x$ , i.e., the six-neighbourhood of  $x$  in 3D space;  $p, q$  are the neighbours of  $x$  with a Euclidean distance of  $\sqrt{2}$  between them;  $SSD(p, q; x)$  represents the sum of squared difference between  $p$  and  $q$  and is calculated based on signal intensity within the same scan;  $\sigma^2$  estimates the level of noise in  $\mathcal{N}_x$  or the whole image domain. Therefore, the voxel-wise similarity measurements between the image representations of  $SSC_{I_H}(x)$  and  $SSC_{I_{CT}}(x)$  under the displacement field  $\vec{\phi}_1$  can be calculated using *SAD* as follows:

$$S(SSC_{I_H}(x), SSC_{I_{CT}}(x); \vec{\phi}_1) = \int |SSC_{I_H}(x) - SSC_{I_{CT}}(x + \vec{\phi}_1)| dx. \quad (4.5)$$

The vector  $SSC(x)$  was further quantised to 64 bits and the *SAD* operation (4.5) was simplified using a hamming window approach [35]. Similarly, <sup>3</sup>He MRI and CT similarity measurements  $S(SSC_{I_{He}}(x), SSC_{I_{CT}}(x); \vec{\phi}_2)$  was calculated in the same way.

Because of complex small feature motion (vessels and airways) and sliding motion between organs (diaphragm motion with approximately rigid rib cage), which results in displacement field discontinuity, we chose total variation of  $\vec{\phi}(x)$  as the regularization term  $R(\vec{\phi})$  in (4.1) to allow for large deformation and to preserve sharp discontinuities [36] as follows:

$$R(\vec{\phi}) = \sum_{j \in D} \int |\nabla \phi^j(x)| dx. \quad (4.6)$$

Based on image similarity (4.5) and regularization (4.6) measurements, here we proposed to co-register CT and <sup>3</sup>He MRI by coupling the image information from the same individual's <sup>1</sup>H MRI. Specifically, we registered CT to <sup>3</sup>He and <sup>1</sup>H MRI simultaneously and used the displacement from one registration to guide the other, namely multi-modality *joint CT-<sup>1</sup>H/<sup>3</sup>He*



*MRI deformable registration.* The proposed joint deformable registration approach uses  $^3\text{He}$  MRI and CT (aligned with  $^1\text{H}$  MRI) as inputs. We enforced the spatial consistency of the two displacement field  $\vec{\phi}_1(x)$  and  $\vec{\phi}_2(x)$  from independent CT- $^1\text{H}$  MRI (4.2) and CT- $^3\text{He}$  MRI (4.3) deformable registration and penalized the differences of the deformation field as follows:

$$E_3(\vec{\phi}_1, \vec{\phi}_2) = \sum_{j \in D} \int |\phi_1^j(x) - \phi_2^j(x)| dx. \quad (4.7)$$

Combining (4.2), (4.3), (4.5), (4.6) and (4.7), we can formulate the *joint CT- $^1\text{H}$ / $^3\text{He}$  MRI deformable registration* approach that simultaneously registers CT to  $^1\text{H}$  and  $^3\text{He}$  MRI with the following objective function:

$$\begin{aligned} \min_{\vec{\phi}_{1,2}} E(\vec{\phi}_1, \vec{\phi}_2) &= \omega_1 \cdot E_1(\vec{\phi}_1) + \omega_2 \cdot E_2(\vec{\phi}_2) + \beta \cdot E_3(\vec{\phi}_1, \vec{\phi}_2) \\ &= \omega_1 \cdot S(SSC_{I_H}(x), SSC_{I_{CT}}(x); \vec{\phi}_1) + \omega_1 \alpha_1 \cdot R(\vec{\phi}_1) + \\ &\quad \omega_2 \cdot S(SSC_{I_{He}}(x), SSC_{I_{CT}}(x); \vec{\phi}_2) + \omega_2 \alpha_2 \cdot R(\vec{\phi}_2) + \\ &\quad \beta \cdot \sum_{j \in D} \int |\phi_1^j - \phi_2^j| dx, \end{aligned} \quad (4.8)$$

where  $\omega_1, \omega_2, \beta$  are positive constraints and balance the weights of energy  $E_1(\vec{\phi}_1)$  (4.2),  $E_2(\vec{\phi}_2)$  (4.3) and  $E_3(\vec{\phi}_1, \vec{\phi}_2)$  (4.7), respectively. In addition, (4.8) couples the image information from  $^1\text{H}$  MRI when extracting the CT- $^3\text{He}$  MRI displacement field to align CT and  $^3\text{He}$  MRI.

#### 4.2.2.2 Multi-Level CT- $^1\text{H}$ / $^3\text{He}$ MRI Registration Framework and Linearization

We used a multi-level framework to reduce the computational complexity and avoid local minima. The image representations  $SSC_{I_m}(x), m \in \{H, CT, He\}$ , were represented by a three-level pyramid sub-image descriptors, i.e.,  $SSC_{I_m}(x) = \{SSC_{I_m}^l(x); l = 3, 2, 1\}$ , where  $SSC_{I_m}^1(x)$  and  $SSC_{I_m}^3(x)$  represent the finest and coarsest level of the original image representation  $SSC_{I_m}(x)$ , respectively. Similarly, we denoted  $(\vec{\phi}_i)^l(x), i \in \{1, 2\}$ , as the extracted displacement field in the  $l^{\text{th}}$ -level for independent CT- $^1\text{H}$  MRI (4.2) and CT- $^3\text{He}$  MRI (4.2) deformable registration. We initiated the joint registration process from the coarsest level ( $l = 3$ ) and re-sampled the result-

ing displacement field  $(\vec{\phi}_{1,2})^3(x)$  to the next level ( $l = 2$ ) and deformed the corresponding image representation  $SSC_{ICr}^2(x)$ . For example, we solved the  $l^{th}$ -level problem of (4.8) as follows:

$$\begin{aligned} \min_{\vec{d}_{1,2}} & \omega_1 \cdot S(SSC_{IH}^l(x), SSC_{ICr}^l(x + (\vec{\phi}_1)^l); (\vec{d}_1)^l) + \omega_1 \alpha_1 \cdot R((\vec{\phi}_1)^l + (\vec{d}_1)^l) + \\ & \omega_2 \cdot S(SSC_{IHe}^l(x), SSC_{ICr}^l(x + (\vec{\phi}_2)^l); (\vec{d}_2)^l) + \omega_2 \alpha_2 \cdot R((\vec{\phi}_2)^l + (\vec{d}_2)^l) + \\ & \beta \cdot \sum_{j \in D} \int |(\phi_1^j)^l + (d_1^j)^l - (\phi_2^j)^l - (d_2^j)^l| dx, \end{aligned} \quad (4.9)$$

where  $(\vec{\phi}_i)^l(x)$ ,  $l \in \{3, 2, 1\}$ , is the displacement field obtained from the previous level  $(\vec{\phi}_i)^{l+1}(x)$ ;  $(\vec{d}_i)^l$  is the displacement field to be extracted for the current level  $l$ . The total displacement field  $(\vec{\phi}_i)^l + (\vec{d}_i)^l$  in the current level were carried over to the next level  $l-1$  as the initial displacement. These steps were iterated until the finest level was reached, leading to the final displacement field associated with the original images/image representations. In fact, the joint registration (4.8) is a special case of its  $l^{th}$ -level implementation (4.9), i.e., when  $(\vec{\phi}_i)^l = 0$ ,  $i \in \{1, 2\}$  for the coarsest level  $l = 3$ . Therefore, we focused on (4.9) as a generalized form of the proposed joint registration problem (4.8).

Now we consider (4.9): the similarity term  $S(\cdot)$  in (4.5) is nonlinear hence the energy model (4.9) is also nonlinear. Previous studies [37, 38] proposed to linearize (4.5) through variational optical-flow estimation and derived  $(\vec{d}_i)^l$  for the current level  $l$  by estimating a series of incremental displacement field  $\vec{\xi}_i$ , i.e.,  $(\vec{d}_i)^l = \sum \vec{\xi}_i$ , following a previous study [39]. As a result, the problem (4.9) is represented by a series of sub-problems as follows:

$$\begin{aligned} \min_{\vec{\xi}_{1,2}} & \omega_1 \cdot \int |S_1^0 + \nabla S_1 \cdot \vec{\xi}_1| dx + \omega_1 \alpha_1 \cdot \sum_{j \in D} \int |\nabla((\phi_1^j)^l + \xi_1^j)| dx + \\ & \omega_2 \cdot \int |S_2^0 + \nabla S_2 \cdot \vec{\xi}_2| dx + \omega_2 \alpha_2 \cdot \sum_{j \in D} \int |\nabla((\phi_2^j)^l + \xi_2^j)| dx + \\ & \beta \cdot \sum_{j \in D} \int |(\phi_1^j)^l + \xi_1^j - (\phi_2^j)^l - \xi_2^j| dx, \end{aligned} \quad (4.10)$$

where  $S_1^0 = SSC_{ICr}^l(x + (\vec{\phi}_1)^l) - SSC_{ICr}^l(x)$  and  $\nabla S_1 = \nabla SSC_{ICr}^l(x + (\vec{\phi}_1)^l)$ .  $S_2^0$  and  $\nabla S_2$  can

be calculated in a similar manner as previously described [38]. The estimated incremental displacement field  $\vec{\xi}_i$  were then used to update  $\vec{\phi}_i^j$  hence  $S_i^0$  and  $\nabla S_i$ ,  $i \in \{1, 2\}$ . Clearly, (4.10) gives rise to a series of convex optimization problem and through variational analysis, we have:

**Proposition 2** *The convex minimization problem (4.10) can be solved through the following maximization problem:*

$$\begin{aligned} \max_{\epsilon_i, \eta_i^j, r^j} L = & \int \left( \epsilon_1 \cdot S_1^0 + \sum_{j \in D} (\phi_1^j)^l \cdot \text{div } \eta_1^j + \sum_{j \in D} r^j \cdot (\phi_1^j)^l \right) dx + \\ & \int \left( \epsilon_2 \cdot S_2^0 + \sum_{j \in D} (\phi_2^j)^l \cdot \text{div } \eta_2^j - \sum_{j \in D} r^j \cdot (\phi_2^j)^l \right) dx, \end{aligned} \quad (4.11)$$

subject to

$$G_1^j(x) := \epsilon_1 \cdot \partial^j S_1 + \text{div } \eta_1^j + r^j = 0 \quad (4.12)$$

and

$$G_2^j(x) := \epsilon_2 \cdot \partial^j S_2 + \text{div } \eta_2^j - r^j = 0, \quad (4.13)$$

where  $|\epsilon_i| \leq \omega_i$ ,  $|\eta_i^j| \leq \omega_i \cdot \alpha_i$  and  $|r^j| \leq \beta$  for  $i \in \{1, 2\}$ ,  $j \in D$ .

The proof of *Proposition 2* is provided in Appendix D.

#### 4.2.2.3 An Efficient Dual Optimization-based Numerical Solver

The *min-max* formulation (D.6) gives an equivalent representation of the *minimization* problem (4.10) associated with the general form (4.9) for the joint CT-<sup>1</sup>H/<sup>3</sup>He MRI registration problem

(4.8). In addition, (D.6) conforms to the Lagrangian form:

$$\max_{\epsilon_i, \eta_i^j, r^j} \min_{\xi_i^j} L + \sum_{i=1}^2 \sum_{j \in D} \langle \xi_i^j, G_i^j \rangle, \quad (4.14)$$

of the *maximization* problem (4.11) and involves the displacement field  $\xi_i^j, i \in \{1, 2\}, j \in D$ , as the multiplier function of the respective linear equality constraints (4.12) and (4.13). Therefore, instead of directly solving the challenging non-smooth and non-linear *minimization* problem (4.10), we can alternatively optimize its equivalent form, the dual *maximization* problem (4.11) by virtue of *Proposition 2*. Here we derive an efficient duality-based optimization scheme based on the augmented Lagrangian algorithm [40] as follows:

$$\max_{\epsilon_i, \eta_i^j, r^j} \min_{\xi_i^j} L + \sum_{i=1}^2 \sum_{j \in D} \langle \xi_i^j, G_i^j \rangle - \frac{c}{2} \sum_{i=1}^2 \sum_{j \in D} \|G_i^j\|^2, \quad (4.15)$$

where  $c$  is a positive scale and the quadratic penalty function is applied to ensure the constraints (4.12) and (4.13) vanish. The numerical implementation of (4.15) is described in Appendix E.

### 4.2.3 Algorithm Implementation

Our approach was implemented in a pipeline through a single Linux bash script by integrating the main components as shown in Fig. 4.1B. In the first step of the implementation, we resampled the original <sup>1</sup>H and <sup>3</sup>He MRI to approximately 1.56×1.56×1.56 mm<sup>3</sup> voxel space using *convert3D* (<http://www.itksnap.org/pmwiki/pmwiki.php?n=Downloads.C3D>) [41] to ensure equal regularization of the displacement field in all three directions. We chose ~1.56 mm in-plane voxel width for better visualization of <sup>3</sup>He MRI fiducials and CT features. We want to emphasize that it is also possible to perform independent anisotropic regularization of the displacement field for the three directions and we are also currently in the process of developing MR image acquisition methods to acquire images with high resolution and isotropic voxel sizes. The pipeline was implemented in series in three *steps*, each

of which comprised of multiple operations. Briefly, *step 1* (S1) initializes CT-<sup>1</sup>H and <sup>3</sup>He-<sup>1</sup>H MRI alignment using the rigid and deformable registration methods provided by *NiftyReg* [19] (<http://cmictig.cs.ucl.ac.uk/wiki/index.php/NiftyReg>) with default parameters. *Step 2* (S2) refines the CT-<sup>3</sup>He MRI registration using the joint CT-<sup>1</sup>H/<sup>3</sup>He MRI deformable registration method described in Sec. 4.2 and the parameters in (4.8) were optimized on a separate dataset of five COPD/asthma patients ( $\{\omega_1, \alpha_1, \omega_2, \alpha_2, \beta\} = \{0.5, 5.0, 0.8, 8.0, 0.5\}$  for joint CT-<sup>1</sup>H/<sup>3</sup>He MRI deformable registration,  $\{\omega_1, \alpha_1\} = \{1.0, 10.0\}$  for direct CT-<sup>1</sup>H MRI deformable registration and  $\{\omega_2, \alpha_2\} = \{1.0, 50.0\}$  for direct CT-<sup>3</sup>He MRI deformable registration). <sup>3</sup>He MRI ventilation defects were segmented using a hierarchical k-means clustering method [33]. CT lung/lobes and airways were provided by Pulmonary Workstation 2.0 and the lung segments were determined by assigning each lung mask voxel to the closest bronchial tree (right bronchi 1-10 = RB1-10 and left bronchi 1-9 = LB1-9) in the same lobe [42]. Finally, *step 3* (S3) calculates whole lung and segmental VDP by normalizing the <sup>3</sup>He ventilation defects to the whole lung and each lung segment [18] deformed using the transformation and displacement field obtained from S1 and S2.

These image analyses were implemented using Matlab (The Mathworks, Inc., Natick, MA, USA) and CUDA (CUDA v6.0, NVIDIA Corp., Santa Clara, CA, USA) programming on a Linux (CentOS 6.7) desktop (Inter(R) CPU i7-3770, 3.4 GHz, 16 G RAM) with a GPU (GeForce, GTX680, NVIDIA Corp., Santa Clara, CA, USA). The CPU read the images, generated the pyramid registration framework, and provided the image descriptors (*SSC* (4.4)) and similarity measurements to the GPU. The GPU performed parallel implementation of the numerical solver described in Sec. 4.2.2.3 and returned the optimized incremental displacement field to the CPU to deform the image descriptors. These steps were iterated for each level until convergence. We used single precision calculations for the GPU-based algorithm implementation and observed convergence errors  $< 10^{-3}$  within 250 iterations.

## 4.2.4 Validation Methods

### 4.2.4.1 Joint CT-<sup>1</sup>H/<sup>3</sup>He MRI Registration Accuracy

CT-<sup>3</sup>He MRI registration accuracy was evaluated using manually identified fiducial markers in CT and <sup>3</sup>He MRI. A single observer (FG with 4 years experience) manually identified 2–5 fiducial pairs for each CT-<sup>3</sup>He MRI dataset pair, five times, at least one week apart. The fiducials were identified in the coronal plane and the locations were refined by checking the axial and sagittal planes as any recognizable and distinct features such as the apex/bottom of the lung, cardiophrenic angle, trachea bifurcation and vessels that were identifiable in both images. In total,  $N = 109$  fiducial pairs (46 for asthma, 34 for COPD GOLD II and 29 for COPD GOLD III) were identified in 35 patients. Figure 4.2A shows representative fiducial pairs used to evaluate CT-<sup>3</sup>He registration accuracy; the transformation and displacement fields were used to transform these fiducials. CT-<sup>3</sup>He registration accuracy was measured using target registration error ( $TRE$ ) [43]. For example, for the  $i^{th}$ ,  $i \in \{1, \dots, N\}$ , pair of fiducials in <sup>3</sup>He ( $f_{He}^i$ ) and CT ( $f_{CT}^i$ ),  $TRE_i$  was calculated as the Euclidean distance between the two points under the displacement  $T$ , i.e.,  $TRE_i = \sqrt{(f_{He}^i - f_{CT}^i(T))^2}$ . We also measured the fiducial localization error ( $FLE$ ) [43] to determine if fiducial identification provided a dominant contribution to  $TRE$ . For the  $i^{th}$ ,  $i \in \{1, \dots, N\}$ , fiducial in CT or <sup>3</sup>He MRI,  $FLE_i$  was calculated as  $\sqrt{\sigma_{i_x}^2 + \sigma_{i_y}^2 + \sigma_{i_z}^2}$ , where  $\sigma_{i_{x,y,z}}^2$  represent the variances of the locations for the  $i^{th}$  fiducial in  $x$ ,  $y$  and  $z$  directions, respectively.

### 4.2.4.2 Regional CT-<sup>3</sup>He MRI Structure-Function Measurements

We evaluated and compared whole lung VDP generated using the automated pipeline and a semi-automated method, previously validated [33]. We also measured mean runtime for the main components and the whole pipeline in Fig. 4.2B.

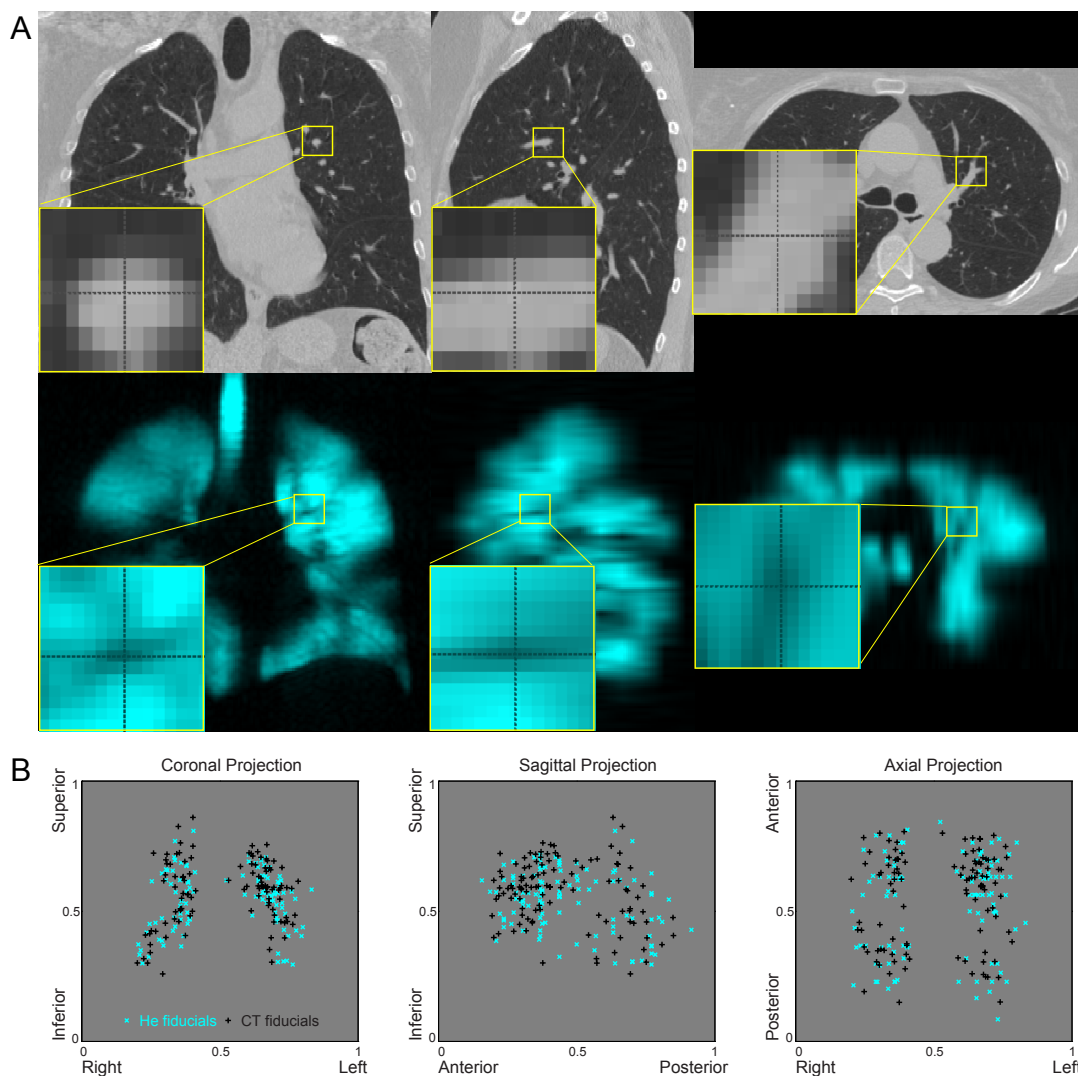


Figure 4.2: Representative CT and  $^3\text{He}$  MRI fiducials and the spatial distribution throughout the lung. A) Top panel: a CT fiducial within inset boxes expanded and identified by crosshairs in coronal, sagittal and axial plane. Bottom panel: a  $^3\text{He}$  MRI fiducial within inset boxes expanded and identified by crosshairs in coronal, sagittal and axial plane. B) Spatial distribution of the 109 pairs of CT (“+”) and  $^3\text{He}$  (“x”) MRI fiducials projected in coronal, sagittal and axial plane. Each fiducial position is normalized to the respective image and shown in anterior/posterior, right/left and superior/inferior directions with “0” representing the right-most, anterior-most and inferior-most, “1” for the left-most, posterior-most and the superior-most of the respective images.

#### 4.2.4.3 Comparison with Other CT- $^3\text{He}$ MRI Registration Methods

The proposed joint CT- $^1\text{H}/^3\text{He}$  MRI registration method was compared with four different approaches while using the same  $^3\text{He}$ - $^1\text{H}$  MRI registration and CT- $^1\text{H}$  MRI inputs as follow:

1) direct CT-<sup>1</sup>H MRI rigid registration using the block matching method [31] using *NiftyReg* [19]; 2) direct CT-<sup>1</sup>H MRI deformable registration using the proposed convex optimization-based registration without coupling <sup>3</sup>He MRI information; 3) direct CT-<sup>3</sup>He MRI deformable registration using the proposed convex optimization-based method without coupling <sup>1</sup>H MRI information; and, 4) direct CT-<sup>1</sup>H MRI registration using B-spline free-form deformation (F3d) [32] with *NiftyReg* [19].

#### 4.2.4.4 Impact of CT-<sup>1</sup>H MRI Alignment

As shown in Fig. 4.1B, the proposed pipeline involves <sup>3</sup>He-<sup>1</sup>H MRI registration (S1-A) and CT-<sup>1</sup>H MRI registration (S1-B) as inputs prior to joint CT-<sup>1</sup>H/<sup>3</sup>He MRI deformable registration (S2-A). In this approach, and as previously described, CT-<sup>1</sup>H MRI registration is the most challenging step [44]. To evaluate the effect of CT-<sup>1</sup>H MRI pre-alignment on overall registration accuracy, we explored modification of the CT-<sup>1</sup>H MRI transformation matrix by  $\pm 10\%$  rotation ( $Rotation_{x,y,z}$ ) and translation ( $Translation_{x,y,z}$ ) and re-ran the joint CT-<sup>1</sup>H/<sup>3</sup>He MRI deformation registration. This modification resulted in six sets of joint CT-<sup>1</sup>H/<sup>3</sup>He MRI registration accuracy measurements.

#### 4.2.4.5 Statistical Analysis

The difference in registration accuracy using joint deformable CT-<sup>1</sup>H/<sup>3</sup>He MRI registration and rigid CT-<sup>1</sup>H MRI registration was tested using paired *t*-tests. Normality of data was determined using Shapiro-Wilk test and when significant, the Mann-Whitney U test for nonparametric data was performed using Statistical Package for the Social Sciences (SPSS version 24, SPSS Inc., Chicago, IL, USA). Differences in CT-<sup>3</sup>He MRI registration accuracy using other comparative methods were evaluated using a one-way analysis of variance (ANOVA) with a Tukey test for *post hoc* pairwise comparisons using SPSS. Automated and semi-automated <sup>3</sup>He MRI whole lung VDP (WL VDP) were compared using paired *t*-tests with SPSS and the correlation was measured using Pearson correlation coefficient (*r*) and Bland-Altman analysis with GraphPad



Table 4.1: Subject demographics and pulmonary function measurements

	All (n = 35)	Asthma (n = 15)	COPD GOLD II (n = 10)	COPD GOLD III (n = 10)
Mean(SD)				
Age yrs	59(15)	46(12)	67(6)	69(12)
Male n	21	6	6	9
BMI kg.m <sup>-2</sup>	28(5)	29(6)	26(3)	27(5)
Pack yrs	-	-	49(17)	36(34)
FVC% <sub>pred</sub>	88(16)	92(14)	94(15)	77(13)
FEV <sub>1</sub> % <sub>pred</sub>	63(24)	79(25)	62(8)	40(5)
FEV <sub>1</sub> /FVC	54(17)	68(16)	50(8)	39(7)
IC% <sub>pred</sub>	97(26)	107(25)	104(16)	75(21)
FRC% <sub>pred</sub>	121(38)	89(20)	126(22)	164(27)
RV% <sub>pred</sub>	143(46)	107(34)	150(26)	191(28)
TLC% <sub>pred</sub>	122(14)	97(12)	116(14)	122(14)
RV/TLC% <sub>pred</sub>	127(28)	108(28)	128(12)	154(18)
DL <sub>co</sub> % <sub>pred</sub>	-	-	60(16)	43(6)
VDP	15(12)	8(8)	14(8)	28(9)

BMI=Body mass index, FVC=Forced vital capacity, FEV<sub>1</sub>=Forced expiratory volume in one second, IC=Inspiratory capacity, FRC=Functional residual capacity, RV=Residual volume, TLC=Total lung capacity, DL<sub>co</sub>=Diffusing capacity for carbon monoxide, %<sub>pred</sub>=Percent predicted, VDP=Hyperpolarized <sup>3</sup>He MRI ventilation defect percent.

Prism version 7.0 (GraphPad Software, Inc., San Diego, CA, USA). Results were considered significant when the probability of making a type I error was less than 5% ( $p < 0.05$ ).

## 4.3 Results

### 4.3.1 Subject Demographics

Table 4.1 provides demographic information for all participants including 15 asthma (6 males/9 females, 42±12 years), 10 COPD GOLD II (6 males/4 females, 67±6 years) and 10 COPD GOLD III (9 males/1 female, 69±12 years) patients. For this diverse patient group that included both COPD and asthma patients with a wide range of MRI ventilation and CT structural abnormalities, mean forced expiratory volume in 1 s (FEV<sub>1</sub>) and FEV<sub>1</sub>/forced vital capacity (FVC) were abnormal, as were lung volumes.

Table 4.2: CT-<sup>3</sup>He MRI registration accuracy using the comparative registration methods for the entire and each patient group. (n=35)

Registration Methods	<i>TRE</i> (mm)			
	All (n=35)	Asthma (n=15)	COPD GOLD II (n=10)	COPD GOLD III (n=10)
Direct CT- <sup>1</sup> H MRI rigid <sup>1</sup>	7.2±2.8*	7.8±2.9*	6.3±2.5*	7.3±2.7*
Direct CT- <sup>1</sup> H MRI deformable <sup>2</sup>	6.5±2.4*	6.9±2.6*	5.6±1.8*	7.0±2.6*
Direct CT- <sup>3</sup> He MRI deformable <sup>3</sup>	6.8±2.7*	6.5±2.7*	6.7±1.9*	7.1±3.3*
Direct CT- <sup>1</sup> H (F3d) <sup>4</sup>	5.5±2.1*	5.9±2.2*	4.7±1.7 <sup>†</sup>	5.6±2.1 <sup>‡</sup>
Joint CT- <sup>1</sup> H/ <sup>3</sup> He MRI deformable	4.4±2.0	4.5±2.0	4.0±1.7	4.8±2.3
ANOVA	<0.0001	<0.0001	<0.0001	<0.0001

\* $p < 0.0001$ ,  $†p = 0.001$ ,  $‡p = 0.007$  for pairwise comparisons of the joint CT-<sup>1</sup>H/<sup>3</sup>He MRI registration method with the other methods; registration methods 1, 2, 3, and 4 correspond to the comparative approaches described in Sec. 4.2.4.3.

### 4.3.2 Joint CT-<sup>1</sup>H/<sup>3</sup>He MRI Registration Accuracy

Figure 4.3A shows joint CT-<sup>1</sup>H/<sup>3</sup>He MRI deformable registration results for a COPD GOLD III subject using the proposed registration framework. Table 4.2 shows the performance of the joint CT-<sup>1</sup>H/<sup>3</sup>He MRI deformable registration framework for the entire database. For manual, observer-driven CT-<sup>3</sup>He fiducial pair identification, *FLE* was 0.16 mm and 0.34 mm for <sup>3</sup>He MRI and CT, respectively. Figure 4.2B shows the distribution of 109 CT-<sup>3</sup>He MRI fiducial pairs (from a single manual round) normalized and projected to right/left, inferior/superior and anterior/posterior directions. Using these fiducials and all other components in Fig. 4.1B as fixed, mean *TRE* was 7.2±2.8 mm and 4.4±2.0 mm using rigid CT-<sup>1</sup>H MRI and joint CT-<sup>1</sup>H/<sup>3</sup>He MRI deformable registration methods, respectively. Figure 4.3A provides the *TRE* distribution using both methods and shows that joint CT-<sup>1</sup>H/<sup>3</sup>He MRI deformable registration *TRE* was shifted to lower values and these were statistically significant ( $p < 0.0001$ ).

Figure 4.3B and 4.3C show the strong and significant relationships of whole lung VDP measured using the proposed pipeline and a semi-automated segmentation method [33] ( $r = 0.93$ ,  $p < 0.0001$ ) and there were no significant differences ( $p = 0.37$ ). Segmental VDP (VDP<sub>RB1-10, LB1-9</sub>) for each patient was also generated and is provided in the supplementary Table F.1 in Appendix F.

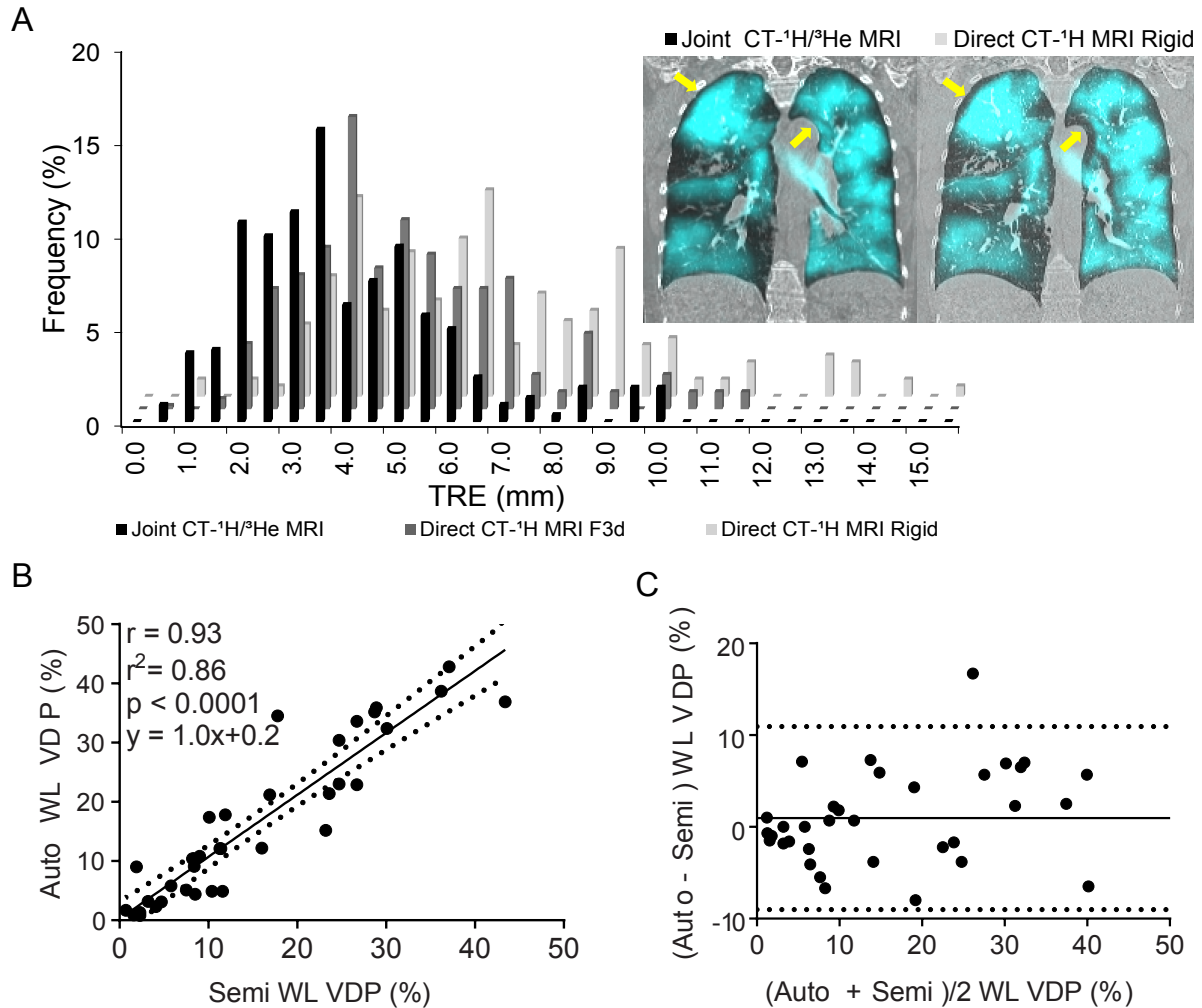


Figure 4.3: CT-<sup>3</sup>He MRI registration accuracy and <sup>3</sup>He MRI WL VDP measurements. A) *TRE* distribution for joint deformable CT-<sup>1</sup>H/<sup>3</sup>He MRI registration (black), direct CT-<sup>1</sup>H MRI free-form deformation registration (gray), and direct CT-<sup>1</sup>H MRI rigid registration (light gray). Representative improvements of using the joint CT-<sup>1</sup>H/<sup>3</sup>He MRI registration method are indicated by yellow arrows. B) Linear correlation of two sets of WL VDP generated by the proposed approach and a semi-automated method. C) Bland-Altman analysis of the two sets of WL VDP. Dotted lines indicate the upper and lower limits and solid lines represent the bias (0.97%).

### 4.3.3 Effect of Coupled <sup>1</sup>H MRI on Registration Accuracy

Table 4.2 provides CT-<sup>3</sup>He MRI registration accuracy by patient subgroup and shows that there were statistically significant differences for the different registration methods ( $p < 0.0001$ ). The *TRE* for multi-modality joint CT-<sup>1</sup>H/<sup>3</sup>He MRI deformable registration was significantly

decreased for the whole group and sub-groups (all pairwise  $p < 0.01$ ).

#### 4.3.4 Effect of CT-<sup>1</sup>H MRI Rigid Registration Matrix and Choice of $\beta$ on Registration Accuracy

Table 4.3 provides CT-<sup>1</sup>H/<sup>3</sup>He registration *TRE* values that were generated by modifying the CT-<sup>1</sup>H MRI rigid registration matrix ( $Rotation_{x,y,z}$  and  $Translation_{x,y,z}$ ). We also evaluated the influence of  $\beta$  (as shown in (4.8)) that controls the weight of the consistent displacement field *prior* on CT-<sup>1</sup>H/<sup>3</sup>He MRI deformable registration. We altered  $\beta = 0.5$  by -15%, -10%, -5%, 5%, 10%, and 15% and observed differences of 0.08, 0.07, 0.02, 0.03, 0.06, and 0.07mm (or 2.0%, 1.6%, 0.6%, 0.7%, 1.5% and 1.9% changes), respectively.

Table 4.3: Influence of CT-<sup>1</sup>H MRI initial rigid alignment on joint CT-<sup>1</sup>H/<sup>3</sup>He deformable registration accuracy.  $Rotation_{x,y,z}$  represent  $\pm 10\%$  error (random sign) added to the rotation components of base CT-<sup>1</sup>H MRI rigid transformation matrixes.  $Translation_{x,y,z}$  represent  $\pm 10\%$  error (random sign) added to the translation components of base CT-<sup>1</sup>H MRI rigid transformation matrixes. (n=35)

$\pm 10\%$ error	<i>TRE</i> (mm)
Rotation <sub>x</sub>	4.6 $\pm$ 2.0
Rotation <sub>y</sub>	4.6 $\pm$ 2.0
Rotation <sub>z</sub>	4.7 $\pm$ 2.1
Translation <sub>x</sub>	4.6 $\pm$ 2.1
Translation <sub>y</sub>	5.3 $\pm$ 2.3
Translation <sub>z</sub>	5.3 $\pm$ 2.4
Base	4.4 $\pm$ 2.0

#### 4.3.5 Runtime

As shown in Fig. 4.1B, the proposed pipeline was fully automated and as shown in Table 4.4, the entire pipeline required  $\sim 11$  min to generate whole lung and segmental CT-<sup>3</sup>He MRI structure-function measurements for each dataset including  $\sim 6.5$  min for *step 1*,  $\sim 4$  min for *step 2*, and  $\sim 0.1$  min for *step 3*. The joint CT-<sup>1</sup>H/<sup>3</sup>He MRI deformable registration (S2-A in Fig. 4.1B) required  $\sim 2.5$  min for GPU-based implementation compared with  $\sim 40$  min running

on a CPU. While the previously validated semi-automated approach [33] requires  $\sim 15$  min, only whole lung VDP may be estimated; segmental VDP cannot be measured using this semi-automated approach without substantial, additional observer interactions.

Table 4.4: Computation time [mean(*SD*)] of the regional CT- $^3\text{He}$  MRI structure-function measurements workflow shown in Fig 4.1B. (n=35)

Time(min)	CPU	GPU
S1-A	3.5(0.2)	3.5(0.2)
S1-B	3(0.3)	3(0.3)
S2-A	40(0.5)	2.5(0.1)
S2-B	0.5(0.1)	0.5(0.1)
S2-C	1(0.1)	1(0.1)
S3-A	0.1(0.0)	0.1(0.0)
Total	47(0.8)	11(0.4)

S1-A,B, S2-A,B,C and S3-A correspond to the main components in the image analysis workflow in Fig. 4.1B.

## 4.4 Discussion

Together, CT lung structure-function measurements and MRI function measurements provide a way to improve our understanding of pulmonary disease pathogenesis and perhaps more importantly, develop and evaluate novel regional therapies. Accordingly, here we developed and evaluated a fully automated pipeline to generate regional pulmonary structure-function measurements by jointly registering CT to  $^1\text{H}$  and  $^3\text{He}$  MRI in a coupled manner. We made some important observations including: 1) joint CT- $^1\text{H}/^3\text{He}$  MRI deformable registration resulted in significantly improved registration accuracy which is important for segmental measurements, 2) there were strong correlations for VDP generated using the joint registration approach with VDP estimated using a previously validated semi-automated method, and, 3) computational speed was consistent with research workflows.

To provide some context, we note that previously described methods [12, 13, 16, 17] relied on manual interactions to identify image features (i.e., landmarks, lung shapes), which require special expertise. In addition, such image features may not be readily available due to

image information content, image quality and physiological abnormalities. Yet other methods [18, 20] co-registered CT and MRI directly or indirectly without optimizing the use of <sup>1</sup>H MRI information and one of these [20] generated CT-<sup>3</sup>He MRI *TRE* of  $\sim 15$  mm in  $\sim 30$  min. In addition, the state-of-art B-spline free-form deformable registration approach [32] yielded an overall registration accuracy of  $5.5 \pm 2.1$  mm for *TRE*, which was significantly different from the proposed approach ( $p < 0.0001$ ), as shown in Table 4.2. These previous pioneering approaches motivated us to continue to discover and design optimal ways to co-register CT, <sup>1</sup>H and functional <sup>3</sup>He MRI. Our method is different from others because of the way we utilized <sup>1</sup>H MRI information by coupling the two individual registrations, rather than treating them separately. By optimizing <sup>1</sup>H MRI information, the CT-<sup>1</sup>H/<sup>3</sup>He MRI joint deformable registration approach achieved a registration accuracy of  $4.4 \pm 2.0$  mm for *TRE* and this was an improvement of  $\sim 2.8$  mm (or  $\sim 40\%$ ) compared to rigid registration methods. The joint registration approach employed image information from both <sup>1</sup>H and <sup>3</sup>He MRI and because <sup>3</sup>He MRI signal voids increase with increasing disease severity, it is more challenging to establish the CT-<sup>3</sup>He MRI correspondences in these cases. To address this important issue, it is important to consider weighting the similarity and/or the regularization terms of the registration model so that there is more weight for regions with greater inhaled gas MRI signal intensity and *vice versa*.

Multi-modality medical image registration is challenging and this is due in part due to the complexity in measuring the correspondence between images [26]. Here we employed a point-wise *self similarity context* that utilizes image signal intensity information for cross-modality image similarity measurements. We want to emphasize that other nonlinear global similarity metrics including mutual information [45] and cross correlation [46, 47] are widely used and may be adapted and incorporated into our registration framework. It is also important to note that previous studies [48] performed image registration by coupling geometric features such as image surfaces with image signal intensity information, and this may be useful for CT-<sup>3</sup>He MRI registration. Furthermore, individual lung registration, i.e., left-left and right-right lung registration, may warrant further investigation.

We observed improved joint CT- $^1\text{H}/^3\text{He}$  MRI registration accuracy as compared with registering CT to  $^1\text{H}$  or  $^3\text{He}$  MRI separately and this differs from previous studies [12, 13, 14, 15, 16, 17, 18, 20], where the value of complementary  $^1\text{H}$  and  $^3\text{He}$  MR image information was not fully exploited. Notably, previous methods treated the complementary  $^1\text{H}/^3\text{He}$  image information separately and registered CT to  $^1\text{H}$  or  $^3\text{He}$  MRI independently. In contrast, our work exploited the valuable complementary  $^1\text{H}/^3\text{He}$  MRI information explicitly by relating the two independent CT- $^1\text{H}$  MRI and CT- $^3\text{He}$  MRI registrations. Direct anatomic CT and functional  $^3\text{He}$  MRI registration is challenging due to the fundamentally different image information content and the presence of  $^3\text{He}$  signal voids. Consequently, CT may be inappropriately deformed to match  $^3\text{He}$  MRI especially in regions with low signal intensities (Fig. 4.4, row 3 column 1), leading to underestimation of whole lung or segmental VDP. This is important in severe lung disease, where there are large regions of MRI signal voids. Previous work [15, 17, 18, 20] also proposed to include  $^1\text{H}$  MRI to facilitate registration by registering CT and  $^1\text{H}$  MRI to  $^3\text{He}$  MRI individually and then summing the two separate registrations together. However, we previously observed significant CT- $^1\text{H}$  MRI registration inaccuracies (Fig. 4.4, row 2 column 2) because of poor  $^1\text{H}$  MR image quality [49]. By “adding” the individual registrations, these individual registration inaccuracies may propagate to the target CT- $^3\text{He}$  MRI registration and result in accumulated registration errors. It is in this context that we proposed a way to maximize the complementary  $^1\text{H}/^3\text{He}$  MRI information by relating the individual registrations in a coupled manner.

We constrained the similarity of the displacement field between individual CT- $^1\text{H}$  MRI and CT- $^3\text{He}$  MRI to provide information as to how to supervise each single registration. For example, single CT- $^1\text{H}$  MRI registration in problematic regions (Fig. 4.4, row 2 column 2) was enhanced with the guidance of single CT- $^3\text{He}$  MRI displacement field (Fig. 4.4, row 3 column 2), leading to the joint CT- $^1\text{H}/^3\text{He}$  MRI registration (Fig. 4.4, row 4 column 2) that was not significantly influenced by  $^1\text{H}$  MRI. We also observed that the joint CT- $^1\text{H}/^3\text{He}$  MRI registration displacement field (purple arrows within yellow inset boxes in Fig.4.4 row 4 column 2) shared

similarity with both single registration displacement field while dominated by CT-<sup>3</sup>He registration, and this supports the notion of a consistent displacement field *prior*. Similarly, with the guidance of single CT-<sup>1</sup>H MRI registration (Fig. 4.4, row 2 column 1), the joint CT-<sup>1</sup>H/<sup>3</sup>He MRI registration (Fig. 4.4, row 4 column 1) was not significantly compromised in the presence of problematic single CT-<sup>3</sup>He MRI registration (Fig. 4.4, row 3 column 1). Similarly, the joint registration displacement field (purple arrows within yellow inset boxes in Fig. 4.4 row 4 column 1) was similar to both single registration displacement field but dominated by CT-<sup>1</sup>H MRI registration. However, in situations where both single CT-<sup>1</sup>H and CT-<sup>3</sup>He MRI registration were suboptimal, the joint CT-<sup>1</sup>H/<sup>3</sup>He MRI registration must be optimized. Supplementary Fig. F.1 in Appendix F provides representative results using the consistent displacement field *prior* for CT-<sup>1</sup>H/<sup>3</sup>He MRI registration.

While we observed promising CT-<sup>3</sup>He MRI registration results by coupling complementary <sup>1</sup>H MRI information, we want to emphasize that the two single registrations require balance in order to assist rather than degrade the target CT-<sup>3</sup>He MRI registration. This was achieved by weighting the contributions of the two individual registrations and the consistent displacement field constraint. After registration, the three components (4.2), (4.3) and (4.7) contributed to the joint registration problem (4.8) by  $\sim 39\%$ ,  $\sim 61\%$  and  $\sim 0.2\%$ , respectively. The joint CT-<sup>1</sup>H/<sup>3</sup>He MRI deformable registration approach requires pre-registered <sup>3</sup>He-<sup>1</sup>H MRI and coarsely registered CT-<sup>1</sup>H MRI as inputs. Therefore, when <sup>3</sup>He-<sup>1</sup>H MRI registration and/or CT-<sup>1</sup>H MRI initial alignment are problematic, the joint CT-<sup>1</sup>H/<sup>3</sup>He MRI registration may be affected. However, these issues can be mitigated in a few ways. For example, it is important to note that we endeavoured to minimize breath-hold differences (and lung volumes) across scans by training and continuously coaching subjects during image acquisition. As a result, the <sup>3</sup>He and <sup>1</sup>H MRI are inherently registered and very minor co-registration effort is required. In situations where further <sup>3</sup>He-<sup>1</sup>H MRI registration refinements are required, the state-of-art registration methods provided by *NiftyReg* can be employed. In addition, we think that our joint registration approach may accommodate minor <sup>3</sup>He-<sup>1</sup>H MRI registration inaccuracies because two



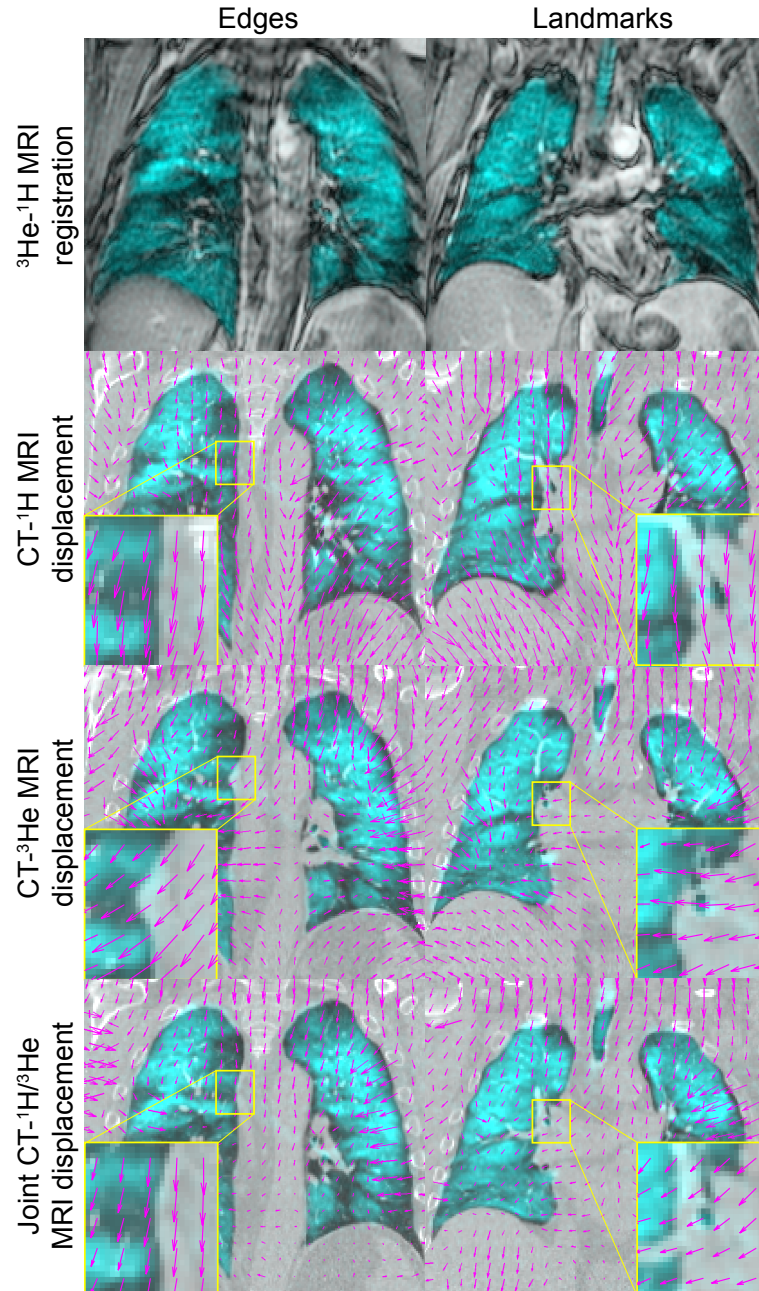


Figure 4.4: Illustration of joint  $CT-^1H/^3He$  MRI registration using consistent deformation *prior*. The 1<sup>st</sup> row shows representative registered  $^3He$  (cyan) and  $^1H$  (gray) MRI as inputs. The 2<sup>nd</sup>, 3<sup>rd</sup> and 4<sup>th</sup> rows show  $CT-^3He$  MRI registration by registering  $CT$  to  $^1H$  MRI (no  $^3He$  information),  $^3He$  MRI (no  $^1H$  information), and both  $^1H$  and  $^3He$  MRI, respectively, where the respective displacement fields (purple vectors) within the inset boxes are shown expanded in yellow boxes. The 1<sup>st</sup> column shows representative improvements of joint  $CT-^1H/^3He$  MRI registration on image edges compared with individual  $CT-^1H$  MRI and  $CT-^3He$  MRI registration, where the joint registration displacement field is consistent with both individual registration but dominated by  $CT-^1H$  MRI registration (no  $^3He$  information). The 2<sup>nd</sup> column shows similar results on image landmarks, where the joint registration displacement field is consistent with both individual registration but dominated by  $CT-^3He$  MRI registration (no  $^1H$  information). Note that  $CT-^1H$  MRI,  $CT-^3He$  MRI and joint  $CT-^1H/^3He$  MRI registration were independently optimized.

registrations are performed, rather than one, with greater weighting on CT-<sup>1</sup>H MRI alignment. Although the two registrations were related to each other in a coupled manner, the strength of the “similarity” constraint on the two displacement field may be adjusted to accommodate <sup>3</sup>He-<sup>1</sup>H MRI registration inaccuracies. Regarding CT-<sup>1</sup>H MRI initial alignment, it is important to note that our joint registration approach only requires coarse CT-<sup>1</sup>H MRI registration as a first step and subsequently refines the alignment by coupling <sup>3</sup>He MRI information. In situations where CT-<sup>1</sup>H MRI initial alignment is not sufficient, the deformable registration approach provided by *NiftyReg* may be employed and the generated deformation field could be used to initialize the following joint CT-<sup>1</sup>H/<sup>3</sup>He MRI deformable registration. These procedures could be employed to assure the general applicability of our approach.

The relatively small differences for the six sets of *TRE* measurements caused by altering the base CT-<sup>1</sup>H MRI rigid alignment suggest that the proposed joint deformable registration approach allows for relatively large CT-<sup>1</sup>H MRI initial registration errors. We note that the relatively large differences for *Translation<sub>yz</sub>* were due to the large translation components in the base CT-<sup>1</sup>H MRI rigid transformation matrixes. In addition, we observed small *TRE* changes (< 2.0%) after altering the weight ( $\beta$  in 4.8 of the similarity measurements between individual registration displacement field. These results suggest that the proposed joint CT-<sup>1</sup>H/<sup>3</sup>He MRI deformable registration approach is relatively insensitive to CT-<sup>1</sup>H MRI rigid registration inaccuracies and the weight of the consistent CT-<sup>1</sup>H and CT-<sup>3</sup>He MRI displacement field *prior*.

The GPU-based implementation of our approach required  $\sim 11$ min to generate segmental CT structure-<sup>3</sup>He MRI function measurements. The overall computational efficiency may be improved in several ways. For example, as shown in Fig. 4.1B, <sup>3</sup>He-<sup>1</sup>H MRI registration and CT-<sup>1</sup>H MRI rigid alignment can be performed in parallel; joint CT-<sup>1</sup>H/<sup>3</sup>He MRI deformable registration (S2-A), <sup>3</sup>He MRI ventilation segmentation (S2-B) and CT lung segments generation (S2-C) can also be implemented simultaneously. The GPU-optimized joint CT-<sup>1</sup>H/<sup>3</sup>He deformable registration required  $\sim 2.5$ min ( $\sim 50\%$  of the time for SSC calculation) compared

with  $\sim 40$ min for CPU-based implementation, and thus greatly enhanced the computational efficiency.

Although this work provides some promising results, we must acknowledge a number of limitations. Previous work suggested that global/local mutual information [50, 51] and cross-correlation [51, 46] may improve cross-modality image similarity measurements and registration performance. While we focused on point-wise image similarity measurements and *prior* knowledge, relaxation or bound optimization techniques [52] may also be employed to incorporate these nonlinear global metrics to the proposed registration framework. The proposed approach performed CT- $^3\text{He}$  MRI registration using full images without lung segmentation [53]. We want to emphasize that our approach provides a generic registration framework when segmentation is not readily available. In addition, we did not enforce that the registration was inverse consistent/symmetric or that the deformation was diffeomorphic, as previously demonstrated [44, 46], and this warrants further investigation. Furthermore, as there was no gold standard for CT- $^3\text{He}$  MRI fiducial pairs and there were  $^3\text{He}$  signal intensity voids where  $^3\text{He}$  fiducials could not be identified, we used manually identified CT- $^3\text{He}$  fiducial pairs on multiple occasions and calculated *TRE* in  $^3\text{He}$  MRI-ventilated lung regions. Therefore, *TRE* measurements were limited to lung regions with adequate inhaled gas MRI signal and this is certainly a limitation of our approach, especially in more severe lung disease where ventilation is highly abnormal. It is important to note that we are in the process of optimizing pulmonary MRI using hyperpolarized  $^{129}\text{Xe}$  gas, which is substantially more abundant and less expensive than  $^3\text{He}$  gas, making it more suitable for widespread clinical translation. We are also optimizing a novel pulmonary MRI method using ultra-short echo-time (UTE) sequences to provide enhanced visualization of pulmonary structures. We think UTE- $^{129}\text{Xe}$  MRI analysis may provide a promising alternative for regional pulmonary structure-function measurements and UTE- $^{129}\text{Xe}$  MRI registration and segmentation will be a focus of our future work. Finally, our approach incorporated external software (*Convert3D* and *NiftyReg*) to facilitate CT- $^3\text{He}$  MRI registration and regional lung structure-function measurements. For the pipeline, we integrated these Linux

tools and other image processing components (Fig. 4.1B) into a single Linux bash script that was fully automated on a Linux terminal. The outputs from these external software tools were automatically entered into the other components without user interaction. We also want to emphasize that we are in the process of developing C/C++ tools and integrating these components into a C/C++-based implementation with a graphical user interface for clinical users and applications.

## 4.5 Conclusion

Regional lung structure-function measurements provide a way to better understand pulmonary disease pathogenesis and develop optimal regional therapies for patients with obstructive lung disease. Here we developed a fully automated pulmonary CT-noble gas MRI image processing pipeline that is required for regional regional lung structure-function analysis. We evaluated the performance of our approach using a diverse patient dataset of 35 COPD and asthma subjects and achieved CT-<sup>3</sup>He MRI registration accuracy, regional structure-function measurements and workflow efficiency suitable for research and clinical applications.

## Bibliography

- [1] Jørgen Vestbo, Suzanne S Hurd, Alvar G Agustí, Paul W Jones, Claus Vogelmeier, Antonio Anzueto, Peter J Barnes, Leonardo M Fabbri, Fernando J Martinez, Masaharu Nishimura, et al. Global strategy for the diagnosis, management, and prevention of chronic obstructive pulmonary disease: GOLD executive summary. *American journal of respiratory and critical care medicine*, 187(4):347–365, 2013.
- [2] Stephen P Peters, Gary Ferguson, Yamo Deniz, and Colin Reisner. Uncontrolled asthma: a review of the prevalence, disease burden and options for treatment. *Respiratory medicine*, 100(7):1139–1151, 2006.

- [3] George R Washko, Grace Parraga, and Harvey O Coxson. Quantitative pulmonary imaging using computed tomography and magnetic resonance imaging. *Respirology*, 17(3):432–444, 2012.
- [4] Jonas Jögi, Björn Jonson, Marie Ekberg, and Marika Bajc. Ventilation–perfusion SPECT with  $^{99m}\text{Tc}$ -DTPA versus technegas: a head-to-head study in obstructive and nonobstructive disease. *Journal of Nuclear Medicine*, 51(5):735–741, 2010.
- [5] Harald E Möller, X Josette Chen, Brian Saam, Klaus D Hagspiel, G Allan Johnson, Talissa A Altes, Eduard E de Lange, and Hans-Ulrich Kauczor. MRI of the lungs using hyperpolarized noble gases. *Magnetic Resonance in Medicine*, 47(6):1029–1051, 2002.
- [6] Sean Fain, Mark L Schiebler, David G McCormack, and Grace Parraga. Imaging of lung function using hyperpolarized helium-3 magnetic resonance imaging: Review of current and emerging translational methods and applications. *Journal of Magnetic Resonance Imaging*, 32(6):1398–1408, 2010.
- [7] Miranda Kirby, Lindsay Mathew, Mohammadreza Heydarian, Roya Etemad-Rezai, David G McCormack, and Grace Parraga. Chronic obstructive pulmonary disease: quantification of bronchodilator effects by using hyperpolarized  $^3\text{He}$  MR imaging. *Radiology*, 261(1):283–292, 2011.
- [8] Giovanni Galluccio and Gabriele Lucantoni. Bronchoscopic lung volume reduction for pulmonary emphysema: preliminary experience with a new novatech® endobronchial silicone one-way valve. *Interactive cardiovascular and thoracic surgery*, 11(2):213–215, 2010.
- [9] Sonali Sethi and Joseph Cicensia. Treatment of PCP-related pneumothorax using one-way endobronchial valves. *CHEST Journal*, 134(4.MeetingAbstracts):p9002–p9002, 2008.
- [10] Thomas R Gildea, Sumita B Khatri, and Mario Castro. Bronchial thermoplasty: a new

- treatment for severe refractory asthma. *Cleveland Clinic journal of medicine*, 78(7):477–485, 2011.
- [11] Adil Al-Mayah, Joanne Moseley, Mike Velec, Shannon Hunter, and Kristy Brock. Deformable image registration of heterogeneous human lung incorporating the bronchial tree. *Medical physics*, 37(9):4560–4571, 2010.
- [12] Rob H Ireland, Chris M Bragg, Mark McJury, Neil Woodhouse, Stan Fischele, Edwin JR Van Beek, Jim M Wild, and Matthew Q Hatton. Feasibility of image registration and intensity-modulated radiotherapy planning with hyperpolarized helium-3 magnetic resonance imaging for non-small-cell lung cancer. *International Journal of Radiation Oncology\* Biology\* Physics*, 68(1):273–281, 2007.
- [13] Robert P Thomen, Ajay Sheshadri, James D Quirk, Jim Kozlowski, Henry D Ellison, Rhonda D Szczesniak, Mario Castro, and Jason C Woods. Regional ventilation changes in severe asthma after bronchial thermoplasty with <sup>3</sup>He MR imaging and CT. *Radiology*, 2014.
- [14] Rob H Ireland, Neil Woodhouse, Nigel Hoggard, James A Swinscoe, Bernadette H Foran, Matthew Q Hatton, and Jim M Wild. An image acquisition and registration strategy for the fusion of hyperpolarized helium-3 MRI and x-ray CT images of the lung. *Physics in medicine and biology*, 53(21):6055, 2008.
- [15] RH Ireland, N Woodhouse, JA Swinscoe, MQ Hatton, and JM Wild. Towards automatic image registration of hyperpolarized <sup>3</sup>He MRI and x-ray CT images of the lung. In *Proc. Int. Soc. Magn. Reson. Med.*, volume 17, page 2197, 2009.
- [16] Lindsay Mathew, Andrew Wheatley, Richard Castillo, Edward Castillo, George Rodrigues, Thomas Guerrero, and Grace Parraga. Hyperpolarized <sup>3</sup>He magnetic resonance imaging: comparison with four-dimensional x-ray computed tomography imaging in lung cancer. *Academic radiology*, 19(12):1546–1553, 2012.

- [17] Fumin Guo, Damien Pike, Sarah Svenningsen, Harvey O Coxson, John J Drozd, Jing Yuan, Aaron Fenster, and Grace Parraga. Development and application of pulmonary structure-function registration methods: towards pulmonary image-guidance tools for improved airway targeted therapies and outcomes. In *SPIE Medical Imaging*, pages 90380Y–90380Y. International Society for Optics and Photonics, 2014.
- [18] F Guo, S Svenningsen, E Bluemke, M Rajchl, J Yuan, A Fenster, and G Parraga. Automated pulmonary lobar ventilation measurements using volume-matched thoracic CT and MRI. In *SPIE Medical Imaging*, pages 941717–941717. International Society for Optics and Photonics, 2015.
- [19] Marc Modat, Gerard R Ridgway, Zeike A Taylor, Manja Lehmann, Josephine Barnes, David J Hawkes, Nick C Fox, and Sébastien Ourselin. Fast free-form deformation using graphics processing units. *Computer methods and programs in biomedicine*, 98(3):278–284, 2010.
- [20] Bilal A Tahir, Andrew J Swift, Helen Marshall, Juan Parra-Robles, Matthew Q Hatton, Ruth Hartley, Richard Kay, Christopher E Brightling, Wim Vos, Jim M Wild, et al. A method for quantitative analysis of regional lung ventilation using deformable image registration of CT and hybrid hyperpolarized gas/<sup>1</sup>H MRI. *Physics in medicine and biology*, 59(23):7267, 2014.
- [21] Brian B Avants, Nicholas J Tustison, Gang Song, Philip A Cook, Arno Klein, and James C Gee. A reproducible evaluation of ANTs similarity metric performance in brain image registration. *Neuroimage*, 54(3):2033–2044, 2011.
- [22] Ora Israel, Maya Mor, Diana Gaitini, Zohar Keidar, Luda Guralnik, Ahuva Engel, Alex Frenkel, Rachel Bar-Shalom, and Abraham Kuten. Combined functional and structural evaluation of cancer patients with a hybrid camera-based PET/CT system using <sup>18</sup>F-FDG. *Journal of Nuclear Medicine*, 43(9):1129–1136, 2002.

- [23] Alun J Lucas, Robert C Hawkes, Pedro Guerra, Richard E Ansorge, Robert E Nutt, John C Clark, Tim D Fryer, and T Adrian Carpenter. Development of a combined micro PET-MR system. In *Nuclear Science Symposium Conference Record, 2006. IEEE*, volume 4, pages 2345–2348. IEEE, 2006.
- [24] Heinz-Peter W Schlemmer, Bernd J Pichler, Matthias Schmand, Ziad Burbar, Christian Michel, Ralf Ladebeck, Kirstin Jattke, David Townsend, Claude Nahmias, Pradeep K Jacob, et al. Simultaneous MR/PET imaging of the human brain: Feasibility study1. *Radiology*, 248(3):1028–1035, 2008.
- [25] Ulas Bagci, Jayaram K Udupa, Neil Mendhiratta, Brent Foster, Ziyue Xu, Jianhua Yao, Xinjian Chen, and Daniel J Mollura. Joint segmentation of anatomical and functional images: Applications in quantification of lesions from PET, PET-CT, MRI-PET, and MRI-PET-CT images. *Medical image analysis*, 17(8):929–945, 2013.
- [26] Aristeidis Sotiras, Christos Davatzikos, and Nikos Paragios. Deformable medical image registration: A survey. *Medical Imaging, IEEE Transactions on*, 32(7):1153–1190, 2013.
- [27] Fumin Guo, Jing Yuan, Martin Rajchl, Sarah Svenningsen, Dante PI Capaldi, Khadija Sheikh, Aaron Fenster, and Grace Parraga. Globally optimal co-segmentation of three-dimensional pulmonary <sup>1</sup>H and hyperpolarized <sup>3</sup>He MRI with spatial consistence prior. *Medical image analysis*, 23(1):43–55, 2015.
- [28] Klaus F Rabe, Suzanne Hurd, Antonio Anzueto, Peter J Barnes, Sonia A Buist, Peter Calverley, Yoshinosuke Fukuchi, Christine Jenkins, Roberto Rodriguez-Roisin, Chris van Weel, et al. Global strategy for the diagnosis, management, and prevention of chronic obstructive pulmonary disease: GOLD executive summary. *American journal of respiratory and critical care medicine*, 176(6):532–555, 2007.
- [29] Global Initiative for Asthma (GINA). Global strategy for asthma management and prevention. <http://www.ginasthma.org/>, 2015.



- [30] Miranda Kirby, Sarah Svenningsen, Amir Owrangi, Andrew Wheatley, Adam Farag, Alexei Ouriadov, Giles E Santyr, Roya Etemad-Rezai, Harvey O Coxson, David G McCormack, et al. Hyperpolarized  $^3\text{He}$  and  $^{129}\text{Xe}$  MR imaging in healthy volunteers and patients with chronic obstructive pulmonary disease. *Radiology*, 265(2):600–610, 2012.
- [31] Sébastien Ourselin, Alexis Roche, Gérard Subsol, Xavier Pennec, and Nicholas Ayache. Reconstructing a 3D structure from serial histological sections. *Image and vision computing*, 19(1):25–31, 2001.
- [32] Daniel Rueckert, Luke I Sonoda, Carmel Hayes, Derek LG Hill, Martin O Leach, and David J Hawkes. Nonrigid registration using free-form deformations: application to breast MR images. *IEEE transactions on medical imaging*, 18(8):712–721, 1999.
- [33] Miranda Kirby, Mohammadreza Heydarian, Sarah Svenningsen, Andrew Wheatley, David G. McCormack, Roya Etemad-Rezai, and Grace Parraga. Hyperpolarized  $^3\text{He}$  magnetic resonance functional imaging semiautomated segmentation. *Academic Radiology*, November 2011.
- [34] Jacques Hadamard. *Lectures on Cauchy’s problem in linear partial differential equations*. Courier Dover Publications, 2003.
- [35] Mattias Paul Heinrich, Mark Jenkinson, Bartłomiej W Papież, Michael Brady, and Julia A Schnabel. Towards realtime multimodal fusion for image-guided interventions using self-similarities. In *Medical Image Computing and Computer-Assisted Intervention–MICCAI 2013*, pages 187–194. Springer, 2013.
- [36] Thomas Pock, Martin Urschler, Christopher Zach, Reinhard Beichel, and Horst Bischof. A duality based algorithm for TV-L1 optical-flow image registration. In *Medical Image Computing and Computer-Assisted Intervention–MICCAI 2007*, pages 511–518. Springer, 2007.

- [37] Yue Sun, Jing Yuan, Wu Qiu, Martin Rajchl, Cesare Romagnoli, and Aaron Fenster. Three-dimensional nonrigid MR-TRUS registration using dual optimization. *IEEE transactions on medical imaging*, 34(5):1085–1095, 2015.
- [38] Martin Rajchl, John SH Baxter, Wu Qiu, Ali R Khan, Aaron Fenster, Terry M Peters, and Jing Yuan. RANCOR: Non-linear image registration with total variation regularization. *arXiv preprint arXiv:1404.2571*, 2014.
- [39] Maximilian Baust, Darko Zikic, Nassir Navab, and GER Munich. Diffusion-based regularisation strategies for variational level set segmentation. In *BMVC*, pages 1–11, 2010.
- [40] Dimitri P Bertsekas. *Nonlinear programming*. 1999.
- [41] Paul A Yushkevich, Joseph Piven, Heather Cody Hazlett, Rachel Gimpel Smith, Sean Ho, James C Gee, and Guido Gerig. User-guided 3D active contour segmentation of anatomical structures: significantly improved efficiency and reliability. *Neuroimage*, 31(3):1116–1128, 2006.
- [42] Jan-Martin Kuhnigk, Volker Dicken, Stephan Zidowitz, Lars Bornemann, Bernd Kuemmerlen, Stefan Krass, Heinz-Otto Peitgen, Silja Yuval, Hans-Holger Jend, Wigbert S Rau, et al. New tools for computer assistance in thoracic CT. Part 1. functional analysis of lungs, lung lobes, and bronchopulmonary segments 1. *RadioGraphics*, 25(2):525–536, 2005.
- [43] J Michael Fitzpatrick, Jay B West, and Calvin R Maurer Jr. Predicting error in rigid-body point-based registration. *Medical Imaging, IEEE Transactions on*, 17(5):694–702, 1998.
- [44] Mattias P Heinrich, Mark Jenkinson, Manav Bhushan, Tahreema Matin, Fergus V Gleeson, Sir Michael Brady, and Julia A Schnabel. MIND: Modality independent neighbourhood descriptor for multi-modal deformable registration. *Medical Image Analysis*, 16(7):1423–1435, 2012.

- [45] Josien PW Pluim, JB Antoine Maintz, and Max A Viergever. Mutual-information-based registration of medical images: a survey. *Medical Imaging, IEEE Transactions on*, 22(8):986–1004, 2003.
- [46] Brian B Avants, Charles L Epstein, Murray Grossman, and James C Gee. Symmetric diffeomorphic image registration with cross-correlation: evaluating automated labeling of elderly and neurodegenerative brain. *Medical image analysis*, 12(1):26–41, 2008.
- [47] Wolfgang Wein, Shelby Brunke, Ali Khamene, Matthew R Callstrom, and Nassir Navab. Automatic CT-ultrasound registration for diagnostic imaging and image-guided intervention. *Medical image analysis*, 12(5):577–585, 2008.
- [48] Anand Joshi, Richard Leahy, Arthur W Toga, and David Shattuck. A framework for brain registration via simultaneous surface and volume flow. In *International Conference on Information Processing in Medical Imaging*, pages 576–588. Springer, 2009.
- [49] CJ Bergin, JM Pauly, and A Macovski. Lung parenchyma: projection reconstruction MR imaging. *Radiology*, 179(3):777–781, 1991.
- [50] Peter Rogelj, Stanislav Kovačič, and James C Gee. Point similarity measures for non-rigid registration of multi-modal data. *Computer vision and image understanding*, 92(1):112–140, 2003.
- [51] Mattias P Heinrich, Mark Jenkinson, Manav Bhushan, Tahreema Matin, Fergus V Gleeson, J Michael Brady, and Julia A Schnabel. Non-local shape descriptor: A new similarity metric for deformable multi-modal registration. In *Medical Image Computing and Computer-Assisted Intervention—MICCAI 2011*, pages 541–548. Springer, 2011.
- [52] Junhwan Kim, Vladimir Kolmogorov, and Ramin Zabih. Visual correspondence using energy minimization and mutual information. In *Computer Vision, 2003. Proceedings. Ninth IEEE International Conference on*, pages 1033–1040. IEEE, 2003.

- [53] Keelin Murphy, Bram Van Ginneken, Joseph M Reinhardt, Sven Kabus, Kai Ding, Xiang Deng, Kunlin Cao, Kaifang Du, Gary E Christensen, Vincent Garcia, et al. Evaluation of registration methods on thoracic CT: the EMPIRE10 challenge. *Medical Imaging, IEEE Transactions on*, 30(11):1901–1920, 2011.

# Chapter 5

## Conclusions and Future Directions

*In this final chapter, I will provide an overview of the research questions and summarized the important findings and conclusions of Chapters 2–4. I will also provide general and study-specific limitations of this thesis with some potential solutions. Finally, based on these findings, I will discuss some future directions of pulmonary MRI studies.*

### 5.1 Overview of Rationale and Research Objectives

COPD and asthma represent a staggering burden on patients, economies and health-care systems worldwide. Despite decades of research, therapeutic interventions than can modify COPD and asthma patient outcomes are still lacking partly due to their high dependence on spirometry measurements made at the mouth [1]. In other words, COPD and asthma are universally diagnosed and monitored based on airflow limitations using FEV<sub>1</sub> measured at the mouth as the primary endpoints [1]. Simple and inexpensive, FEV<sub>1</sub> provides only a global sum of contributions of different pathologies and is insensitive to subtle changes and treatment responses [2, 3]. Therefore, there is an urgent need to develop novel biomarkers to regionally evaluate COPD and asthma.

It has been recently recognized that, in COPD and asthma, the structural and functional abnormalities are regionally heterogeneous [2, 4]. This novel information may be employed to optimize treatment plans, monitor interventional efficacy and develop new treatments. The re-

cent developments in hyperpolarized noble gas ( $^3\text{He}/^{129}\text{Xe}$ ) MRI open a way to understanding the regional nature of pulmonary structural and functional abnormalities. In noble gas MRI, lung function is typically quantified based on signal intensity, which is interpreted as “ventilation”, and regions of signal voids are referred to as ventilation defects that are believed to represent areas of the lung that do not participate in gas distribution [5]. A commonly used noble gas MRI biomarker is ventilation defect percent, which is calculated by normalizing noble gas ventilation defect volumes to the lung cavity. In addition, recent developments in  $^1\text{H}$  MR image acquisition and processing techniques provide a way for visualization and quantification of pulmonary structure and function using existing hospital equipment without exogenous contrast agents. For example, Fourier decomposition of free-breathing MRI (FDMRI) [6] allows for visualization and quantification of pulmonary ventilation/perfusion and multi-volume MRI registration [7, 8] permits assessments of regional lung function. Furthermore, MRI acquisition using ultra-short echo-time (UTE) sequences provides enhanced visualization of lung structure comparable to CT [9]. Moreover, registration of the complementary structural information from CT and functional information from noble gas MRI provides promising potential for better understanding pulmonary disease mechanisms and developing novel treatments [10, 11, 12] for improved patient outcomes.

Clearly, the quantitative evaluation of the regional lung structural and functional information derived from noble gas MRI, conventional  $^1\text{H}$  MRI, and combined CT-noble gas MRI is highly dependent on lung cavity segmentation and cross-modality image registration. However, structural and functional MRI lung segmentation and registration are particularly challenging due to a number of reasons, i.e., low tissue and MRI signal intensity, signal intensity inhomogeneity, magnetic susceptibility, motion artifacts, dramatic changes in lung shapes and protruding vessels. Previous studies have shown that the incorporation of image information from multiple imaging methods [13, 14, 15] and use of high level *prior* knowledge [16, 17] may benefit image analysis. Therefore, the specific objectives of this thesis were: 1) simultaneous lung segmentation from conventional  $^1\text{H}$  and noble gas MRI by coupling the

complementary structural and functional information from respective images (**Chapter 2**), 2) conventional  $^1\text{H}$  MRI (in the absence of noble gas MRI) multi-region segmentation using the known left-to-right lung volume proportion *prior* for regional quantification of lung structural and functional abnormalities (**Chapter 3**), and, 3) deformable CT- $^3\text{He}$  MRI registration under the guidance of complementary CT- $^1\text{H}$  MRI registration to generate lobar and segmental lung structure-function measurements (**Chapter 4**).

## 5.2 Summary and Conclusions

In Chapter 2, a joint segmentation algorithm was developed to segment the lung from pulmonary  $^1\text{H}$  MRI by incorporating the associated hyperpolarized  $^3\text{He}$  MRI information for the purpose of understanding the regional nature of pulmonary structural-functional abnormalities. The joint segmentation problem was formulated as a *coupled continuous min-cut model* and the challenging combinatorial optimization problem was solved globally and exactly by means of convex relaxation. A *coupled continuous max-flow model* that is dual to the convex relaxed *min-cut* formulation was introduced by means of primal-dual variational analysis. The simpler *max-flow* formulation gave rise to an efficient duality-augmented *coupled continuous max-flow* algorithm that was implemented on a graphics processing unit for speed-up. For a clinical dataset of 25 COPD patients ranging in disease severities, an overall *DSC* of  $91.0 \pm 2.8\%$ , *RMSE* of  $4.3 \pm 0.7$  mm,  $|\delta V_E|$  of  $0.42 \pm 0.31$  L and  $|\delta V_P|$  of  $8.8 \pm 6.3\%$  as well as high agreement between algorithm and expert manual lung volumes were achieved. Importantly, significant differences in *DSC*, *RMSE*, *MAXD*,  $\delta V_E$ ,  $\delta V_P$ ,  $|\delta V_E|$  and  $|\delta V_P|$  between the co-segmentation and single  $^1\text{H}$  MRI segmentation were observed (all  $p < 0.0001$ ), suggesting the effectiveness and superiority of incorporating image features from multi-modalities. In addition, two inexperienced observers initialized the algorithm on multiple occasions and low *CoV* ( $< 1\%$  for *DSC* and  $< 5\%$  for *RMSE*) and high *ICC* ( $> 0.97$  for both *DSC* and *RMSE*) were achieved, suggesting that the algorithm is able to generate highly reproducible noble gas MRI structure-function mea-

surements. Furthermore, the GPU-based implementation required  $\sim 25$  s with diminished user interaction and this highlights the potential for efficient clinical workflow using this approach.

With the advancements in novel  $^1\text{H}$  MRI image processing and acquisition methods, i.e., FD MRI, UTE MRI, and multi-volume  $^1\text{H}$  MRI analysis, there is potential to provide regional lung structure-function measurements in the absence of noble gas MRI. In Chapter 3, a general segmentation algorithm was developed to extract the lung from  $^1\text{H}$  MRI for quantitative measurements of pulmonary structural-functional abnormalities. The *prior* knowledge that the right lung is approximately 1.15 times larger than the left lung was employed to assist the segmentation. This *prior* information was incorporated into a Potts model and a *volume proportion-preserved Potts model* was derived, which was approximated through convex relaxation and further represented by a dual *volume proportion-preserved max-flow model*. This formulation led to a linear optimization problem with convex and linear equality constraints that implicitly encoded the proportion *prior*. Two observers initialized the segmentation algorithm by seeding each lung and background of five healthy and 15 asthma subjects five times on five different days. *DSC* of  $91\pm 3\%$  for the left lung,  $92\pm 2\%$  for the right lung, and  $91\pm 2\%$  for the whole lung with *RMSE* of  $4\pm 1$  mm for all three measurements as well as high agreement between algorithm and manually-generated left, right and whole lung volumes were observed. For the two observers, intra- and inter-*CoV* (*ICC*) were  $< 0.5\%$  ( $> 0.91$ ) for *DSC* and  $< 4.5\%$  ( $> 0.93$ ) for *RMSE* for whole lung segmentation. In addition, improvements in lung segmentation leakage compared to a two-region segmentation method, decrease in *SD* for *DSC*, and greater improvements in left lung segmentation than the right lung using the proportion *prior* was observed. This speaks to the advantages of the proposed *volume proportion-preserved* multi-region  $^1\text{H}$  MRI segmentation approach. These findings indicate that the segmentation algorithm may provide the necessary and sufficient accuracy, reproducibility and speed for large-scale and multi-center clinical applications of pulmonary  $^1\text{H}$  MRI.

In Chapter 4, a deformable registration approach was developed to generate regional (lobar and segmental) CT-noble gas MRI structure-function measurements. CT was jointly registered



to pre-registered  $^1\text{H}$  and  $^3\text{He}$  MRI by enforcing the similarity of the displacement field from the two individual registrations. A coarse-to-fine registration framework, variational analysis methods were employed and a dual registration model was derived to solve the original optimization problem under a primal-dual perspective. The dual optimization model gave rise to a multiplier-augmented numerical solver that was parallelized on a graphics processing unit for speed-up. CT- $^3\text{He}$  MRI registration accuracy was measured using *TRE* with repeatedly-identified CT and  $^3\text{He}$  MRI fiducial markers, and the algorithm-generated  $^3\text{He}$  MRI whole lung VDP was compared with a semi-automated reference method. For a diverse group of patients with COPD and asthma, a mean *TRE* of  $4.4 \pm 2.0$  mm was achieved with *FLE* of 0.16 mm for  $^3\text{He}$  MRI and 0.34 mm for CT, respectively. Whole lung VDP generated using the pipeline was strongly correlated ( $r = 0.93$ ,  $p < 0.0001$ ) with the reference method with no significant differences ( $p = 0.37$ ). The fully automated pipeline required  $11 \pm 0.4$  min for GPU-based implementation and these findings suggest that the algorithm provides a way to incorporate regional lung CT- $^3\text{He}$  MRI biomarkers into clinical research and patient care.

## 5.3 Limitations

### 5.3.1 General Limitations

This thesis focused on developing and evaluating pulmonary MRI and CT image processing and analysis algorithms. While evaluation is important to determining the performance of these algorithms and it is extremely difficult to obtain the ground truth, repeated lung segmentation and fiducial identification provided by experienced observers were used as reference standards. Although highly reproducible, these ground truth surrogates may not be perfect, and the sources of the measured disagreement between algorithm results and the “ground truth” cannot be ascertained. In addition, the segmentation algorithms in Chapters 2 and 3 were not fully automated although diminished user interaction was involved. However, previous studies [18, 19] have demonstrated the advantages of such user interactions, i.e., flexibility in refining

and updating the results, and these diminished interactions may be clinically-acceptable and consistent with clinical workflow efficiency. In addition, a fully-automated  $^1\text{H}$  MRI segmentation algorithm has been recently developed, which will be discussed later. The automated segmentation algorithm has been applied to a number of UTE MR images which are extremely challenging to segment. Visual inspection demonstrated the promising potential of this approach for UTE MRI lung segmentation.

Another limitation is that in Chapters 2 and 3, the original images were interpolated prior to segmentation for isotropic segmentation regularization in all the three directions. Alternatively, it is possible to implement anisotropic or independent (regularize one direction more than the others) regularization of the original images without interpolation.

The lung segmentation and registration algorithms presented here were evaluated using pulmonary MRI (anatomical  $^1\text{H}$ ,  $^3\text{He}/^{129}\text{Xe}$ , free-breathing and UTE MRI) acquired at 3.0 Tesla. Currently, both 1.5 Tesla and 3.0 Tesla MR systems are widely used clinically. A few studies have investigated the influence of main magnetic field strength on lung images and biomarkers. For example, a previous study [20] compared  $^3\text{He}$  MRI at 1.5 Tesla (48.6 MHz) and 3.0 Tesla (97.3 MHz) using a similar single-channel, rigid, transmit/receive elliptical chest coils with multi-slice 2D fast-spoiled gradient-recalled echo [FGRE], and reported no significant differences in imaging biomarker measurements. This suggests that the image segmentation and registration algorithms developed here, can be translated to 1.5 Tesla systems. Previous studies have shown that lung  $T2^*$  is  $>2.0$  ms at 1.5 Tesla [20] and 0.4–0.9 ms [21, 22] at 3.0 Tesla. The typical echo-time (TE) is 0.01–0.1 ms for UTE [23, 24] and 1.0 ms for FGRE/balanced steady-state free precession [bSSFP] [25] at 3.0 Tesla. UTE MRI overcomes the challenges of very short  $T2^*$  (0.01–0.1 ms  $<$  0.4 ms). Therefore, it is expected that the 3.0 Tesla MR systems provide improved image quality as compared to 1.5 Tesla because of greater thermal polarization of protons (10 ppm vs 5 ppm). However, this does not mean that UTE MRI of the lung is impossible at 1.5 Tesla [26], and further evaluation/verification is required to determine the utility of the presented image processing algorithms for 1.5 Tesla systems. For

conventional  $^1\text{H}$  MRI (FGRE and bSSFP sequences),  $T2^*$  for lung tissue is larger than TE at 1.5 Tesla ( $2.0\text{ ms} > 1.0\text{ ms}$ ) [20] and shorter at 3.0 Tesla ( $0.9\text{ ms} < 1.0\text{ ms}$ ) [25]. Therefore, it is expected that conventional  $^1\text{H}$  MRI (FGRE and bSSFP) lung signal intensities are greater at 1.5 Tesla than 3.0 Tesla [20]. Image distortion is another factor that influences the performance of image processing algorithms. It is well recognized that the main magnetic field inhomogeneity causes image distortion but this is substantially less obvious at 1.5 Tesla. It should also be noted that different MRI scanner manufacturers employ different shimming methods to improve the main magnetic field inhomogeneity. For these reasons, while we do not expect major challenges when translating the presented segmentation and registration algorithms to 1.5 Tesla pr different scanner systems, we need to be aware of potential issues.

Finally, it is worth noting that the developed segmentation and registration algorithms in Chapters 2–4 were implemented through Linux command lines rather than a graphical user interface (GUI), which is urgently required for widespread clinical applications of these algorithms. With this regard, I am currently developing a GUI-based platform to integrate these algorithms and to provide straightforward algorithm implementation and results visualization.

### 5.3.2 Specific Limitations

**Chapter 2:**  $^1\text{H}$  and  $^3\text{He}$  MRI were jointly segmented by enforcing the similarity of individual image segmentation. However, the characteristic regions of signal voids in  $^3\text{He}$  MRI may render the “similarity” *prior* invalid (i.e., the individual segmentation may be different) although the way of coupling  $^1\text{H}$  and  $^3\text{He}$  MRI information was optimized. To mitigate the “contradicting” effects and facilitate  $^1\text{H}$  MRI segmentation,  $^3\text{He}$  MRI information may be incorporated as an additional channel to  $^1\text{H}$  MRI but without imposing the “similarity” *prior* ( $u_1 \approx u_2$ ). For example, fused  $^1\text{H}$ - $^3\text{He}$  MRI signal intensity  $\{I_H, I_{He}\}$  information instead of  $\{I_H\}$  may be used to generate new data term and the regularization term will be dominated by  $^1\text{H}$  MRI edge information. This formulation does not impose the similarity *prior* but may lead to further issues. For example, model-fitting approaches are not suitable for separating high dimensional image

features and are prone to local minima [27]. In addition, other features such as spatial proximity may be useful for segmentation. In this regard, new features in the form of  $\{I_H, I_{He}, X, Y, Z\}$ , where  $X, Y$  and  $Z$  represent the spatial location of voxels, may be exploited. Previous studies [28, 29] have shown that such complex image features are non-linearly separable but can be well identified using kernel-based approaches. These approaches map the original features into a higher-dimensional Hilbert space, leading to simple linear separation in the new space. This feature formulation may lead to improved segmentation performance but the associated high-order data terms are challenging to optimize directly. Bound optimization techniques [30] may be employed to simplify the original challenging optimization problem by iteratively optimizing the upper-bound formulation until convergence, as previously demonstrated [31]. Another limitation is that the accuracy or reproducibility of the clinically-relevant measurements, i.e.,  $^3\text{He}$  MRI VDP, was not evaluated, and this will be performed in the future. In addition, the segmentation algorithm will be released to the pulmonary imaging research community.

**Chapter 3:** A general  $^1\text{H}$  MRI multi-region segmentation approach was developed to evaluate lung structure and function using advanced  $^1\text{H}$  MRI image processing and acquisition methods in the absence of noble gas MRI. The relationship of the left and right lung volume sizes was investigated to develop a left-to-right lung volume ratio ( $\sim 1/1.15$ ) preserved multi-region segmentation approach. The constant left-to-right lung volume ratio may limit the application of this approach for patients with pathologies, i.e., congenital diaphragmatic hernia and tumors. To generalize this approach, the left-to-right lung volume ratio may be constrained to a range or following a learned distribution *prior* [32]. Similarly, the interactive segmentation approach may be automated using the aforementioned iterative bound optimization techniques [31]. In addition, the segmentation approach was not tested on  $^1\text{H}$  MR images acquired using other methods, i.e., ultra-short echo-time (UTE) MRI, which demonstrate promising potential for lung disease care. UTE MRI provides exquisite visualization of lung structures using short echo-time pulse sequences to minimize the free-induction decay of MR signals and to improve image signal intensities and the contrast in lung parenchyma. While this approach is ideally

suites for studying lung disease especially for patients in whom radiation burden is a major concern, it must be acknowledged that the required image processing, especially lung segmentation, is extremely challenging. Moving forward, the proposed adaptive kernel K-means approach that is capable of incorporating high-dimensional image features may help with the challenging segmentation problem. Furthermore, with the rapid developments of  $^1\text{H}$  MRI acquisition methods, there is the possibility to visualize lung lobes using  $^1\text{H}$  MRI techniques in the future. Accordingly, there is a need to identify lung lobes and/or segments in  $^1\text{H}$  MRI for lung disease management and the proposed volume ratio-preserved multi-region segmentation approach might help.

**Chapter 4:** A deformable registration algorithm was developed to register CT to spatially-aligned  $^1\text{H}$  and  $^3\text{He}$  MRI by enforcing the similarity of the displacement fields from the two individual registrations. The joint registration approach enforced a uniform similarity of the two individual displacement fields. The study subjects present different levels of  $^3\text{He}$  ventilation defects ( $\sim 15\%$ ) and this may confound the use of the uniform “similarity” *prior*. This limitation may be mitigated by weighting the similarity of the displacement fields based on  $^3\text{He}$  MRI signal intensities - more similar displacement fields in higher  $^3\text{He}$  MRI signal intensity regions and *vice versa*. The deformable registration algorithm was not symmetric or diffeomorphic, but this may be implemented following the previous methods [33, 34] to mitigate the biases of choosing fix/moving images. In addition, robust cross-modality image similarity measurements including cross-correlation and mutual information may be incorporated into the registration framework to improve the registration performance but this may lead to challenging optimization problems. Bound optimization techniques [35, 30] provide a way to simplify high-order optimization problems and may be employed to optimize these similarity measurements. Furthermore, the registration approach was not evaluated using  $^{129}\text{Xe}$  MRI, which is more abundant in nature and relatively less expensive as compared to  $^3\text{He}$ , making it more suitable for widespread clinical applications. Another limitation is that the obtained lobar or segmental structure-function measurements were not quantitatively validated because of the

lack of reference standard.

## 5.4 Future Directions

### 5.4.1 2D Free-Breathing $^1\text{H}$ MRI Ventilation Measurements Pipeline

In Chapters 2 and 4, pulmonary MRI and CT segmentation and registration methods were developed to generate and quantify whole lung and regional ventilation maps with the use of inhaled noble gas MRI. These noble gas MRI-derived imaging biomarkers provide promising potential for a better understanding of lung disease mechanisms, monitoring disease progression and developing novel treatments. It is well also recognized that the recent developments of MR image acquisition and processing techniques provide another way to regionally evaluate lung disease using existing MR systems, making them ideally suitable for broad, large-scale, serial and longitudinal evaluations of patients with lung disease including children.

For example, Fourier decomposition of free-breathing pulmonary magnetic resonance imaging (FDMRI) provides a way to visualize and quantify pulmonary ventilation and perfusion without the need for exogenous contrast [6]. FDMRI exploits fast acquisition and deformable registration of a series of free-breathing conventional pulmonary  $^1\text{H}$  MR images. In the spatially aligned images, MRI signal intensity oscillations over time can be decomposed using Fast Fourier Transforms to generate functional ventilation and perfusion maps[36]. Although highly promising, widespread clinical translation has been slow due to a number of reasons including complex image processing components. For example, deformable registration of a whole lung image series is challenging due to the large deformation associated with breathing. Previous studies [37] have demonstrated that image registration can be improved by isolating the object of interest to mitigate the influences from the background. In addition, quantitative evaluation of the derived functional information fundamentally requires lung cavity segmentation. With this regard, the objective was to develop a free-breathing  $^1\text{H}$  MRI lung series segmentation, registration and FD ventilation quantification pipeline to facilitate broad research and clinical

applications of FDMRI.

#### 5.4.1.1 Free-Breathing <sup>1</sup>H MRI Lung Series Multi-Region Segmentation

A *coupled Potts model* was proposed to simultaneously segment <sup>1</sup>H MRI lung series  $I(x) = \{I_i(x), i \in 1 \dots N\}$ ,  $x \in \Omega$ , into the left lung  $\mathcal{R}_{ll}$ , right lung  $\mathcal{R}_{rl}$  and the background  $\mathcal{R}_b$  by employing the inherent similarity of the lung between adjacent slices. Let  $\xi_l(x)$ ,  $l \in L = \{ll, rl, b\}$ , be the indicator function for the segmentation of region  $\mathcal{R}_l$  with  $\xi_l(x) = 1$  for  $x \in \mathcal{R}_l$  and 0 otherwise. Observers placed seeds in the left lung, right lung and background to generate appearance models with *prior* knowledge of each region and to determine the cost  $\rho_l(x)$  [18] for assigning a label  $\xi_l(x)$  to a pixel  $x$ ,  $l \in L$ . The overall <sup>1</sup>H MRI lung series segmentation model was formulated as follows:

$$\min_{\xi_l^i \in \{0,1\}} \sum_{i=1}^N \left\{ \sum_{l \in L} \langle \xi_l^i, \rho_l^i \rangle + \int_{\Omega} g(x) |\nabla \xi_l^i| dx \right\} + \alpha \cdot \sum_{i=1}^{N-1} \sum_{l \in L} \int_{\Omega} |\xi_l^i - \xi_l^{i+1}| dx, \quad (5.1)$$

where  $\alpha > 0$  balances the weight of the Potts energy [38] and the dissimilarity of adjacent image segmentation, and  $g(x)$  was calculated based on image edges.

The segmentation model (5.1) is non-convex and the optimization problem is challenging to solve directly. Here the original segmentation model was approximated by relaxing (5.1) to the continuous domain, i.e.,  $\xi_l(x) \in [0, 1]$ ,  $l \in L$  [38]. The convex-relaxed model was further simplified by deriving an equivalent *coupled continuous max-flow model* as follows:

$$\max_{p^s, p^l, q^l, r^l} \sum_{i=1}^N \int_{\Omega} p_s^i(x) dx, \quad (5.2)$$

subject to a series of linear equality and convex constraints following the variational analysis similar to that in Chapter 2. The simplified *coupled continuous max-flow* model was formulated in a Lagrangian form and an efficient *coupled continuous max-flow* algorithm was developed to derive the globally optimal lung series segmentation  $\xi_l^i(x)$ ,  $l \in L$ ,  $i \in \{1 \dots N\}$ .

### 5.4.1.2 Free-Breathing $^1\text{H}$ MRI Lung Series Registration

The segmented lung series were registered to a slice  $I_0(x)$  at the end of inhalation phase using a three-level coarse-to-fine deformable registration framework to account for large deformation and to improve the computational efficiency. A pixel-wise modality-independent-neighbourhood-descriptor (*MIND*) [34] was employed to measure the similarity between  $I_0(x)$  and  $I_i(x)$ ,  $i \in \{1 \dots N\}$ , and the total-variation of the estimated displacement field was used to regularize the registration problem in the  $l^{\text{th}}$  level as follows:

$$\min_{t(x)} \int_{\Omega} \left| \text{MIND}_0^l(x) - \text{MIND}_i^l(x + T^{l-1} + t^l) \right| dx + \alpha \sum_{d \in \{X, Y\}} \int_{\Omega} \left| \nabla (T_d^{l-1} + t_d^l)(x) \right| dx, \quad (5.3)$$

where  $T_d^{l-1}(x)$  is the displacement field from the  $(l-1)^{\text{th}}$  level,  $t_d^l(x)$  represents the displacement field estimated from the current level  $l$  in direction  $d$ , and  $\alpha$  balances the weight of the similarity and regularization terms. Through optical flow estimation and variational analysis similar to that in Chapter 4, the original registration problem (5.3) can be re-written in a much simpler form by introducing two dual variables  $\omega$  and  $q$  as follows:

$$\max_{|w, q| \leq 1, \alpha} \int_{\Omega} (w \cdot P_0 + \sum_{d=1}^2 T_d^{i-1} \cdot \text{div } q_d) dx \quad (5.4)$$

under the constraint:  $\text{div } q_d - w \cdot \partial_d P = 0$ , where  $P_0$  and  $P$  were calculated as previously described [39]. The displacement field  $t_d^l$  of the current level was decomposed into a series of incremental displacement field that acted as multipliers of the constraints. Therefore, a convex optimization-based deformable registration algorithm was designed following the previous analysis in Chapter 4. All the pair-wise lung registrations (5.3) were implemented in parallel to further improve the computational efficiency of the workflow.

### 5.4.1.3 Fourier Decomposition Analysis

With the registered lung series aligned along the time axis, Fast Fourier transforms of MR signal intensity oscillations for each pixel  $x$  and the concurrently acquired respiratory bellow



data were performed. The frequency of the first ventilation harmonic, corresponding to the respiratory rate, was determined. The magnitude of the MRI signal frequency spectrum at the determined ventilation frequency was used to generate the FD ventilation measurements, as previously described [36]. In the derived FD ventilation map, ventilation defects were determined using a hierarchical K-means approach and quantified as ventilation defect percent (VDP), as previously described [5].

#### 5.4.1.4 A FDMRI Pipeline and Preliminary Results

These individual image processing components were integrated into a pipeline that was implemented on a Linux Desktop (CentOS 6.7, 16 G RAM, Inter(R) i7-3770, 3.4 GHz) with a NVIDIA graphics processing unit (GeForce, GTX TITAN BLACK, NVIDIA Corp., Santa Clara, CA, USA). Free-breathing  $^1\text{H}$  MRI lung series algorithm segmentation was initialized by a single observer (FG) by seeding the left lung, right lung and the background on a single  $^1\text{H}$  MRI slice. Algorithm lung segmentation accuracy was evaluated by comparing algorithm lung masks with expert manual outcomes (FG with 4 years experience) for one breathing cycle ( $\sim 30$  slices) using Dice-similarity-coefficient (*DSC*). The derived FD ventilation information was quantified by clustering the FD ventilation maps into five clusters using a hierarchical k-means segmentation method [5], where the first cluster represents FD ventilation defects. FD VDP was determined by normalizing the ventilation defect volume to the thoracic cavity volume and compared with  $^3\text{He}$  VDP using Pearson correlation coefficient (*r*) and Bland-Altman analysis with GraphPad Prism version 7.00 (GraphPad Software Inc., San Diego, CA, USA). The reproducibility of the pipeline was measured using coefficient-of-variation (*CoV*) and intra-class correlation coefficient (*ICC*) for *DSC* and FD VDP with Statistical Package for the Social Sciences (SPSS) v24.0 (SPSS Inc., Chicago, IL, USA).

The performance of the FDMRI pipeline was evaluated on a clinical dataset of 10 COPD patients. Figure 5.1 shows the derived FD and  $^3\text{He}$  ventilation images of a COPD patient and Fig. 5.2 illustrates the relationships between FD and  $^3\text{He}$  VDP for the patient dataset. The

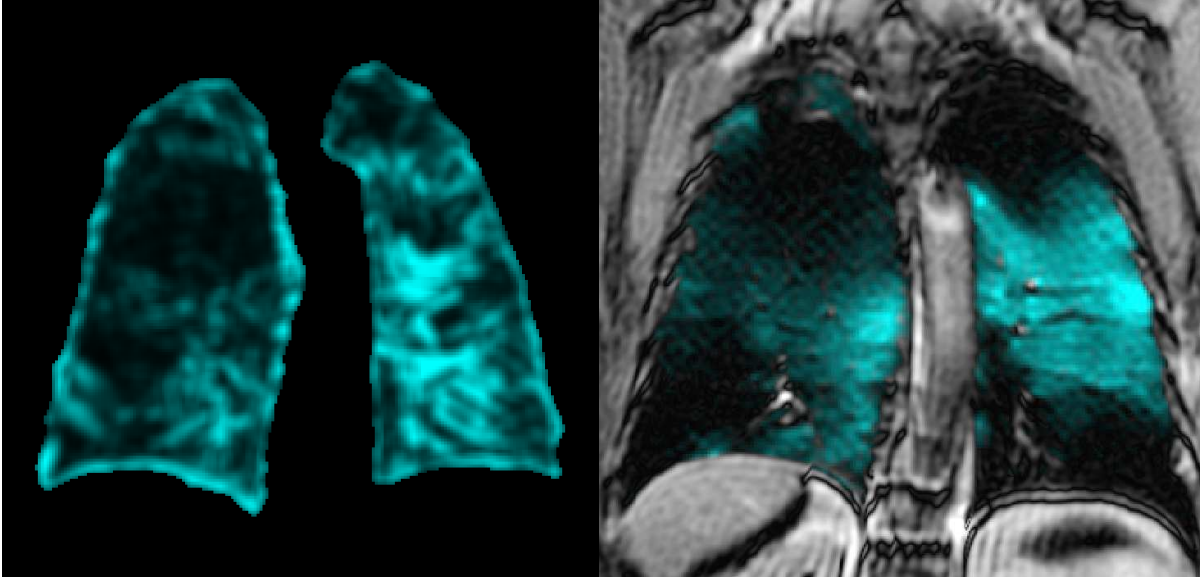


Figure 5.1: FD (left) and hyperpolarized  $^3\text{He}$  MRI (right) ventilation maps for a COPD patient.

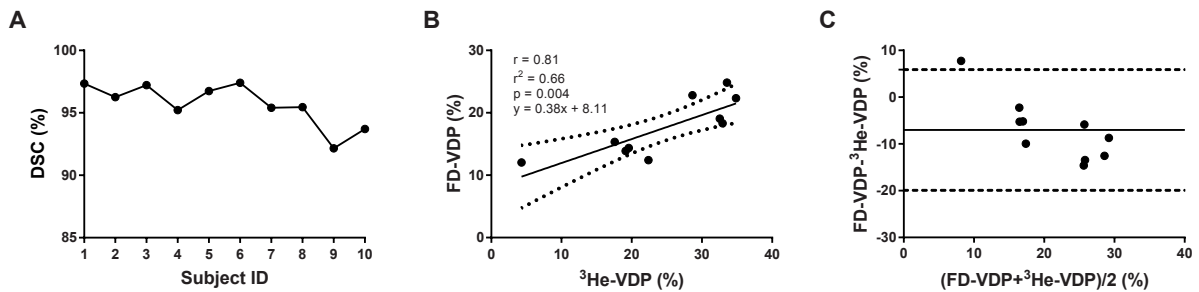


Figure 5.2: Algorithm lung segmentation accuracy and FD-VDP measurements for the 10 subjects. A) Comparison of algorithm lung segmentation and manual lung delineation using DSC. B) Pearson correlation of algorithm FD-VDP and  $^3\text{He}$  MRI VDP. C) Bland-Altman analysis of agreement for FD-VDP and  $^3\text{He}$ -VDP, where solid lines indicate the mean difference and dotted lines represent the upper and lower limits.

pipeline yielded a whole lung  $DSC$  of  $95.7 \pm 1.7\%$  for  $^1\text{H}$  MRI lung series segmentation, with a minimum and maximum of  $91.2\%$  and  $97.5\%$ , respectively. FD VDP was strongly correlated with  $^3\text{He}$  VDP ( $r = 0.81$ ,  $p = 0.004$ ) with a systematic bias of  $-7.0 \pm 6.6\%$ .  $CoV$  ( $ICC$ ) were  $0.4\%$  ( $0.98$ ) and  $4.1\%$  ( $0.98$ ) for whole lung  $DSC$  and FD VDP, respectively. For each patient, the pipeline required  $\sim 45$  min to generate FD VDP, including  $\sim 20$  s for user seeding,  $\sim 2$  min for lung series segmentation,  $\sim 40$  min for lung series registration and  $\sim 2$  min for FD analysis.

These preliminary results demonstrated that the pipeline yielded lung series segmentation, registration and ventilation measurements with high computational efficiency and reproducibility consistent with clinical workflows. This suggests the utility of this approach for large-scale, multi-centre and longitudinal research and clinical applications of free-breathing  $^1\text{H}$  MRI for obstructive lung disease.

### **5.4.2 Fast and High Resolution MRI Acquisition and Reconstruction**

MRI provides excellent soft-tissue contrast and is ideally suited for serial and longitudinal evaluation of lung disease, especially for pediatric patients and young adults because it does not require ionizing radiation. However, compared with other imaging methods such as CT, a major limitation of MRI is the relatively low image acquisition speed due to physical and physiological constraints [40, 41], leading to restricted clinical utility of pulmonary MRI. For example, many lung MR images are acquired during breath-hold conditions, which might be difficult for patients with lung disease because of physiological conditions [42]. Previous work has proposed to improve MRI acquisition speed by undersampling k-space data, but this generally results in decreased image quality, i.e., aliasing, motion artifacts and low image resolution [42, 43]. As a result, a number of important pulmonary MRI applications have been restricted unless rapid MRI acquisition can be performed.

For example, free-breathing pulmonary  $^1\text{H}$  MRI provides a way for visualization and quantification of pulmonary ventilation and perfusion without the need for exogenous contrast agents [6]. Unfortunately, free-breathing pulmonary MRI is currently limited to provide only 2D structural-functional information because of low image acquisition speed [44] while it has been well recognized that COPD and asthma are spatially heterogeneous disease [2, 4]. Therefore, there is an urgent need to develop 3D free-breathing MRI techniques to evaluate the whole lung. This fundamentally requires rapid acquisition of dynamic free-breathing  $^1\text{H}$  MRI volumes, as well as extension of current 2D free-breathing pulmonary  $^1\text{H}$  MRI image processing methods to 3D. Recently, pulmonary  $^1\text{H}$  MRI using ultra-short echo-time (UTE) sequences

has been developed as contrast agent-free alternatives to provide enhanced visualization of lung structure-function using conventional MR systems [23, 24, 9]. UTE MRI employs ultra-short echo-time pulse sequences to minimize signal decay and maximize the visibility of pulmonary parenchyma, airways and vessels [45, 46]. This technique is ideally suited for serial and longitudinal evaluation of pediatric patients and young adults as it does not require ionizing radiation or exogenous contrast and provides lung images with quality that is comparable to thoracic CT [9]. Although highly promising, a major limitation associated with UTE MRI is the low image acquisition speed and poor spatial/temporal image resolution due to over-sampling of the centre of k-space [24].

Paralleling imaging [47, 48] has been developed to reduce MRI scan time, improve image quality and increase spatial/temporal resolution. This technique employs multiple receiver coils to acquire k-space data of the object at a reduced sampling rate. The sensitivity profiles of these receiver coils are measured and used to eliminate aliasing artifacts and to reconstruct the image with full field-of-view. A decade ago, compressive sensing (CS) [49, 50] was first developed in the area of Information Theory and Approximation Theory to reconstruct and recover signals with good accuracy by measuring far fewer signals. CS exploits the compressibility of signals and performs signal reconstruction using undersampled data, i.e., below the Nyquist sampling rate, without significant loss of information. This technique quickly became popular and has been applied to medical imaging including MRI [40] to reduce scan time and CT [51] to reduce the dose. CS is based on three major requirements [40, 41]: 1) sparse representation of the underlying images in some domain, 2) incoherent measurements achieved through irregular sampling such as random sampling, and 3) sparsity-constrained non-linear reconstruction. Since MRI signals give the k-space representation of the object which are implicitly sparse and the k-space undersampling results in incoherent artifacts, it is possible to develop some non-linear reconstruction methods to generate the underlying images by enforcing both the sparsity of k-space measurements and the consistency with the acquired data.

The CS-based image reconstruction problem will be formulated as a two-compartment

model [40]. The first part will minimize the absolute differences ( $L1$  norm) between under-sampled k-space data and the data that corresponds to CS-reconstructed images. The second part will constrain the reconstruction problem by minimizing the total variation (TV) of image intensities. In Chapters 2–4, primal-dual analysis basis methods and convex optimization techniques have been developed to optimize TV- $L1$  energy function. These components provide the foundation to develop and implement CS (potentially combining paralleling imaging methods [41]) for fast and high resolution pulmonary MRI acquisition and reconstruction. These fast image acquisition and reconstruction techniques, once implemented, may facilitate more widespread research and clinical applications of pulmonary MRI including noble gas, 2D/3D free-breathing and UTE MRI for lung disease management.

### 5.4.3 UTE MRI Lung Structure-Function Measurements

Conventional  $^1\text{H}$  MRI of the lung is more challenging than most other organs due to a number of limitations including low proton density, magnetic susceptibility, and motion artifacts [52, 45]. As a result, the lung appears as a black hole and provides little morphological information when conventional MRI pulse sequences are used. In addition, the image quality is generally poor due to motion and partial volume effects. Therefore, clinical applications of conventional pulmonary  $^1\text{H}$  MRI have been limited although the potential has been realized [53].

Recently, ultra-short echo-time (UTE) MRI has been developed to provide enhanced visualization of the lung anatomy using conventional MRI systems. UTE MRI employs short echo-time pulse sequences to minimize signal decay and maximize the visibility of lung parenchyma [45], leading to higher tissue contrast and greater signal intensity inhomogeneity. Previous studies [23, 54, 24] have demonstrated the potential of UTE MRI biomarkers to phenotype lung structural-functional abnormalities and perhaps facilitate the development of novel lung disease treatments. To generate these imaging biomarkers and enable widespread clinical applications of UTE MRI, accurate, reproducible and rapid lung segmentation methods are required. However, UTE MRI lung segmentation is particularly challenging because of MRI signal in-

tensity inhomogeneity, magnetic susceptibility, motion artifacts [52, 45], dramatic change of lung shapes and protruding structure. Previous studies have shown that optimal pulmonary MRI segmentation cannot be achieved using gray level information exclusively [55] and high-dimensional image features may assist complex image segmentation [56]. Motivated by the previous work [56], image signal intensity  $I(x)$ ,  $x \in \Omega$ , and voxel spatial location information  $\{X(x), Y(x), Z(x)\}$  were combined to generate high-dimensional features  $\{I(x), X(x), Y(x), Z(x)\}$  for improved segmentation. An adaptive kernel-based K-means clustering approach as opposed to the commonly-used log-likelihood formulation was employed to construct the data term for a continuous max-flow segmentation model [57].

To test the segmentation approach, a dataset of UTE lung images were acquired in 10 asthma patients who provided written informed consent to a study protocol approved by Health Canada (Appendix H) and the demographic characteristics are provided in Table 5.1. UTE MRI was performed at 3.0 Tesla (Discovery MR750 system, General Electric Health Care [GEHC], Milwaukee, WI, USA) using an eight-channel transmit body coil (127 MHz, maximum excitation power 8.0 kW delivered by a narrow-band RF power amplifier (GEHC, Milwaukee, WI, USA)), a 32-channel torso receive coil (GEHC, Milwaukee, WI, USA) and a proprietary research 3D cones UTE sequence [24]. Coronal image acquisition was performed during inspiration breath-hold of 1.0 L medical grade nitrogen from functional residual capacity (15 s acquisition time; repetition time/echo time/flip angle = 3.5 ms/0.03 ms/5°; field-of-view = 40 cm×40 cm; bandwidth = 125 kHz; matrix = 200 (phase encoding) × 200 (frequency encoding); 18 slices and 10 mm slice thickness), as previously described [24]. Auto shimming was used for UTE MRI acquisitions (chest region) for the centre slice. The maximum magnetic field gradient strength was 5 G/cm for x,y and z gradients and image distortion compensation was enabled by default. Prior to algorithm implementation, the original UTE images were resampled to ~2 mm isotropic voxel size, and one observer seeded the lung and background on a single slice three times on three different days. Algorithm segmentation accuracy was evaluated by comparing algorithm lung masks with manual outputs generated by an experienced observer.

Dice-similarity-coefficient ( $DSC$ ), root-mean-squared-error ( $RMSE$ ) of the distances between two lung surfaces, and absolute percent volume error ( $|\delta V_P|$ ) were employed as region-, surface distance- and volume-based similarity measurements for algorithm and manual results. Algorithm segmentation reproducibility was evaluated by calculating the coefficient-of-variation ( $CoV$ ) and intra-class correlation coefficient ( $ICC$ ) for  $DSC$  and  $RMSE$ . The computational efficiency of this approach was measured using runtime.

Table 5.1: Subject demographics and pulmonary function measurements. (n=10)

Mean(SD)	Asthma (n=10)
Age yrs	46(9)
Male n	5
$FEV_1\%_{pred}$	67(19)
$FVC\%_{pred}$	96(12)
$FEV_1/FVC$	57(15)
$RV\%_{pred}$	140(31)
$TLC\%_{pred}$	107(9)
$RV/TLC\%_{pred}$	39(8)

$FEV_1$ : Forced expiratory volume in one second,  $FVC$ : Functional vital capacity,  $RV$ : Residual volume,  $TLC$ : Total lung capacity,  $\%_{pred}$ : Percent predicted.

Representative UTE MRI lung and voxel labeling probability maps are shown in Fig. 5.3. For ten asthma patients, the segmentation approach yielded a  $DSC$  of  $92.8\pm 2.5\%$ ,  $RMSE$  of  $2.9\pm 0.6$  mm and  $|\delta V_P|$  of  $7.2\pm 3.6\%$ .  $CoV(ICC)$  were  $0.4\%(0.98)$  and  $1.6\%(0.97)$  for  $DSC$  and  $RMSE$ , respectively. The mean runtime for my approach was  $\sim 8$  min using a GPU including  $\sim 5$  s for user seeding.

High reproducibility is required for studies involving large datasets and multiple research investigations such that reliable measurements can be obtained from multiple observers independent of the level of experience. Although high reproducibility and flexibility with limited user interactions were achieved, fully automated segmentation may further benefit clinical translations of UTE MRI by enabling efficient and high throughput clinical workflows. It has been observed that the variability of the user seeding procedure did not markedly influence the segmentation and this might be in part due to the iterative implementation of the algo-

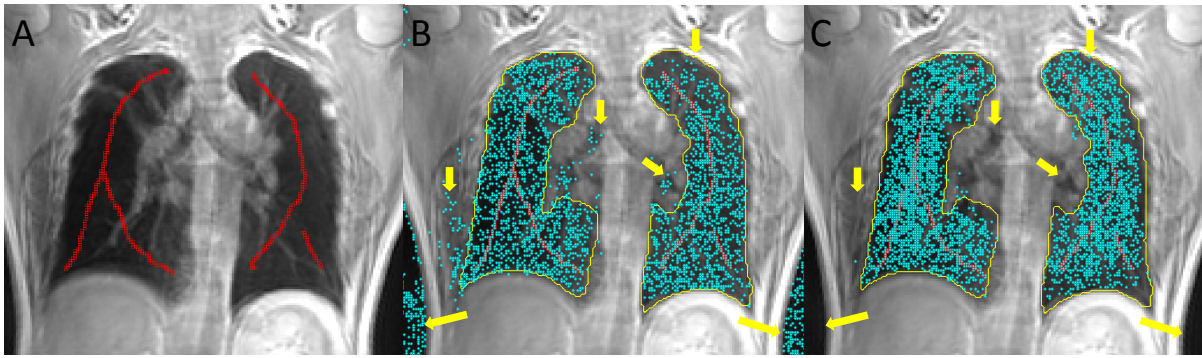


Figure 5.3: Representative UTE MRI lung and voxel labelling probability maps using the adaptive kernel K-mean approach. A) UTE MRI lung signal intensity inhomogeneity and example user seeds (red). B) K-nearest neighbour (cyan) of the user seeds (red) using signal intensity only. C) K-nearest neighbour (cyan) of the user seeds (red) by combining signal intensity and voxel spatial location information. The density of cyan dots relates to the probability of assigning a “lung” label to the voxels. Yellow contours represent manual segmentation and the arrows indicate improvements by incorporating voxel spatial location information (same user seeds used for B) and C)).

rithm that refines the segmentation with previous solutions. Based on this observation, the segmentation algorithm was fully automated using a single atlas image. The atlas image was registered to each individual image and the atlas lung mask was transformed to initialize the iterative segmentation algorithm, as shown in Fig. 5.4. The automated segmentation approach was applied to three asthma subjects with remarkably distinct lung sizes and the preliminary results, as shown in Fig. 5.5, demonstrated promising potential of this approach to address the challenging UTE MRI lung segmentation problem.

In summary, the proposed approach avoids over-fitting of the appearance models generated from user-seeds and algorithm segmentation. The incorporation of spatial location information further improved algorithm segmentation by favoring compact segmentation regions. As a result, the proposed approach required less user seeding and outperformed current methods which use only fixed signal intensity models to describe the object of interest. This new approach involves minimal user interaction, and generates highly reproducible lung segmentation with high computational efficiency consistent with clinical workflows. All of this is consistent with the need for widespread pulmonary UTE MRI in clinical applications.



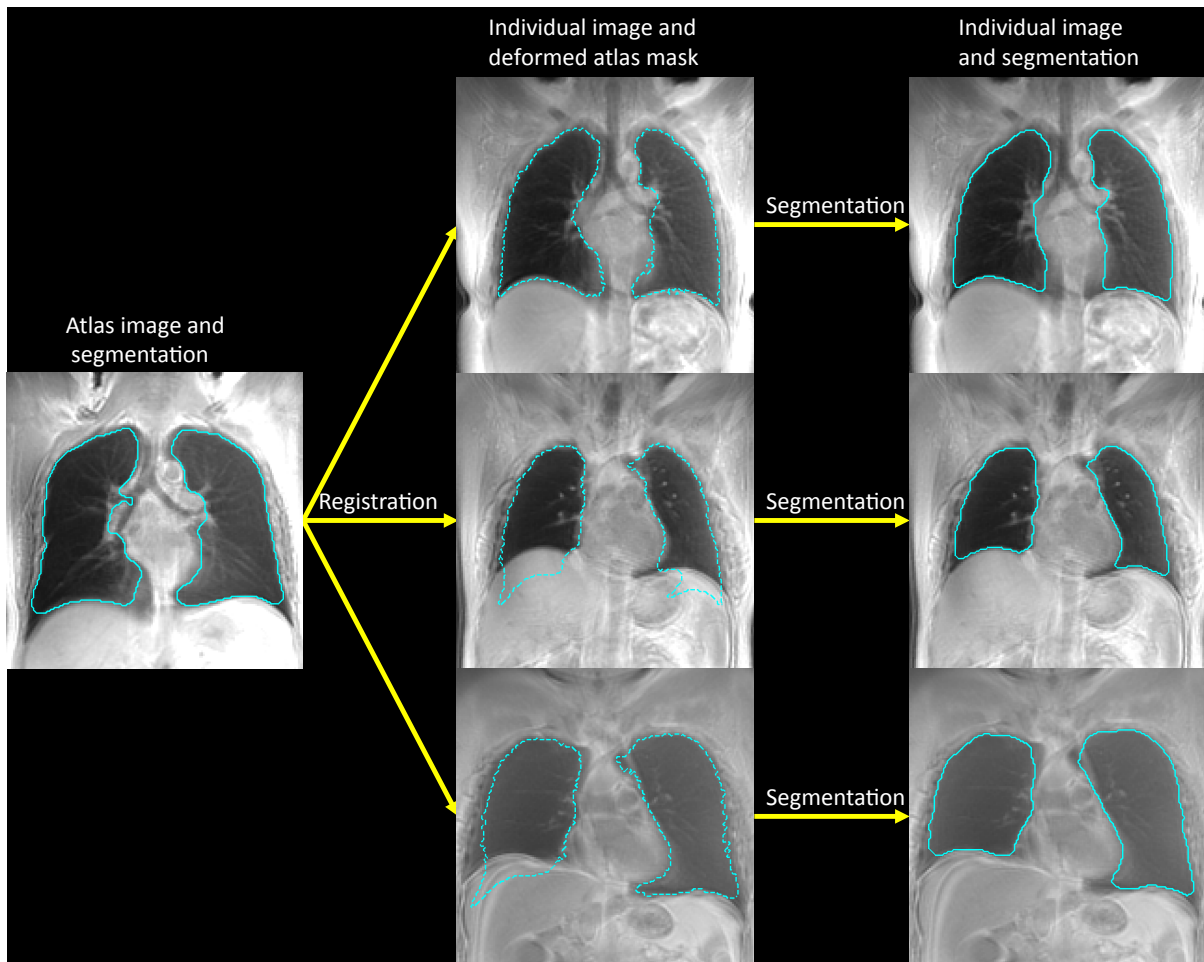


Figure 5.4: Automated UTE MRI lung segmentation workflow and example results for three asthma patients. An atlas image is registered to each individual volume and the pre-segmented lung mask is deformed to initialize the segmentation algorithm. Dash contours represent deformed atlas lung masks and solid contours indicate automated algorithm segmentation results.

#### 5.4.4 Pulmonary Imaging Platform: A GUI-Oriented Pulmonary MRI and CT Image Processing Platform

A number of pulmonary image processing algorithms presented in Chapters 2–4 have been developed and evaluated. The majority of these algorithms were integrated into simple image processing pipelines and implemented through Linux command lines. While easy-to-use, computationally efficient and likely clinically-acceptable, the clinical utility of these algorithms may be further enhanced when a GUI-based implementation platform is provided. For exam-

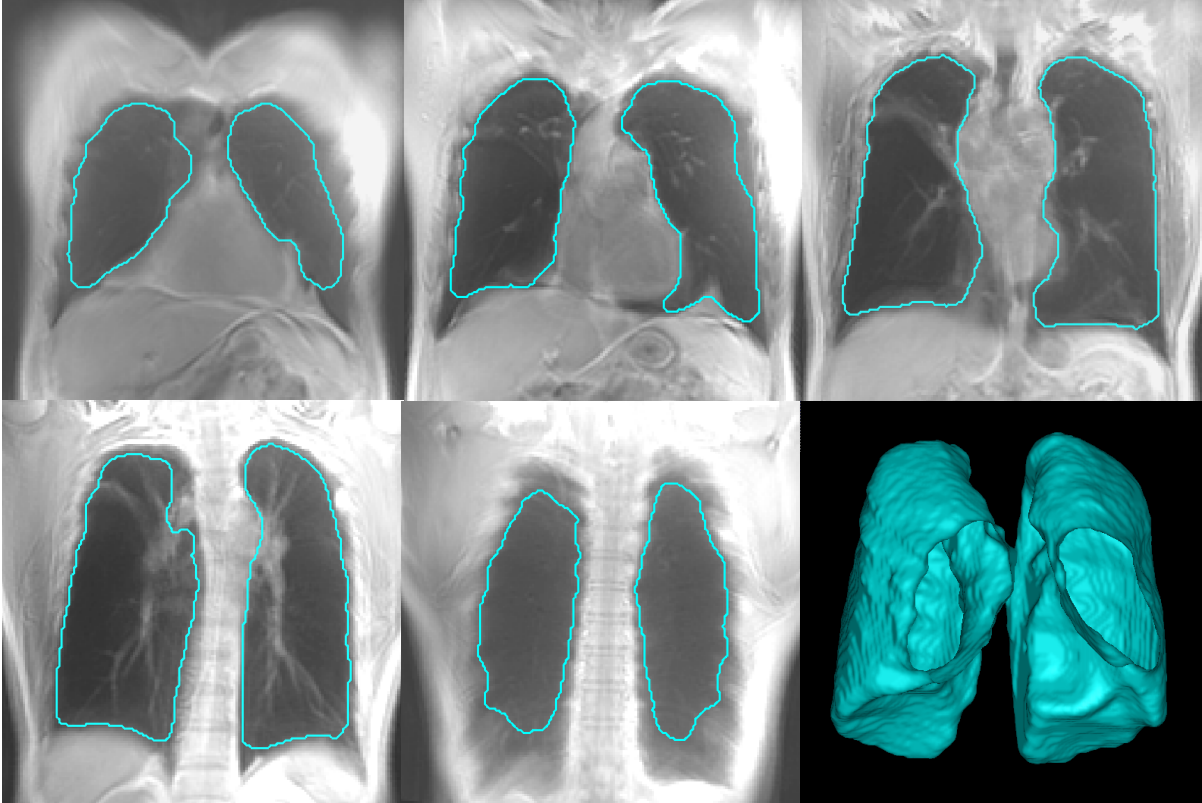


Figure 5.5: Preliminary automated UTE MRI lung segmentation results. Anterior-to-posterior slices and 3D-rendered lung volumes are shown from upper left to lower right.

ple, a GUI can be used to integrate the image processing components, hide these complex algorithms from end users as “black boxes”, and provide intuitive interaction with images and straightforward visualization of the results. In recognition of this, it is necessary and urgent to “pack” these image processing and analysis algorithms into a GUI-based platform for widespread research and clinical applications of the pulmonary imaging methods and imaging biomarkers. I am in the process of developing a GUI-oriented **Pulmonary Imaging Platform (PIP)** with Microsoft Visual Studio and the .net framework to integrate these individual algorithms and a prototyped GUI is shown in Fig. 5.6.

**PIP** will have the following features:

- Simple user interactions for image seeding using a brush tool to initialize and/or refine the segmentation;

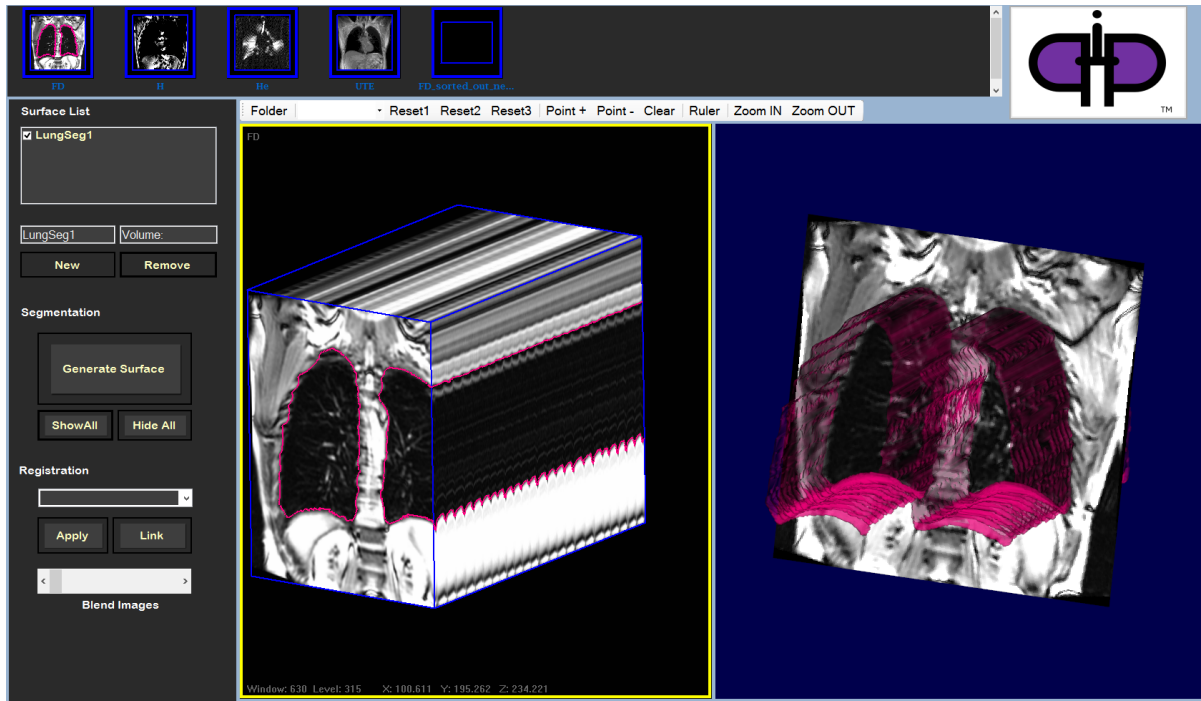


Figure 5.6: Graphical user interface of Pulmonary Imaging Platform.

- Noble gas and  $^1\text{H}$  MRI co-segmentation to generate regional and whole lung structural-functional information, i.e., whole lung VDP;
- $^1\text{H}$  MRI segmentation to provide lung structure-function measurements;
- CT and functional MRI registration for regional lung structure-function measurements, i.e., lobar/segmental VDP and potential treatment decisions;
- 2D and/or 3D free-breathing  $^1\text{H}$  MRI segmentation, registration and functional information quantification, i.e., FD VDP and specific ventilation;
- Interactive and/or fully automated UTE MRI segmentation and multi-volume UTE MRI analysis, i.e., whole lung and/or regional static and/or dynamic signal intensity maps, high/low signal intensity percentage;
- Multi-volume CT-CT, MRI-MRI and CT-MRI parametric response map analyses;

- 2D and/or 3D visualization of the segmentation, registration and quantification results in different views.

These individual components were developed and evaluated in Chapters 2–4. The core algorithms for each component were implemented using C/C++/CUDA that are compatible with **PIP**. The next step is to integrate these algorithms into the **PIP**-GUI and release a robust version of the software system to the pulmonary imaging research community.

## 5.5 Significance and Impact

COPD and asthma represent a staggering burden on patients, economies and health-care systems worldwide. Despite decades of research, therapeutic breakthroughs that can modify disease progression and patient outcomes have not occurred. This is likely due to their high dependence on spirometry airflow measurements made at the mouth. These measurements, although important, have significant limitations and this has motivated us to develop tools to better understand pulmonary disease pathophysiology, design and develop novel treatments with the hope to improve patient care. Pulmonary imaging including pulmonary MRI and CT provides the potential to develop regional and quantitative imaging biomarkers of obstructive lung disease and advance the scope of pulmonary disease research. To facilitate broad clinical applications of these imaging methods, it is urgent to develop image analysis tools that can provide clinically-acceptable and physiologically-relevant intermediate endpoints for pulmonary disease management while compatible with efficient clinical workflow.

In this thesis, optimized pulmonary MRI and CT segmentation, registration and quantification algorithms have been developed to provide a number of imaging biomarkers for lung disease care that require intensive and extensive human expertise. High-level *prior* knowledge in combination with modern optimization techniques were exploited and rapid implementation of these algorithms were provided. These image analysis algorithms demonstrated excellent agreement with reference standards, high computational efficiency and reproducibility with di-

minished and/or without user interactions across a range of respiratory conditions. In addition, the GUI-oriented implementation of these algorithms highlights the capability of clinical translation of these tools. Armed with these powerful computational tools, there is enormous potential to generate sensitive and regional imaging biomarkers, understand disease mechanisms (perhaps the etiology of noble gas ventilation defects), identify disease phenotypes, monitor disease treatment response and perhaps inform therapies in large-scale and multi-center research and clinical investigations of lung disease. Taken together, this work not only fosters the developments of computational image processing theories but also facilitates widespread research and clinical applications of pulmonary imaging methods for lung disease management and advances the scope of pulmonary medicine research.

## Bibliography

- [1] Bartolome R Celli. The importance of spirometry in COPD and asthma: effect on approach to management. *CHEST Journal*, 117(2\_suppl):15S–19S, 2000.
- [2] Peter T Macklem. The physiology of small airways. *American journal of respiratory and critical care medicine*, 157(5):S181–S183, 1998.
- [3] L Shahab, MJ Jarvis, J Britton, and R West. Prevalence, diagnosis and relation to tobacco dependence of chronic obstructive pulmonary disease in a nationally representative population sample. *Thorax*, 61(12):1043–1047, 2006.
- [4] Alvar Agusti, Peter MA Calverley, Bartolome Celli, Harvey O Coxson, Lisa D Edwards, David A Lomas, William MacNee, Bruce E Miller, Steve Rennard, Edwin K Silverman, et al. Characterisation of COPD heterogeneity in the ECLIPSE cohort. *Respiratory research*, 11(1):122, 2010.
- [5] Miranda Kirby, Mohammadreza Heydarian, Sarah Svenningsen, Andrew Wheatley, David G. McCormack, Roya Etemad-Rezai, and Grace Parraga. Hyperpolarized  $^3\text{He}$

- magnetic resonance functional imaging semiautomated segmentation. *Academic Radiology*, November 2011.
- [6] Grzegorz Bauman, Michael Puderbach, Michael Deimling, Vladimir Jellus, Christophe Ched'hotel, Julien Dinkel, Christian Hintze, Hans-Ulrich Kauczor, and Lothar R Schad. Non-contrast-enhanced perfusion and ventilation assessment of the human lung by means of fourier decomposition in proton MRI. *Magnetic resonance in medicine*, 62(3):656–664, 2009.
- [7] Maren Zapke, Hans-Georg Topf, Martin Zenker, Rainer Kuth, Michael Deimling, Peter Kreisler, Manfred Rauh, Christophe Ched'hotel, Bernhard Geiger, and Thomas Rupprecht. Magnetic resonance lung function—a breakthrough for lung imaging and functional assessment? a phantom study and clinical trial. *Respiratory research*, 7(1):106, 2006.
- [8] Francesca Pennati, James D Quirk, Dmitriy A Yablonskiy, Mario Castro, Andrea Aliverti, and Jason C Woods. Assessment of regional lung function with multivolume 1H MR imaging in health and obstructive lung disease: Comparison with 3He MR imaging. *Radiology*, 273(2):580–590, 2014.
- [9] Gaël Dournes, Fanny Menut, Julie Macey, Michaël Fayon, Jean-François Chateil, Marjorie Salel, Olivier Corneloup, Michel Montaudon, Patrick Berger, and François Laurent. Lung morphology assessment of cystic fibrosis using MRI with ultra-short echo time at submillimeter spatial resolution. *European radiology*, 26(11):3811–3820, 2016.
- [10] Giovanni Galluccio and Gabriele Lucantoni. Bronchoscopic lung volume reduction for pulmonary emphysema: preliminary experience with a new novatech® endobronchial silicone one-way valve. *Interactive cardiovascular and thoracic surgery*, 11(2):213–215, 2010.

- [11] Sonali Sethi and Joseph Cicienia. Treatment of PCP-related pneumothorax using one-way endobronchial valves. *CHEST Journal*, 134(4.MeetingAbstracts):p9002–p9002, 2008.
- [12] Thomas R Gildea, Sumita B Khatri, and Mario Castro. Bronchial thermoplasty: a new treatment for severe refractory asthma. *Cleveland Clinic journal of medicine*, 78(7):477–485, 2011.
- [13] Ora Israel, Maya Mor, Diana Gaitini, Zohar Keidar, Luda Guralnik, Ahuva Engel, Alex Frenkel, Rachel Bar-Shalom, and Abraham Kuten. Combined functional and structural evaluation of cancer patients with a hybrid camera-based PET/CT system using 18f-fdg. *Journal of Nuclear Medicine*, 43(9):1129–1136, 2002.
- [14] Ulas Bagci, Jayaram K Udupa, Neil Mendhiratta, Brent Foster, Ziyue Xu, Jianhua Yao, Xinjian Chen, and Daniel J Mollura. Joint segmentation of anatomical and functional images: Applications in quantification of lesions from PET, PET-CT, MRI-PET, and MRI-PET-CT images. *Medical image analysis*, 17(8):929–945, 2013.
- [15] Aristeidis Sotiras, Christos Davatzikos, and Nikos Paragios. Deformable medical image registration: A survey. *Medical Imaging, IEEE Transactions on*, 32(7):1153–1190, 2013.
- [16] Tobias Heimann and Hans-Peter Meinzer. Statistical shape models for 3D medical image segmentation: a review. *Medical image analysis*, 13(4):543–563, 2009.
- [17] Daniel Cremers, Mikael Rousson, and Rachid Deriche. A review of statistical approaches to level set segmentation: integrating color, texture, motion and shape. *International journal of computer vision*, 72(2):195–215, 2007.
- [18] Yuri Y Boykov and M-P Jolly. Interactive graph cuts for optimal boundary & region segmentation of objects in ND images. In *Computer Vision, 2001. ICCV 2001. Proceedings. Eighth IEEE International Conference on*, volume 1, pages 105–112. IEEE, 2001.

- [19] Paul A Yushkevich, Joseph Piven, Heather Cody Hazlett, Rachel Gimpel Smith, Sean Ho, James C Gee, and Guido Gerig. User-guided 3D active contour segmentation of anatomical structures: significantly improved efficiency and reliability. *Neuroimage*, 31(3):1116–1128, 2006.
- [20] Jiangsheng Yu, Yiqun Xue, and Hee Kwon Song. Comparison of lung T2\* during free-breathing at 1.5 T and 3.0 T with ultrashort echo time imaging. *Magnetic resonance in medicine*, 66(1):248–254, 2011.
- [21] Yoshiharu Ohno, Hisanobu Koyama, Takeshi Yoshikawa, Keiko Matsumoto, Masaya Takahashi, Marc Van Cauteren, and Kazuro Sugimura. T2\* measurements of 3-T MRI with ultrashort TEs: capabilities of pulmonary function assessment and clinical stage classification in smokers. *American Journal of Roentgenology*, 197(2):W279–W285, 2011.
- [22] Yoshiharu Ohno, Mizuho Nishio, Hisanobu Koyama, Daisuke Takenaka, Masaya Takahashi, Takeshi Yoshikawa, Sumiaki Matsumoto, Makoto Obara, Marc van Cauteren, and Kazuro Sugimura. Pulmonary MR imaging with ultra-short TEs: utility for disease severity assessment of connective tissue disease patients. *European journal of radiology*, 82(8):1359–1365, 2013.
- [23] Weijing Ma, Khadija Sheikh, Sarah Svenningsen, Damien Pike, Fumin Guo, Roya Etemad-Rezai, Jonathan Leipsic, Harvey O Coxson, David G McCormack, and Grace Parraga. Ultra-short echo-time pulmonary MRI: Evaluation and reproducibility in COPD subjects with and without bronchiectasis. *Journal of Magnetic Resonance Imaging*, 41(5):1465–1474, 2015.
- [24] Khadija Sheikh, Fumin Guo, Dante PI Capaldi, Alexei Ouriadov, Rachel L Eddy, Sarah Svenningsen, and Grace Parraga. Ultrashort echo time MRI biomarkers of asthma. *Journal of Magnetic Resonance Imaging*, 2016.



- [25] Dante PI Capaldi, Khadija Sheikh, Rachel L Eddy, Fumin Guo, Sarah Svenningsen, Parameswaran Nair, David G McCormack, Grace Parraga, Canadian Respiratory Research Network, et al. Free-breathing functional pulmonary MRI: Response to bronchodilator and bronchoprovocation in severe asthma. *Academic Radiology*, 2017.
- [26] JM Wild, H Marshall, M Bock, LR Schad, PM Jakob, M Puderbach, F Molinari, EJR Van Beek, and J Biederer. MRI of the lung (1/3): methods. *Insights into imaging*, 3(4):345–353, 2012.
- [27] Meng Tang, Lena Gorelick, Olga Veksler, and Yuri Boykov. Grabcut in one cut. In *Proceedings of the IEEE International Conference on Computer Vision*, pages 1769–1776, 2013.
- [28] Radha Chitta, Rong Jin, Timothy C Havens, and Anil K Jain. Scalable kernel clustering: Approximate kernel k-means. *arXiv preprint arXiv:1402.3849*, 2014.
- [29] Inderjit S Dhillon, Yuqiang Guan, and Brian Kulis. Kernel k-means: spectral clustering and normalized cuts. In *Proceedings of the tenth ACM SIGKDD international conference on Knowledge discovery and data mining*, pages 551–556. ACM, 2004.
- [30] Kenneth Lange, David R Hunter, and Ilsoon Yang. Optimization transfer using surrogate objective functions. *Journal of computational and graphical statistics*, 9(1):1–20, 2000.
- [31] Meng Tang, Ismail Ben Ayed, Dmitrii Marin, and Yuri Boykov. Secrets of GrabCut and kernel k-means. In *Proceedings of the IEEE International Conference on Computer Vision*, pages 1555–1563, 2015.
- [32] Claudia Nieuwenhuis, Evgeny Strelakovski, and Daniel Cremers. Proportion priors for image sequence segmentation. In *Proceedings of the IEEE International Conference on Computer Vision*, pages 2328–2335, 2013.

- [33] Brian B Avants, Charles L Epstein, Murray Grossman, and James C Gee. Symmetric diffeomorphic image registration with cross-correlation: evaluating automated labeling of elderly and neurodegenerative brain. *Medical image analysis*, 12(1):26–41, 2008.
- [34] Mattias P Heinrich, Mark Jenkinson, Manav Bhushan, Tahreema Matin, Fergus V Gleeson, Michael Brady, and Julia A Schnabel. MIND: Modality independent neighbourhood descriptor for multi-modal deformable registration. *Medical Image Analysis*, 16(7):1423–1435, 2012.
- [35] Junhwan Kim, Vladimir Kolmogorov, and Ramin Zabih. Visual correspondence using energy minimization and mutual information. In *Computer Vision, 2003. Proceedings. Ninth IEEE International Conference on*, pages 1033–1040. IEEE, 2003.
- [36] Grzegorz Bauman, Ulf Lützen, Mathias Ullrich, Thomas Gaass, Julien Dinkel, Gunnar Elke, Patrick Meybohm, Inéz Frerichs, Beata Hoffmann, Jan Borggreffe, et al. Pulmonary functional imaging: qualitative comparison of fourier decomposition mr imaging with spect/ct in porcine lung. *Radiology*, 260(2):551–559, 2011.
- [37] Keelin Murphy, Bram Van Ginneken, Joseph M Reinhardt, Sven Kabus, Kai Ding, Xiang Deng, Kunlin Cao, Kaifang Du, Gary E Christensen, Vincent Garcia, et al. Evaluation of registration methods on thoracic CT: the EMPIRE10 challenge. *Medical Imaging, IEEE Transactions on*, 30(11):1901–1920, 2011.
- [38] Jing Yuan, Egil Bae, Xue-Cheng Tai, and Yuri Boykov. A continuous max-flow approach to potts model. In *Computer Vision—ECCV 2010*, pages 379–392. Springer, 2010.
- [39] Martin Rajchl, John SH Baxter, Wu Qiu, Ali R Khan, Aaron Fenster, Terry M Peters, and Jing Yuan. Rancor: non-linear image registration with total variation regularization. *arXiv preprint arXiv:1404.2571*, 2014.
- [40] Michael Lustig, David Donoho, and John M Pauly. Sparse MRI: The application of

- compressed sensing for rapid MR imaging. *Magnetic resonance in medicine*, 58(6):1182–1195, 2007.
- [41] SS Vasanaawala, MJ Murphy, Marcus T Alley, P Lai, Kurt Keutzer, John M Pauly, and Michael Lustig. Practical parallel imaging compressed sensing MRI: Summary of two years of experience in accelerating body MRI of pediatric patients. In *2011 IEEE International Symposium on Biomedical Imaging: From Nano to Macro*, pages 1039–1043. IEEE, 2011.
- [42] Patricia Noël, Roland Bammer, Caroline Reinhold, and Masoom A Haider. Parallel imaging artifacts in body magnetic resonance imaging. *Canadian Association of Radiologists Journal*, 60(2):91–98, 2009.
- [43] Nathan E Yanasak and Michael J Kelly. MR imaging artifacts and parallel imaging techniques with calibration scanning: a new twist on old problems. *RadioGraphics*, 34(2):532–548, 2014.
- [44] Dante PI Capaldi, Khadija Sheikh, Fumin Guo, Sarah Svenningsen, Roya Etemad-Rezai, Harvey O Coxson, Jonathon A Leipsic, David G McCormack, and Grace Parraga. Free-breathing pulmonary 1H and hyperpolarized 3He MRI: Comparison in copd and bronchiectasis. *Academic radiology*, 22(3):320–329, 2015.
- [45] Colleen J Bergin, Gary M Glover, and John Pauly. Magnetic resonance imaging of lung parenchyma. *Journal of thoracic imaging*, 8(1):12–17, 1993.
- [46] G Wilson Miller, John P Mugler, Rui C Sá, Talissa A Altes, G Kim Prisk, and Susan R Hopkins. Advances in functional and structural imaging of the human lung using proton MRI. *NMR in biomedicine*, 27(12):1542–1556, 2014.
- [47] Daniel K Sodickson and Warren J Manning. Simultaneous acquisition of spatial harmonics (SMASH): fast imaging with radiofrequency coil arrays. *Magnetic resonance in medicine*, 38(4):591–603, 1997.

- [48] Klaas P Pruessmann, Markus Weiger, Markus B Scheidegger, Peter Boesiger, et al. SENSE: sensitivity encoding for fast MRI. *Magnetic resonance in medicine*, 42(5):952–962, 1999.
- [49] David L Donoho. Compressed sensing. *IEEE Transactions on information theory*, 52(4):1289–1306, 2006.
- [50] Emmanuel J Candès, Justin Romberg, and Terence Tao. Robust uncertainty principles: Exact signal reconstruction from highly incomplete frequency information. *IEEE Transactions on information theory*, 52(2):489–509, 2006.
- [51] Kihwan Choi, Jing Wang, Lei Zhu, Tae-Suk Suh, Stephen Boyd, and Lei Xing. Compressed sensing based cone-beam computed tomography reconstruction with a first-order method. *Medical physics*, 37(9):5113–5125, 2010.
- [52] CJ Bergin, DC Noll, JM Pauly, GH Glover, and A Macovski. Mr imaging of lung parenchyma: a solution to susceptibility. *Radiology*, 183(3):673–676, 1992.
- [53] Amir M Owrangi and Grace Parraga. Chest MRI in children: Why bother? *Respirology*, 17(1):3–4, 2012.
- [54] Laura L Walkup, Jean A Tkach, Nara S Higano, Robert P Thomen, Sean B Fain, Stephanie L Merhar, Robert J Fleck, Raouf S Amin, and Jason C Woods. Quantitative magnetic resonance imaging of bronchopulmonary dysplasia in the neonatal intensive care unit environment. *American journal of respiratory and critical care medicine*, 192(10):1215–1222, 2015.
- [55] Alireza Osareh and Bitia Shadgar. A segmentation method of lung cavities using region aided geometric snakes. *Journal of medical systems*, 34(4):419–433, 2010.
- [56] Meng Tang, Dmitrii Marin, Ismail Ben Ayed, and Yuri Boykov. Normalized cut meets MRF. In *European Conference on Computer Vision*, pages 748–765. Springer, 2016.

- [57] Jing Yuan, Egil Bae, and Xue-Cheng Tai. A study on continuous max-flow and min-cut approaches. In *Computer Vision and Pattern Recognition (CVPR), 2010 IEEE Conference on*, pages 2217–2224. IEEE, 2010.

# Appendix A

## Discrete and Continuous

### Min-Cut/Max-Flow

Energy minimization has been successfully established and used in the area of modern image segmentation [1, 2]. For an image domain  $\Omega$ , extracting a single foreground  $s$ , (i.e., with a value 1), from the background  $\Omega \setminus s$ , (i.e., with a value 0), results in solving the following *min-cut* problem:

$$\min_s \int_{\Omega \setminus s} D_s(x) dx + \int_s D_t(x) dx + \alpha |\partial s|, \quad (\text{A.1})$$

which aims to minimize the total region cost (determined by the foreground cost  $D_t(x)$  and background cost  $D_s(x)$ ) and the total area  $|\partial s|$  of the segment  $s$  weighted by  $\alpha$ .

Previous studies have shown that the *min-cut formulation* (A.1) can be globally optimized in discrete domain through combinatorial optimization [1, 3] and in continuous domain [2, 4, 5] via convex optimization. Here, we briefly revisit the two categories of algorithms.

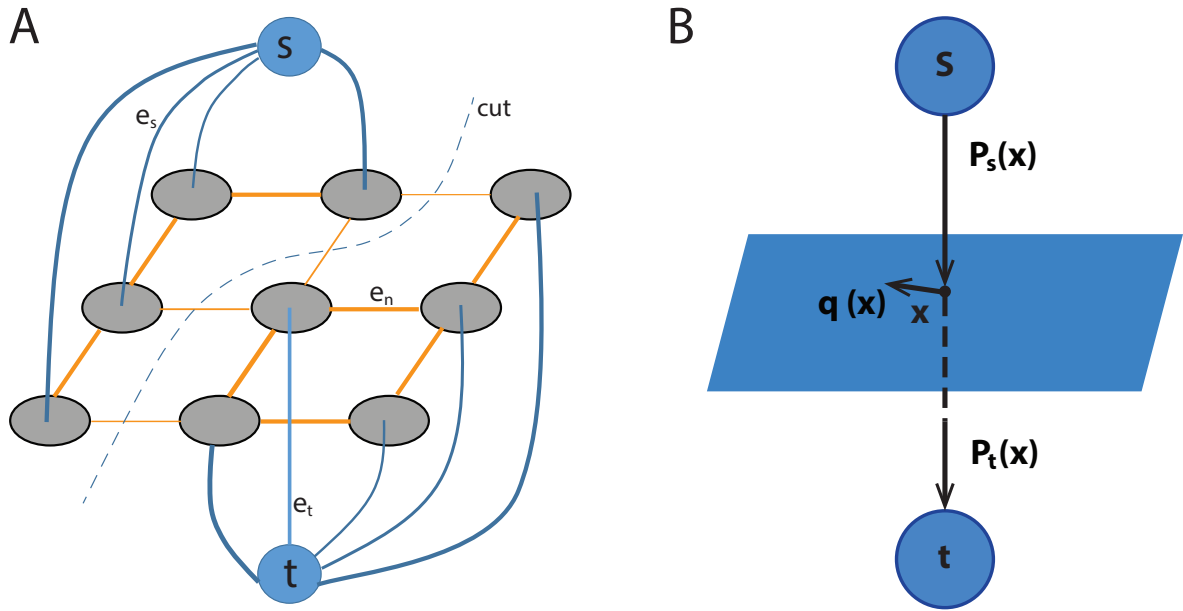


Figure A.1: Max-flow/min-cut graph in A) discrete and B) continuous domain.

## Discrete Min-cut/Max-flow

In discrete domain, segmentation of an image can be achieved by minimizing the following energy function [1, 3]:

$$E(f) = \sum_{p \in P} D_p(l_p) + \sum_{(p,q) \in N} V_{p,q}(l_p, l_q), \quad (\text{A.2})$$

where  $D_p(l_p)$  measures the cost for assigning a label  $l_p$  to pixel  $p$ , and  $V_{p,q}(l_p, l_q)$  measures the cost for assigning labels  $l_p$  and  $l_q$  to two neighboring pixels  $(p, q) \in N$ . Such energy minimization problem can be solved using graph-based methods.

Let  $G = \langle V, E \rangle$  be a graph consisting a vertex set  $V$  and an edge set  $E$  that connects the vertices, as shown in Fig. A.1 (A). The vertex set  $V$  consists of normal nodes such as image pixels and two additional terminals, the source  $s$  and the sink  $t$ , which correspond to the labels that can be assigned to pixels. The edge set  $E$  consists of two types of edges in the graph: spatial edge  $e_n$  that connects neighboring pixels, terminal edges  $e_s$  and  $e_t$  that link pixels to

the terminals  $s$  and  $t$ , respectively. The spatial edges  $e_n$  penalizes the discontinuity between neighboring pixels and the terminal edges  $e_s$  and  $e_t$  correspond to the cost for assigning labels  $l_p$  and  $l_q$  to pixels  $p$  and  $q$ . A *min-cut* divides the vertex set  $V$  into two disjoint sets  $V_s$  and  $V_t$  such that  $s \in V_s$  and  $t \in V_t$  and the achieved cost for all the edges from  $V_s$  to  $V_t$  is the smallest.

Let  $C(e_n)$ ,  $C_s(v)$  and  $C_t(v)$  be the non-negative cost of edges  $e_n$ ,  $e_s$ , and  $e_t$ , respectively. Considering each edge  $e$  as a pipe, the respective cost can be regarded as the capacity or “maximum amount of water”. It has been proved that the *min-cut* can be equivalent achieved by maximizing the flow streaming from  $s$  to  $t$  [6], i.e.,

$$\max_{p_s} \sum_{v \in V \setminus \{s, t\}} p_s(v), \quad (\text{A.3})$$

where the spatial flow  $p(e_n)$ , the source flow  $p_s(v)$  that connects  $s$  to a node  $v$  and the sink flow  $p_t(v)$  that connects a node  $v$  to  $t$  suffice:

- Flow capacity constraints:

$$|p(e_n)| \leq C(e_n); \quad (\text{A.4})$$

$$0 \leq p_s(v) \leq C_s(v); \quad (\text{A.5})$$

$$0 \leq p_t(v) \leq C_t(v). \quad (\text{A.6})$$

- Flow conservation constraints:

$$\sum_{e_n \in N_v} p(e_n) - p_s(v) + p_t(v) = 0. \quad (\text{A.7})$$

## Continuous Min-cut/Max-flow

Recently, [7] employed binary-valued labeling function  $u(x) \in \{0, 1\}$  to study the *min-cut* problem (A.1) in spatially continuous settings and formulated the segmentation problem as a *continuous min-cut model*. In addition, they proposed to solve the challenging non-convex *continuous*



*min-cut* problem by means of convex relaxation, where  $u(x) \in \{0, 1\}$  was relaxed to the convex domain  $u(x) \in [0, 1]$ , and proved that:

**Proposition 3** *Thresholding the optimum  $u^*(x) \in [0, 1]$  of the convex relaxed continuous min-cut model by any parameter  $\alpha \in (0, 1]$  gives the binary function*

$$u^\alpha(x) = \begin{cases} 1, & u^*(x) \geq \alpha \\ 0, & u^*(x) < \alpha \end{cases}, \quad (\text{A.8})$$

*which solves the original continuous min-cut problem globally and exactly.*

Compared with the original challenging combinatorial optimization problem, the *convex relaxed continuous min-cut model* gives rise to a convex optimization problem, which is much simpler in theory and numerical implementation. Furthermore, in analogy with the discrete max-flow model Fig. A.1 (A), [7] proposed a generalized max-flow model in spatially continuous settings, as shown in Fig. A.1 (B),

$$\max_{p_s, p_t, q} \int_{\Omega} p_s(x) dx \quad (\text{A.9})$$

to maximize the total flow streaming from the source to the sink, subject to a series of flow capacity and flow conservation constraints (see [7] for more details).

Through variational analysis, they proved that the *continuous max-flow model* (A.9), under the condition of simple convex constraints and linear equality constraints, is equivalent to the *convex relaxed continuous min-cut* problem as well as the original *continuous min-cut* problem. Based on the modern augmented Lagrangian theories, [7] developed an efficient continuous max-flow based algorithm that employs simple flow-maximization steps and achieved efficient convergence. Compared with the discrete min-cut/max-flow algorithms, the continuous max-flow/min-cut algorithm provides sub-pixel accuracy and can be easily parallelized on modern commercially available graphics hardware to achieve high computational efficiency.

## Bibliography

- [1] Yuri Boykov, Olga Veksler, and Ramin Zabih. Fast approximate energy minimization via graph cuts. *Pattern Analysis and Machine Intelligence, IEEE Transactions on*, 23(11):1222–1239, 2001.
- [2] Tony F Chan, Selim Esedoglu, and Mila Nikolova. Algorithms for finding global minimizers of image segmentation and denoising models. *SIAM Journal on Applied Mathematics*, 66(5):1632–1648, 2006.
- [3] Vladimir Kolmogorov and Ramin Zabih. What energy functions can be minimized via graph cuts? *Pattern Analysis and Machine Intelligence, IEEE Transactions on*, 26(2):147–159, 2004.
- [4] Thomas Pock, Antonin Chambolle, Daniel Cremers, and Horst Bischof. A convex relaxation approach for computing minimal partitions. In *Computer Vision and Pattern Recognition, 2009. CVPR 2009. IEEE Conference on*, pages 810–817. IEEE, 2009.
- [5] Jing Yuan, Egil Bae, and Xue-Cheng Tai. A study on continuous max-flow and min-cut approaches. In *Computer Vision and Pattern Recognition (CVPR), 2010 IEEE Conference on*, pages 2217–2224. IEEE, 2010.
- [6] LR Ford and Delbert Ray Fulkerson. *Flows in networks*, volume 1962. Princeton University Press, 1962.
- [7] Jing Yuan, Egil Bae, Xue-Cheng Tai, and Yuri Boykov. A spatially continuous max-flow and min-cut framework for binary labeling problems. *Numerische Mathematik*, 126(3):559–587, 2014.

# Appendix B

## Duality of the Volume

### Proportion-Preserved Max-Flow Model and Convex Relaxed Potts Model

**Proof** We can rewrite the flow conservation constraints (3.9), (3.10) and (3.11) as follows:

$$G_b(x) := (\operatorname{div} q^b - p_s + p_t^b + p_w^b)(x) = 0; \quad (\text{B.1})$$

$$G_{ll}(x) := (\operatorname{div} q^{ll} - p_s + p_t^{ll} + p_w^{ll})(x) = 0; \quad (\text{B.2})$$

$$G_{rl}(x) := (\operatorname{div} q^{rl} - p_s + p_t^{rl} + p_w^{rl})(x) = 0. \quad (\text{B.3})$$

By introducing the multiplier function  $\xi_i(x)$ ,  $i \in L$ , to the linear equality constraints (B.1) - (B.3), the continuous max-flow model (3.7) can be equivalently expressed as the primal-dual model as follows:

$$\max_{p_s, p_t, q, r} \min_{\xi} \int_{\Omega} p_s dx + \sum_{i \in L} \langle \xi_i, G_i \rangle, \quad (\text{B.4})$$

subject to the flow capacity constraints (3.8). Obviously, we have

$$(3.7) \iff (B.4).$$

Following [1], the energy function (B.4) is linear in both the multiplier  $\xi_i$ ,  $i \in L$ , and flow variables  $(p_s, p_t, q, r)$  and the *min/max* operators are inter-changeable.

Through simple re-organizing of (B.4), we have:

$$\max_{p_s, p_t, q, r} \min_{\xi} \left\langle 1 - \sum_{i \in L} \xi_i, p_s \right\rangle + \sum_{i \in L} \langle \xi_i, p_t^i \rangle + \sum_{i \in L} \langle \xi_i, \text{div } q^i \rangle + r \left( \int_{\Omega} \xi_{ll} - \gamma \int_{\Omega} \xi_{rl} \right). \quad (B.5)$$

Similar to the analysis [2], maximization over the free source flow  $p_s$  results in  $\sum_{i \in L} \xi_i(x) = 1$ ,  $\forall x \in \Omega$ , since  $p_s$  is unconstrained. Maximization of the sink flow  $p_t^i$ ,  $i \in L$ , in (B.5) over sink flow constraints (3.8), leads to

$$\max_{p_t^i(x) \leq \rho_i(x)} \sum_{i \in L} \langle \xi_i, p_t^i \rangle = \sum_{i \in L} \langle \xi_i, \rho_i \rangle \quad (B.6)$$

Following the analysis [3], maximization of the spatial flow  $q^i$ ,  $i \in L$ , in (B.5) over the spatial flow restrictions in (3.8) gives rise to

$$\max_{|q^i(x)| \leq g(x)} \sum_{i \in L} \langle \xi_i, \text{div } q^i \rangle = \sum_{i \in L} \int_{\Omega} g(x) |\nabla \xi_i| dx. \quad (B.7)$$

In addition, with the help of conjugate representation of absolute function, we can equally rewrite the last term in (3.6) as

$$\begin{aligned} \alpha \left| \int_{\Omega} \xi_{ll} - \gamma \int_{\Omega} \xi_{rl} \right| &= \max_{|w| \leq 1} \alpha w \left( \int_{\Omega} \xi_{ll} - \gamma \int_{\Omega} \xi_{rl} \right) \\ &= \max_{|r| \leq \alpha} r \left( \int_{\Omega} \xi_{ll} - \gamma \int_{\Omega} \xi_{rl} \right). \end{aligned} \quad (B.8)$$

We refer the readers to [2] for more details for these variational analysis.

With the help of the analysis (15) and (16), we can conclude the equivalence of the volume proportion preserved max-flow model (7) and the convex relaxed volume proportion preserved min-cut model (6).

## **Bibliography**

- [1] Ivar Ekeland and Roger Temam. *Convex analysis and variational problems*, volume 28. Siam, 1999.
- [2] Jing Yuan, Egil Bae, Xue-Cheng Tai, and Yuri Boykov. A continuous max-flow approach to potts model. In *Computer Vision—ECCV 2010*, pages 379–392. Springer, 2010.
- [3] E Giusti. *Minimal surfaces and functions of bounded variation*. Number 80. Springer, 1984.

# Appendix C

## A Volume Proportion-Preserved Continuous Max-Flow Algorithm

We explored the augmented Lagrangian function in an iterative manner:

$$\max_{p_s, p_t, q, r} \min_{\xi} \int_{\Omega} p_s dx + \sum_{i \in L} \langle \xi_i, G_i \rangle - \frac{c}{2} \sum_{i \in L} \|G_i(x)\|^2, \quad (\text{C.1})$$

subject to the flow capacity constraints (3.8) with scale  $c > 0$ . The optimization problem (C.1) can be split into smaller sub-problems that involve optimization of independent flow variables and labeling function simultaneously. For example, at each  $k$ -th iteration:

- Optimize (C.1) over the spatial flows  $q^i(x), i \in L$ , *s.t.* (3.8) with the initial/updated variables  $(\xi; p_s, p_t, r)^k$ , which gives rise to

$$(q^i)^{k+1} := \arg \max_{|q^i(x)| \leq g(x)} -\frac{c}{2} \|\text{div } q^i - F_i^k\|^2,$$

where  $F_i^k = (p_s)^k - (p_t)^k - (p_w^i)^k + (\xi_i)^k/c$ . This can be solved by the projected gradient algorithm [1]:

$$\text{Proj}_{|q^i(x)| \leq g(x)}((q^i)^k + \tau \nabla(\text{div}(q^i)^k - F_i^k)), \quad (\text{C.2})$$

where  $\tau > 0$  is the step-size for convergence.

- Optimize (C.1) over the sink flows  $p_i^i(x)$ ,  $i \in L$ , s.t. (3.8) with the initial/updated variables  $(\xi; p_s, q, r)^k$ , which amounts to

$$(p_i^i)^{k+1} := \arg \max_{p_i^i(x) \leq \rho_i(x)} -\frac{c}{2} \|p_i^i + T_i^k\|^2,$$

where  $T_i^k = \text{div}(q^i)^{k+1} - (p_s)^k + (p_w^i)^k - (\xi_i)^k/c$ . This can be solved exactly by:

$$(p_i^i)^{k+1} = \min(\rho_i, -T_i^k). \quad (\text{C.3})$$

- Optimize (C.1) over the free source flow  $p_s(x)$  with the initial/updated variables  $(\xi; p_t, q, r)^k$ , which results in

$$(p_s)^{k+1} := \arg \max_{p_s(x)} \int_{\Omega} p_s dx - \frac{c}{2} \sum_{i \in L} \|p_s - J_i^k\|^2,$$

where  $J_i^k = \text{div}(q^i)^{k+1} + (p_i^i)^{k+1} + (p_w^i)^k - (\xi_i)^k/c$ ,  $i \in L$ . This can be explicitly solved by:

$$(p_s)^{k+1} = \frac{\sum_{i \in L} J_i^k + 1/c}{3}. \quad (\text{C.4})$$

- Optimize (C.1) over  $r \in [-\alpha, \alpha]$ , with the initial/updated variables  $(u; p_s, p_t, q)^k$ , which leads to

$$(r)^{k+1} := \arg \max_{|r| \leq \alpha} -\frac{c}{2} \|r + H_1^k\|^2 - \frac{c}{2} \|\gamma r - H_2^k\|^2,$$

where  $H_1^k = \text{div}(q^l)^{k+1} - (p_s)^{k+1} + (p_t^l)^{k+1} - (\xi_l)^k/c$  and  $H_2^k = \text{div}(q^{rl})^{k+1} - (p_s)^{k+1} + (p_t^{rl})^{k+1} - (\xi_{rl})^k/c$ . This can be computed by:

$$(r)^{k+1} = \frac{-\int_{\Omega} H_1^k + \gamma \int_{\Omega} H_2^k}{(1 + \gamma^2)}, \quad (\text{C.5})$$

which is then used to update  $p_w^i$ ,  $i \in L$ , following (3.9), (3.10) and (3.11).

- Update the characteristic function  $\xi_i(x)$ ,  $i \in L$ , by

$$(\xi_i)^{k+1} = (\xi_i)^k - c \cdot (G_i)^{k+1}(x), \quad (\text{C.6})$$

where  $(G_i)^{k+1}$  is the flow residue in the current iteration.

- Update  $k = k + 1$  and repeat the above steps until convergence.

The final optimum integer characteristic function  $\xi_i^*(x)$  can be obtained by finding the maximum value of  $\xi_i(x)$ ,  $i \in L$ , across the 4<sup>th</sup> dimension.

## Bibliography

- [1] Antonin Chambolle. An algorithm for total variation minimization and applications. *Journal of Mathematical Imaging and Vision*, 20(1):89–97, January 2004.



# Appendix D

## Proof of Proposition 2

**Proof** Given function  $f(x)$ , its absolute function  $|f(x)|$  can be equally rewritten in its conjugate form, i.e.,  $|f(x)| = \max_{|g(x)| \leq 1} g(x) \cdot f(x)$ . As such, we can rewrite the 1<sup>st</sup> and 3<sup>rd</sup> terms in (4.10) as

$$\begin{aligned} & \omega_1 \cdot \int |S_1^0 + \nabla S_1 \cdot \vec{\xi}_1| dx + \omega_2 \cdot \int |S_2^0 + \nabla S_2 \cdot \vec{\xi}_2| dx = \\ & \max_{|\epsilon_{1,2}|} \int \epsilon_1 \cdot (S_1^0 + \nabla S_1 \cdot \vec{\xi}_1) dx + \int \epsilon_2 \cdot (S_2^0 + \nabla S_2 \cdot \vec{\xi}_2) dx, \end{aligned} \quad (\text{D.1})$$

where  $|\epsilon_i| \leq \omega_i$ ,  $\vec{\xi}_i = [\xi_i^x, \xi_i^y, \xi_i^z]^T$ ,  $i \in \{1, 2\}$ . Similarly, the 2<sup>nd</sup> term can be reformulated as:

$$\begin{aligned} \omega_1 \alpha_1 \cdot \sum_{j \in D} \int |\nabla((\phi_1^j)^l + \xi_1^j)| dx &= \max_{|\eta_1^j|} \sum_{j \in D} \int \eta_1^j \cdot \nabla((\phi_1^j)^l + \xi_1^j) dx \\ &= \max_{|\eta_1^j|} \sum_{j \in D} \int \text{div} \eta_1^j \cdot ((\phi_1^j)^l + \xi_1^j) dx, \quad |\eta_1^j| \leq \omega_1 \alpha_1, \end{aligned} \quad (\text{D.2})$$

and the 4<sup>th</sup> term can be expressed in a similar manner:

$$\begin{aligned} \omega_2 \alpha_2 \cdot \sum_{j \in D} \int |\nabla((\phi_2^j)^l + \xi_2^j)| dx &= \max_{|\eta_2^j|} \sum_{j \in D} \int \eta_2^j \cdot \nabla((\phi_2^j)^l + \xi_2^j) dx \\ &= \max_{|\eta_2^j|} \sum_{j \in D} \int \text{div} \eta_2^j \cdot ((\phi_2^j)^l + \xi_2^j) dx, \quad |\eta_2^j| \leq \omega_2 \alpha_2. \end{aligned} \quad (\text{D.3})$$

In addition, the 5<sup>th</sup> term can be represented by:

$$\begin{aligned} & \beta \cdot \sum_{j \in D} \int |((\phi_1^j)^l + \xi_1^j) - ((\phi_2^j)^l + \xi_2^j)| \, dx = \\ & \max_{|r^j|} \sum_{j \in D} \int r^j \cdot ((\phi_1^j)^l + \xi_1^j - (\phi_2^j)^l - \xi_2^j) \, dx, \end{aligned} \quad (\text{D.4})$$

where  $|r^j| \leq \beta$ .

By combining (D.1), (D.2), (D.3) and (D.4), we can see that (4.10) can be written as:

$$\begin{aligned} & \min_{\xi_i^j} \max_{\epsilon_i, \eta_i^j, r^j} \int \epsilon_1 \cdot (S_1^0 + \nabla S_1 \cdot \vec{\xi}_1) \, dx + \int \epsilon_2 \cdot (S_2^0 + \nabla S_2 \cdot \vec{\xi}_2) \, dx + \\ & \sum_{j \in D} \int \operatorname{div} \eta_1^j ((\phi_1^j)^l + \xi_1^j) \, dx + \sum_{j \in D} \int \operatorname{div} \eta_2^j ((\phi_2^j)^l + \xi_2^j) \, dx + \\ & \sum_{j \in D} \int r^j \cdot ((\phi_1^j)^l + \xi_1^j - (\phi_2^j)^l - \xi_2^j) \, dx, \end{aligned} \quad (\text{D.5})$$

where  $|\epsilon_i| \leq \omega_i$ ,  $|\eta_i^j| \leq \omega_i \cdot \alpha_{1,2}$  and  $|r^j| \leq \beta$ ,  $i \in \{1, 2\}$ . Through simple re-organizing, we observe that (D.5) leads to:

$$\begin{aligned} & \min_{\xi_i^j} \max_{\epsilon_i, \eta_i^j, r^j} \int (\epsilon_1 \cdot S_1^0 + \sum_{j \in D} \nabla(\phi_1^j)^l \cdot \eta_1^j + \sum_{j \in D} r^j \cdot (\phi_1^j)^l) \, dx + \\ & \int (\epsilon_2 \cdot S_2^0 + \sum_{j \in D} \nabla(\phi_2^j)^l \cdot \eta_2^j - \sum_{j \in D} r^j \cdot (\phi_2^j)^l) \, dx + \\ & \sum_{j \in D} \int \xi_1^j \cdot (\epsilon_1 \cdot \partial^j S_1 + \operatorname{div} \eta_1^j + r^j) \, dx + \\ & \sum_{j \in D} \int \xi_2^j \cdot (\epsilon_2 \cdot \partial^j S_2 + \operatorname{div} \eta_2^j - r^j) \, dx. \end{aligned} \quad (\text{D.6})$$

Clearly, variational analysis of the free variables  $\xi_i^j$ ,  $i \in \{1, 2\}$ ,  $j \in D$ , shows that (D.6) actually leads to the linear equality constraints (4.12) and (4.13) and the maximization problem (4.11).

Therefore, *Proposition 2* is proved.

## **Bibliography**

# Appendix E

## An Efficient Numerical Solver

The augmented Lagrangian function (4.15) that involves three dual variables  $\epsilon$ ,  $\eta$  and  $r$  can be optimized by splitting the overall problem into a series of sub-problems, each of which optimizes one variable while keeping the others fixed and the process is iterated until convergence.

The  $k$ -th iteration involves the following steps:

- Let  $k = 1$  and initialize  $(\epsilon_i)^k$ ,  $(\eta_i^j)^k$ ,  $(r)^k$  and  $(\xi_i^j)^k$ ,  $i \in \{1, 2\}$ ,  $j \in D$ , to 0.
- Maximize  $(\epsilon_1)^{k+1}$  by keeping the other variables  $\{(\eta_1^j, r^j, \xi_1^j)^k\}$ ,  $j \in D$ , fixed. This leads to the following optimization problem:

$$\max_{|\epsilon_1| \leq \omega_1} \int \epsilon_1 \cdot S_1^0 dx - \frac{c}{2} \sum_{j \in D} \|G_1^j\|^2, \quad (\text{E.1})$$

which can be computed exactly with:

$$(\epsilon_1)^{k+1} = \frac{S_1^0 - c \sum_{j \in D} \partial^j S_1 \cdot (\text{div } \eta_1^j + r^j)}{c \sum_{j \in D} (\partial^j S_1)^2}.$$

- Maximize  $(\eta_1^j)^{k+1}$ ,  $j \in D$ , using the updated variables  $\{(\epsilon_1)^{k+1}, (r^j, \xi_1^j)^k\}$ , i.e.,

$$\max_{|\eta_1^j| \leq \omega_1 \alpha_1} \int \eta_1^j \cdot \nabla (\phi_1^j)^l dx - \frac{c}{2} \|G_1^j\|^2. \quad (\text{E.2})$$

This leads to three convex optimization problems where *Chambolle's* projected gradient algorithm [1] applies.

- Maximize  $(\epsilon_2)^{k+1}$  and  $(\eta_2^j)^{k+1}$  following the similar steps as for  $(\epsilon_1)^{k+1}$  and  $(\eta_1^j)^{k+1}$ .
- Maximize  $(r^j)^{k+1}$ ,  $j \in D$ , by fixing the other updated variables  $\{(\epsilon_i, \eta_i^j)^{k+1}, (\xi_i^j)^k\}$ ,  $i \in \{1, 2\}$ .

This can be solved by

$$\max_{|r^j| \leq \beta} \sum_{j \in D} \int r^j \cdot (\phi_1^j)^l dx - \frac{c}{2} \sum_{j \in D} \|G_1^j\|^2 - \sum_{j \in D} \int r^j \cdot (\phi_2^j)^l dx - \frac{c}{2} \sum_{j \in D} \|G_2^j\|^2. \quad (\text{E.3})$$

Clearly,  $(r^j)^{k+1}$  can be obtained by

$$(r^j)^{k+1} = \left\{ (\phi_1^j)^l + c \cdot (\epsilon_2 \cdot \partial^j S_2 + \text{div } \eta_2^j) - (\phi_2^j)^l - c \cdot (\epsilon_1 \cdot \partial^j S_1 + \text{div } \eta_1^j) \right\} / 2, \quad (\text{E.4})$$

truncated by  $\beta$ , i.e.,  $(r^j)^{k+1} = \max(\min((r^j)^{k+1}, \beta), -\beta)$ .

- Re-calculate  $(\xi_i^j)^{k+1}$ ,  $i = \{1, 2\}$ ,  $j \in D$ , using the updated variables  $\{(\epsilon_i, \eta_i^j, r^j)^{k+1}\}$  for  $G_i^j$  following

$$(\xi_1^j)^{k+1} = (\xi_1^j)^k - c \cdot G_1^j \quad (\text{E.5})$$

and

$$(\xi_2^j)^{k+1} = (\xi_2^j)^k - c \cdot G_2^j. \quad (\text{E.6})$$

- Let  $k = k + 1$  and iterate the above steps until convergence.

The obtained incremental deformation field  $\vec{\xi}_i^z$  were used to generate the final deformation  $\vec{\phi}_i$ ,  $i \in \{1, 2\}$  in (4.2) and (4.3) and deform CT towards  $^1\text{H}$  and  $^3\text{He}$  MRI.

## Bibliography

- [1] Antonin Chambolle. An algorithm for total variation minimization and applications. *Journal of Mathematical imaging and vision*, 20(1-2):89–97, 2004.

# **Appendix F**

## **Supplementary Materials**

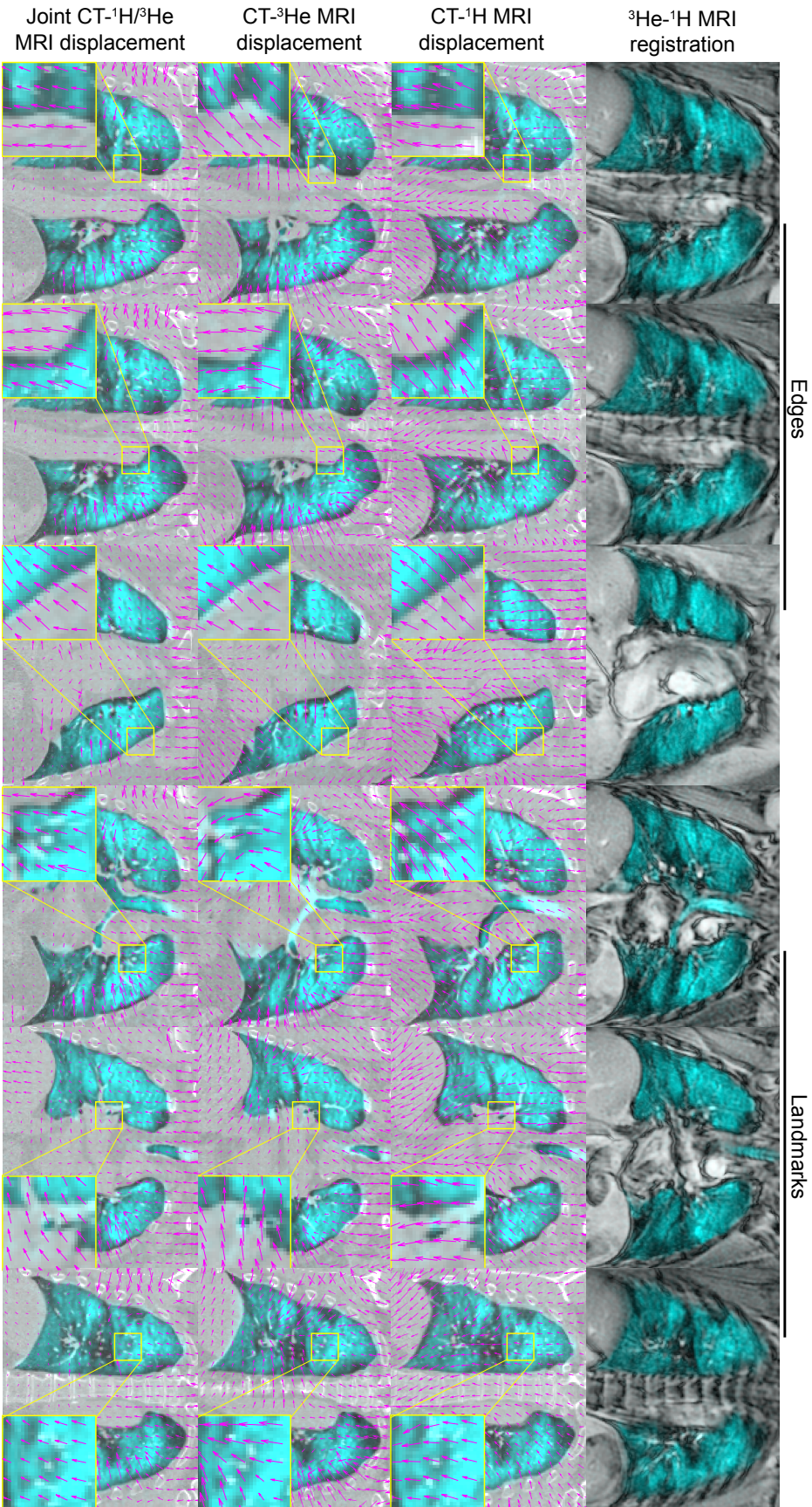


Figure F.1: Illustration of joint CT- $^1\text{H}/^3\text{He}$  MRI registration using consistent deformation prior. The 1<sup>st</sup> row shows representative registered  $^3\text{He}$  (cyan) and  $^1\text{H}$  (gray) MRI as inputs. The 2<sup>nd</sup>, 3<sup>rd</sup>, and 4<sup>th</sup> rows show CT- $^3\text{He}$  MRI registration by registering CT to  $^1\text{H}$  MRI only,  $^3\text{He}$  MRI only, and  $^1\text{H}$  and  $^3\text{He}$  MRI both, respectively, where the respective displacement fields (purple vectors) within the inset boxes are shown expanded in yellow boxes. The 1<sup>st</sup> and 4<sup>th</sup> columns show representative improvements of joint CT- $^1\text{H}/^3\text{He}$  MRI registration on image edges and landmarks compared with individual CT- $^1\text{H}$  MRI and CT- $^3\text{He}$  MRI registration, where the joint registration displacement field is consistent with both individual registration but dominated by CT- $^1\text{H}$  MRI registration (no  $^3\text{He}$  information). The 2<sup>nd</sup> and 5<sup>th</sup> columns show similar results on image edges and landmarks, where the joint registration displacement field is consistent with both individual registration but dominated by CT- $^3\text{He}$  MRI registration (no  $^1\text{H}$  information). The 3<sup>rd</sup> and 6<sup>th</sup> columns show CT- $^1\text{H}/^3\text{He}$  MRI registration displacement fields consistent with both individual registrations on image edges and landmarks.



Table F.1: <sup>3</sup>He MRI segmental ventilation defect percent (VDP) for the entire database. (n=35)

Subject	LB1	LB2	LB3	LB4	LB5	LB6	LB7	LB8	LB9	RB1	RB2	RB3	RB4	RB5	RB6	RB7	RB8	RB9	RB10
S1	3.7	11.2	0.4	1.4	2.4	2.0	13.2	2.9	5.3	3.2	1.8	2.3	0.2	0.1	2.5	6.1	3.0	15.7	19.6
S2	4.4	5.7	3.7	2.2	3.3	19.0	6.3	7.7	14.1	0.7	1.7	0.9	4.3	32.5	16.3	1.9	2.6	10.1	11.5
S3	44.8	88.6	85.2	12.8	8.3	97.4	24.4	47.4	52.1	43.8	94.2	18.7	82.6	44.1	92.2	63.8	18.2	28.1	41.1
S4	1.5	4.0	1.1	1.6	0.9	0.4	1.0	0.5	0.6	3.0	0.6	0.4	0.2	1.9	0.0	3.0	0.4	4.3	2.0
S5	4.4	3.8	1.5	0.0	2.7	0.6	2.0	1.2	3.6	3.6	1.0	1.6	1.2	3.0	0.0	6.3	2.0	3.3	4.8
S6	2.1	5.5	5.2	5.2	0.4	3.9	2.5	2.3	4.0	4.0	6.3	4.0	0.3	32.7	14.9	25.3	9.8	47.0	28.5
S7	0.7	0.2	0.0	0.2	0.2	0.2	0.2	2.6	0.6	1.1	0.1	0.0	0.6	2.6	0.0	0.6	0.5	3.7	0.0
S8	0.0	0.0	0.0	0.0	0.0	0.0	0.0	0.0	0.0	0.0	0.0	0.0	0.0	0.0	0.0	0.0	0.0	0.0	0.0
S9	4.9	2.1	5.7	1.7	5.5	9.1	0.2	20.4	20.6	18.3	10.3	10.0	9.3	26.3	5.7	12.8	6.3	25.9	20.1
S10	0.1	3.9	1.1	6.2	4.9	0.7	1.6	1.0	2.2	2.6	0.5	3.1	35.9	11.0	1.3	19.8	4.4	9.2	3.8
S11	3.6	4.7	4.3	3.9	3.6	2.1	2.0	0.1	2.0	7.1	1.5	3.8	3.0	4.2	2.6	7.1	0.1	1.4	2.2
S12	6.0	2.3	6.4	6.0	28.8	2.4	11.2	2.7	3.7	12.1	7.9	13.0	11.5	20.9	3.4	26.0	8.4	18.6	10.7
S13	2.8	1.2	0.3	0.3	0.1	0.6	0.3	0.3	0.1	5.8	1.6	0.6	0.0	0.3	0.7	2.1	0.4	1.6	0.1
S14	3.6	0.1	2.6	2.8	0.2	1.1	2.3	0.4	1.7	2.2	0.1	0.4	0.1	2.7	0.2	1.5	9.9	2.7	1.0
S15	6.6	6.7	4.5	6.3	24.6	25.5	11.3	28.0	23.3	11.2	2.8	7.0	3.4	0.0	21.1	10.7	6.7	28.3	49.1
S16	7.3	8.6	4.6	1.7	2.8	61.7	0.9	13.1	20.9	14.0	4.2	24.2	11.2	4.3	3.1	10.3	15.7	53.9	17.7
S17	15.8	8.6	15.9	25.0	20.9	38.7	14.1	29.5	21.0	22.8	14.5	17.8	17.0	13.7	19.8	19.0	13.0	14.6	21.6
S18	13.0	11.9	38.1	37.1	82.6	42.9	18.4	12.3	23.9	32.0	10.0	16.3	15.8	21.1	14.9	41.0	13.3	30.9	29.8
S19	3.3	1.2	4.6	5.4	0.0	5.9	3.1	3.5	4.6	5.1	1.1	4.5	37.8	10.6	1.6	8.2	1.7	3.3	2.5
S20	5.6	4.4	7.7	7.1	4.3	8.4	2.6	3.1	6.4	6.6	3.0	1.9	0.4	5.1	3.6	6.9	2.0	6.2	7.1
S21	6.5	7.1	23.1	9.5	15.5	6.6	16.9	7.5	7.5	8.5	12.0	5.5	6.1	9.5	17.6	17.8	0.0	10.2	20.5
S22	12.4	10.4	6.5	2.0	8.3	19.1	3.7	9.8	15.6	9.2	10.0	1.0	11.7	11.4	16.0	21.7	4.9	37.5	16.0
S23	6.2	10.6	3.4	2.6	5.0	17.0	3.7	3.2	6.8	4.5	6.0	2.2	3.3	20.6	2.6	9.6	4.5	9.9	8.1
S24	2.3	2.9	5.6	14.1	41.9	14.8	33.5	86.9	82.3	4.3	8.8	17.6	26.2	52.6	56.3	79.2	77.4	98.7	98.3
S25	7.5	5.3	4.6	4.6	29.3	55.6	63.2	62.8	79.2	9.9	7.1	6.4	6.1	37.6	62.8	62.4	42.4	39.2	49.0
S26	17.1	6.1	8.8	2.0	18.4	30.1	11.7	12.1	21.1	31.2	58.7	26.2	7.8	12.1	21.7	53.7	47.9	37.2	46.4
S27	14.3	8.0	15.8	57.5	83.7	18.7	12.5	4.0	11.7	22.7	65.8	40.0	21.7	26.6	28.1	24.5	12.7	9.9	14.8
S28	55.5	52.3	65.8	34.3	19.8	24.1	17.7	29.6	23.8	45.9	39.4	14.5	26.2	37.7	22.5	20.0	31.4	55.4	33.1
S29	11.9	9.3	11.5	20.9	14.4	17.8	8.9	19.4	23.4	13.6	16.1	18.7	14.1	25.6	16.1	34.5	13.0	10.9	18.2
S30	16.9	5.6	25.3	100.0	8.6	45.0	47.9	64.3	71.1	9.4	22.1	18.3	39.2	39.0	26.1	32.4	74.5	54.9	46.6
S31	13.4	53.1	67.3	25.6	69.0	60.5	58.0	48.0	72.1	38.8	22.7	10.6	4.6	19.7	23.2	35.4	18.6	53.7	44.7
S32	26.2	20.4	6.6	6.6	17.5	25.3	44.4	72.5	65.0	5.6	43.0	9.0	19.6	36.3	51.9	67.5	77.5	78.5	87.2
S33	19.9	29.3	13.1	42.8	74.3	71.5	23.3	30.0	47.5	11.7	41.6	26.9	39.8	36.5	61.7	65.2	60.2	81.1	70.9
S34	22.8	24.6	30.2	52.7	50.7	50.6	57.9	39.6	42.4	19.5	35.5	48.5	35.1	67.2	25.2	78.3	30.4	47.2	60.0
S35	13.7	3.2	5.5	1.9	24.1	29.7	14.2	60.4	46.5	13.6	21.0	10.8	5.6	8.9	17.5	15.9	5.7	15.1	32.4

## **Appendix G**

# **Permission for Reproduction of Scientific Articles**



# RightsLink®

[Home](#)
[Account Info](#)
[Help](#)


**Title:** Globally optimal co-segmentation of three-dimensional pulmonary 1H and hyperpolarized 3He MRI with spatial consistence prior

**Author:** Fumin Guo, Jing Yuan, Martin Rajchl, Sarah Svenningsen, Dante PI Capaldi, Khadija Sheikh, Aaron Fenster, Grace Parraga

**Publication:** Medical Image Analysis

**Publisher:** Elsevier

**Date:** July 2015

Copyright © 2015 Elsevier B.V. All rights reserved.

Logged in as:

Fumin Guo

[LOGOUT](#)

## Order Completed

Thank you for your order.

This Agreement between Fumin Guo ("You") and Elsevier ("Elsevier") consists of your license details and the terms and conditions provided by Elsevier and Copyright Clearance Center.

Your confirmation email will contain your order number for future reference.

### [Printable details.](#)

License Number	4157280771641
License date	Jul 27, 2017
Licensed Content Publisher	Elsevier
Licensed Content Publication	Medical Image Analysis
Licensed Content Title	Globally optimal co-segmentation of three-dimensional pulmonary 1H and hyperpolarized 3He MRI with spatial consistence prior
Licensed Content Author	Fumin Guo, Jing Yuan, Martin Rajchl, Sarah Svenningsen, Dante PI Capaldi, Khadija Sheikh, Aaron Fenster, Grace Parraga
Licensed Content Date	Jul 1, 2015
Licensed Content Volume	23
Licensed Content Issue	1
Licensed Content Pages	13
Type of Use	reuse in a thesis/dissertation
Portion	full article
Format	both print and electronic
Are you the author of this Elsevier article?	Yes
Will you be translating?	No
Title of your thesis/dissertation	Pulmonary Image Segmentation and Registration Algorithms: Towards Regional Evaluation of Obstructive Lung Disease
Expected completion date	Aug 2017
Estimated size (number of pages)	300
Requestor Location	

Total 0.00 USD

[ORDER MORE](#)

[CLOSE WINDOW](#)

Copyright © 2017 Copyright Clearance Center, Inc. All Rights Reserved. [Privacy statement](#). [Terms and Conditions](#).  
Comments? We would like to hear from you. E-mail us at [customercare@copyright.com](mailto:customercare@copyright.com)



RightsLink®

Home

Account Info

Help



WILEY

**Title:** Anatomical pulmonary magnetic resonance imaging segmentation for regional structure-function measurements of asthma

Logged in as:  
Fumin Guo

LOGOUT

**Author:** F. Guo, S. Svenningsen, R. L. Eddy, D. P. I. Capaldi, K. Sheikh, A. Fenster, G. Parraga

**Publication:** Medical Physics

**Publisher:** John Wiley and Sons

**Date:** Nov 30, 2016

© 2016 American Association of Physicists in Medicine

### Order Completed

Thank you for your order.

This Agreement between Fumin Guo ("You") and John Wiley and Sons ("John Wiley and Sons") consists of your license details and the terms and conditions provided by John Wiley and Sons and Copyright Clearance Center.

Your confirmation email will contain your order number for future reference.

### [Printable details.](#)

License Number	4157280092612
License date	Jul 27, 2017
Licensed Content Publisher	John Wiley and Sons
Licensed Content Publication	Medical Physics
Licensed Content Title	Anatomical pulmonary magnetic resonance imaging segmentation for regional structure-function measurements of asthma
Licensed Content Author	F. Guo, S. Svenningsen, R. L. Eddy, D. P. I. Capaldi, K. Sheikh, A. Fenster, G. Parraga
Licensed Content Date	Nov 30, 2016
Licensed Content Pages	16
Type of use	Dissertation/Thesis
Requestor type	Author of this Wiley article
Format	Print and electronic
Portion	Full article
Will you be translating?	No
Title of your thesis / dissertation	Pulmonary Image Segmentation and Registration Algorithms: Towards Regional Evaluation of Obstructive Lung Disease
Expected completion date	Aug 2017
Expected size (number of pages)	300
Requestor Location	

Publisher Tax ID	EU826007151
Billing Type	Invoice
Billing address	

Total	0.00 USD
-------	----------

Would you like to purchase the full text of this article? If so, please continue on to the content ordering system located here: [Purchase PDF](#)

If you click on the buttons below or close this window, you will not be able to return to the content ordering system.

[ORDER MORE](#)

[CLOSE WINDOW](#)



RightsLink®

Home

Account  
Info

Help



**WILEY**

**Title:** Thoracic CT-MRI coregistration for regional pulmonary structure–function measurements of obstructive lung disease

Logged in as:  
Fumin Guo

LOGOUT

**Author:** Fumin Guo, Sarah Svenningsen, Miranda Kirby, Dante PI Capaldi, Khadija Sheikh, Aaron Fenster, Grace Parraga

**Publication:** Medical Physics

**Publisher:** John Wiley and Sons

**Date:** Apr 11, 2017

© 2017 American Association of Physicists in Medicine

### Order Completed

Thank you for your order.

This Agreement between Fumin Guo ("You") and John Wiley and Sons ("John Wiley and Sons") consists of your license details and the terms and conditions provided by John Wiley and Sons and Copyright Clearance Center.

Your confirmation email will contain your order number for future reference.

#### [Printable details.](#)

License Number	4157280509545
License date	Jul 27, 2017
Licensed Content Publisher	John Wiley and Sons
Licensed Content Publication	Medical Physics
Licensed Content Title	Thoracic CT-MRI coregistration for regional pulmonary structure–function measurements of obstructive lung disease
Licensed Content Author	Fumin Guo, Sarah Svenningsen, Miranda Kirby, Dante PI Capaldi, Khadija Sheikh, Aaron Fenster, Grace Parraga
Licensed Content Date	Apr 11, 2017
Licensed Content Pages	16
Type of use	Dissertation/Thesis
Requestor type	Author of this Wiley article
Format	Print and electronic
Portion	Full article
Will you be translating?	No
Title of your thesis / dissertation	Pulmonary Image Segmentation and Registration Algorithms: Towards Regional Evaluation of Obstructive Lung Disease
Expected completion date	Aug 2017
Expected size (number of pages)	300
Requestor Location	

Publisher Tax ID	EU826007151
Billing Type	Invoice
Billing address	

Total 0.00 USD

Would you like to purchase the full text of this article? If so, please continue on to the content ordering system located here: [Purchase PDF](#)

If you click on the buttons below or close this window, you will not be able to return to the content ordering system.

**ORDER MORE**

**CLOSE WINDOW**

Copyright © 2017 Copyright Clearance Center, Inc. All Rights Reserved. [Privacy statement](#). [Terms and Conditions](#).  
Comments? We would like to hear from you. E-mail us at [customer@copyright.com](mailto:customer@copyright.com)

# **Appendix H**

## **Health Science Research Ethics Board**

### **Approval Notices**



## Office of Research Ethics

The University of Western Ontario  
 Room 4180 Support Services Building, London, ON, Canada N6A 5C1  
 Telephone: (519) 661-3036 Fax: (519) 850-2466 Email: ethics@uwo.ca  
 Website: www.uwo.ca/research/ethics

### Use of Human Subjects - Ethics Approval Notice

**Principal Investigator:** Dr. G. Parraga

**Review Number:** 15930

**Review Level:** Full Board

**Review Date:** February 10, 2009

**Protocol Title:** Longitudinal Study of Helium-3 Magnetic Resonance Imaging of COPD

**Department and Institution:** Diagnostic Radiology & Nuclear Medicine, Robarts Research Institute

**Sponsor:** INTERNAL RESEARCH FUND-UWO

**Ethics Approval Date:** May 25, 2009

**Expiry Date:** November 30, 2013

**Documents Reviewed and Approved:** UWO Protocol, Letter of information & consent form for Patients dated March 26/09 & Letter of information & consent form for Healthy Volunteers dated March 26/09

**Documents Received for Information:** Protocol, January 27, 2009; IB, ed 6, 09 Sep. 05

This is to notify you that The University of Western Ontario Research Ethics Board for Health Sciences Research Involving Human Subjects (HSREB) which is organized and operates according to the Tri-Council Policy Statement: Ethical Conduct of Research Involving Humans and the Health Canada/ICH Good Clinical Practice Practices: Consolidated Guidelines; and the applicable laws and regulations of Ontario has reviewed and granted approval to the above referenced study on the approval date noted above. The membership of this REB also complies with the membership requirements for REB's as defined in Division 5 of the Food and Drug Regulations.

The ethics approval for this study shall remain valid until the expiry date noted above assuming timely and acceptable responses to the HSREB's periodic requests for surveillance and monitoring information. If you require an updated approval notice prior to that time you must request it using the UWO Updated Approval Request Form.

During the course of the research, no deviations from, or changes to, the protocol or consent form may be initiated without prior written approval from the HSREB except when necessary to eliminate immediate hazards to the subject or when the change(s) involve only logistical or administrative aspects of the study (e.g. change of monitor, telephone number). Expedited review of minor change(s) in ongoing studies will be considered. Subjects must receive a copy of the signed information/consent documentation.

Investigators must promptly also report to the HSREB:

- a) changes increasing the risk to the participant(s) and/or affecting significantly the conduct of the study;
- b) all adverse and unexpected experiences or events that are both serious and unexpected;
- c) new information that may adversely affect the safety of the subjects or the conduct of the study.

If these changes/adverse events require a change to the information/consent documentation, and/or recruitment advertisement, the newly revised information/consent documentation, and/or advertisement, must be submitted to this office for approval.

Members of the HSREB who are named as investigators in research studies, or declare a conflict of interest, do not participate in discussion related to, nor vote on, such studies when they are presented to the HSREB.

Chair of HSREB: Dr. Joseph Gilbert

#### Ethics Officer to Contact for Further Information

<input checked="" type="checkbox"/> Janice Sutherland (jsutherl@uwo.ca)	<input type="checkbox"/> Elizabeth Wambolt (ewambolt@uwo.ca)	<input type="checkbox"/> Grace Kelly (grace.kelly@uwo.ca)	<input type="checkbox"/> Denise Grafton (dgrafton@uwo.ca)
--	---	--	--

*This is an official document. Please retain the original in your files.*

cc: ORE File  
LHRI



### Office of Research Ethics

The University of Western Ontario  
 Room 5150 Support Services Building, London, ON, Canada N6A 3K7  
 Telephone: (519) 661-3036 Fax: (519) 850-2466 Email: ethics@uwo.ca  
 Website: www.uwo.ca/research/ethics

### Use of Human Subjects - Ethics Approval Notice

---

**Principal Investigator:** Dr. G. Parraga **Review Level:** Expedited  
**Review Number:** 15928 **Revision Number:** 6  
**Review Date:** January 06, 2011 **Approved Local # of Participants:** 34  
**Protocol Title:** Hyperpolarized Helium-3 Magnetic Resonance Ventilation Heterogeneity and Airway Hyper-Responsiveness in Asthma  
**Department and Institution:** Imaging, Robarts Research Institute  
**Sponsor:** INTERNAL RESEARCH FUND-UWO  
**Ethics Approval Date:** January 07, 2011 **Expiry Date:** March 31, 2011  
**Documents Reviewed and Approved:** Addition of healthy volunteers (10), revised study methodology, revised inclusion criteria and revised letter of information & consent form dated Nov.25/10

**Documents Received for Information:**

---

This is to notify you that The University of Western Ontario Research Ethics Board for Health Sciences Research Involving Human Subjects (HSREB) which is organized and operates according to the Tri-Council Policy Statement: Ethical Conduct of Research Involving Humans and the Health Canada/ICH Good Clinical Practice Practices: Consolidated Guidelines; and the applicable laws and regulations of Ontario has reviewed and granted approval to the above referenced revision(s) or amendment(s) on the approval date noted above. The membership of this REB also complies with the membership requirements for REB's as defined in Division 5 of the Food and Drug Regulations.

The ethics approval for this study shall remain valid until the expiry date noted above assuming timely and acceptable responses to the HSREB's periodic requests for surveillance and monitoring information. If you require an updated approval notice prior to that time you must request it using the UWO Updated Approval Request Form.

During the course of the research, no deviations from, or changes to, the protocol or consent form may be initiated without prior written approval from the HSREB except when necessary to eliminate immediate hazards to the subject or when the change(s) involve only logistical or administrative aspects of the study (e.g. change of monitor, telephone number). Expedited review of minor change(s) in ongoing studies will be considered. Subjects must receive a copy of the signed information/consent documentation.

Investigators must promptly also report to the HSREB:

- a) changes increasing the risk to the participant(s) and/or affecting significantly the conduct of the study;
- b) all adverse and unexpected experiences or events that are both serious and unexpected;
- c) new information that may adversely affect the safety of the subjects or the conduct of the study.

If these changes/adverse events require a change to the information/consent documentation, and/or recruitment advertisement, the newly revised information/consent documentation, and/or advertisement, must be submitted to this office for approval.

Members of the HSREB who are named as investigators in research studies, or declare a conflict of interest, do not participate in discussion related to, nor vote on, such studies when they are presented to the HSREB.

Chair of HSREB: Dr. Joseph Gilbert  
 FDA Ref. #: IRB 0000940

Ethics Officer to Contact for Further Information		
<input checked="" type="checkbox"/> Janice Sutherland (jsutherl@uwo.ca)	<input type="checkbox"/> Elizabeth Wambolt (ewambolt@uwo.ca)	<input type="checkbox"/> Grace Kelly (grace.kelly@uwo.ca)

*This is an official document. Please retain the original in your files.*

cc: ORE File  
 LHRI





**Western  
Research**

**Use of Human Participants - Initial Ethics Approval Notice**

Research Ethics

**Principal Investigator:**Dr. Grace Parraga  
**File Number:**104200  
**Review Level:**Full Board  
**Protocol Title:**Hyperpolarized Magnetic Resonance Imaging in Asthma Pre- and Post-Bronchial Thermoplasty  
**Department & Institution:**Schulich School of Medicine and Dentistry/Imaging,Robarts Research Institute  
**Sponsor:**Lawson Health Research Institute

**Ethics Approval Date:**January 03, 2014  
**Ethics Expiry Date:**February 28, 2017

**Documents Reviewed & Approved & Documents Received for Information:**

Document Name	Comments	Version Date
Instruments	Asthma Quality of Life Questionnaire with Standardized Activities (AQLQ(S))	2013/08/15
Instruments	Asthma Control Questionnaire	2013/08/15
Instruments	Modified Borg Scale Questionnaire	2013/08/15
Instruments	mMRC Dyspnea Score Questionnaire	2013/08/15
Protocol	Robarts Protocol-Received for Information	2013/12/19
Letter of Information & Consent	version 2	2013/12/19
Western University Protocol	including Study Design diagram	

This is to notify you that the University of Western Ontario Health Sciences Research Ethics Board (HSREB) which is organized and operates according to the Tri-Council Policy Statement: Ethical Conduct of Research Involving Humans and the Health Canada/ICH Good Clinical Practice Practices: Consolidated Guidelines; and the applicable laws and regulations of Ontario has reviewed and granted approval to the above referenced study on the approval date noted above. The membership of this HSREB also complies with the membership requirements for REB's as defined in Division 5 of the Food and Drug Regulations.

The ethics approval for this study shall remain valid until the expiry date noted above assuming timely and acceptable responses to the HSREB's periodic requests for surveillance and monitoring information. If you require an updated approval notice prior to that time you must request it using the University of Western Ontario Updated Approval Request form.

Member of the HSREB that are named as investigators in research studies, or declare a conflict of interest, do not participate in discussions related to, nor vote on, such studies when they are presented to the HSREB.

The Chair of the HSREB is Dr. Joseph Gilbert. The HSREB is registered with the U.S. Department of Health & Human Services under the IRB registration number IRB 00000940.

**Signature**

**Ethics Officer to Contact for Further Information**

 Erika Basile (ekbasile@uwo.ca)	Grace Kelly (grace.kelly@uwo.ca)	Mina Makhani (mmakhani@uwo.ca)	Vivian Tran (vivian.tran@uwo.ca)
--	-------------------------------------	-----------------------------------	-------------------------------------

*This is an official document. Please retain the original in your files.*



**Western  
Research**

Research Ethics

**Western University Health Science Research Ethics Board  
HSREB Annual Continuing Ethics Approval Notice**

**Date:** October 21, 2016

**Principal Investigator:** Dr. Grace Parraga

**Department & Institution:** Schulich School of Medicine and Dentistry\Imaging,Robarts Research Institute

**Review Type:** Full Board

**HSREB File Number:** 4819

**Study Title:** A single-centre pilot study exploring the utility of magnetic resonance imaging in patients with chronic lung disease (REB #13743)

**Sponsor:**

**HSREB Renewal Due Date & HSREB Expiry Date:**

Renewal Due -2017/10/31

Expiry Date -2017/11/16

The Western University Health Science Research Ethics Board (HSREB) has reviewed the Continuing Ethics Review (CER) Form and is re-issuing approval for the above noted study.

The Western University HSREB operates in compliance with the Tri-Council Policy Statement Ethical Conduct for Research Involving Humans (TCPS2), the International Conference on Harmonization of Technical Requirements for Registration of Pharmaceuticals for Human Use Guideline for Good Clinical Practice (ICH E6 R1), the Ontario Freedom of Information and Protection of Privacy Act (FIPPA, 1990), the Ontario Personal Health Information Protection Act (PHIPA, 2004), Part 4 of the Natural Health Product Regulations, Health Canada Medical Device Regulations and Part C, Division 5, of the Food and Drug Regulations of Health Canada.

Members of the HSREB who are named as Investigators in research studies do not participate in discussions related to, nor vote on such studies when they are presented to the REB.

The HSREB is registered with the U.S. Department of Health & Human Services under the IRB registration number IRB 00000940.

~~Ethics Officer~~, on behalf of Dr. Joseph Gilbert, HSREB Chair

Ethics Officer: Erika Basile \_\_\_ Katelyn Harris \_\_\_ Nicole Kaniki \_\_\_ Grace Kelly \_\_\_ Vikki Tran \_\_\_ Karen Gopaul ✓



**Western  
Research**

Research Ethics

**Use of Human Participants - Ethics Approval Notice**

Principal Investigator: Dr. Grace Parraga  
 File Number: 103516  
 Review Level: Full Board  
 Approved Local Adult Participants: 200  
 Approved Local Minor Participants: 0  
 Protocol Title: Structure and Function MRI of Asthma  
 Department & Institution: Schulich School of Medicine and Dentistry/Imaging, Robarts Research Institute  
 Sponsor:  
 Ethics Approval Date: April 08, 2013  
 Ethics Expiry Date: March 31, 2020

**Documents Reviewed & Approved & Documents Received for Information:**

Document Name	Comments	Version Date
Protocol	Robarts Protocol - Received for information only	2013/02/06
Instruments	Telephone Script	2013/03/14
Letter of Information & Consent	ROB0037 ICF March 13 2013	2013/03/13
Western University Protocol	(including study instruments & questionnaires)	

This is to notify you that the University of Western Ontario Health Sciences Research Ethics Board (HSREB) which is organized and operates according to the Tri-Council Policy Statement: Ethical Conduct of Research Involving Humans and the Health Canada/ICH Good Clinical Practice Practices: Consolidated Guidelines; and the applicable laws and regulations of Ontario has reviewed and granted approval to the above referenced study on the approval date noted above. The membership of this HSREB also complies with the membership requirements for REB's as defined in Division 5 of the Food and Drug Regulations.


The ethics approval for this study shall remain valid until the expiry date noted above assuming timely and acceptable responses to the HSREB's periodic requests for surveillance and monitoring information. If you require an updated approval notice prior to that time you must request it using the University of Western Ontario Updated Approval Request form.

Member of the HSREB that are named as investigators in research studies, or declare a conflict of interest, do not participate in discussions related to, nor vote on, such studies when they are presented to the HSREB.

The Chair of the HSREB is Dr. Joseph Gilbert. The HSREB is registered with the U.S. Department of Health & Human Services under the IRB registration number IRB 00000940.

\_\_\_\_\_  
 Signat

**Ethics Officer to Contact for Further Information**

 Janice Sutherland (jsuther@uwo.ca)	Grace Kelly (grace.kelly@uwo.ca)	Shantel Walcott (swalcot@uwo.ca)
---	-------------------------------------	-------------------------------------

*This is an official document. Please retain the original in your files.*

Western University, Research, Support Services Bldg., Rm. 5150  
 London, ON, Canada N6A 3K7 t. 519.661.3036 f. 519.850.2466 www.uwo.ca/research/services/ethics

# Appendix I

## Curriculum Vitae

### EDUCATION

- 2013 – 2017 Doctor of Philosophy  
Robarts Research Institute  
Graduate Program in Biomedical Engineering  
The University of Western Ontario, London, ON, CANADA
- 2009 – 2012 MEd, Department of Biomedical Engineering  
Image Processing and Intelligence Control Key Laboratory of  
Education Ministry of China  
Huazhong University of Science and Technology, P.R.China
- 2005 – 2009 BSc, Bioinformation Technology  
Huazhong University of Science and Technology, P.R.China

## POSITIONS

- 2013 – 2017 **Doctoral Research Assistant**  
 Graduate Program in Biomedical Engineering  
 The University of Western Ontario, London, ON, CANADA  
 Supervisors: Dr. Grace Parraga and Dr. Aaron Fenster
- 2012 – 2013 **Doctoral Research Assistant**  
 School of Biomedical Engineering  
 McMaster University, Hamilton, ON, CANADA  
 Supervisor: Dr. Hao Peng
- 2009 – 2012 **Master's Research Assistant**  
 Medical Ultrasound Laboratory  
 Department of Biomedical Engineering  
 Huazhong University of Science and Technology, P.R.China  
 Supervisors: Dr. Mingyue Ding
- 2009 – 2009 **Undergraduate Thesis**  
 Department of Bioinformation Technology  
 Huazhong University of Science and Technology, P.R.China  
 Supervisors: Dr. Mingyue Ding

## HONORS, AWARDS and SCHOLARSHIPS

2017 *NSERC Postdoc Fellowship*, CAD \$45,000/year, 2017-2019.

2017 *IWPFI Best Scientific Exhibition Award*, IWPFI, 2017.

2017 *ISMRRM Trainee Educational Stipend Award*, USD \$475, ISMRRM (*Declined*).

2016 *ISMRRM Trainee Educational Stipend Award*, USD \$475, ISMRRM.

- 2015 *ISMRM Merit Award: Magna Cum Laude*, ISMRM.
- 2015 *ISMRM Trainee Educational Stipend Award*, USD \$460, ISMRM.
- 2015 *Robert F. Wagner Best Student Paper Award 2<sup>nd</sup> Place*, USD \$500, SPIE.
- 2015 *Robert F. Wagner Best Student Paper Award Finalist*, SPIE.
- 2014 *Robert F. Wagner Best Student Paper Award Finalist*, SPIE.
- 2013 *Western Graduate Research Scholarship*, CAD \$17,500/year, The University of Western Ontario, 2013-2017.
- 2011 *Scholarship of Research Excellence*, USD \$500, Shanghai United Imaging Healthcare Ltd., Shanghai, P.R. China.
- 2010 *Outstanding Graduate Student and Public Sustainability Award*, USD \$200, Huazhong University of Science and Technology, P.R.China.
- 2008 *Academic Excellence Award*, USD \$300, Huazhong University of Science and Technology, P.R.China (Top 5%).
- 2007 *National Encouragement Award*, USD \$200, Huazhong University of Science and Technology, P.R.China (Top 5%).
- 2006 *Academic Progress Award*, USD \$250, Huazhong University of Science and Technology, P.R.China (Top 5%).

## **PUBLICATIONS and PRESENTATIONS**

### **A. Referred Journal Manuscripts ( n = 18 )**

- 1 DPI Capaldi, J Baxter, J McLeod, RL Eddy, S Svenningsen, **F Guo**, P Nair, DG McCormack, and G Parraga. Dynamic Free-breathing Pulmonary Magnetic Resonance Imaging

- to Quantify Regional Specific-Ventilation in Asthma. *Radiology*. (2017, submitted, Ms.# RAD-17-1993)
- 2 A Ouriadov, DPI Capaldi, E Lessard, **F Guo**, H Young, DG McCormack and G Parraga. Undersampled Diffusion-weighted  $^{129}\text{Xe}$  MRI Morphometry of Airspace Enlargement: Feasibility in Chronic Obstructive Pulmonary Disease. *Magnetic Resonance in Medicine*. (2017, submitted, Ms.# MRM-17-18049)
  - 3 DPI Capaldi, K Sheikh, RL Eddy, **F Guo**, S Svenningsen, P Nair, and G Parraga. Free-breathing Pulmonary MRI Ventilation Response to Bronchodilator and Provocation in Severe Asthma. *Academic Radiology* (2017).
  - 4 **F Guo**, S Svenningsen, M Kirby, DPI Capaldi, K Sheikh, A Fenster, and G Parraga. Thoracic CT-MRI Co-Registration for Regional Pulmonary Structure-Function Measurements of Obstructive Lung Disease. *Medical Physics* 44.5 (2017): 1718-1733.
  - 5 K Sheikh, **F Guo**, DPI Capaldi, A Ouriadov, RL Eddy, S Svenningsen, DG McCormack, HO Coxson, and G Parraga. Ultrashort echo time MRI biomarkers of asthma. *Journal of Magnetic Resonance Imaging* (2016).
  - 6 S Svenningsen, **F Guo**, DG McCormack, and G Parraga. Non-Cystic Fibrosis Bronchiectasis: Regional Abnormalities and Response to Airway Clearance Therapy using Pulmonary Functional Magnetic Resonance Imaging. *Academic Radiology* 24.1 (2017): 4-12.
  - 7 S Svenningsen, P Nair, **F Guo**, DG McCormack, and G Parraga. Is Ventilation Heterogeneity related to Asthma Control? *European Respiratory Journal* (2016): ERJ-00393.
  - 8 D Leary, S Svenningsen, **F Guo**, S Bhatawadekar, G Parraga and GN Maksym. Hyperpolarized  $^3\text{He}$  Magnetic Resonance Imaging Ventilation Defects in Asthma: Relationship to Airway Mechanics. *Physiological reports* 4.7 (2016): e12761.

- 9 **F Guo**, S Svenningsen, R Eddy, DPI Capaldi, K Sheikh, A Fenster, and G Parraga. Anatomical Pulmonary Magnetic Resonance Imaging Segmentation for Regional Structure-Function Measurements in Asthma. *Medical Physics* 43.6 (2016): 2911-2926.
- 10 DPI Capaldi, **F Guo**, and G Parraga. Imaging How and Where We Breathe Oxygen: Another Big Short? *Journal of thoracic disease* 8.3 (2016): E204.
- 11 DPI Capaldi, N Zha, **F Guo**, D Pike, DG McCormack, M Kirby, and G Parraga. Pulmonary Imaging Biomarkers of Gas-trapping and Emphysema in COPD:  $^3\text{He}$  MRI and CT Parametric Response Maps. *Radiology* 279.2 (2016): 597-608.
- 12 D Pike, M Kirby, **F Guo**, DPI Capaldi, A Ouriadov, DG McCormack, and G Parraga. Regional Heterogeneity of Chronic Obstructive Pulmonary Disease Phenotypes: Pulmonary  $^3\text{He}$  Magnetic Resonance Imaging and CT. *COPD: Journal of Chronic Obstructive Pulmonary Disease* (2016): 1-9.
- 13 D Pike, M Kirby, **F Guo**, DG McCormack, and G Parraga. Ventilation Heterogeneity in Ex-smokers without Airflow Limitation. *Academic radiology* 22.8 (2015): 1068-1078.
- 14 S Svenningsen, G Paulin, K Sheikh, **F Guo**, A Hasany, M Kirby, R Etemad-Rezai, DG McCormack, and G Parraga. Oscillatory Positive Expiratory Pressure in Chronic Obstructive Pulmonary Disease. *COPD: Journal of Chronic Obstructive Pulmonary Disease* 13.1 (2016): 66-74.
- 15 **F Guo**, J Yuan, M Rajchl, S Svenningsen, DPI Capaldi, K Sheikh, A Fenster, and G Parraga. Globally Optimal Co-Segmentation of Three-dimensional Pulmonary  $^1\text{H}$  and Hyperpolarized  $^3\text{He}$  MRI with Spatial Consistence Prior. *Medical image analysis* 23.1 (2015): 43-55.
- 16 DPI Capaldi, K Sheikh, **F Guo**, S Svenningsen, R Etemad-Rezai, HO Coxson, JA Leipsic, DG McCormack, and G Parraga. Free-breathing Pulmonary and Hyperpolarized



- <sup>3</sup>He MRI: Comparison in COPD and Bronchiectasis. *Academic radiology* 22.3 (2015): 320-329.
- 17 S Svenningsen, **F Guo**, M Kirby, S Choy, A Wheatley, DG McCormack, and G Parraga. Pulmonary Functional Magnetic Resonance Imaging: Asthma Temporal-Spatial Maps. *Academic radiology* 21.11 (2014): 1402-1410.
- 18 W Ma, K Sheikh, S Svenningsen, D Pike, **F Guo**, R EtemadRezai, J Leipsic, HO Coxson, DG McCormack, and G Parraga. Ultrashort Echo Time pulmonary MRI: Evaluation and Reproducibility in COPD Subjects with and without Bronchiectasis. *Journal of Magnetic Resonance Imaging* 41.5 (2015): 1465-1474.

## **B. Published Refereed Conference Papers ( n = 5 )**

- 1 **F Guo**, DPI Capaldi, RD Cesare, A Fenster, and G Parraga. Registration Pipeline for Pulmonary Free-Breathing <sup>1</sup>H MRI Ventilation Measurements. *SPIE Medical Imaging. International Society for Optics and Photonics*, 2017.
- 2 **F Guo**, S Svenningsen, E Bluemke, M Rajchl, J Yuan, A Fenster, and G Parraga. Automated Pulmonary Lobar Ventilation Measurements Using Volume-matched Thoracic CT and MRI. *SPIE Medical Imaging. International Society for Optics and Photonics*, 2015. **(Best Student Paper Award Finalist and 2<sup>nd</sup> Place)**
- 3 W Qiu, M Rajchl, **F Guo**, Y Sun, E Ukwatta, A Fenster, and J Yuan. 3D Prostate TRUS Segmentation Using Globally Optimized Volume-Preserving Prior. *Medical Image Computing and Computer- Assisted Intervention (MICCAI)*, 2014.
- 4 **F Guo**, D Pike, S Svenningsen, HO Coxson, JJ Drozd, J Yuan, A Fenster, and G Parraga. Development and Application of Pulmonary Structure-Function Registration Methods: Towards Pulmonary Image-Guidance Tools for Improved Airway- Targeted Therapies

and Outcomes. SPIE Medical Imaging. International Society for Optics and Photonics, 2014. (**Best Student Paper Award Finalist**)

- 5 **F Guo**, M Ding, and X Zhang. Fast Image Matching based on Multi-Core DSP. Intelligent Computation and Bio-Medical Instrumentation (ICBMI), 2011 International Conference on. IEEE, 2011.

### **Peer Reviewed Published Conference Abstracts ( n = 20 )**

- 1 HM Young, **F Guo**, RL Eddy, C Church, G Maksym and G Parraga. Forced Oscillation Technique and MRI Predictions of Airway Reactance in Moderate-severe Asthma. ERS International Congress, Milan, Italy, September 9-13 2017.
- 2 **F Guo**, K Sheikh, R Peters, M Carl, A Fenster, G Parraga. Ultra-short Echo-time MRI Lung Segmentation using High-Dimensional Features and Continuous Max-Flow. International Workshop for Pulmonary Functional Imaging (IWPMFI), Seoul, Republic of Korea, March 2017.
- 3 **F Guo**, K Sheikh, R Peters, M Carl, A Fenster, G Parraga. Ultra-short Echo-time MRI Lung Segmentation using High-Dimensional Features and Continuous Max-Flow. International Society of Magnetic Resonance in Medicine (ISMRM), Annual Scientific Meeting, Honolulu, US, April 2017.
- 4 A Ouriadov, E Lessard, **F Guo**, HM Young, A Bhalla, DG McCormack, G Parraga. Accelerated Diffusion-weighted  $^{129}\text{Xe}$  MRI Morphometry of Emphysema in COPD and Alpha-1 Antitrypsin Deficiency Patients. International Society of Magnetic Resonance in Medicine (ISMRM), Annual Scientific Meeting, Honolulu, US, April 2017.
- 5 A Ouriadov, E Lessard, **F Guo**, HM Young, A Bhalla, M Kirby, HO Coxson, DG McCormack, G Parraga. Biomarkers of Emphysema in COPD and Alpha-1 Antitrypsin

- Deficiency:  $^{129}\text{Xe}$  MRI Morphomics. American Thoracic Society (ATS), Annual Scientific Meeting, Washington DC, US, May 2017.
- 6 **F Guo**, K Sheikh, R Eddy, DPI Capaldi, DG McCormack, A Fenster, and G Parraga. A Segmentation Pipeline for Measuring Pulmonary Ventilation Suitable for Clinical Workflows and Decision-making. International Society for Magnetic Resonance in Medicine (ISMRM), Annual Scientific Meeting, Singapore, May 2016.
  - 7 DPI Capaldi, A Lausch, K Sheikh, **F Guo**, DG McCormack, and G Parraga. Pulmonary Imaging Biomarkers of COPD for Personalized Treatment and Better Outcomes. International Society for Magnetic Resonance in Medicine (ISMRM), Annual Scientific Meeting, Singapore, May 2016.
  - 8 K Sheikh, **F Guo**, A Ouriadov, DPI Capaldi, S Svenningsen, M Kirby, DG McCormack, H O Coxson, and G Parraga. Ventilation Estimates in Severe Uncontrolled Asthma using 3D Single Breath-hold Ultra-short Echo Time MRI. International Society for Magnetic Resonance in Medicine (ISMRM), Annual Scientific Meeting, Singapore, May 2016.
  - 9 K Sheikh, **F Guo**, S Svenningsen, A Ouriadov, DPI Capaldi, RL Eddy, DG McCormack, and G Parraga, What Does Magnetic Resonance Imaging Signal-Intensity mean in Asthma? American Thoracic Society (ATS), Annual Scientific Meeting 2016, San Francisco, US, May 2016.
  - 10 **F Guo**, S Svenningsen, RL Eddy, M Fennema, DG McCormack, and G Parraga. Towards Image-guided Asthma Therapy: A Clinical Pipeline to Generate MRI Sub-segmental Ventilation Measurements. American Thoracic Society (ATS), Annual Scientific Meeting, San Francisco, US, May 2016.
  - 11 K Sheikh, A Ouriadov, **F Guo**, DPI Capaldi, DG McCormack, and G Parraga. Structure-Function Magnetic Resonance Imaging of Bronchopulmonary Dysplasia as an Alterna-

- tive to Pulmonary CT. International Workshop for Pulmonary Functional Imaging (IW-PFI), Edinburgh, UK, September 2015.
- 12 **F Guo**, S Svenningsen, A Fenster, and G Parraga. Automated Identification of Spatial Relationship between CT Airway and  $^3\text{He}$  MRI Ventilation Defects: Towards Airway-Targeted Asthma Bronchial Thermoplasty. International Workshop for Pulmonary Functional Imaging (IWPFPI), Edinburgh, UK, September 2015.
  - 13 S Svenningsen, **F Guo**, R Etemad-Rezai, DG McCormack, and G Parraga. Automated Registration-Segmentation Pipeline to Generate Lobar Ventilation Measurements in Diffuse and Localized Bronchiectasis. International Society for Magnetic Resonance in Medicine (ISMRM), Annual Scientific Meeting, Toronto, CANADA, May 2015.
  - 14 D Pike, DPI Capaldi, S Mattonen, **F Guo**, A Ward, DG McCormack, and G Parraga. Second-Order Texture Analysis of Hyperpolarized  $^3\text{He}$  MRI Beyond the Ventilation Defect. International Society for Magnetic Resonance in Medicine (ISMRM), Annual Scientific Meeting, Toronto, CANADA, May 2015.
  - 15 **F Guo**, S Svenningsen, A Fenster, and G Parraga. Three-Dimensional Pulmonary  $^1\text{H}$  MRI Multi-Region Segmentation Using Convex Optimization. International Society for Magnetic Resonance in Medicine (ISMRM), Annual Scientific Meeting, Toronto, CANADA, May 2015.
  - 16 **F Guo**, DG McCormack, and G Parraga. Relationship of Plethysmography Lung Volumes with  $^1\text{H}$  Magnetic Resonance Imaging Measurements. American Thoracic Society (ATS), Annual Scientific Meeting, Denver, US, May 2015.
  - 17 DPI Capaldi, **F Guo**, S Svenningsen, DG McCormack, and G Parraga. Fourier-Decomposition Pulmonary Magnetic Resonance Imaging Ventilation Defects in Ex-smokers: Relationship to Emphysema and  $^3\text{He}$  Ventilation Defects. Radiological Society of North America

(RSNA), Annual Scientific Meeting, Chicago, USA November 28-December 2, 2014.  
Trainee Prize Finalist.

- 18 D Pike, M Kirby, **F Guo**, DD Sin, HO Coxson, DG McCormack, and G Parraga. Sex, Airways Disease and Emphysema in Ex-smokers with and without Airflow Limitation. American Thoracic Society (ATS), Annual Scientific Meeting, San Diego, US, May 2014.
- 19 DPI Capaldi, **F Guo**, S Svenningsen, W Ma, K Sheikh, R Etemad-Rezai, J Leipsic, HO Coxson, DG McCormack, and G Parraga. Comparison of Pulmonary <sup>1</sup>H non-contrast and Hyperpolarized <sup>3</sup>He MRI Ventilation Abnormalities in Bronchiectasis and COPD. International Society for Magnetic Resonance in Medicine (ISMRM), Annual Scientific Meeting, Milano, Italy, May 2014.
- 20 K Sheikh, W Ma, **F Guo**, S Svenningsen, TM Peters, HO Coxson, DG McCormack, R Etemad-Rezai, and G Parraga. Two Dimensional Radial Pulmonary Ultra-short Echo Time <sup>1</sup>H MRI: Reproducibility in COPD and Bronchiectasis. International Society for Magnetic Resonance in Medicine (ISMRM), Annual Scientific Meeting, Milano, Italy, May 2014.

### **Peer Reviewed Oral Presentations ( n = 10 )**

- 1 S Svenningsen, P Nair, **F Guo**, DG McCormack and G Parraga. Is Ventilation Heterogeneity related to Asthma Control? Canadian Respiratory Research Network (CRRN) Annual General Meeting, Ottawa, Ontario, Canad, January 2017.
- 2 K Sheikh, **F Guo**, A Ouriadov, DPI Capaldi, S Svenningsen, M Kirby, DG McCormack, H O Coxson, and G Parraga. Ventilation Estimates in Severe Uncontrolled Asthma using 3D Single Breath-hold Ultra-short Echo Time MRI. International Society for Magnetic Resonance in Medicine (ISMRM), Annual Scientific Meeting, Singapore, May 2016.

- 3 K Sheikh, **F Guo**, S Svenningsen, A Ouriadov, DPI Capaldi, RL Eddy, DG McCormack, and G Parraga, What Does Magnetic Resonance Imaging Signal-Intensity mean in Asthma? American Thoracic Society (ATS), Annual Scientific Meeting, San Francisco, US, May 2016.
- 4 **F Guo**, S Svenningsen, A Fenster, and G Parraga. Automated Identification of Spatial Relationship between CT Airway and  $^3\text{He}$  MRI Ventilation Defects: Towards Airway-Targeted Asthma Bronchial Thermoplasty. International Workshop for Pulmonary Functional Imaging (IWPMFI), Edinburgh, UK, September 2015.
- 5 **F Guo**, S Svenningsen, A Fenster, and G Parraga. Three-Dimensional Pulmonary  $^1\text{H}$  MRI Multi-Region Segmentation Using Convex Optimization. International Society for Magnetic Resonance in Medicine (ISMRM), Annual Scientific Meeting, Toronto, CANADA, May 2015.
- 6 **F Guo**, S Svenningsen, E Bluemke, M Rajchl, J Yuan, A Fenster, and G Parraga. Automated Pulmonary Lobar Ventilation Measurements using Volume-matched Thoracic CT and MRI. SPIE Medical Imaging. International Society for Optics and Photonics, February 2015.
- 7 DPI Capaldi, **F Guo**, S Svenningsen, DG McCormack, and G Parraga. Fourier-Decomposition Pulmonary Magnetic Resonance Imaging Ventilation Defects in Ex-smokers: Relationship to Emphysema and  $^3\text{He}$  Ventilation Defects. Radiological Society of North America (RSNA), Annual Scientific Meeting, Chicago, USA November 28-December 2, 2014. Trainee Prize Finalist.
- 8 D Pike, M Kirby, **F Guo**, DD Sin, HO Coxson, DG McCormack, and G Parraga. Sex, Airways Disease and Emphysema in Ex-smokers with and without Airflow Limitation. American Thoracic Society (ATS), Annual Scientific Meeting, San Diego, US, May 2014.

- 9 **F Guo**, D. Pike, S Svenningsen, HO Coxson, J. Drozd, J Yuan, A Fenster, and G Parraga. Development and Application of Pulmonary Structure-Function Registration Methods: Towards Pulmonary Image-Guidance Tools for Improved Airway-Targeted Therapies and Outcomes. Proceedings of the Society for Photo-optical Instrumentation Engineers (SPIE), San Diego, USA, February 2014.
- 10 **F Guo**, M Ding, and X Zhang. Fast Image Matching based on Multi-Core DSP. IEEE Xplore, Intelligent Computation and Bio-Medical Instrumentation (ICBIMI), International Conference on IEEE, Wuhan, P.R.China, December 2011.

### **Peer Reviewed Poster Presentations ( n = 20 )**

- 1 A Ouriadov, E Lessard, **F Guo**, HM Young, A Bhalla, HO Coxson, DG McCormack, G Parraga. Biomarkers of Emphysema in COPD and Alpha-1 Antitrypsin Deficiency:  $^{129}\text{Xe}$  MRI Morphomics. American Thoracic Society Annual Scientific Meeting 2017, Washington DC, US, May 2017.
- 2 **F Guo**, K Sheikh, R Peters, M Carl, A Fenster, G Parraga. Ultra-short Echo-time MRI Lung Segmentation using High-Dimensional Features and Continuous Max-Flow. International Society of Magnetic Resonance in Medicine Annual Scientific Meeting (ISMRM), Annual Scientific Meeting, Honolulu, US, April 2017.
- 3 A Ouriadov, E Lessard, **F Guo**, HM Young, A Bhalla, DG McCormack, G Parraga. Accelerated Diffusion-weighted  $^{129}\text{Xe}$  MRI Morphometry of Emphysema in COPD and Alpha-1 Antitrypsin Deficiency Patients. International Society of Magnetic Resonance in Medicine Annual Scientific Meeting (ISMRM), Annual Scientific Meeting, Honolulu, US, April 2017.
- 4 **F Guo**, K Sheikh, R Peters, M Carl, A Fenster, G Parraga. Ultra-short Echo-time MRI Lung Segmentation using High-Dimensional Features and Continuous Max-Flow. In-

- ternational Workshop for Pulmonary Functional Imaging (IWPF), Seoul, Republic of Korea, March 2017.
- 5 **F Guo**, S Svenningsen, RL Eddy, M Fennema, DG McCormack, and G Parraga. Towards Image-guided Asthma Therapy: A Clinical Pipeline to Generate MRI Sub-segmental Ventilation Measurements. American Thoracic Society (ATS), Annual Scientific Meeting, San Francisco, US, May 2016.
  - 6 **F Guo**, K Sheikh, R Eddy, DPI Capaldi, DG McCormack, A Fenster, and G Parraga. A Segmentation Pipeline for Measuring Pulmonary Ventilation Suitable for Clinical Workflows and Decision-making. International Society for Magnetic Resonance in Medicine (ISMRM), Annual Scientific Meeting, Singapore, May 2016.
  - 7 DPI Capaldi, A Lausch, K Sheikh, **F Guo**, DG McCormack, and G Parraga. Pulmonary Imaging Biomarkers of COPD for Personalized Treatment and Better Outcomes. International Society for Magnetic Resonance in Medicine (ISMRM), Annual Scientific Meeting, Singapore, May 2016.
  - 8 K Sheikh, A Ouriadov, **F Guo**, DPI Capaldi, DG McCormack, and G Parraga. Structure-Function Magnetic Resonance Imaging of Bronchopulmonary Dysplasia as an Alternative to Pulmonary CT. International Workshop for Pulmonary Functional Imaging (IWPF), Edinburgh, UK, September 2015.
  - 9 **F Guo**, S Svenningsen, A Fenster, and G Parraga. Three-Dimensional Pulmonary  $^1\text{H}$  MRI Multi-Region Segmentation Using Convex Optimization. International Society for Magnetic Resonance in Medicine (ISMRM), Annual Scientific Meeting, Toronto, CANADA, May 2015.
  - 10 S Svenningsen, **F Guo**, R Etemad-Rezai, DG McCormack, and G Parraga. Automated Registration-Segmentation Pipeline to Generate Lobar Ventilation Measurements in Diffuse and Localized Bronchiectasis. International Society for Magnetic Resonance in



- Medicine (ISMRM), Annual Scientific Meeting, Toronto, CANADA, May 2015.
- 11 D Pike, DPI Capaldi, S Mattonen, **F Guo**, A Ward, DG McCormack, and G Parraga. Second-Order Texture Analysis of Hyperpolarized  $^3\text{He}$  MRI Beyond the Ventilation Defect. International Society for Magnetic Resonance in Medicine (ISMRM), Annual Scientific Meeting, Toronto, CANADA, May 2015.
  - 12 D Pike, M Kirby, **F Guo**, DD Sin, HO Coxson, DG McCormack, and G Parraga. Sex, Airways Disease and Emphysema in Ex-smokers with and without Airflow Limitation. American Thoracic Society (ATS), San Diego, US, May 2014.
  - 13 **F Guo**, DG McCormack, and G Parraga. Relationship of Plethysmography Lung Volumes with  $^1\text{H}$  Magnetic Resonance Imaging Measurements. American Thoracic Society (ATS), Annual Scientific Meeting, Denver, US, May 2015.
  - 14 DPI Capaldi, **F Guo**, S Svenningsen, W Ma, K Sheikh, R Etemad-Rezai, J Leipsic, HO Coxson, DG McCormack, and G Parraga. Comparison of Pulmonary  $^1\text{H}$  non-contrast and Hyperpolarized  $^3\text{He}$  MRI Ventilation Abnormalities in Bronchiectasis and COPD. International Society for Magnetic Resonance in Medicine (ISMRM), Annual Scientific Meeting, Milano, Italy, May 2014.
  - 15 K Sheikh, W Ma, **F Guo**, S Svenningsen, TM Peters, HO Coxson, DG McCormack, R Etemad-Rezai, and G Parraga. Two Dimensional Radial Pulmonary Ultra-short Echo Time  $^1\text{H}$  MRI: Reproducibility in COPD and Bronchiectasis. International Society for Magnetic Resonance in Medicine (ISMRM), Annual Scientific Meeting, Milano, Italy, May 2014.
  - 16 K Sheikh, W Ma, **F Guo**, S Svenningsen, TM Peters, HO Coxson, DG McCormack, R Etemad-Rezai, and G Parraga. Two Dimensional Radial Pulmonary Ultra-short Echo Time  $^1\text{H}$  MRI: Reproducibility in COPD and Bronchiectasis. Imaging Network of Ontario (ImNO), Annual Scientific Meeting, Toronto, ON, March 2014.

- 17 **F Guo**, D Pike, S Svenningsen, HO Coxson, JJ Drozd, J Yuan, A Fenster, and G Parraga. Development and Application of Pulmonary Structure-Function Registration Methods: Towards Pulmonary Image-Guidance Tools for Improved Airway-Targeted Therapies and Outcomes. Imaging Network of Ontario (ImNO), Annual Scientific Meeting, Toronto, ON, March 2014.
- 18 K Sheikh, W Ma, **F Guo**, S Svenningsen, TM Peters, HO Coxson, DG McCormack, R Etemad-Rezai, and G Parraga. Two Dimensional Radial Pulmonary Ultra-short Echo Time <sup>1</sup>H MRI: Reproducibility in COPD and Bronchiectasis. London Health Research Day (LHRD), Schulich School of Medicine and Dentistry, Western University, March 2014.
- 19 D Pike, M Kirby, **F Guo**, DD Sin, HO Coxson, DG McCormack, and G Parraga. Sex, Airways Disease and Emphysema in Ex-smokers with and without Airflow Limitation. London Health Research Day (LHRD), Schulich School of Medicine and Dentistry, Western University, March 2014.
- 20 **F Guo**, D Pike, S Svenningsen, HO Coxson, J Drozd, J Yuan, A Fenster, and G Parraga. Development and Application of Pulmonary Structure-Function Registration Methods: Towards Pulmonary Image-Guidance Methods for Improved Airway Targeted Therapies and Outcomes. London Health Research Day (LHRD), Schulich School of Medicine and Dentistry, Western University, March 2014.

## **PATENTS ( n = 3 )**

- 1 X Zhang, **F Guo**, L Yao, L Li, M Ding, Y Xiong, Z Yin, Y Wang. An Image Transmitting and Processing System based on FPGA and Multi-Core DSP. Chinese Innovation Patent. Application number: 201210402219.5
- 2 X Zhang, **F Guo**, M Zhang, X Li, M Ding, Y Xiong, Z Yin, Y Wang. A Fast Parallel Im-

age Matching Method based on Multi-core DSP. Chinese Innovation Patent. Application number: 201210398873.3 (Pending)

- 3 X Zhang, **F Guo**, Y Wang, L Li, M Ding, Y Xiong, Z Yin, Y Wang. A FPGA and DSP-based Data Transmitting System Using Ping-pang Mechanism. Chinese Innovation Patent. Application number: 201210401211.7 (Pending)

## **PROFESSIONAL MEMBERSHIPS**

2017 – 2018 International Workshop on Pulmonary Functional Imaging (IWPMI)

**Student Member**

2015 – 2016 International Workshop on Pulmonary Functional Imaging (IWPMI)

**Student Member**

2015 – 2016 Canadian Thoracic Society (CTS)

**Student Member**

2014 – 2015 International Society for Optics and Photonics (SPIE)

**Student Member**

2014 – present International Society of Magnetic Resonance in Medicine (ISMRM)

**Student Member**

2014 – present American Thoracic Society (ATS)

**Student Member**